ELECTROMAGNETIC ANALYSIS OF MICROWAVE COMPONENTS

Linda P.B. Katehi

January 1992

FINAL REPORT TO TEXAS INSTRUMENTS

Attn: Dr. Oren Kesler

ELECTROMAGNETIC ANALYSIS OF MICROWAVE COMPONENTS

Submitted by

Linda P.B. Katehi
Associate Professor
Department of Electrical Engineering and
Computer Science
The University of Michigan
Ann Arbor, MI 48109-2122

Period of Study: **January 1, 1991- December 31, 1991**
Cost: $15,000
Date of Submission: January 20, 1992.

A. FINAL REPORT

1. TEXAS INSTRUMENTS Award: EECS 390442

2. Period Covered By This Report: January 1, 1991-December 31, 1992

3. Title of Proposal: Electromagnetic Analysis of Microwave Components

4. Name of Institution: University of Michigan

5. Principal Investigator: Linda P.B. Katehi

7. List of Manuscripts Published or Submitted for Publication/Presentation Under Texas Instruments Sponsorship During This Reporting Period:

1. Norman L. VandenBerg and Linda P.B. Katehi, "Broadband Vertical Interconnects Using Slot-Coupled Shielded Microstrip Lines," IEEE Trans. on Microwave Theory and Techniques, Vol.40, No.1, January 1992, pp.81-88. **(Appendix A)**

2. Norman L. VandenBerg, "Full-wave Analysis of Microstrip-fed Slot Antennas and Couplers," Ph.D Dissertation, The University of Michigan, Ann Arbor, 1991. **(Appendix B)**

3. Norman L. VandenBerg and Linda P.B. Katehi, "Generalized Full-Wave Treatment of Shielded Multi-Layer Structures Using the Vector Wave Function Field Expansion Method," submitted to the Journal of Electromagnetic Waves and Applications (JEWA). **(Appendix C)**

4. L. Rexberg, N.I. Dib and L.P.B. Katehi, "A Microshield Line Loop Antenna for Sub-mm Wavelength Applications," submitted for presentation in the 1992 IEEE AP-S International Symposium in Chicago, Illinois, July 1992. **(Appendix D)**

8. List of Interim Reports Generated From This Work:

1. Norman L.VandenBerg, "Dimensions for Initial T-Bar Slot Measurements and Progress Report," December 13,1990. **(Appendix E)**

2. Norman L.VandenBerg, "An Investigation of a Stripline Slot Coupler," January 16, 1991. **(Appendix F)**

3. Norman L.VandenBerg, "On Deriving the Slot Impedance of T-Bar Fed Slot," January 29, 1991. **(Appendix G)**

4. Norman L.VandenBerg, "Corrected Results for Stripline Slot Coupler," March 7, 1991. **(Appendix H)**

5. Norman L.VandenBerg, "Report on Model Development for T-Bar Fed Slots," October 9, 1991. **(Appendix I)**

6. Norman L.VandenBerg, "Addendum to Radiation Laboratory Report RL877," October 14, 1991. **(Appendix J)**

I. Introduction

The research conducted during this study has concentrated on the following projects: a) Study of Broadband Vertical Interconnects Using Aperture Coupled Shielded Microstrip Lines b) Full-Wave Analysis of Microstrip Fed Slot Antennas c) Analysis of a Aperture Type Loop Antenna d) Development of Novel Techniques for the Treatment of Complex Geometries. In addition to Texas Instruments support, all of the above projects have been partially supported by NSF as part of the PYI matching funds program. The progress in each one of these projects is summarized below.

II. Study of Broadband Vertical Interconnects Using Aperture Coupled Shielded Microstrip Lines.

A full-wave space-domain integral equation analysis of aperture coupled shielded microstrip lines has been performed based on the Equivalence Principle. The formulation has the capability to model multi-layered substrates through the derivation of the associated dyadic Green's function which represents the layers through impedance boundary conditions (Appendix C). The method of Moments is used to solve for the line currents and slot voltage with even and odd mode excitations which are then intepreted through transmission line analysis to determine the two-port scattering parameters. A parametric study together with experimental data is presented which demonstrates the behavior of the coupler and the accuracy of the technique (see Appendices A,B).

III. Full-Wave Analysis of Microstrip Fed Slot Antennas.

Recently, complex systems have imposed new antenna requirements with demands for compact conformability, reduced weight, and higher order antenna functions such as electronic beam stearing, polarization control and power generation. A suitable alternative

approach employing stripline-fed series slots isolated from higher order modes by shorting pins has been widely applied in the past. However, despite the advantages of such an arrangement wide use has been hindered by the lack of accurate computational models. The necessity for such models is intensified by the narrow-bandwidth properties of these slot radiators.

During the reporting period, we have studied the properties of these slot antennas and the effect of the pin curtains on the resonant characteristics (see Appendix B) and we have investigated ways to increase their bandwidth. Specifically, we extensively analyzed, using the Full-Wave method described in Appendix B, the performance of a narrow cavity-backed slot which was excited by a T-shaped stripline. The analysis indicated the bandwidth of this slot is rather insensitive to the shape of the feeding stripline in contrary to what was anticipated. Results of these study are provided in the interim reports Appendices E,G and I.

Since the submission of the last interim report we have concentrated in the following two projects:

IV. Analysis of a Aperture Type Loop Antenna

We have initiated a study on aperture type antennas which could provide potential for wider bandwidth and the flexibility to integrate different planar technologies (microstrip with coplanar and slotline geometries). As a first step towards this study, we analyzed a microshield loop antenna excited by a microshield line (a coplanar with a shielding microcavity as shown in figure 1 of Appendix D). From the preliminary study performed so far, we have found that this antenna exhibits some interesting properties. In fact, as the results indicate, an appropriate monolithic matching network placed in front of the antenna could provide much wider bandwidths than the ones attained using simple longitudinal slots. The results presented in Appendix D by no means provide an optimum

design. They just unveil the existing potential. Further and most systematic work in this subject is planned for the next period.

V. Development of Novel Techniques for the Treatment of Complex Geometries

During the past two months we have initiated an effort in developing a hybrid technique for the analysis of complex circuit or antenna geometries. This technique is a combination of the integral equation and the finite element method. At the present time, the graduate student working in this problem has already formulated the part of the method which deals with the integral equation. He is currently developing the finite element part of the technique using edge elements. Due to the complexity of the problem the first results from this effort are expected at the end of the next reporting period.

APPENDIX A

Norman L. VandenBerg and Linda P.B. Katehi

Broadband Vertical Interconnects Using Slot-Coupled Shielded Microstrip Lines

Broadband Vertical Interconnects Using Slot-Coupled Shielded Microstrip Lines

Norman L. VandenBerg *Member, IEEE*, and Linda P. B. Katehi, *Senior Member, IEEE*

Abstract—**A full-wave space-domain integral equation analysis of aperture coupled shielded microstrip lines is presented based on the Equivalence Principle. The formulation includes the capability to model multi-layered substrates through the derivation of the associated dyadic Green's functions which represent the layers through impedance boundary conditions. The method of moments is used to solve for the line currents and slot voltage with even and odd mode excitations which are then interpreted through transmission line analysis to determine the two-port scattering parameters. A parametric study together with experimental data is presented which demonstrates the behavior of the coupler and the accuracy of the technique.**

I. Introduction

TRANSITIONS from microstrip to slotline have long been recognized as important circuit elements. Two such transitions can be combined to form interconnects between lines and by using lines on opposite sides of the slot plane, a vertical transition is made. The basic structure, in a variety of forms, has a wide range of applications to both broadband and narrowband connections and can be used as a building block for interconnects [1], phase shifters and inverters [2], directional couplers [3], filters [4], and many other microwave components [5].

The advent of monolithic techniques for microwave and millimeter-wave circuits has amplified the need for accurate analysis techniques to account for the effects of shielding structures as well as the interaction between circuit elements which may be closely spaced. These effects may not be accounted for by some methods such as simple transmission line analysis, especially as frequency increases. Additionally, high-frequency interconnect approaches are required which must be accurately modeled for design and also must fit well in a monolithic fabrication scheme. In this regard, the presented approach has significant appeal over via holes since it implements a vertical interconnect while requiring only planar elements which can be accurately modeled.

Numerous investigators have presented approximate analytical techniques to characterize these structures with applications to circuit elements [4]–[8]. A full-wave analysis for microstrip-to-slotline has been reported in [9] with applications to open structures. A quasi-static analysis has been provided in [10], however, this may not be sufficient, particularly for higher frequencies where end effects and higher order mode coupling become more significant. A more recent paper [11] presents a transmission line analysis with excellent results, however, the method does not account for radiation if the structure is open, interactions with the shielding if it is closed as in our case, or other electromagnetic effects which become more severe as frequency is increased. Hybrid methods which combine two-dimensional full-wave analysis with transmission line theory, as in [12], should certainly extend the validity of such models, however, may still not account for all discontinuity effects, especially since it is usually desirable to minimize the overall size which will tend to allow transitions to interact. Our approach uses a three-dimensional full-wave space-domain integral equation method employing the method of moments with Galerkin's procedure to account for all possible interactions.

Manuscript received March 1, 1991; revised July 10, 1991. This work was supported by Texas Instruments under contract UM/EECS:390442, the National Science Foundation under contract ECS:8657951, and by the NASA Center for Space Terahertz Technology.

The authors are with the Radiation Laboratory, the University of Michigan, 1301 Beal Avenue, Ann Arbor, MI 48109-2122.

IEEE Log Number 9103898.

II. Integral Equation Formulation and Network Analysis

The basic structure of the coupler to be discussed is as shown in Fig. 1. Variations on this geometry include cases with microstrip lines on the same side of the slot; multilayered substrates/superstrates; reverse couplers where the lines exit on the same wall; and with additional parallel slots and lines, among others, but can all be analyzed using the same approach.

The analysis proceeds as follows: the slot is replaced on both sides by an equivalent magnetic current backed by a perfectly conducting wall, representing the tangential electric field in the slot (all walls will be assumed to be perfect conductors). The problem is thereby separated into independent regions, coupled together by magnetic currents as shown in Fig. 2. This figure illustrates the treatment of finite slot thickness by introducing an intervening cavity. Eliminating the cavity and replacing $\bar{K}_L$ and $\bar{K}_U$ by $\bar{K}$ reduces the slot to the infinitesimally thin case which will be assumed here. Using the same current on either side enforces the continuity of the electric field in the slot. The fields in the cavities can now be written in terms of integrals as follows:

$$\bar{E} = -j\omega\mu \iint \bar{\bar{G}}_{eJ} \cdot \bar{J}\, dS' - \iint \bar{\bar{G}}_{eK} \cdot \bar{K}\, dS' \quad (1)$$

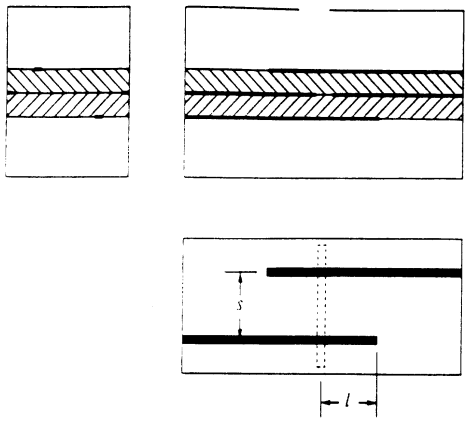

Fig. 1. Geometry of basic coupler.

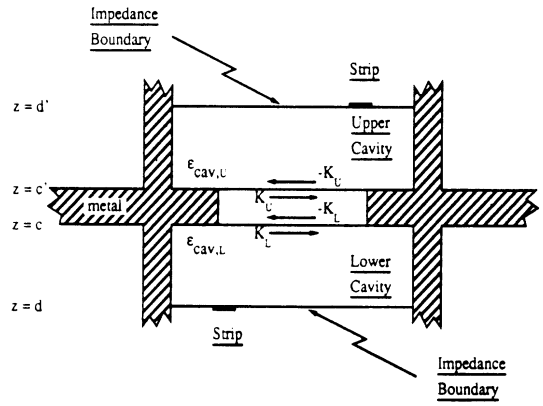

Fig. 2. Electric and equivalent magnetic currents for microstrip-to-microstrip coupler with a "thick" slot.

$$\bar{H} = \iint \bar{\bar{G}}_{mJ} \cdot \bar{J}\, dS' - j\omega\epsilon \iint \bar{\bar{G}}_{mK} \cdot \bar{K}\, dS' \qquad (2)$$

The subscripts on the Green's functions indicate whether the function is of the electric (e) or magnetic (m) field type for electric (J) or magnetic (K) currents.

By using the appropriate rectangular cavity Green's functions, the fields in the cavities satisfy the boundary conditions on the walls. The remaining boundary conditions, zero tangential electric fields on the strips and continuous tangential magnetic fields in the slot, allow us to write the integral equations which are

$$-j\omega\mu \iint_{\text{strip}_L} \bar{\bar{G}}_{eJ} \cdot \bar{J}_L\, dS' - \iint_{\text{slot}} \bar{\bar{G}}_{eK} \cdot \bar{K}\, dS' = 0^* \qquad (3)$$

$$\iint_{\text{strip}_L} \bar{\bar{G}}_{mJ} \cdot \bar{J}_L\, dS'$$

$$- j\omega \iint_{\text{slot}} [\epsilon_L \bar{\bar{G}}_{mK} + \epsilon_U \bar{\bar{G}}_{mK}] \cdot \bar{K}\, dS'$$

$$- \iint_{\text{strip}_U} \bar{\bar{G}}_{mJ} \cdot \bar{J}_U\, dS' = 0 \qquad (4)$$

$$\iint_{\text{slot}} \bar{\bar{G}}_{eK} \cdot \bar{K}\, dS' - j\omega\mu \iint_{\text{strip}_U} \bar{\bar{G}}_{eJ} \cdot \bar{J}_U\, dS' = 0^* \qquad (5)$$

where 0* implies that the field is nonzero at gap generator locations. Equations (3) and (5) are evaluated on the lower and upper strips respectively, and (4) on the slot. The subscripts U and L indicate whether the source is in the upper or lower cavity.

The longitudinal current components are now expanded in terms of piecewise sinusoidal functions with a Maxwellian transverse distribution satisfying the edge conditions for narrow strips and slots. In general, the currents are written in terms of both longitudinal and transverse components however, in this case, it will be assumed that both the slot and the strips are narrow enough so that the longitudinal components of current dominate their behavior and the transverse components can be neglected. The integral equations can now be written as a generalized matrix equation in conventional method of moments fashion. Using Galerkin's procedure, the matrix is nearly symmetric, the exception being the negative signs in the off-diagonal quadrants representing the coupling terms between the slot and microstrip lines:

$$\begin{bmatrix} \mathbf{Z}_{LL} & \mathbf{Y}_{LK} = -\mathbf{Z}_{KL}^T & 0 \\ \mathbf{Z}_{KL} = -\mathbf{Y}_{LK}^T & \mathbf{Y}_{LL} + \mathbf{Y}_{UU} & \mathbf{Z}_{KU} = -\mathbf{Y}_{UK}^T \\ 0 & \mathbf{Y}_{UK} = -\mathbf{Z}_{KU}^T & \mathbf{Z}_{UU} \end{bmatrix}$$

$$\begin{bmatrix} I_L \\ V_K \\ I_U \end{bmatrix} = \begin{bmatrix} 0^* \\ 0 \\ 0^* \end{bmatrix} \qquad (6)$$

where T indicates a transposed matrix and the "*" indicates the exceptions at the gap generators used for excitation of the lines. In addition to the relations indicated, for a symmetric structure only three of the submatrices are unique and the matrix will then have "mirror" symmetry with respect to the cross diagonal when properly loaded. The structures discussed here will be assumed lossless and symmetric for simplicity, although the more general case can be handled with the same approach.

The inverted matrix is then used with even and odd gap generator excitations at the line ends to find the currents on the microstrip lines. From the even and odd currents, even and odd impedances are found by measuring d defined as the relative distance from a standing wave maxima to the location of the slot. The expression for the reflection coefficient referenced to the slot then reduces to

$$\Gamma = -e^{j4\pi d/\lambda_g} \qquad (7)$$

which produces an impedance according to

$$Z = \frac{1 + \Gamma}{1 - \Gamma}. \qquad (8)$$

The even and odd impedances are then combined to form the Z-parameters which, because of the assumed sym-

metry are given by the simple expressions:

$$Z_{11} = \frac{Z_o + Z_e}{2} = Z_{22} \tag{9}$$

$$Z_{21} = \frac{Z_o - Z_e}{2} = Z_{12}. \tag{10}$$

Finally, the even and odd impedances may be combined to produce S-parameters through the transformations:

$$S_{11} = \frac{Z_{11}^2 - Z_{21}^2 - 1}{Z_{11}^2 + 2Z_{11} - Z_{21}^2 + 1} = S_{22} \tag{11}$$

$$S_{21} = \frac{2Z_{21}}{Z_{11}^2 + 2Z_{11} - Z_{21}^2 + 1} = S_{12} \tag{12}$$

which are used to characterize the coupling behavior.

III. Derivation of the Dyadic Green's Functions

In order to solve the integral equations, the Dyadic Green's functions must be known. They are solutions to the dyadic Helmholtz equations:

$$\nabla \times \nabla \times \bar{\bar{G}}_{eJ} - k^2 \bar{\bar{G}}_{eJ} = \bar{\bar{I}}\delta(\bar{R} - \bar{R}') \tag{13}$$

$$\nabla \times \nabla \times \bar{\bar{G}}_{mJ} - k^2 \bar{\bar{G}}_{mJ} = \nabla \times [\bar{\bar{I}}\delta(\bar{R} - \bar{R}')] \tag{14}$$

$$\nabla \times \nabla \times \bar{\bar{G}}_{mK} - k^2 \bar{\bar{G}}_{mK} = \bar{\bar{I}}\delta(\bar{R} - \bar{R}')] \tag{15}$$

$$\nabla \times \nabla \times \bar{\bar{G}}_{eK} - k^2 \bar{\bar{G}}_{eK} = \nabla \times \bar{\bar{I}}\delta(\bar{R} - \bar{R}') \tag{16}$$

where the primed vectors throughout, in this case $\bar{R}'$, indicate a function of the source coordinates. As can be seen, these equations are highly symmetric and in fact, once we have solved one set, the solution to the second set is almost trivial. Note however, that while the second pair of equations can be produced by application of the Duality Principle, the solutions cannot because duality does not apply to the boundary conditions [13]. The equations may be solved by a variety of techniques including vector potential methods or, as we have done, through a field expansion method which represents the solutions in terms of vector wave functions (VWF's). This latter approach has been developed to a straightforward procedure employing dyadic analysis to produce all components of the dyads in one exercise. For the sake of brevity, only the final results with be given here. A more detailed derivation is available in [14].

The Green's functions can be generalized to represent any layered structure of the type illustrated in Fig. 3. The use of impedance boundary conditions allow for the treatment of multi-layered substrates and superstrates as may be encountered in monolithic or other microwave circuits. The procedure is to find the Green's function for the layer containing the strip or slot by applying transmission line theory to the other layers to obtain the impedance boundary conditions (η) corresponding to each mode. Subsequently, the fields in the other layers can be found from the homogeneous solutions to (13)–(16) and a pair of coupling coefficients for each layer. The solutions are expanded in terms of LSE and LSM modes to facilitate finding the fields in the remaining layers since these modes are decoupled on the boundaries and can be individually matched to identical modes in adjacent layers. This also produces a one-to-one uniqueness in the impedance condition for each mode. The coupling coefficients are then readily found by matching the tangential field components at successive layers.

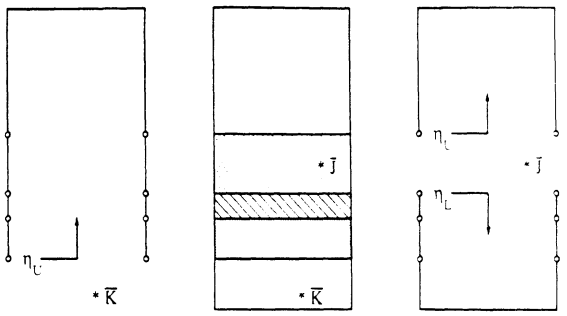

Fig. 3. Impedance boundary condition representation of a sample multilayered structure.

The impedance boundary conditions require the fields to satisfy

$$\eta = \frac{\hat{x} \cdot \bar{E}}{\hat{y} \cdot \bar{H}} : \frac{\hat{x} \cdot \nabla \times \bar{\bar{G}}_{mJ}}{\hat{y} \cdot \bar{\bar{G}}_{mJ}} = j\omega\epsilon\eta. \tag{17}$$

For simpler notation, η_e will be the wave impedance associated with the LSE modes and η_m will be used for the LSM modes. $\tilde{\eta}_e$ and $\tilde{\eta}_m$ will denote normalization to the wave impedances in each layer and are defined as

$$\tilde{\eta}_{ei} = \frac{k_{zi}\eta_{ei}}{\omega\mu} \quad \tilde{\eta}_{mi} = \frac{\omega\epsilon\eta_{mi}}{k_{zi}}. \tag{18}$$

These impedance boundary conditions derive from the recognition that the layered structures are simply sequential sections of homogeneously filled rectangular waveguide sections. We can then evaluate the impedance conditions using transmission line analysis and the wave impedances for the various layers as illustrated in Fig. 3. The impedances on a given layer upper boundary are found by the transmission line equation

$$\tilde{\eta}_{ei} = \frac{k_{zi}}{k_{z(i-1)}} \left[\frac{\tilde{\eta}_{e(i-1)} + j \tan k_{z(i-1)} l_{(i-1)}}{1 + j\tilde{\eta}_{e(i-1)} \tan k_{z(i-1)} l_{(i-1)}} \right] \tag{19}$$

$$\tilde{\eta}_{mi} = \frac{\epsilon_i k_{z(i-1)}}{\epsilon_{(i-1)} k_{zi}} \left[\frac{\tilde{\eta}_{m(i-1)} + j \tan k_{z(i-1)} l_{(i-1)}}{1 + j\tilde{\eta}_{m(i-1)} \tan k_{z(i-1)} l_{(i-1)}} \right] \tag{20}$$

where the index i is iterated from the top wall ($\eta_{e0} = \eta_{m0} = 0$) through successive lower layers to the layer of interest (l_i is the thickness of the ith layer). A similar process is used for the lower layers in which case the iteration proceeds from the lowest layer upwards and the wave impedance is negative.

The final results can be written as

$$\bar{\bar{G}}_{mJ} = \sum_{m=0}^{\infty}\sum_{n=0}^{\infty} \frac{2j(2-\delta_{mn})k_i}{abk_z(k_x^2+k_y^2)} \left\{ \frac{\begin{pmatrix} \overline{\mathfrak{M}}_{oo}[\tilde{\eta}_{mU};k_x,k_y,k_z(z-c)]\,\overline{\mathfrak{N}}'_{oo}[\tilde{\eta}_{mL};k_x,k_y,k_z(z'-d)] \\ \overline{\mathfrak{M}}_{oo}[\tilde{\eta}_{mL};k_x,k_y,k_z(z-d)]\,\overline{\mathfrak{N}}'_{oo}[\tilde{\eta}_{mU};k_x,k_y,k_z(z'-c)] \end{pmatrix}}{(\tilde{\eta}_{mU}-\tilde{\eta}_{mL})\cos k_z(c-d) - j(\tilde{\eta}_{mU}\tilde{\eta}_{mL}-1)\sin k_z(c-d)} \right.$$

$$\left. + \frac{\begin{pmatrix} \overline{\mathfrak{N}}_{ee}[\tilde{\eta}_{eU};k_x,k_y,k_z(z-c)]\,\overline{\mathfrak{M}}'_{ee}[\tilde{\eta}_{eL};k_x,k_y,k_z(z'-d)] \\ \overline{\mathfrak{N}}_{ee}[\tilde{\eta}_{eL};k_x,k_y,k_z(z-d)]\,\overline{\mathfrak{M}}'_{ee}[\tilde{\eta}_{eU};k_x,k_y,k_z(z'-c)] \end{pmatrix}}{(\tilde{\eta}_{eU}-\tilde{\eta}_{eL})\cos k_z(c-d) - j(\tilde{\eta}_{eU}\tilde{\eta}_{eL}-1)\sin k_z(c-d)} \right\} \quad \text{for } z \gtrless z' \tag{21}$$

and

$$\bar{\bar{G}}_{eJ} = \frac{1}{k_i^2}\hat{z}\hat{z}\delta(\bar{R}-\bar{R}') + \sum_{m=0}^{\infty}\sum_{n=0}^{\infty} \frac{2j(2-\delta_{mn})}{abk_z(k_x^2+k_y^2)}$$

$$\cdot \left\{ \frac{\begin{pmatrix} \overline{\mathfrak{M}}_{ee}[\tilde{\eta}_{eU};k_x,k_y,k_z(z-c)]\,\overline{\mathfrak{M}}'_{ee}[\tilde{\eta}_{eL};k_x,k_y,k_z(z'-d)] \\ \overline{\mathfrak{M}}_{ee}[\tilde{\eta}_{eL};k_x,k_y,k_z(z-d)]\,\overline{\mathfrak{M}}'_{ee}[\tilde{\eta}_{eU};k_x,k_y,k_z(z'-c)] \end{pmatrix}}{(\tilde{\eta}_{eU}-\tilde{\eta}_{eL})\cos k_z(c-d) - j(\tilde{\eta}_{eU}\tilde{\eta}_{eL}-1)\sin k_z(c-d)} \right.$$

$$\left. + \frac{\begin{pmatrix} \overline{\mathfrak{N}}_{oo}[\tilde{\eta}_{mU};k_x,k_y,k_z(z-c)]\,\overline{\mathfrak{N}}'_{oo}[\tilde{\eta}_{mL};k_x,k_y,k_z(z'-d)] \\ \overline{\mathfrak{N}}_{oo}[\tilde{\eta}_{mL};k_x,k_y,k_z(z-d)]\,\overline{\mathfrak{N}}'_{oo}[\tilde{\eta}_{mU};k_x,k_y,k_z(z'-c)] \end{pmatrix}}{(\tilde{\eta}_{mU}-\tilde{\eta}_{mL})\cos k_z(c-d) - j(\tilde{\eta}_{mU}\tilde{\eta}_{mL}-1)\sin k_z(c-d)} \right\} \quad \text{for } z \gtrless z' \tag{22}$$

where c and d are the upper and lower coordinates of the source layer. The δ_{mn} terms is the Kronecker delta defined as $\delta_{mn} = 1$ for $m = 0$ or $n = 0$ and zero otherwise. As indicated, the top lines apply for $z > z'$ and the bottom lines for $z < z'$ where primes throughout indicate functions of the source coordinates. The functions $\overline{\mathfrak{M}}$ and $\overline{\mathfrak{N}}$ are defined by

$$\overline{\mathfrak{M}}_{oo}[\eta,\alpha] = \eta\overline{M}_{ooo}[\alpha] + j\overline{M}_{ooe}[\alpha] \tag{23}$$

$$\overline{\mathfrak{M}}_{ee}[\eta,\alpha] = \eta\overline{M}_{eee}[\alpha] - j\overline{M}_{eeo}[\alpha] \tag{24}$$

$$\overline{\mathfrak{N}}_{oo}[\eta,\alpha] = \eta\overline{N}_{ooo}[\alpha] + j\overline{N}_{ooe}[\alpha] \tag{25}$$

$$\overline{\mathfrak{N}}_{ee}[\eta,\alpha] = \eta\overline{N}_{eee}[\alpha] - j\overline{N}_{eeo}[\alpha]. \tag{26}$$

The vector wave functions $\overline{M}$ and $\overline{N}$ are defined by

$$\overline{M} = \nabla \times \Psi\hat{x}_i = \frac{1}{k}\nabla \times \overline{N} \tag{27}$$

$$\overline{N} = \frac{1}{k}\nabla \times \nabla \times \Psi\hat{x}_i = \frac{1}{k}\nabla \times \overline{M} \tag{28}$$

where $k^2 = k_x^2 + k_y^2 + k_z^2$, Ψ is a scalar function and $\hat{x}_i$ is a unit vector called the "piloting vector" which determines the nature of the field expansion. In our case, choosing $\hat{x}_i = \hat{z}$, the normal to the layer interfaces, results in a correspondence between the leading $\overline{M}$ and $\overline{N}$ VWF's appearing in $\bar{\bar{G}}_{mJ}$ and the LSM and LSE modes, respectively. (In contrast, it should be noted that leading $\overline{M}$ and $\overline{N}$ functions correspond to the LSE and LSM modes, respectively, when they appear in $\bar{\bar{G}}_{eJ}$). The forms of Ψ are chosen to satisfy the boundary conditions on the walls of the cavity and are given by

$$\Psi_{\substack{ooo \\ eee}} = \begin{cases} \sin k_x x \sin k_y y \sin k_z z \\ \cos k_x x \cos k_y y \cos k_z z \end{cases} \tag{29}$$

$$\Psi_{\substack{ooe \\ eeo}} = \begin{cases} \sin k_x x \sin k_y y \cos k_z z \\ \cos k_x x \cos k_y y \sin k_z z \end{cases} \tag{30}$$

with $k_x = m\pi/a$, $k_y = n\pi/b$ and $k_z = \sqrt{k_i^2 - k_m^2 - k_n^2}$. The subscripts here and on the $\overline{M}$ and $\overline{N}$ functions indicate whether the trigonometric dependencies are even or odd (cosine or sine, respectively).

The solutions for the equivalent magnetic current $\overline{K}$ are virtually identical with the following notational replacements:

$$\overline{M} \Leftrightarrow \overline{N} \tag{31}$$

$$\bar{\bar{G}}_{eJ} \Rightarrow \bar{\bar{G}}_{mK} \tag{32}$$

$$\bar{\bar{G}}_{mJ} \Rightarrow \bar{\bar{G}}_{eK}. \tag{33}$$

Note that the $\overline{M} \Leftrightarrow \overline{N}$ replacements are what make these substitutions different from those dictated by the Duality Principle. It is these substitutions which compensate for the change in boundary conditions from the Dirichlet to Neumann conditions when the Duality Principle is applied. Expansion of these functions then yield all the components of the various Green's functions.

IV. Numerical and Experimental Results

A coupler with the geometry of Fig. 1 was analyzed using the above techniques. The parameters which can be varied in this design are numerous, consequently, only a few variations will be presented here. In all cases, although not required in general, symmetric geometry is maintained to simplify the even and odd mode analysis, as discussed above. Also, in all cases the cross-section for the cavity is 0.25 × 0.25 in.; the substrate is 0.025 in. thick with $\epsilon_r = 10.6$; and the slot and line widths are 0.025 in. The cavity length is varied for the numerical results and fixed at 2.0 in. for the measurements. This dimension does not affect the results since for all frequencies considered here, the cavity is below the cutoff frequency of the higher order microstrip modes and the reference plane was taken to be at the slot.

To illustrate the behavior of the coupler, we first examine the influence of various parameters at fixed operating frequencies. The effect of the line stub length (l) is shown in Fig. 4. It can be seen that the stub is initially too long for an ideal match at this frequency. However, as the stub is progressively shortened, a certain length "matches" the two port coupler and with further shortening the match gets progressively worse. We can interpret this effect by examining the equivalent circuit shown in Fig. 5. Variation of the stub length has the effect of changing the position of the current maxima (virtual shorts) and minima (virtual opens) on the lines relative to the slot, thus varying the degree of coupling through the slot represented by the coupling transformers. Consequently, the peak coupling occurs when line stub length places a current maximum below the slot or lengths in odd multiples of $\sim\lambda/4$. The opposite effect occurs when the line stub is approximately in multiples of $\lambda/2$ in length so that there is a virtual open circuit beneath the slot, in which case there would be very little coupling between the line and slot.

A similar effect is observed for variations in slot length (L_s) as illustrated in Fig. 6. Again using the transmission line analogy, one can interpret this effect by transforming the impedances at the ends of the slot to the center. These end impedances are nearly short circuits, the difference being due to fringing fields which extend beyond the ends of the slot line, fully accounted for by the full-wave analysis. At the matching length, the resulting transformed reactances at the center cancel the reactance associated with the junction, thereby matching the two ports. As the slot becomes very short, the field in the slot is effectively "short circuited," thus coupling is reduced. S_{21} then tends to zero while S_{11} approaches unity (since the structure is closed and assumed lossless). All of these effects would be expected to repeat as the slot length increases in multiples of λ, however, for the case studied here, the maximum slot length is limited by the dimensions of the shielding package which have been chosen to allow only the dominant microstrip mode to propagate.

To generate a frequency response, the programs are run at each frequency of interest and the slot and line lengths

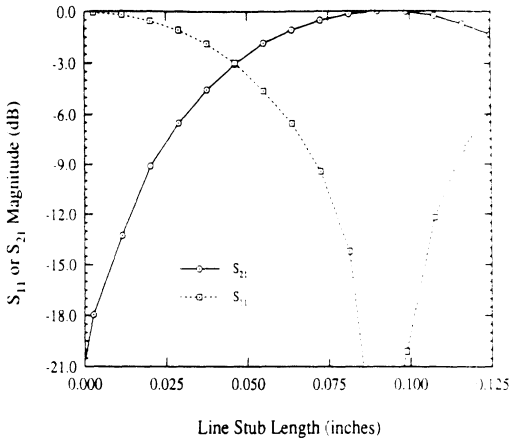

Fig. 4. Effect of the line stub length (l) on S_{21} and S_{11} magnitudes ($L_s = 0$, $L_s = 0.25$ inches and $f = 12.0$ GHz).

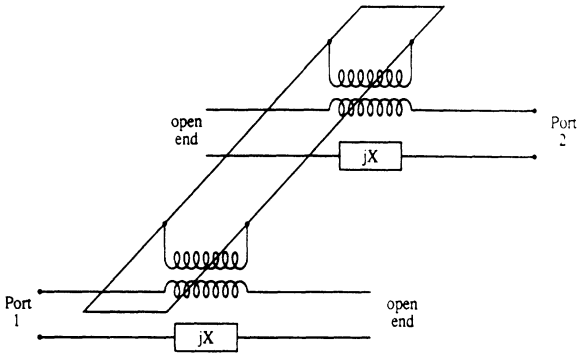

Fig. 5. Equivalent circuit for a 2-port coupler.

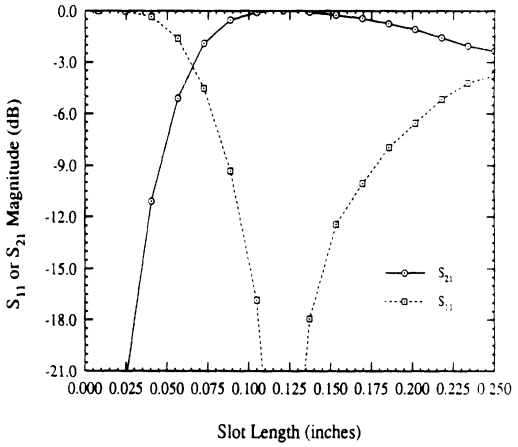

Fig. 6. Effect of the slot length on S_{21} and S_{11} magnitudes ($L_s = 0$, $l = 0.049$ inches and $f = 18.0$ GHz).

are varied to form a parametric database. (The most significant computation time is in the generation of the matrix. This takes approximately 30–45 min per frequency on an ~25 MIPS machine such as the IBM RS6000/320. One matrix is sufficient for all variations of slot and line stub lengths). The database is then scanned to assemble frequency response plots as a function of the geometric parameters. To verify the results, we have designed and constructed the fixture shown in Fig. 7. This fixture allows sample substrates with various line and slot dimensions to be installed in various combinations to allow fre-

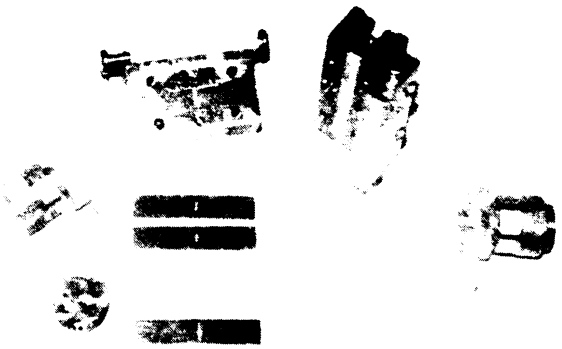

Fig. 7. Photograph of coupler fixture assembly.

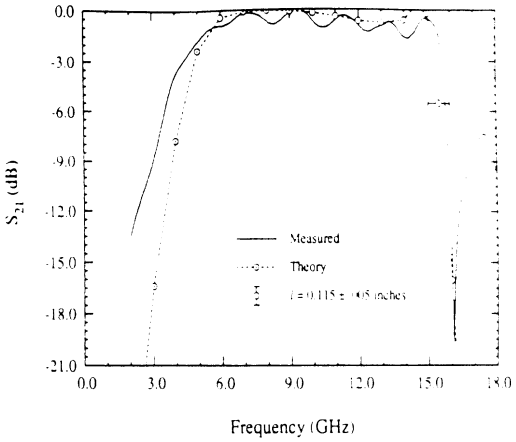

Fig. 8. Comparison of theory and experiment for S_{21} magnitudes with s = 0, l = 0.115 in., L_s = 0.250 in. The error bar indicates the influence on the high frequency corner by a ±0.005 inch change in stub length.

quency response measurements. A number of circuit boards were made in two sets: One set of boards was double-sided with a microstrip line etched to certain lengths relative to a slot etched in the ground plane on the opposite side. The second set was one-sided boards with microstrip lines of corresponding lengths designed to be held against the boards of the first set by the fixture.

Measurement of one of the assemblies is shown in Fig. 8 in comparison to corresponding numerical results. The position of the high frequency corner of the response was found to be very sensitive to the length of the line stub. As discussed above, this corner is controlled by the length at which the stub is approximately $\lambda/2$. Since the effective dielectric constant for the microstrip is approximately $\epsilon_{eff} = 7.8$ at 17.0 GHz, a null is predicted in the response in that neighborhood so there is good agreement with the results shown. A theoretical curve for $l = 0.115$ inches is also shown which gives an indication of the sensitivity to the stub length. The error bar on the high end indicates the sensitivity of the high frequency corner to a ±5 mil error in line stub length which is well within the expected tolerance errors for positioning the stubs relative to the slot, so we conclude that the results are in excellent agreement. In fact, we were able to move the upper board slightly toward the slot to expand the stub length somewhat which did shift the high corner to a lower frequency as expected. However, this also created problems with the match at the Eisenhart microstrip launchers so these results are not shown.

The "sidelobe" which can be seen at the high frequency end, is also attributed to tolerance errors for the line stub lengths. A difference in lengths would produce multiple nulls in the response at the high end which would be expected to have a sidelobe inbetween. Because of the high sensitivity to line length, owing in part to the high dielectric constant, the amplitude and span of the sidelobe is a strong function of the relative line stub lengths, which can also be observed when the boards are slightly shifted as described above. The sidelobes does not appear in the theoretical result since a difference in stub lengths between the upper and lower lines introduces an asymmetry which has not been included in the current numerical model and contradicts some of the assumptions stated for the network analysis. A more general model is planned to include this capability as well.

The ripple in all the measurements can be shown to result from mismatch at the microstrip launchers. The measurements are particularly sensitive to this connection because of the high dielectric constant of the substrate. They occurred in varying degrees throughout our measurements and are also influenced by small air gaps between the connector assembly, fixture and substrates. The ripple could probably be removed by more sophisticated deembedding techniques however this requires additional fixtures. Nevertheless, the ripple shown in the results presented here in not substantial and does not significantly interfere with the fundamental behavior of the devices. Also, the broadening of the low frequency response is typical in the measurements. We were not able to identify a direct cause for this effect, however, we suspect that it may also be related to the fixture/connector interface since we have not de-embedded these transitions. We also postulated that some of the anomalies might be caused by the side-wall grooves in the fixture which hold the double-sided board in place. This possibility was eliminated however by installing movable side-wall shorts which are visible in Fig. 7.

The remaining discrepancy is perhaps a slight additional loss found in some of the measured results. To deembed the losses for the structure, a through line was measured and the remaining measurements were post-processed to compensate for conductor and dielectric losses on the microstrip lines. This process however does not correct for losses associated with the slot including both conductor and dielectric losses and additional losses on the cavity walls, plus losses due to the added line lengths. The remaining differences are thus attributed to these factors together with measurement errors and are judged to be within acceptable limits.

Measurements on a different line stub length are shown

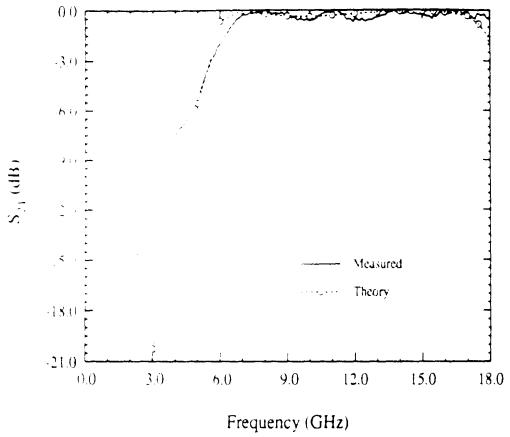

Fig. 9. Comparison of experiment and theory for S_{21} magnitudes with s = 0, l = 0.080 in., L_s = 0.250 in. illustrating the control of the high frequency corner with the line stub length by comparison with Fig. 8.

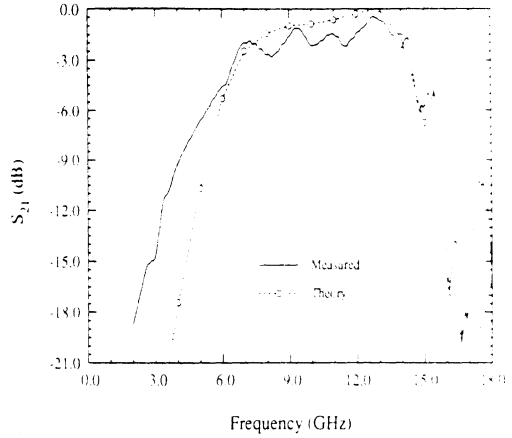

Fig. 11. Comparison showing the effect of line separation with l = 0.115 in., L_s = 0.250 in. and s = 0.125 in.

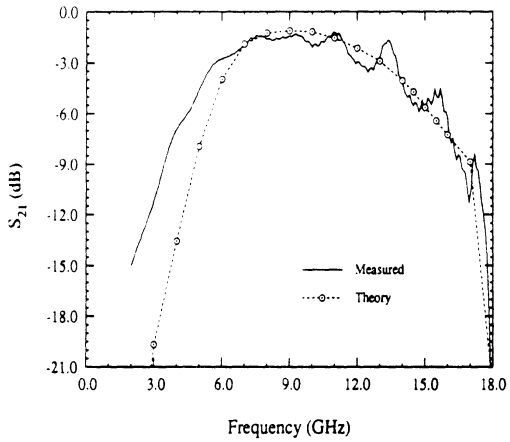

Fig. 10. Experimental and theory for S_{21} magnitudes with s = 0, l = 0.110 in., L_s = 0.153 in. showing the effect of shortening the slot length.

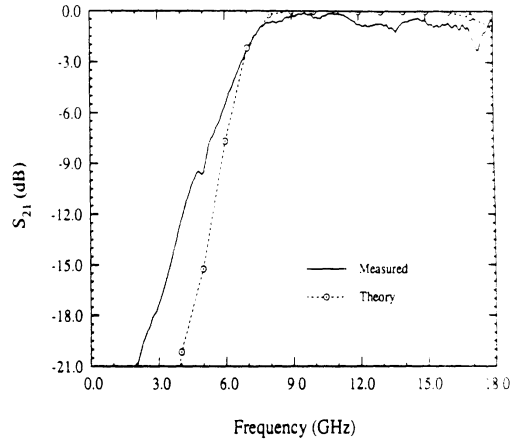

Fig. 12. The effect of line separation with shorter line stub length; l = 0.080 in., L_s = 0.250 in. and s = 0.125 in

in Fig. 9 again showing good agreement with the theoretical results. In this case, the shortening of the stub length has moved the high frequency corner out of the range of the measurements. What is interesting to note about this case is that the low frequency corner of the response is quite insensitive to this change in stub length. Also of particular interest is the wide bandwidth of this transition.

Fig. 10 illustrates the effect of shortening the slot length. One consequence is reduced coupling in the passband which was also demonstrated in Fig. 6. We also see in this result, some movement of the high frequency null due to a shortening of the line stub length.

The final plots, Figs. 11 and 12, show the influence of the line separation parameter (s) on the frequency response. The figures correspond to Figs. 8 and 9, respectively, which have s = 0, showing in general, a narrowing of the frequency passband as s is increased. This is to be expected since we have now introduced an additional length parameter which can influence the response through its relationship to wavelength. Here again, the numerical model is judged to have correctly predicted the coupler behavior after the experimental artifacts are considered.

V. Conclusion

A set of integral equations for aperture coupled shielded microstrip lines has been introduced based on Green's function integrals and the Equivalence Principle. The associated dyadic Green's functions in the form of waveguide LSE and LSM modes have been derived which allow for a full-wave analysis, accounting for all electromagnetic interactions of the microstrip—slot coupler, including the capability for multi-layered substrates and superstrates. By expanding the unknown line currents and slot voltage in terms of subsectional basis functions and applying the method of moments together with even and odd mode transmission line analysis, the two-port scattering coefficients can be determined to characterize the coupling behavior.

The frequency response plots shown demonstrate the utility of the structure as an interconnect. With proper selection of the geometric parameters such as line and slot widths, lengths, line separation, substrate heights and materials, the frequency response can be tailored to give the required center frequency, bandwidth, shape, etc. As has been shown, very wide bandwidths can be achieved which makes the structure very versatile. Avoidance of via-holes

for RF transitions and their inherent limitations by the use of planar structures to form vertical interconnects, together with the ability of the model to accurately predict the coupler behavior as demonstrated by experimental results, are especially important considerations for design of monolithic circuits. In addition, although the approach discussed here uses certain simplifying assumptions about the symmetry of the structures, the technique can be readily adapted to the general case.

REFERENCES

[1] R. H. Jansen, R. G. Arnold, and I. G. Eddison, "A comprehensive CAD approach to the design of MMIC's up to MM-wave frequencies," *IEEE Trans. Microwave Theory Tech.*, vol. 36, no. 2, pp. 208-219, Feb. 1988.

[2] K. G. Gupta, R. Garg, and I. J. Bahl, *Microstrip Lines and Slotlines*. Norwood, MA: Artech House, 1979.

[3] T. Tanaka, K. Tsunoda, and M. Aikawa, "Slot-coupled directional couplers between double-sided substrate microstrip lines and their applications," *IEEE Trans. Microwave Theory Tech.*, vol. 36, no. 12, pp. 1752-1757, Dec. 1988.

[4] E. A. Mariani and J. P. Agrios, "Slot-line filters and couplers," *IEEE Trans. Microwave Theory Tech.*, vol. MTT-18, no. 12, pp. 1089-1095, Dec. 1970.

[5] M. Aikawa and H. Ogawa, "Double-sided MIC's and their applications," *IEEE Trans. Microwave Theory Tech.*, vol. 37, no. 2, pp. 406-413, Feb. 1989.

[6] S. B. Cohn, "Slot line on a dielectric substrate," *IEEE Trans. Microwave Theory Tech.*, vol. MTT-17, no. 10, pp. 768-778, Oct. 1969.

[7] E. A. Mariani, C. P. Heinzman, J. P. Agrios, and S. B. Cohn, "Slot line characteristics," *IEEE Trans. Microwave Theory Tech.*, vol. MTT-17, no. 12, pp. 1091-1096, Dec. 1969.

[8] J. B. Knorr, "Slot-line transitions," *IEEE Trans. Microwave Theory Tech.*, vol. MTT-22, no. 5, pp. 548-554, May 1974.

[9] H. Yang and N. G. Alexopoulos, "A dynamic model for microstrip-slotline transition and related structures," *IEEE Trans. Microwave Theory Tech.*, vol. 36, no. 2, pp. 286-293, Feb. 1988.

[10] S. Yamamoto, T. Azakami, and K. Itakura, "Slit-coupled strip transmission lines," *IEEE Trans. Microwave Theory Tech.*, vol. MTT-14, no. 11, pp. 542-553, Nov. 1966.

[11] B. Schüppert, "Microstrip/slotline transitions: Modeling and experimental investigatin," *IEEE Trans. Microwave Theory Tech.*, vol. 36, no. 8, pp. 1272-1282, Aug. 1988.

[12] H. Ogawa, T. Hirota, and M. Aikawa, "New MIC power dividers using coupled microstrip-slot lines: Two-sided MIC power dividers," *IEEE Trans. Microwave Theory Tech.*, vol. MTT-33, no. 11, pp. 1155-1164, Nov. 1985.

[13] R. E. Collin, *Field Theory of Guided Waves*. McGraw-Hill, 1960, pp. 29-34.

[14] N. L. VandenBerg, "Full-wave analysis of microstrip-fed slot antennas and couplers," Ph.D. dissertation, The University of Michigan, Ann Arbor, 1991.

Norman L. VandenBerg (S'80-M'82-S'87-M'91) received the B.S.E.E., M.S.E.E., and Ph.D. degrees from the University of Michigan, Ann Arbor in 1980, 1982, and 1991, respectively.

From December 1982 to August 1987 he was employed by the Allied-Bendix Guidance Systems Division—Mishawaka Operations in Indiana, where he worked on experimental microwave and millimeter-wave spread spectrum radars. Since then he has worked at the Radiation Laboratory of the University of Michigan on numerical modeling of electromagnetic fields with applications to circuits and antennas.

Dr. VandenBerg is a member of Eta Kappa Nu, Tau Beta Pi and the IEEE AP, MTT and EMC societies.

Linda P. B. Katehi (S'81-M'84-SM'89) received the B.S.E.E. degree from the National Technical University of Athens, Greece, in 1977 and the M.S.E.E. and Ph.D. degrees from the University of California, Los Angeles, in 1981 and 1984 respectively.

In September 1984 she joined the faculty of the Electrical Engineering and Computer Science Department of the University of Michigan, Ann Arbor. Since then, she has been involved in the modeling and computer-aided design of millimeter-wave and near-millimeter-wave monolithic circuits and antennas.

In 1984 Dr. Katehi received the W. P. King Award and in 1985 the S. A. Schelkunoff Award from the Antennas and Propagation Society. In 1987 she received an NSF Presidential Young Investigator Award and an URSI Young Scientist Fellowship. She is a member of Sigma Xi.

APPENDIX B

Norman L. VandenBerg

Full-wave Analysis of Microstrip-fed Slot Antennas and Couplers

FULL-WAVE ANALYSIS OF MICROSTRIP-FED SLOT ANTENNAS AND COUPLERS

by

Norman L. VandenBerg
Linda P. B. Katehi

Radiation Laboratory
Department of Electrical Engineering and Computer Science
The University of Michigan
Ann Arbor, MI 48109-2122

Report No. 877
August 13, 1991

This report is the unabridged Ph.D. thesis of Dr. Norman L. VandenBerg of the Department of Electrical Engineering and Computer Science, the University of Michigan. The research was supported by the second author through a Graduate Student Research Assistantship with funding from various sources.

ACKNOWLEDGEMENTS

Before presenting the material in this document which is a summary of some of the work I have performed over the past four years, I would like to thank and acknowledge the many people and organizations who have contributed to and supported this research.

First, I would like to express my appreciation to the *Radiation Laboratory* and *Center for Space Terahertz Technology* for financial support in the form of a Research Assistantship. In particular, I thank Professors Val Liepa and Chen-To Tai for support in the first year of my return to the University, and Professor Linda Katehi for the remainder of my stay.

A special debt of gratitude is owed to Professor Tai for many years of teaching and encouragement. My first course with Professor Tai was a Junior level course on Vector Calculus in my undergraduate days and since then I have had the priviledge of attending three other courses under his tutelage, including his course on Dyadic Green's Functions in Electromagnetic Theory. As the reader may note, Professor Tai's approach has had a strong influence on my work and I hope that I have been able to contribute in at least a small way to the methodology he has pioneered.

I also would like to thank many of my associates who have contributed to this effort. I especially thank Dr. William Harokopus and Mr. Andrew Engel, not only for their friendship but their technical contributions as well. I also thank other members of our group, including Miss Emilie VanDeventer and Messrs. Nihad Dib and George Eleftheriades for numerous helpful discussions. In addition, I would like to express my appreciation to

Mr. Jeffrey Collins, Drs. Kamal Sarabandi, Kasra Barkeshli, Jianming Jin, Mark Ricoy, Leland Pierce and many others too numerous to mention for their contributions through both technical discussions and camaraderie.

A special mention is deserved by Dr. Harry LaFuse at the Allied-Bendix Guidance Systems Division - Mishawaka, whose generous contribution of many classic text and reference books on my departure to return to graduate studies, has made an invaluable contribution to this work. Also, I am grateful to the Allied-Bendix Communications Division for their support in making many fixtures and measurements for the verification of the slot antenna models, and to Texas Instruments for their similar support.

Finally I would like to thank my committee members for their helpful suggestions and careful review of the manuscript. I especially acknowledge my advisor, Dr. Linda Katehi, for her support and encouragement; she has been a constant source of ideas and insights which have greatly contributed to this work.

PREFACE

This dissertation expounds on the thesis that numerical methods and models can be developed which are sufficiently accurate to enable a microwave engineer to design microstrip-fed slot devices, without resorting to the empirical or semi-empirical techniques characteristic of more traditional methods. This possibility is of importance since the traditional approaches are typically time-consuming and therefore expensive. The advantages of numerical models are widely recognized, not only in the microwave industry, but in many other fields as well. With the rapid development of personal computers and workstations in terms of availability and processing power, computer-aided design (CAD) capability is becoming even more important for the development of technology.

Slots have been used in microwave designs for many years, particularly in waveguide-fed antenna arrays. Stripline, and more recently, microstrip line has also been used frequently, especially when there are active microwave components involved. It is now recognized that combinations of these types of structures and devices offer many significant advantages and will be needed to meet the requirements for advanced, state-of-the-art systems which have recently been proposed. Additional changes in technology have created the need for the ability to analyze structures with multi-layered substrates and superstrates and, increasingly, there has been a push toward higher and higher operating frequencies. For these reasons, we have developed the analytical and numerical methods to be presented here. It will be shown that many of these issues can be addressed in terms of computer-aided design and a considerable advancement and improvement over previous work in this

area has been achieved.

In Chapter I, we begin by introducing various historical aspects of the use of slots in microwave antennas. Through an examination of these devices in the context of present thinking, we will define the types of problems to be analyzed in this work; specifically, microstrip-fed slot antenna elements and couplers. The basis for the numerical models will be formulated in terms of integral equations. Full-wave analysis by means of exact Green's functions is used with a view toward application of these methods at high frequencies where other methods generally fail.

Chapter II will present the derivations of the necessary dyadic Green's functions which will be used throughout the remainder of the work. The approach will use a 'field expansion method' in terms of vector wave functions which will be explained and defined. The method of scattering superposition will be used and a method, not previously presented for this approach, employing impedance boundary conditions and field matching proceedures will be developed. The entire approach is in contrast to the more widely used, and perhaps more familiar, 'vector potential method'. Some comparisons to and deficiencies with past usages of the latter approach will be pointed out. To further illustrate the differences, the method of scattering superposition with impedance boundary conditions as applied to the vector potential method will be illustrated by example in the appendix, since even for this method, there are significant advantages that have not previously been presented.

The application of the method of moments to the integral equations is detailed in Chapter III. The treatment will be generalized to include variations on the main thrust of the work, to show how slots and lines can be modelled with arbitrary orientations relative to each other and the shielding structure. Although the applications discussed in later chapters impose some simplifying assumptions on the geometry, the material here lays the groundwork for further extensions to the work which may be implemented at a later date.

Also included in Chapter III is some discussion of mathematical relations and programming techniques which have been used to greatly reduce the computation time for generating the required matrix elements.

Several applications are introduced in Chapter IV. This chapter is devoted to the discussion of problems which can be reduced to two dimensions. The first part demonstrates the procedures for treatment of layered structures through analytical field matching throughout the layers. Applications discussed include the evaluation of transmission line parameters for microstrip lines and the visualization of field behavior for both shielded strip and slot lines. The accuracy of the technique is verified for microstrip by comparing to data available in the literature and a commercial computer-aided design package. The second part deals with the development of a model for scattering from vertical wires in waveguides. For small diameter wires, the model can be greatly simplified compared to approaches used in the literature. The validity of the model is verified by comparison to experimental measurements. The motivation for the work in this chapter is to support the modelling of applications discussed in Chapter VI.

Chapter V presents the analysis of microstrip-fed slot couplers. Expressions for the S-parameters which characterize their behavior are derived based on network analysis of even- and odd-mode excitations of the structure. The procedure is referred to as the 'Standing Wave Method' and involves an interpretation of the method of moments solution for currents on the microstrip lines. This has become a sort of 'standard' approach to a variety of similar problems but has some drawbacks as will be pointed out. Also presented in this chapter is a discussion of the fixture design and experimental results which verify the accuracy and validity of the method.

Chapter VI introduces the radiating slot or antenna element problem by deriving an alternative approach for finding network parameters. The method is based on an application

of the Reciprocity Theorem and is here referred to as the 'Reaction Theorem Method' or 'Reaction Method'. The requirement for a new approach is a consequence of the limitations of the Standing Wave Method discussed in Chapter V. Historically, the Reaction Method was introduced many years ago for application to simple waveguide-fed slots; however, for our use, the structures are more complex and as a result, the application of the method is also. The details of how the technique is applied are discussed in this chapter, together with experimental results which demonstrate the capability of the numerical methods.

In Chapter VII, a variation of the radiating slot is explored. In this case, a slot of finite thickness is introduced. Instead of simply making the slot thicker, which can also be modelled by this approach and has been treated through more approximate methods in the past, the case where the strip-fed slot couples to the radiating slot through an intervening section of rectangular waveguide is presented. In this case, we find the important result that the slots can be detuned to extend the bandwidth of the element.

The dissertation concludes with Chapter VIII which summarizes the techniques developed. The points where the effort is judged to have succeeded are outlined as well as where the numerical models fail. In the latter cases, the suspected causes for deficiencies in the approach are discussed along with recommendations for remedies. These issues form the basis of suggestions for the extension of this work and exploration of related areas. Specifically, the treatment of a 'T-bar' fed slot is discussed. This is a slot fed by a microstrip line terminated in a T-junction, whose branch arms are short-circuited to the cavity side walls. A similar device has been previously shown to provide extended bandwidth for cavity-backed aperture antennas.

A few final comments about the mechanics of this work: A number of programs were developed for the numerical modelling and analysis of the structures discussed as well as for post-processing the data. These programs were written almost exclusively in FORTRAN

and run on a variety of machines, including the University of Michigan IBM 3090/600E mainframe and IBM RS6000 workstations for the numerically intensive operations. A majority of the remaining processing was performed on HP/Apollo workstations, primarily a DN2500. The manuscript was typeset using LaTeX text processing software with macros developed at the University of Michigan for dissertation formats. Rectangular two-dimensional plots used throughout were produced in PostScript by a menu-driven plotting program developed jointly by the author and Dr. Leland Pierce. Smith Chart plots were produced by similar programs developed by the author. Most of the drawings were generated using either XFig or directly with PostScript and incorporated in PostScript form.

TABLE OF CONTENTS

DEDICATION ii

ACKNOWLEDGEMENTS iii

PREFACE v

LIST OF FIGURES xiii

LIST OF TABLES xvii

LIST OF APPENDICES xviii

CHAPTER

I. INTRODUCTION 1

1.1 Motivation and Background 1
1.2 General Description of Analysis Approach 5
1.3 Integral Equations and Notation 6
1.3.1 Dyadic Green's Functions for Physical Quantities 7
1.3.2 Dyadic Green's Functions for "Dual" Quantities 8
1.3.3 Integral Solutions to Helmholtz Equations using Dyadic Green's Functions 10
1.4 Formulation by Application of Boundary Conditions 12

II. DYADIC GREEN'S FUNCTIONS 18

2.1 Impedance Boundary Conditions for Layered Structures 19
2.2 Dyadic Green's Functions for an Infinite Covered Half Space 22
2.2.1 Magnetic Current 22
2.2.2 Electric Current 31
2.3 Dyadic Green's Functions for Layer Filled Rectangular Waveguides 33
2.3.1 The Parallel Plate Green's Function 33
2.3.2 Rectangular Waveguide with Electric Currents 37
2.3.3 Rectangular Waveguide with Magnetic Currents 39
2.4 Dyadic Green's Functions for Layer Filled Rectangular Cavities . . 40
2.4.1 Homogeneously Filled Rectangular Waveguide: TE and TM Modes 40
2.4.2 Cavity with Opposing Impedance Walls: Electric Current 43

2.4.3 TE and TM Modes in Homogeneously Filled Rectangular Waveguide and Cavities with Opposing Impedance Walls: Magnetic Currents 44

III. METHOD OF MOMENTS FORMULATION 47

3.1 Definition of Coordinate Systems and Basis Functions 47
3.2 Excitation Models 53
3.3 Expansion of the Dyadic Green's Functions for the Cavity 56
3.4 Identification and Reduction of the Integrands 61
3.5 Integration 64
3.6 Numerical Evaluation Considerations 66
3.6.1 Precomputation 66
3.6.2 Transformations 67
3.6.3 Convergence, Algorithms and Run-Time 69

IV. ANALYSIS OF TWO-DIMENSIONAL STRUCTURES 77

4.1 Application to General Multi-layered Shielded Microstrip Structures 78
4.1.1 LSE Modes 81
4.1.2 LSM Modes 83
4.1.3 Cross Terms 84
4.1.4 Integration of Power and Reaction terms 85
4.1.5 Applications 86
4.2 Application to Multi-layered Slotline 93
4.2.1 LSE Modes 93
4.2.2 LSM Modes 95
4.2.3 Cross Terms 96
4.2.4 Application to Finline and Suspended Finline 97
4.3 Scattering from Pins in Rectangular Waveguide 99
4.3.1 Reflection Coefficient Formula Derived from the Reciprocity Theorem 100
4.3.2 Method of Moments Formulation 102
4.3.3 Validation 103
4.4 Summary and Conclusions 113

V. COUPLING THROUGH STRIP-FED SLOTS 114

5.1 Network Analysis 114
5.2 Fixture Design 117
5.3 Numerical and Experimental Results 118
5.4 Summary 126

VI. ANALYSIS OF STRIP-FED RADIATING SLOTS 128

6.1 Equivalent Slot Impedance 130
6.2 Numerical Results and Measurements 132

6.3 Summary 145

VII. MODELLING OF THICK-SLOTS 147

7.1 Numerical Results for Waveguide Coupled Slots 148
7.2 Summary and Conclusions 153

VIII. CONCLUSIONS AND RECOMMENDATIONS FOR FUTURE WORK 154

8.1 Summary of Achievements 155
8.1.1 Two-Dimensional Analysis 155
8.1.2 Couplers 156
8.1.3 Radiating Slots 157
8.1.4 Modelling of Thick Slots 158
8.2 Model Limitations 159
8.3 Recommendation for Future Work 160

APPENDICES 164

BIBLIOGRAPHY 191

LIST OF FIGURES

Figure

1.1 A hypothetical integrated antenna employing numerous slot coupling structures. 4

1.2 Cavity layout and equivalent magnetic currents for a radiating slot. . . . 13

1.3 Electric and equivalent magnetic currents for microstrip-to-microstrip coupler with a 'thick' slot. 17

2.1 Impedance boundary condition representation of a multi-layered structure. 21

2.2 Layered infinite space as represented by impedance boundary conditions. . 26

2.3 Parallel plate waveguide coordinate system. 34

3.1 Cavity (x, y) and Strip-fixed (v, ν) Coordinate System. 48

3.2 Current Expansion Functions. 49

3.3 Slot-fixed Coordinate System (ζ, ξ). 50

3.4 Convergence behavior for several parameters of a centered shielded microstrip transmission line. Dimensions a = b = .25, w = h = .025, ϵ_r = 9.7. Terminal values at 1000 modes were Z_o = 49.63Ω, $\epsilon_{r,eff.}$ = 6.90, $H_X = 12.45A/\lambda_o$. 70

3.5 Convergence behavior for peak normalized resistance versus maximum mode number. 74

3.6 Convergence of resonant slot length as a function of the number of modes. 75

4.1 A shielded stripline, uniform in the $\hat{y}$ direction with multi-layered substrate and superstrate. 79

4.2 Effective relative dielectric constant for shielded microstrip on alumina (a = b = 250 mils, W = 25 mils, ϵ_r = 9.7) compared to measurements [19] and *Touchstone* [20]. 87

4.3 Characteristic impedance for shielded microstrip on alumina (a = b = 250 mils, W = 25 mils, ϵ_r = 9.7) compared to *Touchstone*. 87

4.4 Multi-mode propagation constants for the even modes in shielded microstrip (a = b = 12.7 mm, h = 1.27 mm, w = .635 mm ϵ_r = 8.875). . . 89

4.5 Stripline field distribution for the dominant propagating mode. 90

4.6 Microstrip field distribution for the dominant propagating mode. 91

4.7 Suspended microstrip field distribution for the dominant propagating mode. 92

4.8 Finline field distribution for the dominant mode. 97

4.9 Suspended finline field distribution for the dominant mode. 98

4.10 A grid of vertical wires in rectangular waveguide. 100

4.11 Equivalent circuit for single post in rectangular waveguide. 103

4.12 Magnitude and phase of reflection coefficient for a single conducting post in rectangular waveguide. Point match Method of Moments (MoM) results compared to the data of Marcuvitz [48] (λ/a = 1.4). 104

4.13 Behavior of element values for the equivalent circuit given by Marcuvitz [48] (λ/a = 1.4). 105

4.14 Input impedance as a function of post diameter with a matched load port. Post diameter increases in the counter-clockwise direction from d/a = .005 to d/a = .25 in .005 steps, demonstrating the transition of the input impedance from inductive to capacitive. 106

4.15 Shunt susceptance behavior for up to seven wires placed evenly spaced across waveguide cross section. 107

4.16 Reflection coefficient measurements for a single post at various offsets from the centerline compared to predictions from the simplified model. Wire diameters (d = .025, .033, .039 in.) increase in the counter-clockwise direction. 109

4.17 Reflection coefficient measurements for pairs of wires at various offsets from the centerline compared to predicted values. Wire diameters (d = .025, .033, .039 in.) increase in the counter-clockwise direction. 110

4.18 Measured reflection coefficients for centered wire grids of equal spacing and increasing number. Wire diameters (d = .025, .033, .039 in.) increase in the counter-clockwise direction. 111

4.19 Measured and predicted reflection coefficients for wire grids with a single pin missing in the sequence. Wire diameters (d = .025, .033, .039 in.) increase in the counter-clockwise direction. 112

5.1 Geometry of basic coupler. 115

5.2 Measurement of location of current peak relative to the slot for standing wave calculation. 116

5.3 Photograph of coupler fixture assembly. 118

5.4 Effect of the line stub length (l) on S_{21} and S_{11} magnitudes ($s = 0, L_s =$ 0.25 inches and f = 12.0 GHz). 119

5.5 Equivalent circuit for a 2-port coupler. 120

5.6 Effect of the slot length on S_{21} and S_{11} magnitudes ($s = 0, l =$ 0.049 inches and f = 18.0 GHz). 121

5.7 Comparison of theory and experiment for S_{21} magnitudes with $s = 0, l =$ 0.115 in., L_s = 0.250 inches. The error bar indicates the influence on the high frequency corner of a ±.005 inch change in stub length. 122

5.8 Comparison of experiment and theory for S_{21} magnitudes with $s = 0, l =$ 0.080 in., L_s = 0.250 inches, illustrating the control of the high frequency corner with the line stub length by comparison to Figure 5.7. 124

5.9 Experiment and theory for S_{21} magnitudes with $s = 0, l$ = 0.110 in., L_s = 0.153 inches, showing the effect of shortening the slot length. 125

5.10 Comparison showing the effect of line separation with l = 0.115 in., $L_s =$ 0.250 in. and s = 0.125 inches. 125

5.11 The effect of line separation with shorter line stub length; l = 0.080 in., L_s = 0.250 in. and s = 0.125 inches. 126

6.1 Strip-fed cavity-backed slots with coupler-fed and series-fed corporate feed arrangements. 129

6.2 Two cases for application of the Reciprocity Theorem. 130

6.3 Normalized resistance as a function of slot offset compared to Shavit's measurements [67]. 133

6.4 Resonant length as a function of slot offset compared to measurements [67]. 134

6.5 Photograph of slot assembly pieces in various stages of fabrication. . . . 136

6.6 Uncompensated peak normalized resistance as a function of slot offset compared to measurements for uncovered slots. 137

6.7 Predicted resonant length as a function of slot offset for uncovered slots. Crosses indicate actual test piece dimensions to be compared with the frequency curve corresponding to the measured resonant frequencies listed in the table. 139

6.8 Sensitivity of resonant length to cavity length dimension 'a'. 140

6.9 Compensated peak normalized resistance as a function of slot offset compared to measurements for uncovered slots. 142

6.10 Compensated peak normalized resistance as a function of slot offset compared to measurements for covered slots. 143

7.1 Stripline excitation of waveguide-coupled slots. 148

7.2 Typical variation of impedance as a function of slot length for a conventional 'thin' slot with slot offset as a parameter. 149

7.3 Variation of impedance as a function of slot length with the difference in top and bottom slot lengths as a parameter. 149

7.4 Slot coupling (resistance) and resonant length dependence on offset and waveguide length (L_W). 150

7.5 Apparent bandwidth comparison for identical slots versus slots with different lengths based on an interpretation of the relationship of slot length to wavelength. 151

7.6 Apparent bandwidth comparison for identical slots versus slots with different lengths based on calculations at selected frequencies. 152

8.1 T-Bar fed slot geometry. 161

8.2 Two cases for application of the Reciprocity Theorem for the T-bar fed case. 162

B.1 The derivative of an arbitrary discontinuous function. 177

LIST OF TABLES

Table

6.1 Measured resonant frequencies (GHz) and predicted resonant slot lengths for uncovered slots with compensated cavity length. (Deviation from actual slot length listed in parenthesis in percent.) 142

6.2 Measured resonant frequencies (GHz) and predicted resonant slot lengths for covered slots with compensated cavity length. (Deviation from the actual slot length listed in parenthesis in percent.) 144

LIST OF APPENDICES

Appendix

A. Vector Wave Function Expansions and Relations 165

B. On the Use of Vector Potential Functions for the Derivation of Green's Functions 171

B.1 Potential Theory Solutions for Electric Currents 171
B.2 Field Behavior - Electric Current 179
B.3 Potential Theory Solutions for Magnetic Currents 181
B.4 Field Behavior - Magnetic Current 183
B.5 Partitioning 184

C. On the Use of Vector Potentials with the Method of Scattering Superposition 186

CHAPTER I

INTRODUCTION

1.1 Motivation and Background

The use of slots in microwave circuits can be traced back at least as far as the 1940's to the research efforts associated with World War II. This is particularly true in antenna designs where slots have been used extensively as the primary radiating elements, but also in feed networks as couplers. With the advent of monolithic microwave circuit technology and also for more traditional construction methods, transitions from microstrip to slotline are also becoming increasingly important in the design of microwave and millimeter-wave circuit elements. Two such transitions can be combined to form interconnects between lines and by using lines on opposite sides of the slot plane, a vertical transition can be made without the use of via-holes. The basic structure, in a variety of forms, has a wide range of applications to both broadband and narrowband connections and can be used as a building block for interconnects [35], phase shifters and inverters [30], directional couplers [80], filters [50], and many other microwave components [2]. Whether used as a coupling element between guided wave structures or to free space, both applications require accurate analysis and design tools in order to minimize costly, time-consuming empirical techniques and rework.

Many papers have been published on the design of slotted waveguide antennas over the past forty-five years including "classics" by Stevenson [71] and Oliner [57], among

others [51, 4, 5]. Elliot and his associates have contributed many important works on the analysis and design of slotted rectangular waveguides and arrays [22, 23, 58, 70, 40]. More recently, slots which are fed by microstrip or stripline have received attention [59, 62, 67] due to advantages in cost, size, weight and conformability, among others. The development of variations and new analytical techniques is ongoing [16, 8, 17, 87].

Numerous investigators have also presented approximate analytical techniques to characterize these types of structures with applications to circuit elements [12, 49, 50, 41, 2]. For example, a quasi-static analysis has been provided in [89], however, this may not be sufficient, particularly for higher frequencies where end effects and higher order mode coupling become more significant. A more recent paper [66] presents a transmission line analysis with excellent results, however, similar shortcomings would be expected. Hybrid methods which combine two-dimensional full-wave analysis with transmission line theory as in [56], should certainly extend the validity of such models, but still may not account for all discontinuity effects. Exact methods for microstrip-to-slotline transitions have only recently begun to appear, such as the case reported in [91] which has applications to open structures.

For couplers, practical considerations suggest that a shielding structure will almost always be present. In fact, in many cases, a shielding structure must be introduced in order to reduce crosstalk and to control undesirable coupling to other structures in the package (for example, DC control lines in phase shifters have been known to unexpectedly become part of the microwave circuit). For antennas, cavity-backed slots have been used for similar reasons; for example, to reduce internal mutual coupling on the feed network side of an array. This often both simplifies the design process and improves the achievable performance. For instance, it has been shown that the internal isolation of the slots in phase steerable antennas can significantly improve scanning performance [47].

For these reasons, the slots studied here will be enclosed by a cavity at least on one side. The dimensions of the cavity can have a strong influence on the electrical behavior of the slot. In some cases, these dimensions are used to control the slot characteristics and in others they are used to suppress undesirable effects. In practice, slot antennas are often covered by a protective dielectric sheet. The capability to handle these cases will also be included in the analysis discussed here by employing the exact Green's function for an infinite covered ground plane. This function will be evaluated by a combination of numerical and analytical techniques as described in [36], however, the details will not be reiterated here. Also included is the capability to model multi-layered substrates and superstrates which is becoming increasingly important for monolithic circuits and for systems which may combine many circuit functions through three dimensional integration over multiple layers.

An example of a hypothetical structure which employs numerous transitions of the type to be analyzed is illustrated in Figure 1.1. Shown is a slot antenna array loosely based on a conventional waveguide fed slot array. Conventional arrays typically use waveguide-to-waveguide slot coupling to feed slotted waveguide branch lines. Here we assume the individual slots are fed by microstrip-to-microstrip slot couplers as illustrated by the lowest three layers of Figure 1.1. Each radiating slot is internally isolated by a cavity which may contain active devices for power generation for example. The feed network may contain additional active sources coupled by combinations of microstrip and slotlines and may be built on multilayered substrates for integration of additional antenna functions, such as phase control, frequency conversion, detection, etc. This example illustrates just one application with features drawn from topics being considered in the current literature which also verifies the need for more accurate and advanced analysis and design tools for the types of structures to be considered.

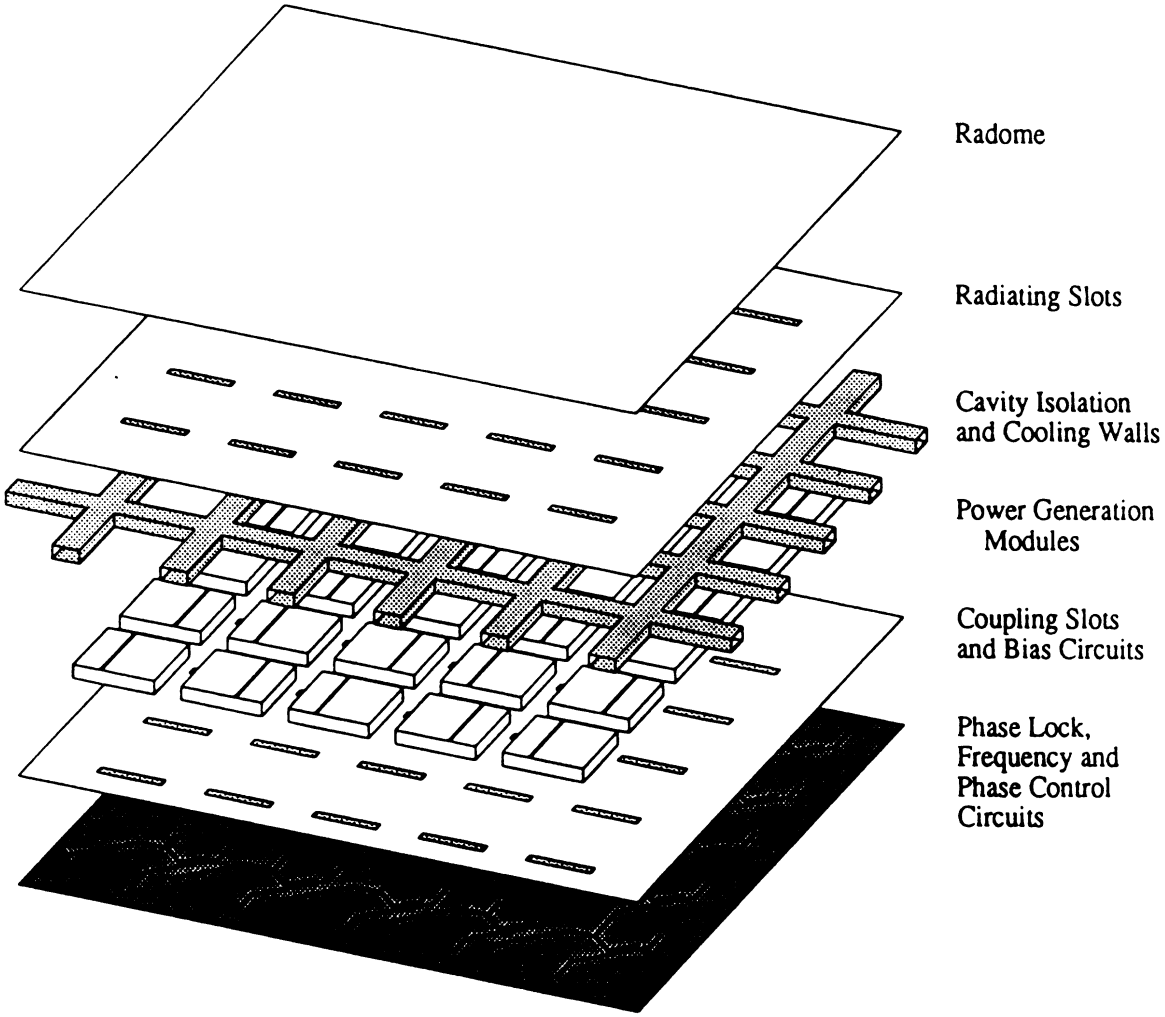

Figure 1.1: A hypothetical integrated antenna employing numerous slot coupling structures.

1.2 General Description of Analysis Approach

For coupling through slots, the distribution (shape, amplitude and phase) of the field in the slot is vital to the determination of the slot coupling behavior. For radiating slots, this distribution has been investigated by Elliott [23] and others [59, 67, 70] by treating the case of an isolated slot in an infinite ground plane. With the Green's function for a half space and the fields in rectangular waveguide, they were able to write an integral equation. The equation was solved by the Method of Moments to determine the field distribution. Subsequently, the scattering parameters of the slot were found by an application of the Reciprocity Theorem.

The same approach will be used here for radiating slots, referred to here as the 'Reaction Theorem Method' or 'Reaction Method'; although the presence of the strip and, especially for microstrip, the inhomogeneous filling of the rectangular cross section precludes the use of simple rectangular waveguide field solutions. In previous works [67], the presence of the strip has been neglected by assuming a similarity between the strip modes and empty waveguide modes. This not only places certain restrictions on the position of the strip between the ground planes but also does not take into account the influence of the strip on the fields near the slot. Here, the formulation will be generalized to include not only the case of stripline where the cross section is homogeneously filled, but also the possibility of multiple layer substrates and superstrates, allowing microstrip or more complex structures to be analyzed. This will require the solution to the two-dimensional 'waveguide' problem in addition to the three-dimensional 'cavity' solution which is the primary focus of this work. The relative position of the strip within the shield will also be unrestricted which has not been the case in some of the previous works.

For couplers, the same shielded strip substrate/superstrate capability will be included. However, in this case, an alternative method will be used to extract the coupling parame-

ters. This will be referred to as the 'Standing Wave Method' and is based on a more detailed modelling of the strip current. The scattering parameters are extracted from the positions of peaks in the strip current standing wave pattern, evaluated for even and odd excitations of the structure. Although the Reciprocity Method is more general, the Standing Wave Method is somewhat simpler and therefore may be more convenient.

In many cases the thickness of the ground plane is very small and the slot can be considered infinitesimally thin. However, for both types elements it may be necessary to make a 'thick' slot for structural purposes or heat dissipation, for example. In fact, we have found that this feature may be used to another advantage which is to broaden the operating bandwidth of the element. These cases can be treated by the same techniques and will be included in the formulation.

Highly accurate models are needed to reliably design these types of elements. Therefore, a full-wave space-domain integral equation approach solved by the Method of Moments will be used as opposed to quasi-static, modified quasi-static dispersion analysis, or other similarly limited techniques. This approach is preferred since we can find exact Green's functions for the structures described which account for all possible electromagnetic interactions. It also allows application of these techniques to problems without restriction as to the size of dimensions relative to wavelength.

1.3 Integral Equations and Notation

In this section, appropriate integral equations will be derived. One of the primary purposes of this section is to introduce the notation and conventions used throughout the text and some of the fundamental equations and relationships which will be needed.

1.3.1 Dyadic Green's Functions for Physical Quantities

It is well known that time harmonic electromagnetic fields must satisfy Maxwell's Equations ($e^{j\omega t}$ time convention assumed and suppressed throughout):

$$\nabla \times \overline{\mathrm{E}} = -j\omega\mu\,\overline{\mathrm{H}} \tag{1.1}$$

$$\nabla \times \overline{\mathrm{H}} = \bar{\mathrm{J}} + j\omega\epsilon\,\overline{\mathrm{E}} \tag{1.2}$$

where the constitutive relations $\overline{\mathrm{D}} = \epsilon\,\overline{\mathrm{E}}$ and $\overline{\mathrm{B}} = \mu\,\overline{\mathrm{H}}$ have been assumed. Also, $\bar{\mathrm{J}}$ is defined in terms of the movement of electric charge with time by the Continuity relation:

$$\nabla \cdot \bar{\mathrm{J}} = -j\omega\rho \tag{1.3}$$

Understanding these to be the governing independent equations, by taking the divergence of Equations (1.1) and (1.2), it is found that the fields also obey

$$\nabla \cdot \overline{\mathrm{E}} = \frac{\rho}{\epsilon} \tag{1.4}$$

$$\nabla \cdot \overline{\mathrm{H}} = 0 \tag{1.5}$$

That the fields must satisfy the Helmholtz wave equation is readily derived by taking the curl of Equation (1.1) and substituting (1.2) into the result, yielding

$$\nabla \times \nabla \times \overline{\mathrm{E}} - k^2\,\overline{\mathrm{E}} = -j\omega\mu\bar{\mathrm{J}} \tag{1.6}$$

where $k^2 = \omega^2\mu\epsilon$. Similarly, it can be shown that $\overline{\mathrm{H}}$ must satisfy

$$\nabla \times \nabla \times \overline{\mathrm{H}} - k^2\,\overline{\mathrm{H}} = \nabla \times \bar{\mathrm{J}} \tag{1.7}$$

Dyadic Green's functions can be introduced to represent the solutions to these equations for infinitesimal current sources. For instance, $\bar{\bar{\mathrm{G}}}_{e\mathrm{J}}$ will be used to represent the solution to Equation (1.6) in the form

$$\bar{\bar{\mathrm{G}}}_{e\mathrm{J}} = [\,\overline{\mathrm{E}}^{(x)}\hat{x} + \overline{\mathrm{E}}^{(y)}\hat{y} + \overline{\mathrm{E}}^{(z)}\hat{z}]$$

Here, $\overline{E}^{(x)}$ is the field resulting from an $\hat{x}$ directed current source

$$\bar{J}^{(x)} = -\frac{\delta(\bar{R} - \bar{R}')}{j\omega\mu}\hat{x} \tag{1.9}$$

and so forth for the $\hat{y}$ and $\hat{z}$ components so that

$$\nabla \times \nabla \times \bar{\bar{G}}_{eJ} - k^2\bar{\bar{G}}_{eJ} = \bar{\bar{I}}\delta(\bar{R} - \bar{R}') \tag{1.10}$$

where

$$\bar{\bar{I}}\delta(\bar{R} - \bar{R}') = -j\omega\mu[\bar{J}^{(x)}\hat{x} + \bar{J}^{(y)}\hat{y} + \bar{J}^{(z)}\hat{z}] \tag{1.11}$$

Likewise, for the magnetic fields, the dyadic Green's function must satisfy

$$\nabla \times \nabla \times \bar{\bar{G}}_{mJ} - k^2\bar{\bar{G}}_{mJ} = \nabla \times [\bar{\bar{I}}\delta(\bar{R} - \bar{R}')] \tag{1.12}$$

where $\bar{\bar{G}}_{mJ}$ represents

$$\bar{\bar{G}}_{mJ} = -j\omega\mu[\overline{H}^{(x)}\hat{x} + \overline{H}^{(y)}\hat{y} + \overline{H}^{(z)}\hat{z}] \tag{1.13}$$

From Equation (1.10) and (1.12) it is seen that $\bar{\bar{G}}_{eJ}$ is related to $\bar{\bar{G}}_{mJ}$ by

$$\nabla \times \bar{\bar{G}}_{eJ} = \bar{\bar{G}}_{mJ} \tag{1.14}$$

$$\nabla \times \bar{\bar{G}}_{mJ} = \bar{\bar{I}}\delta(\bar{R} - \bar{R}') + k^2\bar{\bar{G}}_{eJ} \tag{1.15}$$

The terminology and notation which we use to refer to these functions is that $\bar{\bar{G}}_{eJ}$ is the dyadic Green's function of the electric field type (subscript 'e') for an electric current (subscript 'J'). Similarly, $\bar{\bar{G}}_{mJ}$ represents the dyadic Green's function of the magnetic field type (subscript 'm') for an electric current.

1.3.2 Dyadic Green's Functions for "Dual" Quantities

The Duality Principle entails the proposal of a system of equations where

$$\nabla \times \overline{E} = -j\omega\mu\,\overline{H} - \overline{K} \tag{1.16}$$

$$\nabla \times \overline{H} = j\omega\epsilon\,\overline{E} \tag{1.17}$$

$\overline{K}$ representing a fictitious magnetic current. This current in introduced as a matter of convenience by which we can represent tangential electric fields in terms of equivalent magnetic currents according to the Equivalence Principle. We then can take advantage of the duality between these and the "physical" quantity equations to generate solutions to the equations [32, pp.98-116]. The Helmholtz wave equations for this system are

$$\nabla \times \nabla \times \overline{H} - k^2 \overline{H} = -j\omega\epsilon \overline{K} \tag{1.18}$$

$$\nabla \times \nabla \times \overline{E} - k^2 \overline{E} = -\nabla \times \overline{K} \tag{1.19}$$

Using the representation

$$\bar{\bar{G}}_{mK} = [\overline{H}^{(x)}\hat{x} + \overline{H}^{(y)}\hat{y} + \overline{H}^{(z)}\hat{z}] \tag{1.20}$$

$\bar{\bar{G}}_{mK}$ satisfies

$$\nabla \times \nabla \times \bar{\bar{G}}_{mK} - k^2 \bar{\bar{G}}_{mK} = \bar{\bar{I}}\delta(\bar{R} - \bar{R}') \tag{1.21}$$

where the inhomogeneous term represents

$$\bar{\bar{I}}\delta(\bar{R} - \bar{R}') = -j\omega\epsilon[\overline{K}^{(x)}\hat{x} + \overline{K}^{(y)}\hat{y} + \overline{K}^{(z)}\hat{z}] \tag{1.22}$$

with

$$\overline{K}^{(x)} = -\frac{\delta(\bar{R} - \bar{R}')}{j\omega\epsilon}\hat{x} \tag{1.23}$$

and so forth for the $\hat{y}$ and $\hat{z}$ components. Similarly, $\bar{\bar{G}}_{eK}$ satisfies

$$\nabla \times \nabla \times \bar{\bar{G}}_{eK} - k^2 \bar{\bar{G}}_{eK} = \nabla \times \bar{\bar{I}}\delta(\bar{R} - \bar{R}') \tag{1.24}$$

where $\bar{\bar{G}}_{eK}$ represents

$$\bar{\bar{G}}_{eK} = j\omega\epsilon[\overline{E}^{(x)}\hat{x} + \overline{E}^{(y)}\hat{y} + \overline{E}^{(z)}\hat{z}] \tag{1.25}$$

Here it is evident that

$$\nabla \times \bar{\bar{G}}_{mK} = \bar{\bar{G}}_{eK} \tag{1.26}$$

$$\nabla \times \bar{\bar{G}}_{eK} = \bar{\bar{I}}\delta(\bar{R} - \bar{R}') + k^2 \bar{\bar{G}}_{mK} \tag{1.27}$$

The notation and terminology are the same as before with the magnetic current represented by the subscript 'K'.

1.3.3 Integral Solutions to Helmholtz Equations using Dyadic Green's Functions

Once $\bar{\bar{G}}_{eJ}$, $\bar{\bar{G}}_{mJ}$, $\bar{\bar{G}}_{eK}$ and $\bar{\bar{G}}_{mK}$ are known for a particular geometry and set of boundary conditions, it is possible to find the corresponding field quantity for any distribution of electric or magnetic current. The relationship to be used can be derived from the vector-dyadic Green's second identity:

$$\begin{aligned} &\iiint [\bar{P} \cdot \nabla \times \nabla \times \bar{\bar{Q}} - (\nabla \times \nabla \times \bar{P}) \cdot \bar{\bar{Q}}]\, dV \\ &= -\iint_S \left\{ [\hat{n} \times \nabla \times \bar{P}] \cdot \bar{\bar{Q}} + (\hat{n} \times \bar{P}) \cdot \nabla \times \bar{\bar{Q}} \right\} dS \end{aligned} \tag{1.28}$$

To find the integral solution to

$$\nabla \times \nabla \times \bar{E} - k^2 \bar{E} = -j\omega\mu \bar{J} \tag{1.29}$$

we use the electric dyadic Green's function with an electric current source, $\bar{\bar{G}}_{eJ}$. By letting $\bar{P} = \bar{E}$ and $\bar{\bar{Q}} = \bar{\bar{G}}_{eJ}$ in Equation (1.28), we find that

$$\begin{aligned} \bar{E}(\bar{R}) \;=\; & -j\omega\mu \iiint \bar{J}(\bar{R}') \cdot \bar{\bar{G}}_{eJ}(\bar{R}', \bar{R})\, dV' \\ & - \iint_S \left\{ [\hat{n} \times \nabla' \times \bar{E}(\bar{R}')] \cdot \bar{\bar{G}}_{eJ}(\bar{R}', \bar{R}) \right. \\ & \left. + [\hat{n} \times \bar{E}(\bar{R}')] \cdot \nabla' \times \bar{\bar{G}}_{eJ}(\bar{R}', \bar{R}) \right\} dS' \end{aligned} \tag{1.30}$$

Note that in the process of deriving this result, the notation of $\bar{R}$ and $\bar{R}'$ has been interchanged in keeping with our conventional usage of $\bar{R}'$ as the source position vector and $\bar{R}$ as the observation position vector. (Primes throughout will be used to indicate source coordinates.) Using the vector-dyadic identity of triple products:

$$\bar{a} \cdot (\bar{b} \times \bar{\bar{c}}) = -\bar{b} \cdot (\bar{a} \times \bar{\bar{c}}) = (\bar{a} \times \bar{b}) \cdot \bar{\bar{c}} \tag{1.31}$$

Equation (1.30) can be re-written as

$$\begin{aligned}\overline{E}(\bar{R}) &= -j\omega\mu \iiint \bar{J}(\bar{R}') \cdot \bar{\bar{G}}_{eJ}(\bar{R}', \bar{R})\, dV' \\ &\quad + \iint_S \Big\{ [\nabla' \times \overline{E}(\bar{R}')] \cdot [\hat{n} \times \bar{\bar{G}}_{eJ}(\bar{R}', \bar{R})] \\ &\qquad - [\hat{n} \times \overline{E}(\bar{R}')] \cdot [\nabla' \times \bar{\bar{G}}_{eJ}(\bar{R}', \bar{R})] \Big\}\, dS' \end{aligned} \tag{1.32}$$

In our application, $\bar{\bar{G}}_{eJ}$ is used in a cavity with impedance walls representing the source layer. It is assumed that the region outside this layer is bounded by the impedance walls and a surface which requires either the radiation condition or the Dirichlet condition for the $\overline{E}$ and $\bar{\bar{G}}_e$ functions so that the $[\hat{n}\times\ ]$ terms in Equation (1.32) evaluate to zero on the boundary. We also assume that this region contains no sources. If such is the case, the surface integrals of Equation (1.32) disappear and we are left with

$$\overline{E}(\bar{R}) = -j\omega\mu \iiint \bar{\bar{G}}_{eJ}(\bar{R}, \bar{R}') \cdot \bar{J}(\bar{R}')\, dV' \tag{1.33}$$

Here, the symmetry property of the dyadic Green's function:

$$\bar{\bar{G}}_{eJ}(\bar{R}, \bar{R}') = \left[\bar{\bar{G}}_{eJ}(\bar{R}', \bar{R})\right]^T \tag{1.34}$$

has been applied ('T' indicating 'the transpose'), which can be shown using dyadic-dyadic Green's second identity as outlined in [76] under the assumptions stated above.

We can find the integral solution to

$$\nabla \times \nabla \times \overline{H} - k^2 \overline{H} = \nabla \times \bar{J} \tag{1.35}$$

by returning to Equation (1.28) which with $\overline{P} = \overline{H}$ and $\bar{\bar{Q}} = \bar{\bar{G}}_{mJ}$, reduces to

$$\overline{H}(\bar{R}) = \iiint \bar{\bar{G}}_{mJ}(\bar{R}, \bar{R}') \cdot \bar{J}(\bar{R}')\, dV' \tag{1.36}$$

using assumptions similar to those for the $\overline{E}$ fields with the appropriate radiation or Neumann boundary conditions enclosing the impedance walls. Alternatively, Equation (1.36)

can be obtained directly from Equation (1.33) by using

$$\overline{H}(\bar{R}) = -\frac{1}{j\omega\mu}\nabla \times \overline{E}(\bar{R}) \tag{1.37}$$

and

$$\nabla \times \bar{\bar{G}}_{eJ} = \bar{\bar{G}}_{mJ} \tag{1.38}$$

The procedure for the magnetic currents is exactly the same resulting in

$$\overline{H}(\bar{R}) = -j\omega\epsilon \iiint \bar{\bar{G}}_{mK}(\bar{R}, \bar{R}') \cdot \overline{K}(\bar{R}')\, dV' \tag{1.39}$$

and

$$\overline{E}(\bar{R}) = -\iiint \bar{\bar{G}}_{eK}(\bar{R}, \bar{R}') \cdot \overline{K}(\bar{R}')\, dV' \tag{1.40}$$

1.4 Formulation by Application of Boundary Conditions

We now derive a set of integral equations by enforcing the boundary conditions for the problem. To begin, we replace the slot openings in each region by a tangential, conductor-backed equivalent magnetic current in accordance with the Equivalence Principle as illustrated in Figure 1.2 (all conducting walls will be assumed to have perfect conductivity). The problem is thereby separated into independent regions, coupled together by the magnetic currents as shown in the figure which also illustrates the treatment of finite slot thickness. Since $\overline{K} = -\hat{n} \times \overline{E}$, using the same current on either side of the slot openings enforces the continuity of the electric field in the slot.

In addition to the boundary conditions at the cavity walls, slot walls, ground plane surface and dielectric interfaces which will be satisfied by finding the appropriate Green's functions, we must also satisfy the following boundary conditions:

$$\hat{n} \times \overline{E}^{int} = \bar{\mathcal{E}} \tag{1.41}$$

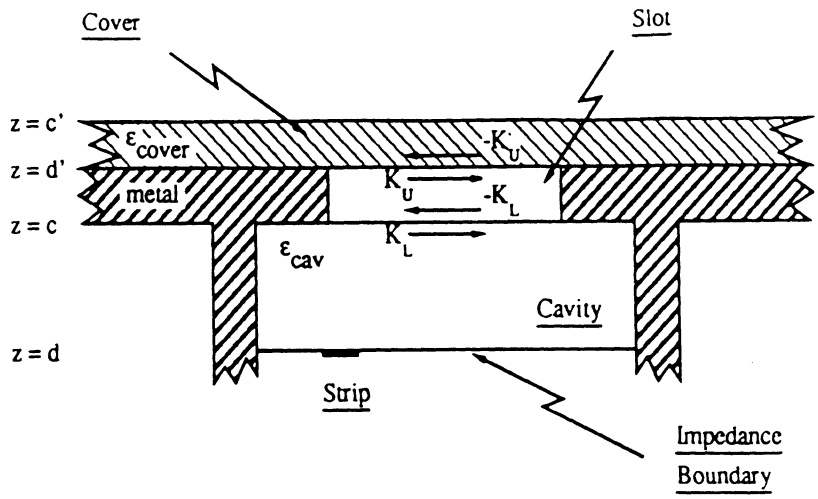

Figure 1.2: Cavity layout and equivalent magnetic currents for a radiating slot.

on the microstrip;

$$\hat{n} \times \overline{H}^{int} - \hat{n} \times \overline{H}^{slot_L} = \bar{\mathcal{H}} \tag{1.42}$$

at the slot opening to the cavity; and

$$\hat{n} \times \overline{H}^{slot_U} - \hat{n} \times \overline{H}^{ext} = \bar{\mathcal{H}} \tag{1.43}$$

at the slot opening in the dielectric covered plane. The $\bar{\mathcal{E}}$ function is a vector describing the source and is normally set to zero except when a gap generator is used to excite the line[1]. The $\bar{\mathcal{H}}$ function is used in Equation (1.42) when the slot is excited internally[2], or in Equation (1.43) when the source is external[3]. When $\bar{\mathcal{E}}$ is set identically to zero, Equation (1.41) enforces the boundary condition that the tangential electric field is to be zero on the strip. Equations (1.42) and (1.43) enforce continuity of the tangential magnetic fields over the slot openings when $\bar{\mathcal{H}}$ is set to zero. The 'U' and 'L' subscripts will be used

[1]The gap generator is used only for the coupler problem as a mechanism for even and odd excitation of the lines.

[2]The right hand side will be set to the incident $\overline{H}$ field of the dominant strip mode for the Reaction Method formulation.

[3]The right hand side can be set to an incident plane wave field for the analysis of the slot as a scatterer or receiving antenna, however, this problem will not be discussed further in this work.

throughout to indicate the upper and lower slot openings for the general case of a 'thick' slot.

The electric field, $\overline{E}^{int}$, in the interior of the cavity can be written as an integral in terms of the electric and magnetic currents in the cavity using the relationships outlined in Section 1.3.3:

$$\overline{E}^{int} = -j\omega\mu_c \iint_{strip} \bar{\bar{G}}_{eJ,int} \cdot \bar{J}_s \; dS' - \iint_{slot_L} \bar{\bar{G}}_{eK,int} \cdot \overline{K}_L \; dS' \qquad (1.44)$$

Similarly, $\overline{H}^{int}$ anywhere in the cavity is given by

$$\overline{H}^{int} = \iint_{strip} \bar{\bar{G}}_{mJ,int} \cdot \bar{J}_s \; dS' - j\omega\epsilon_c \iint_{slot_L} \bar{\bar{G}}_{mK,int} \cdot \overline{K}_L \; dS' \qquad (1.45)$$

For a thick slot as shown, the $\overline{H}$ field in the slot can be written as

$$\overline{H}^{slot} = j\omega\epsilon_s \iint_{slot_L} \bar{\bar{G}}_{mK,slot} \cdot \overline{K}_L \; dS' - j\omega\epsilon_s \iint_{slot_U} \bar{\bar{G}}_{mK,slot} \cdot \overline{K}_U \; dS' \qquad (1.46)$$

The external $\overline{H}$ field is given by

$$\overline{H}^{ext} = j\omega\epsilon_d \iint_{slot_U} \bar{\bar{G}}_{mK,ext} \cdot \overline{K}_U \; dS' \qquad (1.47)$$

Using these expressions in the boundary conditions given by Equations (1.41-1.43), we arrive at the integral equations for the problem:

$$-j\omega\mu_c \iint_{strip} \hat{n} \times \bar{\bar{G}}^{strip}_{eJ,int} \cdot \bar{J}_s \; dS' \; - \iint_{slot_L} \hat{n} \times \bar{\bar{G}}^{strip}_{eK,int} \cdot \overline{K}_L \; dS' = \bar{\mathcal{E}} \qquad (1.48)$$

$$\begin{aligned} \iint_{strip} \hat{n} \times \bar{\bar{G}}^{slot_L}_{mJ,int} \cdot \bar{J}_s \; dS' \; &- \; j\omega\epsilon_c \iint_{slot_L} \hat{n} \times \bar{\bar{G}}^{slot_L}_{mK,int} \cdot \overline{K}_L \; dS' \\ -j\omega\epsilon_s \iint_{slot_L} \hat{n} \times \bar{\bar{G}}^{slot_L}_{mK,slot} \cdot \overline{K}_L \; dS' \; &+ \; j\omega\epsilon_s \iint_{slot_U} \hat{n} \times \bar{\bar{G}}^{slot_L}_{mK,slot} \cdot \overline{K}_U \; dS' = \bar{\mathcal{H}} \end{aligned} \qquad (1.49)$$

$$\begin{aligned} j\omega\epsilon_s \iint_{slot_L} \hat{n} \times \bar{\bar{G}}^{slot_U}_{mK,slot} \cdot \overline{K}_L \; dS' \; &- \; j\omega\epsilon_s \iint_{slot_U} \hat{n} \times \bar{\bar{G}}^{slot_U}_{mK,slot} \cdot \overline{K}_U \; dS' \\ &- \; j\omega\epsilon_d \iint_{slot_U} \hat{n} \times \bar{\bar{G}}^{slot_U}_{mK,ext} \cdot \overline{K}_U \; dS' = \bar{\mathcal{H}} \end{aligned} \qquad (1.50)$$

where the superscripts on the dyads imply evaluation of the dyad at the indicated location. Throughout this work, Equation (1.48) and similar types will be referred to as an electric field integral equation (EFIE) since it is derived from a boundary condition on the electric field. Similarly, both Equations (1.49) and (1.50) are magnetic field integral equations (MFIEs).

Since each of Equations (1.48–1.50) involve the $[\hat{n}\times\ ]$ term, from here on it will be dropped with the understanding that only the tangential components of the various dyads are used. Equations (1.48–1.50) can then be written:

$$-j\omega\mu_c \iint_{strip} \bar{\bar{G}}^{strip}_{eJ,int} \cdot \bar{J}_s \, dS' - \iint_{slot_L} \bar{\bar{G}}^{strip}_{eK,int} \cdot \bar{K}_L \, dS' = \bar{\mathcal{E}} \tag{1.51}$$

$$\iint_{strip} \bar{\bar{G}}^{slot_L}_{mJ,int} \cdot \bar{J}_s \, dS' - j\omega \iint_{slot_L} \left[\epsilon_c \bar{\bar{G}}^{slot_L}_{mK,int} + \epsilon_s \bar{\bar{G}}^{slot_L}_{mK,slot}\right] \cdot \bar{K}_L \, dS' + j\omega\epsilon_s \iint_{slot_U} \bar{\bar{G}}^{slot_L}_{mK,slot} \cdot \bar{K}_U \, dS' = \bar{\mathcal{H}} \tag{1.52}$$

$$j\omega\epsilon_s \iint_{slot_L} \bar{\bar{G}}^{slot_U}_{mK,slot} \cdot \bar{K}_L \, dS' - j\omega \iint_{slot_U} \left[\epsilon_s \bar{\bar{G}}^{slot_U}_{mK,slot} + \epsilon_d \bar{\bar{G}}^{slot_U}_{mK,ext}\right] \cdot \bar{K}_U \, dS' = \bar{\mathcal{H}} \tag{1.53}$$

where all the terms involving $\hat{z}$ are excluded[4]. The unknown currents $\bar{J}_s$, $\bar{K}_L$ and $\bar{K}_U$ can have only tangential components on each of their respective structures, we therefore have six scalar unknowns. Since only the tangential components of $\bar{\bar{G}}$ are used, Equations (1.51-1.53) represent six scalar integral equations which are sufficient to solve for the unknown currents.

For convenience of notation, we redefine Equations (1.51–1.53) as:

$$\iint_{strip} \bar{\bar{G}}^{(11)} \cdot \bar{J}_s \, dS' + \iint_{slot_L} \bar{\bar{G}}^{(13)} \cdot \bar{K}_L \, dS' = \bar{\mathcal{E}} \tag{1.54}$$

$$\iint_{strip} \bar{\bar{G}}^{(31)} \cdot \bar{J}_s \, dS' + \iint_{slot_L} \bar{\bar{G}}^{(33)} \cdot \bar{K}_L \, dS' + \iint_{slot_U} \bar{\bar{G}}^{(35)} \cdot \bar{K}_U \, dS' = \bar{\mathcal{H}} \tag{1.55}$$

$$\iint_{slot_L} \bar{\bar{G}}^{(53)} \cdot \bar{K}_L \, dS' + \iint_{slot_U} \bar{\bar{G}}^{(55)} \cdot \bar{K}_U \, dS' = \bar{\mathcal{H}} \tag{1.56}$$

[4]Throughout most of this work we will consistently use $\hat{n} = \hat{z}$ where $\hat{n}$ will be orthogonal to the currents involved. Therefore, no integral equation or Green's function evaluation will involve the $\hat{z}$ components which will subsequently be ignored.

where

$$\bar{\bar{G}}^{(11)} = -j\omega\mu_c \bar{\bar{G}}^{strip}_{eJ,int} \tag{1.57}$$

$$\bar{\bar{G}}^{(13)} = -\bar{\bar{G}}^{strip}_{eK,int} \tag{1.58}$$

$$\bar{\bar{G}}^{(31)} = \bar{\bar{G}}^{slot_L}_{mJ,int} \tag{1.59}$$

$$\bar{\bar{G}}^{(33)} = -j\omega \left[\epsilon_c \bar{\bar{G}}^{slot_L}_{mK,int} + \epsilon_s \bar{\bar{G}}^{slot_L}_{mK,slot} \right] \tag{1.60}$$

$$\bar{\bar{G}}^{(35)} = j\omega\epsilon_s \bar{\bar{G}}^{slot_L}_{mK,slot} \tag{1.61}$$

$$\bar{\bar{G}}^{(53)} = j\omega\epsilon_s \bar{\bar{G}}^{slot_U}_{mK,slot} \tag{1.62}$$

$$\bar{\bar{G}}^{(55)} = -j\omega \left[\epsilon_s \bar{\bar{G}}^{slot_U}_{mK,slot} + \epsilon_d \bar{\bar{G}}^{slot_U}_{mK,ext} \right] \tag{1.63}$$

For the radiating slot problem, it remains to find the various dyadic Green's function components, solve the equations for the unknown currents, and interpret the results to obtain parameters which characterize the slot's electrical behavior and properties.

The coupler problem differs only in the final equation. Equation (1.56) which involves the Green's function for the half-space is replaced by an EFIE as follows. The field on the upper slot is now contained by another cavity which may also have a conducting strip as illustrated in Figure 1.3. Under these circumstances, we then have the following integral equations:

$$-j\omega\mu \iint_{strip_L} \bar{\bar{G}}^{strip_L}_{eJ} \cdot \bar{J}_L \, dS' - \iint_{slot_L} \bar{\bar{G}}^{strip_L}_{eK} \cdot \bar{K}_L \, dS' = \bar{\mathcal{E}} \tag{1.64}$$

$$\iint_{strip_L} \bar{\bar{G}}^{slot_L}_{mJ} \cdot \bar{J}_L \, dS' - j\omega \iint_{slot_L} \left[\epsilon_L \bar{\bar{G}}^{slot_L}_{mK} + \epsilon_{slot} \bar{\bar{G}}^{slot_L}_{mK} \right] \cdot \bar{K}_L \, dS' + j\omega\epsilon_{slot} \iint_{slot_U} \bar{\bar{G}}^{slot_L}_{mK} \cdot \bar{K}_U \, dS' = \bar{\mathcal{H}} \tag{1.65}$$

$$\iint_{strip_U} \bar{\bar{G}}^{slot_U}_{mJ} \cdot \bar{J}_U \, dS' + j\omega \iint_{slot_U} \left[\epsilon_U \bar{\bar{G}}^{slot_U}_{mK} + \epsilon_{slot} \bar{\bar{G}}^{slot_U}_{mK} \right] \cdot \bar{K}_U \, dS' - j\omega\epsilon_{slot} \iint_{slot_U} \bar{\bar{G}}^{slot_U}_{mK} \cdot \bar{K}_L \, dS' = \bar{\mathcal{H}} \tag{1.66}$$

$$-j\omega\mu \iint_{strip_U} \bar{\bar{G}}^{strip_U}_{eJ} \cdot \bar{J}_U \, dS' + \iint_{slot_U} \bar{\bar{G}}^{strip_U}_{eK} \cdot \bar{K}_U \, dS' = \bar{\mathcal{E}} \tag{1.67}$$

The subscripts U and L here indicate whether the source is associated with the upper or

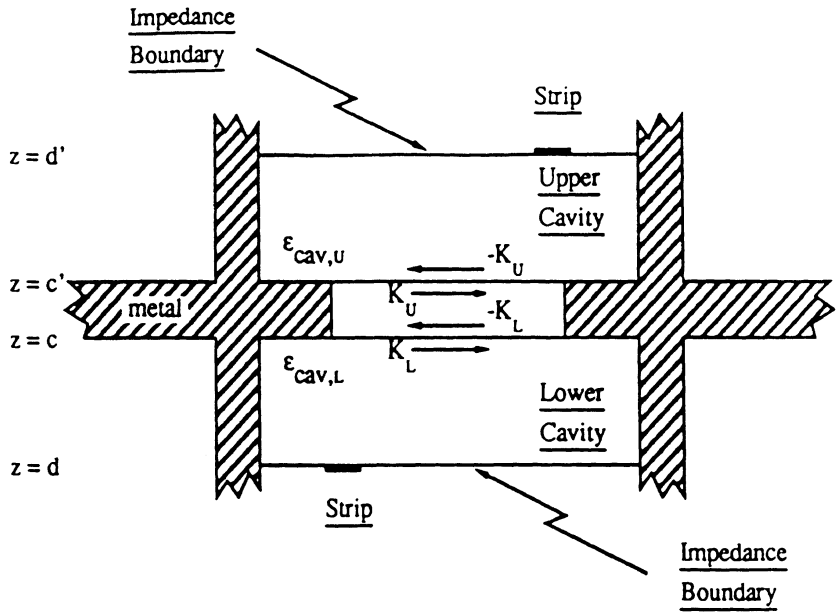

Figure 1.3: Electric and equivalent magnetic currents for microstrip-to-microstrip coupler with a 'thick' slot.

lower cavity strip or slot opening.

CHAPTER II

DYADIC GREEN'S FUNCTIONS

In this chapter, the dyadic Green's functions needed to evaluate the integral equations are derived. The method used in all cases is a 'field expansion method' using Vector Wave Functions (VWFs) as opposed to the perhaps more conventional, 'vector potential method'. Some of the Green's functions derived will not be needed in the later analysis but are included in this chapter for completeness.

The use of vector wave functions with dyadic analysis is presented as an alternative. It has the advantage of producing the complete dyadic Green's function in one solution. The process also may involve a reduced number of simultaneous algebraic equations which must be solved for unknown coefficients as compared to the vector potential method. The disadvantage of the approach is that it requires dyadic analysis which may be unfamiliar, although it is quite straightforward.

The field expansion approach using VFWs has been extensively detailed by Tai over an extended period of time [72]-[79]. Nevertheless, the method is not widely employed which may be due to several factors including:

1. Early development of the technique involved the use of the vector wave functions designated $\bar{L}$, $\bar{M}$ and $\bar{N}$. As will be shown, the $\bar{M}$ and $\bar{N}$ functions have clear, physical interpretations, however, the interpretation of the $\bar{L}$ functions is somewhat obscure

and its handling, at times, somewhat difficult. Consequently, the approach may have been avoided.

2. An oversight in [72] but corrected in [77], stirred up some controversy which may have caused some to avoid the method (see [11] also for details and a list of references).

The current method is more mature, having evolved to a stage where the previous difficulties have been eliminated. Problems can now be solved in a methodical and straightforward manner with no difficulties in physical interpretation (the need for the $\bar{L}$ functions can be avoided).

2.1 Impedance Boundary Conditions for Layered Structures

It can be shown that a plane wave in a homogeneous region exhibits a constant wave impedance defined by the ratio of a component of the electric field to an orthogonal component of the magnetic field, both transverse to a given direction [6, p.142]. A 'plane wave expansion' of the field is convenient in many problems due to this property. For many canonical structures, the expansion itself is unnecessary since wave impedances can be derived directly. For instance, modal wave impedances for homogeneously filled rectangular waveguides are well known. In somewhat more complex structures such as those treated here, the boundaries are still always planar owing to the rectangular geometry. As a result, wave impedance surfaces can be chosen to conform to the boundaries and the wave impedance concept becomes a vehicle through which the boundary conditions can be applied in a simple way.

The dyadic Green's functions for all of the structures treated here will be derived using this approach. As the Equivalence Principle states, the fields in a given layer depend only on the fields at the boundaries and internal sources. We therefore can derive the Green's function for the source layer alone with the other layers represented by impedance

boundary conditions applied at the layer interfaces. In this way the Green's function can be generalized to represent any number of layers above or below the source layer. The approach greatly simplifies the analysis of the total structure by allowing the fields to be found first for the source layer alone. Once they are found, expressions for the fields in the remaining layers can be immediately written in terms of the homogeneous solutions by matching tangential components on the boundaries. As in [13], this process is greatly facilitated by expanding the solutions in terms of 'Longitudinal-Section Electric' (LSE) and 'Longitudinal-Section Magnetic' (LSM) fields because the field matching procedure can then be done on a one-to-one basis. (An individual mode on one side of an interface matches an identical mode on the other side exactly, with an appropriate coefficient.)

The impedance boundary conditions, as used here, are not to be confused with the approximate impedance boundary conditions discussed in [63, 64]. Both usages may be exact under certain circumstances. The present usage is in the context of the modal impedances of various structures and is exact under the assumption of perfectly conducting walls where applicable. For example, the approach is exact for a closed, perfectly-conducting rectangular cavity with uniform side walls. A counter-example is a cavity with perfectly conducting side walls, but which is open on one end: terminating the open end with the impedance of free-space as proposed by some, is not exact since this condition is not exact. For all structures studied in this work, the geometries are such that the representation is exact to the extent that perfectly conducting walls can be assumed.

In our structures, the impedance boundary conditions require the fields to satisfy

$$\eta = \frac{\hat{x} \cdot \overline{\mathrm{E}}}{\hat{y} \cdot \overline{\mathrm{H}}} \tag{2.1}$$

For electric currents, this becomes

$$\frac{\hat{x} \cdot \bar{\bar{\mathrm{G}}}_{eJ}}{\hat{y} \cdot \bar{\bar{\mathrm{G}}}_{mJ}} = \frac{j\eta}{\omega\mu} \qquad \text{or} \qquad \frac{\hat{x} \cdot \nabla \times \bar{\bar{\mathrm{G}}}_{mJ}}{\hat{y} \cdot \bar{\bar{\mathrm{G}}}_{mJ}} = j\omega\epsilon\eta \tag{2.2}$$

Similarly for the equivalent magnetic current Green's functions, the impedance boundary conditions are;

$$\frac{\hat{x}\cdot\bar{\bar{G}}_{eK}}{\hat{y}\cdot\bar{\bar{G}}_{mK}} = j\omega\epsilon\eta \qquad \text{or} \qquad \frac{\hat{x}\cdot\bar{\bar{G}}_{eK}}{\hat{y}\cdot\nabla\times\bar{\bar{G}}_{eK}} = \frac{j\eta}{\omega\mu} \tag{2.3}$$

For simpler notation, η_e will be the wave impedance associated with the LSE modes and η_m will be used for the LSM modes. Furthermore, $\tilde{\eta}_e$ and $\tilde{\eta}_m$ will denote normalization to the intrinsic modal impedance in the layer and are defined as

$$\tilde{\eta}_{ei} = \frac{k_{zi}\eta_{ei}}{\omega\mu} \tag{2.4}$$

$$\tilde{\eta}_{mi} = \frac{\omega\epsilon\eta_{mi}}{k_{zi}} \tag{2.5}$$

where i is an index associated with the i^{th} layer.

We can then evaluate the impedance conditions using transmission line analysis and wave impedances for the various layers as illustrated in Figure 2.1. The impedances on a

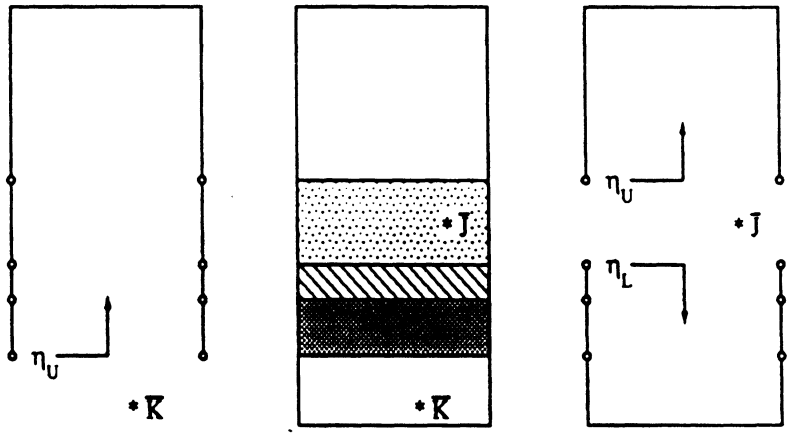

Figure 2.1: Impedance boundary condition representation of a multi-layered structure.

given layer's upper boundary are found by the transmission line equation

$$\tilde{\eta}_{ei} = \frac{k_{zi}}{k_{z(i-1)}}\left[\frac{\tilde{\eta}_{e(i-1)} + j\tan k_{z(i-1)}l_{(i-1)}}{1 + j\tilde{\eta}_{e(i-1)}\tan k_{z(i-1)}l_{(i-1)}}\right] \tag{2.6}$$

$$\tilde{\eta}_{mi} = \frac{\epsilon_i k_{z(i-1)}}{\epsilon_{(i-1)}k_{zi}}\left[\frac{\tilde{\eta}_{m(i-1)} + j\tan k_{z(i-1)}l_{(i-1)}}{1 + j\tilde{\eta}_{m(i-1)}\tan k_{z(i-1)}l_{(i-1)}}\right] \tag{2.7}$$

where the index i is iterated from the top layer through successive lower layers to the layer of interest with l_i the thickness of the i^{th} layer. (We have assumed that $\mu_r = 1$ throughout this work.) Similarly, for the lower layers, since the wave impedance is negative,

$$\tilde{\eta}_{ei} = \frac{k_{zi}}{k_{z(i+1)}} \left[\frac{\tilde{\eta}_{e(i+1)} - j \tan k_{z(i+1)} l_{(i+1)}}{1 - j\tilde{\eta}_{e(i+1)} \tan k_{z(i+1)} l_{(i+1)}} \right] \tag{2.8}$$

$$\tilde{\eta}_{mi} = \frac{\epsilon_i k_{z(i+1)}}{\epsilon_{(i+1)} k_{zi}} \left[\frac{\tilde{\eta}_{m(i+1)} - j \tan k_{z(i+1)} l_{(i+1)}}{1 - j\tilde{\eta}_{m(i+1)} \tan k_{z(i+1)} l_{(i+1)}} \right] \tag{2.9}$$

where here the iteration proceeds from the lowest layer upwards.

2.2 Dyadic Green's Functions for an Infinite Covered Half Space

We begin with the derivation of the Green's function for an infinite covered half-space. The method of solution closely parallels that of the other cases, except for the boundary conditions, so that by covering this case in greater detail some of the steps for the later cases may be omitted. For completeness, we also include the solutions for electric currents in this section, although this function is not needed for the characterization of the slot. It is, however, widely used in the analysis of open microstrip and microstrip patch antennas.

2.2.1 Magnetic Current

The dyadic Green's functions for the slot problems use a magnetic current ($\overline{K}$) as the source. They are the solutions to the dyadic Helmholtz equations:

$$\nabla \times \nabla \times \bar{\bar{G}}_{mK} - k^2 \bar{\bar{G}}_{mK} = \bar{\bar{I}} \delta(\bar{R} - \bar{R}') \tag{2.10}$$

$$\nabla \times \nabla \times \bar{\bar{G}}_{eK} - k^2 \bar{\bar{G}}_{eK} = \nabla \times \bar{\bar{I}} \delta(\bar{R} - \bar{R}') \tag{2.11}$$

The key to eliminating the need for the $\bar{L}$ vector wave functions, and thus simplifying the analysis, is in the choice of which of Equations (2.10) or (2.11) to solve first.

The functions $\bar{L}$, $\bar{M}$ and $\bar{N}$ form a complete set of solutions to the homogeneous equation

$\nabla \times \nabla \times \bar{F} - \kappa^2 \bar{F} = 0$. They are defined in the general forms

$$\bar{L} = \nabla\Psi \tag{2.12}$$

$$\bar{M} = \nabla \times \Psi\hat{x}_i = \frac{1}{\kappa}\nabla \times \bar{N} \tag{2.13}$$

$$\bar{N} = \frac{1}{\kappa}\nabla \times \nabla \times \Psi\hat{x}_i = \frac{1}{\kappa}\nabla \times \bar{M} \tag{2.14}$$

where Ψ is a scalar function solution to the equation $\nabla^2\Psi + \kappa^2\Psi = 0$ chosen to satisfy the boundary conditions of the problem; $\hat{x}_i$ is a unit vector called the 'piloting vector'; and κ is the separation constant $\kappa^2 = k_x^2 + k_y^2 + k_z^2$.

Following the Ohm-Rayleigh method as described by Tai [72], we can find the *particular* solutions by expanding the right hand sides of (2.10–2.11) in terms of the eigenfunctions $\bar{L}$, $\bar{M}$ and $\bar{N}$ with unknown vector coefficients; deriving the values of the coefficients using the orthogonality properties of the VWFs; expanding the dyadic in terms of the same functions with scalar coefficients; and enforcing the equations by performing the derivative operations. From Equations (2.12–2.14) it can be seen that only $\bar{L}$ can have a non-zero divergence and since the right hand side of (2.11) has no divergence, the $\bar{L}$ function is not needed in its solution. We therefore find the solution of (2.11) first. It can also be shown that $\bar{\bar{G}}_{mK}$ and $\bar{\bar{G}}_{eK}$ are related by

$$\nabla \times \bar{\bar{G}}_{mK} = \bar{\bar{G}}_{eK} \tag{2.15}$$

$$\nabla \times \bar{\bar{G}}_{eK} = \bar{\bar{I}}\delta(\bar{R} - \bar{R}') + k^2\bar{\bar{G}}_{mK} \tag{2.16}$$

so that $\bar{\bar{G}}_{mK}$ can be found from (2.16) once $\bar{\bar{G}}_{eK}$ is known. This is the essence of the method described in [77].

As with the vector potential method (see Appendix C), we begin as if the space were infinite and homogeneous. We therefore expand the field in terms of VWF's for free space defined by

$$\Psi = e^{-j(k_x x + k_y y + k_z z)} \tag{2.17}$$

To simplify later application of the boundary conditions, we choose the piloting vector to be $\hat{z}$. The orthogonality properties of these functions are then

$$\iiint_V \bar{\mathrm{M}}(k_x, k_y, k_z) \cdot \bar{\mathrm{N}}(-k'_x, -k'_y, -k'_z)\, dV = 0 \tag{2.18}$$

$$\begin{aligned} &\iiint_V \bar{\mathrm{M}}(k_x, k_y, k_z) \cdot \bar{\mathrm{M}}(-k'_x, -k'_y, -k'_z)\, dV \\ = &\iiint_V \bar{\mathrm{N}}(k_x, k_y, k_z) \cdot \bar{\mathrm{N}}(-k'_x, -k'_y, -k'_z)\, dV \\ = &\ (2\pi)^3(k_x^2 + k_y^2)\delta(k_x - k'_x)\delta(k_y - k'_y)\delta(k_z - k'_z) \end{aligned} \tag{2.19}$$

where the volume of integration corresponds to the entire space.

To find $\bar{\bar{\mathrm{G}}}_{eK}$ we first let

$$\nabla \times \left[\bar{\bar{\mathrm{I}}}\delta(\bar{R} - \bar{R}')\right] = \int_{-\infty}^{\infty}\int_{-\infty}^{\infty}\int_{-\infty}^{\infty} dk_x dk_y dk_z \left[\bar{\mathrm{M}}(k_x, k_y, k_z)\,\bar{\mathrm{A}} + \bar{\mathrm{N}}(k_x, k_y, k_z)\,\bar{\mathrm{B}}\right] \tag{2.20}$$

By taking the anterior scalar product of Equation (2.20) with $\bar{\mathrm{M}}(-k'_x, -k'_y, -k'_z)$ and $\bar{\mathrm{N}}(-k'_x, -k'_y, -k'_z)$ respectively, and integrating throughout V, we can determine the unknown vector coefficients $\bar{\mathrm{A}}$ and $\bar{\mathrm{B}}$ through the orthogonality properties. The results are

$$\bar{\mathrm{A}} = \frac{\kappa \bar{\mathrm{N}}'(-k_x, -k_y, -k_z)}{(2\pi)^3(k_x^2 + k_y^2)} \tag{2.21}$$

$$\bar{\mathrm{B}} = \frac{\kappa \bar{\mathrm{M}}'(-k_x, -k_y, -k_z)}{(2\pi)^3(k_x^2 + k_y^2)} \tag{2.22}$$

in which the primed functions are defined with respect to (x', y', z'), the site of the source at $\bar{\mathrm{R}} = \bar{\mathrm{R}}'$. Thus,

$$\begin{aligned} \nabla \times \left[\bar{\bar{\mathrm{I}}}\delta(\bar{\mathrm{R}} - \bar{\mathrm{R}}')\right] = &\frac{1}{(2\pi)^3}\int_{-\infty}^{\infty}\int_{-\infty}^{\infty}\int_{-\infty}^{\infty} \frac{\kappa dk_x dk_y dk_z}{(k_x^2 + k_y^2)} \\ &\cdot \left[\bar{\mathrm{M}}(k_x, k_y, k_z)\bar{\mathrm{N}}'(-k_x, -k_y, -k_z) + \bar{\mathrm{N}}(k_x, k_y, k_z)\bar{\mathrm{M}}'(-k_x, -k_y, -k_z)\right] \end{aligned} \tag{2.23}$$

Now we let

$$\begin{aligned} \bar{\bar{\mathrm{G}}}_{eK} = &\frac{1}{(2\pi)^3}\int_{-\infty}^{\infty}\int_{-\infty}^{\infty}\int_{-\infty}^{\infty} \frac{\kappa dk_x dk_y dk_z}{(k_x^2 + k_y^2)} \\ &\cdot \left[a\bar{\mathrm{M}}(k_x, k_y, k_z)\bar{\mathrm{N}}'(-k_x, -k_y, -k_z) + b\bar{\mathrm{N}}(k_x, k_y, k_z)\bar{\mathrm{M}}'(-k_x, -k_y, -k_z)\right] \end{aligned} \tag{2.24}$$

with a and b unknown scalar coefficients, and substitute into Equation (2.11) yielding

$$a = b = \frac{1}{\kappa^2 - k^2} = \frac{1}{[k_z^2 - (k^2 - k_x^2 - k_y^2)]} \tag{2.25}$$

The integration with respect to k_z in Equation (2.24) can now be carried out in closed form by applying Cauchy's theorem:

$$\bar{\bar{G}}_{eK} = -\frac{jk}{8\pi^2}\int_{-\infty}^{\infty}\int_{-\infty}^{\infty}\frac{dk_x dk_y}{k_z(k_x^2+k_y^2)}\left[\bar{M}(\pm k_z)\bar{N}'(\mp k_z) + \bar{N}(\pm k_z)\bar{M}'(\mp k_z)\right] \qquad z \gtrless z' \tag{2.26}$$

where $k_z = \sqrt{k^2 - k_x^2 - k_y^2}$ (note that κ becomes k). As indicated, the top sign applies when $z > z'$ and the bottom sign when $z < z'$. This condition is a result of requiring the solution to satify the radiation condition at infinity which determines whether the contour of integration is closed in the upper or lower half-plane. Also, from here on it will be understood that the primed functions, $\bar{M}'$ and $\bar{N}'$, have $-k_x$, $-k_y$ or $-k_z$ arguments, unless indicated otherwise.

We now can write $\bar{\bar{G}}_{mK}$ by performing the operations indicated by Equation (2.16). This can be done almost by inspection using the relations between $\bar{M}$ and $\bar{N}$ from Equations (2.13) and (2.14) except for the discontinuity which occurs at $z = z'$. As in [77], it can be shown that these relations apply but an additional term is needed to account for the discontinuity at the source; specifically,

$$\begin{aligned}\nabla \times \bar{\bar{G}}_{eK} = &-\frac{jk^2}{8\pi^2}\int_{-\infty}^{\infty}\int_{-\infty}^{\infty}\frac{dk_x dk_y}{k_z(k_x^2+k_y^2)}\left[\bar{M}(\pm k_z)\bar{M}'(\mp k_z) + \bar{N}(\pm k_z)\bar{N}'(\mp k_z)\right] \\ &+ \bar{\bar{I}}_t\delta(\bar{R} - \bar{R}') \qquad z \gtrless z'\end{aligned} \tag{2.27}$$

where the transverse idemfactor, $\bar{\bar{I}}_t = \hat{x}\hat{x} + \hat{y}\hat{y}$, appears in this case as a result of the combination of the choice of the piloting vector $\hat{z}$ and the partitioning of the z dependence. Notice that the singular terms come from the second derivative of

$$f(z) = \begin{cases} e^{-jk_z(z-z')} & z > z' \\ e^{jk_z(z-z')} & z < z' \end{cases} \tag{2.28}$$

or the first derivative of

$$g(z) = \frac{\partial f(z)}{\partial z} = jk_z \begin{cases} -e^{-jk_z(z-z')} & z > z' \\ e^{jk_z(z-z')} & z < z' \end{cases} \tag{2.29}$$

which is

$$\frac{\partial g(z)}{\partial z} = \frac{\partial^2 f(z)}{\partial z^2} = -k_z^2 \begin{cases} e^{-jk_z(z-z')} & z > z' \\ e^{jk_z(z-z')} & z < z' \end{cases} - 2jk_z\delta(z-z') \tag{2.30}$$

This term has sometimes been overlooked in the potential function method as well, as discussed in Appendix B. Thus, Equation (2.16) leads to

$$\bar{\bar{G}}_{mK} = -\frac{1}{k^2}\hat{z}\hat{z}\delta(\bar{R}-\bar{R}') - \frac{j}{8\pi^2}\int_{-\infty}^{\infty}\int_{-\infty}^{\infty}\frac{dk_x dk_y}{k_z(k_x^2+k_y^2)} \cdot \left[\bar{M}(\pm k_z)\bar{M}'(\mp k_z) + \bar{N}(\pm k_z)\bar{N}'(\mp k_z)\right] \quad z \gtrless z' \tag{2.31}$$

We now divide the infinite space into layers surrounding the source point above and below. The layered structure can be represented by impedance boundary conditions for the source layer as previously described and as illustrated in Figure 2.2. We then apply

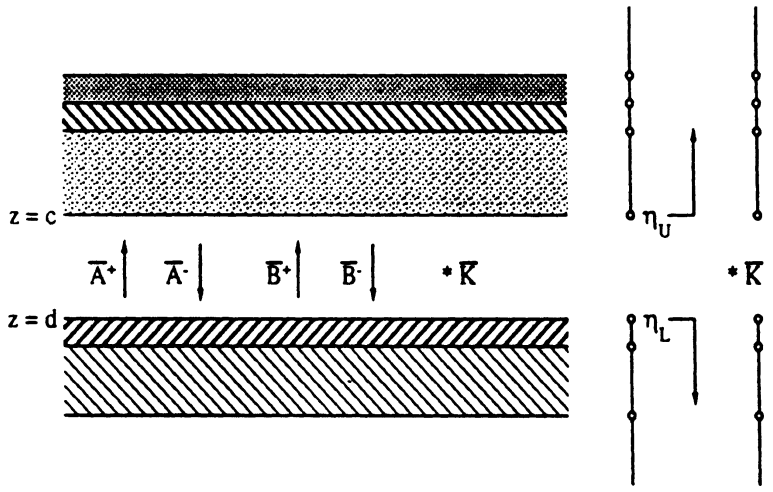

Figure 2.2: Layered infinite space as represented by impedance boundary conditions.

the method of scattering superposition to this case by letting

$$\bar{\bar{G}}_{eK} = \bar{\bar{G}}_{eK}^{(P)} + \bar{\bar{G}}_{eK}^{(S)} \tag{2.32}$$

$\bar{\bar{G}}^{(P)}_{eK}$ is the particular solution found above for the infinite space which may be referred to as the primary term, and $\bar{\bar{G}}^{(S)}_{eK}$ - the secondary or scattered fields - is made up of solutions to the homogeneous equation as follows:

$$\bar{\bar{G}}^{(S)}_{eK} = -\frac{jk}{8\pi^2}\int_{-\infty}^{\infty}\int_{-\infty}^{\infty}\frac{dk_x dk_y}{k_z(k_x^2+k_y^2)} \cdot\left[\bar{M}(k_z)\,\bar{A}^{+} + \bar{M}(-k_z)\,\bar{A}^{-} + \bar{N}(k_z)\,\bar{B}^{+} + \bar{N}(-k_z)\,\bar{B}^{-}\right] \tag{2.33}$$

where $\bar{A}^{+}, \bar{A}^{-}, \bar{B}^{+}$ and $\bar{B}^{-}$ are unknown vector coefficients to be determined. The physical interpretation of this procedure is that the $\pm$ coefficients represent the waves traveling in the $\pm\hat{z}$ directions as a result of reflections, i.e., scattering, from the interfaces. In evaluating the boundary conditions, it is also useful to find $\bar{\bar{G}}_{mK}$ through $\nabla \times \bar{\bar{G}}_{eK} = k^2\bar{\bar{G}}_{mK}$ which is the source-free version of Equation (2.16). Hence,

$$\bar{\bar{G}}^{(S)}_{mK} = -\frac{j}{8\pi^2}\int_{-\infty}^{\infty}\int_{-\infty}^{\infty}\frac{dk_x dk_y}{k_z(k_x^2+k_y^2)} \cdot\left[\bar{N}(k_z)\,\bar{A}^{+} + \bar{N}(-k_z)\,\bar{A}^{-} + \bar{M}(k_z)\,\bar{B}^{+} + \bar{M}(-k_z)\,\bar{B}^{-}\right] \tag{2.34}$$

Note that additional boundary conditions need only be imposed at the newly introduced interfaces and not at the source, since the primary fields satisfy all boundary conditions at the source and the secondary terms are continuous there.

Applying the boundary conditions at the top and bottom of the source layer, we derive the following set of algebraic equations for the unknown coefficients:

$$(\tilde{\eta}_{eU}-1)e^{-jk_y c}\,\bar{A}^{+} - (\tilde{\eta}_{eU}+1)e^{jk_y c}\,\bar{A}^{-} = -(\tilde{\eta}_{eU}-1)e^{-jk_y c}\bar{N}'(-k_z) \tag{2.35}$$

$$(\tilde{\eta}_{eL}-1)e^{-jk_y d}\,\bar{A}^{+} - (\tilde{\eta}_{eL}+1)e^{jk_y d}\,\bar{A}^{-} = (\tilde{\eta}_{eL}+1)e^{jk_y d}\bar{N}'(k_z) \tag{2.36}$$

and

$$(\tilde{\eta}_{mU}-1)e^{-jk_y c}\,\bar{B}^{+} + (\tilde{\eta}_{mU}+1)e^{jk_y c}\,\bar{B}^{-} = -(\tilde{\eta}_{mU}-1)e^{-jk_y c}\bar{M}'(-k_z) \tag{2.37}$$

$$(\tilde{\eta}_{mL}-1)e^{-jk_y d}\,\bar{B}^{+} + (\tilde{\eta}_{mL}+1)e^{jk_y d}\,\bar{B}^{-} = -(\tilde{\eta}_{mL}+1)e^{jk_y d}\bar{M}'(k_z) \tag{2.38}$$

Here the 'U' and 'L' notation indicates the upper and lower interface conditions respectively.

These four equations decouple into two pairs due to a judicious choice of the piloting vector in the VWFs. Because the piloting vector was chosen as the unit vector normal to the layer interfaces, the $\bar{M}$ and $\bar{N}$ VWFs appearing in $\bar{\bar{G}}_{mK}$ correspond to the LSM and LSE modes of the structure respectively. (In contrast, it should be noted that $\bar{M}$ and $\bar{N}$ correspond to the LSE and LSM modes, respectively, when they appear in $\bar{\bar{G}}_{eK}$.) As is well known, the LSE and LSM modes are decoupled on the interfaces, that is, the tangential components of an individual mode on the interface can be matched by an identical mode in the adjacent layer, therefore the coefficients are decoupled. That there are only four equations is a result of the fact that the field in a given layer depends only on the field in the adjacent layers.

The solutions are easily found to be

$$\bar{A}^{+} = -\frac{e^{jk_y d}\left[(\tilde{\eta}_{eU}-1)(\tilde{\eta}_{eL}+1)e^{-jk_y c}\bar{N}'(-k_z)+(\tilde{\eta}_{eU}+1)(\tilde{\eta}_{eL}+1)e^{jk_y c}\bar{N}'(k_z)\right]}{(\tilde{\eta}_{eU}+1)(\tilde{\eta}_{eL}-1)e^{jk_y(c-d)}-(\tilde{\eta}_{eU}-1)(\tilde{\eta}_{eL}+1)e^{-jk_y(c-d)}} \tag{2.39}$$

$$\bar{A}^{-} = -\frac{e^{-jk_y c}\left[(\tilde{\eta}_{eU}-1)(\tilde{\eta}_{eL}-1)e^{-jk_y d}\bar{N}'(-k_z)+(\tilde{\eta}_{eU}-1)(\tilde{\eta}_{eL}+1)e^{jk_y d}\bar{N}'(k_z)\right]}{(\tilde{\eta}_{eU}+1)(\tilde{\eta}_{eL}-1)e^{jk_y(c-d)}-(\tilde{\eta}_{eU}-1)(\tilde{\eta}_{eL}+1)e^{-jk_y(c-d)}} \tag{2.40}$$

$$\bar{B}^{+} = \frac{e^{jk_y d}\left[(\tilde{\eta}_{mU}-1)(\tilde{\eta}_{mL}+1)e^{-jk_y c}\bar{M}'(-k_z)-(\tilde{\eta}_{mU}+1)(\tilde{\eta}_{mL}+1)e^{jk_y c}\bar{M}'(k_z)\right]}{(\tilde{\eta}_{mU}+1)(\tilde{\eta}_{mL}-1)e^{jk_y(c-d)}-(\tilde{\eta}_{mU}-1)(\tilde{\eta}_{mL}+1)e^{-jk_y(c-d)}} \tag{2.41}$$

$$\bar{B}^{-} = -\frac{e^{-jk_y c}\left[(\tilde{\eta}_{mU}-1)(\tilde{\eta}_{mL}-1)e^{-jk_y d}\bar{M}'(-k_z)-(\tilde{\eta}_{mU}-1)(\tilde{\eta}_{mL}+1)e^{jk_y d}\bar{M}'(k_z)\right]}{(\tilde{\eta}_{mU}+1)(\tilde{\eta}_{mL}-1)e^{jk_y(c-d)}-(\tilde{\eta}_{mU}-1)(\tilde{\eta}_{mL}+1)e^{-jk_y(c-d)}} \tag{2.42}$$

With some algebraic manipulation and use of the relations found in Appendix A, we now can write

$$\bar{\bar{G}}_{eK} = \frac{jk}{4\pi^2}\int_{-\infty}^{\infty}\int_{-\infty}^{\infty}\frac{dk_x dk_y}{k_z(k_x^2+k_y^2)}$$

$$\left\{ \frac{\left(\begin{bmatrix} \tilde{\eta}_{eU}\bar{M}_e[k_z(z-c)] - j\bar{M}_o[k_z(z-c)] \end{bmatrix} \begin{bmatrix} \tilde{\eta}_{eL}\bar{N}'_e[k_z(z'-d)] - j\bar{N}'_o[-k_z(z'-d)] \end{bmatrix} \right)}{\left(\begin{bmatrix} \tilde{\eta}_{eL}\bar{M}_e[k_z(z-d)] - j\bar{M}_o[k_z(z-d)] \end{bmatrix} \begin{bmatrix} \tilde{\eta}_{eU}\bar{N}'_e[k_z(z'-c)] - j\bar{N}'_o[-k_z(z'-c)] \end{bmatrix} \right)}{(\tilde{\eta}_{eU} - \tilde{\eta}_{eL})\cos k_z(c-d) - j(\tilde{\eta}_{eU}\tilde{\eta}_{eL} - 1)\sin k_z(c-d)} \right.$$

$$\left. + \frac{\left(\begin{bmatrix} \tilde{\eta}_{mU}\bar{N}_o[k_z(z-c)] + j\bar{N}_e[k_z(z-c)] \end{bmatrix} \begin{bmatrix} \tilde{\eta}_{mL}\bar{M}'_o[k_z(z'-d)] + j\bar{M}'_e[-k_z(z'-d)] \end{bmatrix} \right)}{\left(\begin{bmatrix} \tilde{\eta}_{mL}\bar{N}_o[k_z(z-d)] + j\bar{N}_e[k_z(z-d)] \end{bmatrix} \begin{bmatrix} \tilde{\eta}_{mU}\bar{M}'_o[k_z(z'-c)] + j\bar{M}'_e[-k_z(z'-c)] \end{bmatrix} \right)}{(\tilde{\eta}_{mU} - \tilde{\eta}_{mL})\cos k_z(c-d) - j(\tilde{\eta}_{mU}\tilde{\eta}_{mL} - 1)\sin k_z(c-d)} \right\}$$

$$\text{for } z \gtrless z' \qquad (2.43)$$

where the $\bar{M}_o$ and $\bar{N}_e$ functions are defined by

$$\Psi^{e}_{o}(k_z) = \begin{cases} \cos(k_z z)e^{-j(k_x x + k_y y)} \\ \sin(k_z z)e^{-j(k_x x + k_y y)} \end{cases} \qquad (2.44)$$

This expression contains all components of the dyadic Green's function separated into LSE and LSM modes. Note that our convention will be to denote even and odd trigonometric dependence by the substripts 'e' and 'o'. In order to avoid any ambiguity when these subscripts are used, the corresponding k_x, k_y or k_z arguments will be shown explicitly in the same order, sometimes followed by other arguments as appropriate (see Appendix A). The magnetic field type is given by

$$\bar{\bar{G}}_{mK} = -\frac{1}{k^2}\hat{z}\hat{z}\delta(\bar{R} - \bar{R}') + \frac{j}{4\pi^2}\int_{-\infty}^{\infty}\int_{-\infty}^{\infty}\frac{dk_x dk_y}{k_z(k_x^2 + k_y^2)}$$

$$\left\{ \frac{\left(\begin{bmatrix} \tilde{\eta}_{mU}\bar{M}_o[k_z(z-c)] + j\bar{M}_e[k_z(z-c)] \end{bmatrix} \begin{bmatrix} \tilde{\eta}_{mL}\bar{M}'_o[k_z(z'-d)] + j\bar{M}'_e[-k_z(z'-d)] \end{bmatrix} \right)}{\left(\begin{bmatrix} \tilde{\eta}_{mL}\bar{M}_o[k_z(z-d)] + j\bar{M}_e[k_z(z-d)] \end{bmatrix} \begin{bmatrix} \tilde{\eta}_{mU}\bar{M}'_o[k_z(z'-c)] + j\bar{M}'_e[-k_z(z'-c)] \end{bmatrix} \right)}{(\tilde{\eta}_{mU} - \tilde{\eta}_{mL})\cos k_z(c-d) - j(\tilde{\eta}_{mU}\tilde{\eta}_{mL} - 1)\sin k_z(c-d)} \right.$$

$$+\left(\begin{array}{l}\left[\tilde{\eta}_{eU}\tilde{\mathrm{N}}_e[k_z(z-c)]-j\tilde{\mathrm{N}}_o[k_z(z-c)]\right]\left[\tilde{\eta}_{eL}\tilde{\mathrm{N}}'_e[k_z(z'-d)]-j\tilde{\mathrm{N}}'_o[-k_z(z'-d)]\right] \\ \left[\tilde{\eta}_{eL}\tilde{\mathrm{N}}_e[k_z(z-d)]-j\tilde{\mathrm{N}}_o[k_z(z-d)]\right]\left[\tilde{\eta}_{eU}\tilde{\mathrm{N}}'_e[k_z(z'-c)]-j\tilde{\mathrm{N}}'_o[-k_z(z'-c)]\right]\end{array}\right)$$

$$\Bigg\}\Big/\,(\tilde{\eta}_{eU}-\tilde{\eta}_{eL})\cos k_z(c-d)-j(\tilde{\eta}_{eU}\tilde{\eta}_{eL}-1)\sin k_z(c-d)$$

$$\text{for } z\gtrless z' \qquad (2.45)$$

When applied to the case of a slot on an infinite, perfectly conducting ground plane, $\tilde{\eta}_L$ is set to zero. For a single dielectric cover layer, on the upper interface we set

$$\tilde{\eta}_{eU} = \frac{k}{k_o} \qquad (2.46)$$

$$\tilde{\eta}_{mU} = \epsilon_r \frac{k_o}{k} \qquad (2.47)$$

corresponding to the normalized impedance boundary conditions for free-space above the slab. For a slot in the ground plane with its axis along $\hat{x}$, we take the $z > z'$ terms which results in

$$G_{mKxx} = \frac{1}{4\pi^2}\int_{-\infty}^{\infty}\int_{-\infty}^{\infty}\frac{dk_x dk_y}{k_z(k_x^2+k_y^2)}e^{-j[k_x(x-x')+k_y(y-y')]}$$

$$\left\{\left[\frac{\epsilon_r k_n \sin k_z(z-d)+jk_z\cos k_z(z-d)}{\epsilon_r k_n\cos k_z(c-d)+jk_z\sin k_z(c-d)}\right]+\frac{k_x^2k_z^2}{k^2}\left[\frac{k_z\sin k_z(z-d)+jk_n\cos k_z(z-d)}{k_z\cos k_z(c-d)+jk_n\sin k_z(c-d)}\right]\right\} \qquad (2.48)$$

By transforming the spectral integrals to a cylindrical coordinate system the double integrations can be replaced by a single radial integral on recognition of the integral representations of Bessel functions in the angular variable. Through some very tedious algebraic manipulations, the result can be transformed from the present form, which separates the LSE and LSM modes, to a hybrid form which can be compared to the result in Appendix C or with previously published forms [38, 36]; although not necessary for numerical evaluation.

2.2.2 Electric Current

For the case of the electric current source, the steps are exactly the same as in the preceding section, except here the Helmholtz equations take the forms:

$$\nabla \times \nabla \times \bar{\bar{G}}_{eJ} - k^2 \bar{\bar{G}}_{eJ} = \bar{\bar{I}}\delta(\bar{R} - \bar{R}') \tag{2.49}$$

$$\nabla \times \nabla \times \bar{\bar{G}}_{mJ} - k^2 \bar{\bar{G}}_{mJ} = \nabla \times \bar{\bar{I}}\delta(\bar{R} - \bar{R}') \tag{2.50}$$

where now we solve for $\bar{\bar{G}}_{mJ}$ first. Due to the similarity to the previous set of Helmholtz equations and because of the way the VWFs have been defined - particularly the symmetry introduced in the curl relationships - the solution proceeds with identical equations but with the following notational replacements:

$$\bar{M} \Longleftrightarrow \bar{N} \tag{2.51}$$

$$\bar{\bar{G}}_{eK} \Longrightarrow \bar{\bar{G}}_{mJ} \tag{2.52}$$

$$\bar{\bar{G}}_{mK} \Longrightarrow \bar{\bar{G}}_{eJ} \tag{2.53}$$

The process is similar to replacements made under the guidance of the Duality Principle, however, it is important to note the difference. The replacements dictated by the Duality Principle alone would result in functions which satify 'dual' boundary conditions, i.e., the electric field dyadics would satisfy the Neumann rather than the Dirichlet conditions on the conducting boundaries [13, pp. 29–39]. By replacing the $\bar{M}$ and $\bar{N}$ functions with each other, the true boundary conditions remain valid since these functions are complementary with respect to these boundary conditions. Although it would be interesting to more generally state and define this process under a heading such as say, the 'Similarity Principle', the development and proof is beyond the intended scope of this work, however, we will use it repeatedly.

The final result then is

$$\bar{\bar{G}}_{mJ} = \frac{jk}{4\pi^2}\int_{-\infty}^{\infty}\int_{-\infty}^{\infty}\frac{dk_x dk_y}{k_z(k_x^2+k_y^2)}$$

$$\left\{\frac{\left(\begin{bmatrix}\bar{\eta}_{mU}\bar{M}_o[k_z(z-c)]+j\bar{M}_e[k_z(z-c)]\end{bmatrix}\begin{bmatrix}\bar{\eta}_{mL}\bar{N}'_o[k_z(z'-d)]+j\bar{N}'_e[-k_z(z'-d)]\end{bmatrix}\right)}{\left(\begin{bmatrix}\bar{\eta}_{mL}\bar{M}_o[k_z(z-d)]+j\bar{M}_e[k_z(z-d)]\end{bmatrix}\begin{bmatrix}\bar{\eta}_{mU}\bar{N}'_o[k_z(z'-c)]+j\bar{N}'_e[-k_z(z'-c)]\end{bmatrix}\right)}{(\bar{\eta}_{mU}-\bar{\eta}_{mL})\cos k_z(c-d)-j(\bar{\eta}_{mU}\bar{\eta}_{mL}-1)\sin k_z(c-d)}\right.$$

$$\left.+\frac{\left(\begin{bmatrix}\bar{\eta}_{eU}\bar{N}_e[k_z(z-c)]-j\bar{N}_o[k_y(z-c)]\end{bmatrix}\begin{bmatrix}\bar{\eta}_{eL}\bar{M}'_e[k_z(z'-d)]-j\bar{M}'_o[-k_y(z'-d)]\end{bmatrix}\right)}{\left(\begin{bmatrix}\bar{\eta}_{eL}\bar{N}_e[k_z(z-d)]-j\bar{N}_o[k_y(z-d)]\end{bmatrix}\begin{bmatrix}\bar{\eta}_{eU}\bar{M}'_e[k_z(z'-c)]-j\bar{M}'_o[-k_y(z'-c)]\end{bmatrix}\right)}{(\bar{\eta}_{eU}-\bar{\eta}_{eL})\cos k_z(c-d)-j(\bar{\eta}_{eU}\bar{\eta}_{eL}-1)\sin k_z(c-d)}\right\}$$

$$\text{for}\quad z\gtrless z' \qquad (2.54)$$

$\bar{\bar{G}}_{eJ}$ can be found by substituting the coefficients into equations similar to Equations (2.32-2.34), but also can be derived from $\bar{\bar{G}}_{mJ}$ directly, applying Equation (1.15) with special care in performing the derivatives at the source discontinuity. The final expression is

$$\bar{\bar{G}}_{eJ} = -\frac{1}{k^2}\hat{z}\hat{z}\delta(\bar{R}-\bar{R}') + \frac{j}{4\pi^2}\int_{-\infty}^{\infty}\int_{-\infty}^{\infty}\frac{dk_x dk_y}{k_z(k_x^2+k_y^2)}$$

$$\left\{\frac{\left(\begin{bmatrix}\bar{\eta}_{eU}\bar{M}_e[k_z(z-c)]-j\bar{M}_o[k_y(z-c)]\end{bmatrix}\begin{bmatrix}\bar{\eta}_{eL}\bar{M}'_e[k_z(z'-d)]-j\bar{M}'_o[-k_y(z'-d)]\end{bmatrix}\right)}{\left(\begin{bmatrix}\bar{\eta}_{eL}\bar{M}_e[k_z(z-d)]-j\bar{M}_o[k_y(z-d)]\end{bmatrix}\begin{bmatrix}\bar{\eta}_{eU}\bar{M}'_e[k_z(z'-c)]-j\bar{M}'_o[-k_y(z'-c)]\end{bmatrix}\right)}{(\bar{\eta}_{eU}-\bar{\eta}_{eL})\cos k_z(c-d)-j(\bar{\eta}_{eU}\bar{\eta}_{eL}-1)\sin k_z(c-d)}\right.$$

$$\left.+\frac{\left(\begin{bmatrix}\bar{\eta}_{mU}\bar{N}_o[k_z(z-c)]+j\bar{N}_e[k_z(z-c)]\end{bmatrix}\begin{bmatrix}\bar{\eta}_{mL}\bar{N}'_o[k_z(z'-d)]+j\bar{N}'_e[-k_z(z'-d)]\end{bmatrix}\right)}{\left(\begin{bmatrix}\bar{\eta}_{mL}\bar{N}_o[k_z(z-d)]+j\bar{N}_e[k_z(z-d)]\end{bmatrix}\begin{bmatrix}\bar{\eta}_{mU}\bar{N}'_o[k_z(z'-c)]+j\bar{N}'_e[-k_z(z'-c)]\end{bmatrix}\right)}{(\bar{\eta}_{mU}-\bar{\eta}_{mL})\cos k_z(c-d)-j(\bar{\eta}_{mU}\bar{\eta}_{mL}-1)\sin k_z(c-d)}\right\}$$

$$\text{for}\quad z\gtrless z' \qquad (2.55)$$

2.3 Dyadic Green's Functions for Layer Filled Rectangular Waveguides

The electric and magnetic dyadic Green's functions for an electric current source in rectangular waveguide are needed for the radiating slot problem. As will be shown later, the electric type is used in an integral equation approach to solve for the propagation constants of the structure. Once a propagation constant has been determined for a selected mode, both the electric and magnetic fields on the entire cross-section are required to apply the Reaction Method to the three-dimensional cavity problem. The magnetic current case is not needed in the main body of this work but will be discussed briefly in Chapter IV.

As in [79], the solution for the multi-layered waveguide problem is built upon the solution for the parallel plate problem. The parallel plate waveguide solution has already been obtained in the previous section if we set $\tilde{\eta}_U = \tilde{\eta}_L = 0$ on the source layer boundaries. However, although the parallel plate solution we need is based on VWFs defined with respect to a piloting vector $\hat{z}$ as was used above, the desired planes for the parallel plates are defined by $x = 0$ and $x = a$ which do not correspond to the impedance boundaries used previously. Therefore, the parallel plate solution will first be derived based on the appropriate conducting planes followed by the layered rectangular waveguide solution.

2.3.1 The Parallel Plate Green's Function

A parallel plate waveguide shown in Figure 2.3 is formed by bounding walls at $x = 0$ and $x = a$ filled with a uniform dielectric material represented by the wavenumber k_i, where i will ultimately represent the i^{th} layer of a waveguide containing a source. We now define the functions

$$\bar{M}_o(k_x) = \nabla \times \Psi_o(k_x)\hat{z} = \nabla \times \left[\sin(m\pi x/a)e^{-j(k_y y + k_z z)}\hat{z}\right] \tag{2.56}$$

$$\bar{N}_e(k_x) = \frac{1}{\kappa}\nabla \times \nabla \times \Psi_e(k_x)\hat{z} = \frac{1}{\kappa}\nabla \times \nabla \times \left[\cos(m\pi x/a)e^{-j(k_y y + k_z z)}\hat{z}\right] \tag{2.57}$$

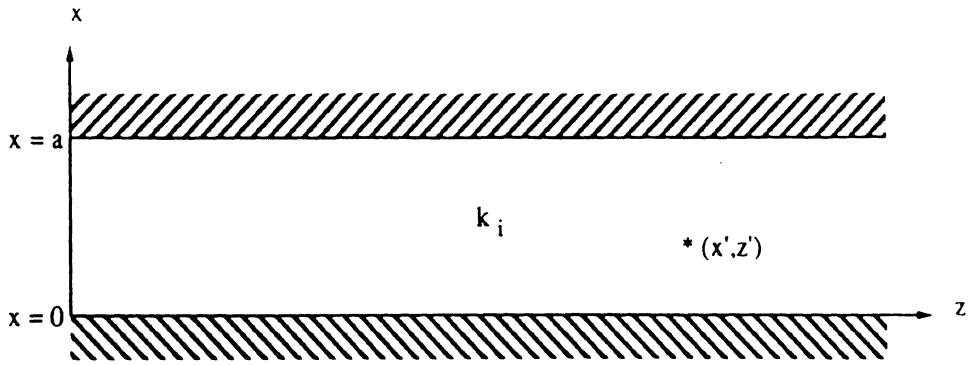

Figure 2.3: Parallel plate waveguide coordinate system.

which satisfy $\nabla \times \nabla \times \overline{\mathrm{F}} - \kappa^2 \overline{\mathrm{F}} = 0$ where $\kappa = \sqrt{k_x^2 + k_y^2 + k_z^2}$ and the boundary condition

$$\hat{x} \times \overline{\mathrm{F}} = 0 \qquad (\text{i.e.,} \quad \hat{x} \times \overline{\mathrm{E}} = 0) \tag{2.58}$$

at $x = 0$ and $x = a$. The wavenumbers k_y and k_z are two continuously distributed eigenvalues and $k_x = m\pi/a$ where m is an integer including $m = 0$ for $\tilde{\mathrm{N}}_e$.

The orthogonality properties of these functions are

$$\iiint_V \tilde{\mathrm{M}}_o^e(m, k_y, k_z) \cdot \tilde{\mathrm{N}}_e^o(m', k_y', k_z')\, dV = 0 \tag{2.59}$$

for any combination of even and odd functions and for any two sets of eigenvalues (m, k_y, k_z) and (m', k_y', k_z'). The volume of integration corresponds to the entire space inside the parallel plate waveguide. The normalization constants of these functions are stated by the following relations:

$$\begin{aligned} & \iiint_V \tilde{\mathrm{M}}_e(m, k_y, k_z) \cdot \tilde{\mathrm{M}}_e(m', -k_y', -k_z')\, dV \\ = & \iiint_V \tilde{\mathrm{N}}_e(m, k_y, k_z) \cdot \tilde{\mathrm{N}}_e(m', -k_y', -k_z')\, dV \\ = & \begin{cases} 0 & m \neq m' \\ (1 + \delta_m) 2\pi^2 a (k_x^2 + k_y^2) \delta(k_y - k_y') \delta(k_z - k_z') & m = m' = 0, 1, 2, \ldots \end{cases} \end{aligned} \tag{2.60}$$

$$
\begin{aligned}
&\iiint_V \bar{\mathrm{M}}_o(m,k_y,k_z)\cdot\bar{\mathrm{M}}_o(m',-k_y',-k_z')\,dV \\
=\;&\iiint_V \bar{\mathrm{N}}_o(m,k_y,k_z)\cdot\bar{\mathrm{N}}_o(m',-k_y',-k_z')\,dV \\
=\;&\begin{cases} 0 & m\neq m' \\ 2\pi^2 a(k_x^2+k_y^2)\delta(k_y-k_y')\delta(k_z-k_z') & m=m'=1,2,\ldots \end{cases}
\end{aligned}
\tag{2.61}
$$

where δ_m is the Kronecker delta function defined by $\delta_m = \begin{cases} 1 & m=0 \\ 0 & m\neq 0 \end{cases}$

To find $\bar{\bar{\mathrm{G}}}_{mJ}$ we first let

$$
\nabla\times[\bar{\bar{\mathrm{I}}}\delta(\bar{R}-\bar{R}')] = \int_{-\infty}^{\infty}\int_{-\infty}^{\infty} dk_y dk_z \sum_{m=0}^{\infty}[\bar{\mathrm{M}}_o(m,k_y,k_z)\,\bar{\mathrm{A}}_o + \bar{\mathrm{N}}_e(m,k_y,k_z)\,\bar{\mathrm{B}}_e] \tag{2.62}
$$

By taking the anterior scalar product of Equation (2.62) with $\bar{\mathrm{M}}_o(m',-k_y',-k_z')$ and $\bar{\mathrm{N}}_e(m',-k_y',-k_z')$ respectively, and integrating throughout V, we can determine the vector coefficients $\bar{\mathrm{A}}_o$ and $\bar{\mathrm{B}}_e$ through the orthogonality properties. They are

$$
\bar{\mathrm{A}}_o = \frac{(2-\delta_m)\kappa\bar{\mathrm{N}}_o'(m,-k_y,-k_z)}{4\pi^2 a(k_x^2+k_y^2)} \tag{2.63}
$$

$$
\bar{\mathrm{B}}_e = \frac{(2-\delta_m)\kappa\bar{\mathrm{M}}_e'(m,-k_y,-k_z)}{4\pi^2 a(k_x^2+k_y^2)} \tag{2.64}
$$

In Equations (2.63) and (2.64) the primed functions are defined with respect to (x',y',z'), the location of the source. Although for $m=0$ the function $\bar{\mathrm{N}}_o'$ vanishes, $m=0$ is included, as implied by the factor $(2-\delta_m)$ in Equation (2.63), to put it in a form similar to Equation (2.64). Substituting Equations (2.63) and (2.64) into (2.62) we obtain

$$
\begin{aligned}
\nabla\times[\bar{\bar{\mathrm{I}}}\delta(\bar{R}-\bar{R}')] \;=\; &\int_{-\infty}^{\infty}\int_{-\infty}^{\infty} dk_y dk_z \sum_{m=0}^{\infty}\frac{(2-\delta_m)\kappa}{4\pi^2 a(k_x^2+k_y^2)} \\
&\cdot\left[\bar{\mathrm{M}}_o(m,k_y,k_z)\bar{\mathrm{N}}_o'(m,-k_y,-k_z)+\bar{\mathrm{N}}_e(m,k_y,k_z)\bar{\mathrm{M}}_e'(m,-k_y,-k_z)\right]
\end{aligned}
\tag{2.65}
$$

Now we let

$$
\begin{aligned}
\bar{\bar{\mathrm{G}}}_{mJ} \;=\; &\int_{-\infty}^{\infty}\int_{-\infty}^{\infty} dk_y dk_z \sum_{m=0}^{\infty}\frac{(2-\delta_m)\kappa}{4\pi^2 a(k_x^2+k_y^2)} \\
&\cdot\left[\mathrm{a}\bar{\mathrm{M}}_o(m,k_y,k_z)\bar{\mathrm{N}}_o'(m,-k_y,-k_z)+\mathrm{b}\bar{\mathrm{N}}_e(m,k_y,k_z)\bar{\mathrm{M}}_e'(m,-k_y,-k_z)\right]
\end{aligned}
\tag{2.66}
$$

Substituting Equations (2.65) and (2.66) into (1.12), and making use the relations given by Equations (2.13) and (2.14), one finds

$$a = b = \frac{1}{\kappa^2 - k_i^2} \tag{2.67}$$

as before. The integration with respect to k_z can be carried out in closed form by applying the residue theorem together with the radiation condition yielding

$$\bar{\bar{G}}_{mJ} = -\int_{-\infty}^{\infty} dk_y \sum_{m=0}^{\infty} \frac{j(2-\delta_m)k_i}{4\pi a k_z (k_x^2 + k_y^2)}$$
$$\cdot \left[\bar{M}_o(m, k_y, \pm k_z)\bar{N}_o'(m, -k_y, \mp k_z) + \bar{N}_e(m, k_y, \pm k_z)\bar{M}_e'(m, -k_y, \mp k_z)\right] \quad z \gtrless z' \tag{2.68}$$

where $k_z = \sqrt{k_i^2 - k_x^2 - k_y^2}$. Again, the top sign applies to $z > z'$ and the bottom sign to $z < z'$. Now applying Equation (1.15), again through use of the relationships given by Equations (2.13) and (2.14), and taking into account the discontinuity at the source, we can write

$$\bar{\bar{G}}_{eJ} = -\frac{1}{k_i^2}\hat{z}\hat{z}\delta(\bar{R} - \bar{R}') - \int_{-\infty}^{\infty} dk_y \sum_{m=0}^{\infty} \frac{j(2-\delta_m)}{4\pi a k_z (k_x^2 + k_y^2)}$$
$$\cdot \left[\bar{M}_e(m, k_y, \pm k_z)\bar{M}_e'(m, -k_y, \mp k_z) + \bar{N}_o(m, k_y, \pm k_z)\bar{N}_o'(m, -k_y, \mp k_z)\right] \quad z \gtrless z' \tag{2.69}$$

The solutions for the magnetic current follow the same procedure yielding

$$\bar{\bar{G}}_{mK} = -\frac{1}{k_i^2}\hat{z}\hat{z}\delta(\bar{R} - \bar{R}') - \int_{-\infty}^{\infty} dk_y \sum_{m=0}^{\infty} \frac{j(2-\delta_m)}{4\pi a k_z (k_x^2 + k_y^2)}$$
$$\cdot \left[\bar{M}_o(m, k_y, \pm k_z)\bar{M}_o'(m, -k_y, \mp k_z) + \bar{N}_e(m, k_y, \pm k_z)\bar{N}_e'(m, -k_y, \mp k_z)\right] \quad z \gtrless z' \tag{2.70}$$

$$\bar{\bar{G}}_{eK} = -\int_{-\infty}^{\infty} dk_y \sum_{m=0}^{\infty} \frac{j(2-\delta_m)k_i}{4\pi a k_z (k_x^2 + k_y^2)}$$
$$\left[\bar{M}_e(m, k_y, \pm k_z)\bar{N}_e'(m, -k_y, \mp k_z) + \bar{N}_o(m, k_y, \pm k_z)\bar{M}_o'(m, -k_y, \mp k_z)\right] \quad z \gtrless z' \tag{2.71}$$

Note again that this can also be obtained from the previous case by simply replacing $\bar{\bar{G}}_{eJ} \Longrightarrow \bar{\bar{G}}_{mK}$, $\bar{\bar{G}}_{mJ} \Longrightarrow \bar{\bar{G}}_{eK}$, and $\bar{M} \Longleftrightarrow \bar{N}$.

2.3.2 Rectangular Waveguide with Electric Currents

We now construct the dyadic Green's function for the source layer of a multi-layered rectangular waveguide (see Figure 2.1) by using the parallel plate Green's function solutions above and the method of scattering superposition. Let

$$\bar{\bar{G}}_{mJ} = \bar{\bar{G}}^{(P)}_{mJ} + \bar{\bar{G}}^{(S)}_{mJ} \tag{2.72}$$

where $\bar{\bar{G}}^{(P)}_{mJ}$ is the parallel plate solution and $\bar{\bar{G}}^{(S)}_{mJ}$ is defined as

$$\bar{\bar{G}}^{(S)}_{mJ} = -\int_{-\infty}^{\infty} dk_y \sum_{m=0}^{\infty} \frac{j(2-\delta_m)k_i}{4\pi a k_z (k_x^2+k_y^2)} \cdot \left[\bar{N}_e(m,k_y,k_z)\,\bar{A}^+ + \bar{N}_e(m,k_y,-k_z)\,\bar{A}^- + \bar{M}_o(m,k_y,k_z)\,\bar{B}^+ + \bar{M}_o(m,k_y,-k_z)\,\bar{B}^-\right] \tag{2.73}$$

representing fields which are scattered from the dielectric layer interfaces located at $z = c$ and $z = d$. The unknown vector coefficients, $\bar{A}^+$, $\bar{A}^-$, $\bar{B}^+$ and $\bar{B}^-$, can be found by applying the upper (η_U) and lower (η_L) impedance boundary conditions for the layer. This produces two pairs of equations for the unknown coefficients:

$$(\tilde{\eta}_{eU}-1)e^{-jk_zc}\,\bar{A}^+ - (\tilde{\eta}_{eU}+1)e^{jk_zc}\,\bar{A}^- = -(\tilde{\eta}_{eU}-1)e^{-jk_zc}\bar{M}'_e(m,-k_y,k_z) \tag{2.74}$$

$$(\tilde{\eta}_{eL}-1)e^{-jk_zd}\,\bar{A}^+ - (\tilde{\eta}_{eL}+1)e^{jk_zd}\,\bar{A}^- = (\tilde{\eta}_{eL}+1)e^{jk_zd}\bar{M}'_e(m,-k_y,-k_z) \tag{2.75}$$

and

$$(\tilde{\eta}_{mU}-1)e^{-jk_zc}\,\bar{B}^+ + (\tilde{\eta}_{mU}+1)e^{jk_zc}\,\bar{B}^- = -(\tilde{\eta}_{mU}-1)e^{-jk_zc}\bar{N}'_o(m,-k_y,k_z) \tag{2.76}$$

$$(\tilde{\eta}_{mL}-1)e^{-jk_zd}\,\bar{B}^+ + (\tilde{\eta}_{mL}+1)e^{jk_zd}\,\bar{B}^- = -(\tilde{\eta}_{mL}+1)e^{jk_zd}\bar{N}'_o(m,-k_y,-k_z) \tag{2.77}$$

Notice that these equations are identical to Equations (2.33–2.35) with the replacements:

$$\bar{M}'(\pm k_z) \Longrightarrow \bar{M}'_e(m,-k_y,\pm k_z) \tag{2.78}$$

$$\bar{N}'(\pm k_z) \Longrightarrow \bar{N}'_o(m,-k_y,\pm k_z) \tag{2.79}$$

This feature is characteristic of all of the solutions we will be dealing with, and should be expected since the functions differ only in whether the functional dependence is exponential

or trigonometric. As a result, the solutions are identical to Equations (2.39-2.42) with the corresponding notational substitutions.

Algebraic manipulation of Equations (2.68,2.72) and (2.73) and use of the relations given in Appendix A then leads to

$$\bar{\bar{G}}_{mJ} = \int_{-\infty}^{\infty} dk_y \sum_{m=0}^{\infty} \frac{j(2-\delta_m)k_i}{2\pi a k_z (k_x^2+k_y^2)} \left\{ \frac{\begin{pmatrix} \bar{\mathcal{M}}_o[\tilde{\eta}_{mU};m,k_z(z-c)]\,\bar{\mathcal{N}}_o'[\tilde{\eta}_{mL};m,k_z(z'-d)] \\ \bar{\mathcal{M}}_o[\tilde{\eta}_{mL};m,k_z(z-d)]\,\bar{\mathcal{N}}_o'[\tilde{\eta}_{mU};m,k_z(z'-c)] \end{pmatrix}}{(\tilde{\eta}_{mU}-\tilde{\eta}_{mL})\cos k_z(c-d) - j(\tilde{\eta}_{mU}\tilde{\eta}_{mL}-1)\sin k_z(c-d)} + \frac{\begin{pmatrix} \bar{\mathcal{N}}_e[\tilde{\eta}_{eU};m,k_z(z-c)]\,\bar{\mathcal{M}}_e'[\tilde{\eta}_{eL};m,k_z(z'-d)] \\ \bar{\mathcal{N}}_e[\tilde{\eta}_{eL};m,k_z(z-d)]\,\bar{\mathcal{M}}_e'[\tilde{\eta}_{eU};m,k_z(z'-c)] \end{pmatrix}}{(\tilde{\eta}_{eU}-\tilde{\eta}_{eL})\cos k_z(c-d) - j(\tilde{\eta}_{eU}\tilde{\eta}_{eL}-1)\sin k_z(c-d)} \right\}$$

$$\text{for} \quad z \gtrless z' \qquad (2.80)$$

where we have now defined the new operator functions, $\bar{\mathcal{M}}_{e_o}$ and $\bar{\mathcal{N}}_{e_o}$, for the sake of compact notation:

$$\bar{\mathcal{M}}_o[\eta;\alpha] = \eta\bar{\mathrm{M}}_{oo}[\alpha] + j\bar{\mathrm{M}}_{oe}[\alpha] \qquad (2.81)$$

$$\bar{\mathcal{M}}_e[\eta;\alpha] = \eta\bar{\mathrm{M}}_{ee}[\alpha] - j\bar{\mathrm{M}}_{eo}[\alpha] \qquad (2.82)$$

$$\bar{\mathcal{N}}_o[\eta;\alpha] = \eta\bar{\mathrm{N}}_{oo}[\alpha] + j\bar{\mathrm{N}}_{oe}[\alpha] \qquad (2.83)$$

$$\bar{\mathcal{N}}_e[\eta;\alpha] = \eta\bar{\mathrm{N}}_{ee}[\alpha] - j\bar{\mathrm{N}}_{eo}[\alpha] \qquad (2.84)$$

Since α here is $[m, k_z(z-c)]$ and m is associated with k_x, we recognize that the 'e' and 'o' subscripts in this case imply trigonometric functions of x and z. Also recall that the primed functions use $-k_y$.

We can find $\bar{\bar{G}}_{eJ}$ as we did in the parallel plate case, by performing the derivatives

indicated by Equation (1.15):

$$\bar{\bar{G}}_{eJ} = -\frac{1}{k_i^2}\hat{z}\hat{z}\delta(\bar{R}-\bar{R}') + \int_{-\infty}^{\infty} dk_y \sum_{m=0}^{\infty} \frac{j(2-\delta_m)}{2\pi a k_z (k_x^2+k_y^2)}$$

$$\left\{ \frac{\begin{pmatrix} \bar{\mathcal{M}}_e[\tilde{\eta}_{eU}; m, k_z(z-c)]\ \bar{\mathcal{M}}'_e[\tilde{\eta}_{eL}; m, k_z(z'-d)] \\ \bar{\mathcal{M}}_e[\tilde{\eta}_{eL}; m, k_z(z-d)]\ \bar{\mathcal{M}}'_e[\tilde{\eta}_{eU}; m, k_z(z'-c)] \end{pmatrix}}{(\tilde{\eta}_{eU}-\tilde{\eta}_{eL})\cos k_z(c-b) - j(\tilde{\eta}_{eU}\tilde{\eta}_{eL}-1)\sin k_z(c-b)} \right.$$

$$\left. + \frac{\begin{pmatrix} \bar{\mathcal{N}}_o[\tilde{\eta}_{mU}; m, k_z(z-c)]\ \bar{\mathcal{N}}'_o[\tilde{\eta}_{mL}; m, k_z(z'-d)] \\ \bar{\mathcal{N}}_o[\tilde{\eta}_{mL}; m, k_z(z-d)]\ \bar{\mathcal{N}}'_o[\tilde{\eta}_{mU}; m, k_z(z'-c)] \end{pmatrix}}{(\tilde{\eta}_{mU}-\tilde{\eta}_{mL})\cos k_z(c-b) - j(\tilde{\eta}_{mU}\tilde{\eta}_{mL}-1)\sin k_z(c-b)} \right\}$$

$$\text{for} \quad z \gtrless z' \qquad (2.85)$$

Both $\bar{\bar{G}}_{eJ}$ and $\bar{\bar{G}}_{mJ}$ involve a spectral integral which can be reduced by Cauchy's Theorem, once the impedance functions are specified.

2.3.3 Rectangular Waveguide with Magnetic Currents

The magnetic current cases can be found through the same method or 'Similarity Principle' substitutions (section 2.2.2) to obtain

$$\bar{\bar{G}}_{mK} = -\frac{1}{k_i^2}\hat{z}\hat{z}\delta(\bar{R}-\bar{R}') + \int_{-\infty}^{\infty} dk_y \sum_{m=0}^{\infty} \frac{j(2-\delta_m)}{2\pi a k_z (k_x^2+k_y^2)}$$

$$\left\{ \frac{\begin{pmatrix} \bar{\mathcal{M}}_o[\tilde{\eta}_{mU}; m, k_z(z-c)]\ \bar{\mathcal{M}}'_o[\tilde{\eta}_{mL}; m, k_z(z'-d)] \\ \bar{\mathcal{M}}_o[\tilde{\eta}_{mL}; m, k_z(z-d)]\ \bar{\mathcal{M}}'_o[\tilde{\eta}_{mU}; m, k_z(z'-c)] \end{pmatrix}}{(\tilde{\eta}_{mU}-\tilde{\eta}_{mL})\cos k_z(c-b) - j(\tilde{\eta}_{mU}\tilde{\eta}_{mL}-1)\sin k_z(c-b)} \right.$$

$$\left. + \frac{\begin{pmatrix} \bar{\mathcal{N}}_e[\tilde{\eta}_{eU}; m, k_z(z-c)]\ \bar{\mathcal{N}}'_e[\tilde{\eta}_{eL}; m, k_z(z'-d)] \\ \bar{\mathcal{N}}_e[\tilde{\eta}_{eL}; m, k_z(z-d)]\ \bar{\mathcal{N}}'_e[\tilde{\eta}_{eU}; m, k_z(z'-c)] \end{pmatrix}}{(\tilde{\eta}_{eU}-\tilde{\eta}_{eL})\cos k_z(c-b) - j(\tilde{\eta}_{eU}\tilde{\eta}_{eL}-1)\sin k_z(c-b)} \right\}$$

$$\text{for} \quad z \gtrless z' \qquad (2.86)$$

and

$$\bar{\bar{G}}_{eK} = \int_{-\infty}^{\infty} dk_y \sum_{m=0}^{\infty} \frac{j(2-\delta_m)k_i}{2\pi a k_y (k_x^2 + k_z^2)} \left\{ \frac{\begin{pmatrix} \bar{\mathcal{M}}_e[\tilde{\eta}_{eU}; m, k_z(z-c)]\, \bar{\mathcal{N}}'_e[\tilde{\eta}_{eL}; m, k_z(z'-d)] \\ \bar{\mathcal{M}}_e[\tilde{\eta}_{eL}; m, k_z(z-d)]\, \bar{\mathcal{N}}'_e[\tilde{\eta}_{eU}; m, k_z(z'-c)] \end{pmatrix}}{(\tilde{\eta}_{eU} - \tilde{\eta}_{eL}) \cos k_z(c-b) - j(\tilde{\eta}_{eU}\tilde{\eta}_{eL} - 1) \sin k_z(c-b)} + \frac{\begin{pmatrix} \bar{\mathcal{N}}_o[\tilde{\eta}_{mU}; m, k_z(z-c)]\, \bar{\mathcal{M}}'_o[\tilde{\eta}_{mL}; m, k_z(z'-d)] \\ \bar{\mathcal{N}}_o[\tilde{\eta}_{mL}; m, k_z(z-d)]\, \bar{\mathcal{M}}'_o[\tilde{\eta}_{mU}; m, k_z(z'-c)] \end{pmatrix}}{(\tilde{\eta}_{mU} - \tilde{\eta}_{mL}) \cos k_z(c-b) - j(\tilde{\eta}_{mU}\tilde{\eta}_{mL} - 1) \sin k_z(c-b)} \right\}$$

$$\text{for} \quad z \gtrless z' \quad (2.87)$$

2.4 Dyadic Green's Functions for Layer Filled Rectangular Cavities

The scattering superposition approach can now be applied to the result of the previous section directly to obtain the dyadic Green's functions for the cavity problem by introducing conducting walls at $y = 0$ and $y = b$ and applying scattering superposition to the $\pm\hat{y}$ directed waves. As an alternative, one can take a somewhat simpler approach by first deriving the dyadic Green's function for a waveguide with its axis along the $\hat{z}$ direction (k_y becomes $n\pi/b$). Then scattering superposition is applied along the $\hat{z}$ direction with impedance boundary conditions to obtain the result for the cavity (see also [72, 75, 79]). This will be the approach demonstrated here since the intermediate Green's functions will also be needed in Chapter IV.

2.4.1 Homogeneously Filled Rectangular Waveguide: TE and TM Modes

As with the use of the half-space solution as a building-block for the previous solutions, the preceding modal representations of layered rectangular waveguides are not in a convenient form for the formation of the cavity solution. Again, the VWFs there are defined

with the normal to the layer interfaces, resulting in the LSE and LSM mode representation. What is more convenient here is the solution for a homogeneously filled rectangular waveguide expressed in terms of VWFs defined to represent the modes Transverse-Electric (TE) and Transverse-Magnetic (TM) to the waveguide axis. We again will first find $\bar{\bar{G}}_{mJ}^{(W)}$ from which $\bar{\bar{G}}_{eJ}^{(W)}$ will follow.

$\bar{\bar{G}}_{mJ}^{(W)}$ must satisfy the wave equation:

$$\nabla \times \nabla \times \bar{\bar{G}}_{mJ}^{(W)} - k_i^2 \bar{\bar{G}}_{mJ}^{(W)} = \nabla \times \left[\bar{\bar{I}}\delta(\bar{R} - \bar{R}')\right] \tag{2.88}$$

To construct the solution we will need the vector wave functions satisfying the Neumann boundary conditions which are:

$$\bar{M}_{oo}(k_x, k_y) = \nabla \times \Psi_{oo}(k_x, k_y)\hat{z} \tag{2.89}$$

$$\bar{N}_{ee}(k_x, k_y) = \frac{1}{\kappa}\nabla \times \nabla \times \Psi_{ee}(k_x, k_y)\hat{z} \tag{2.90}$$

where

$$\Psi_{\substack{ee \\ oo}}(k_x, k_y) = \begin{bmatrix} \cos k_x x \cos k_y y \\ \\ \sin k_x x \sin k_y y \end{bmatrix} e^{-jk_z z} \tag{2.91}$$

with $k_x = k_m = m\pi/a$ and $k_y = k_n = n\pi/b$.

Following the Ohm-Rayleigh method as before, we expand the source term as

$$\nabla \times \left[\bar{\bar{I}}\delta(\bar{R} - \bar{R}')\right] = \int_{-\infty}^{\infty} dk_z \sum_{m=0}^{\infty}\sum_{n=0}^{\infty} \left[\bar{M}_{oo}(k_x, k_y)\,\bar{A} + \bar{N}_{ee}(k_x, k_y)\,\bar{B}\right] \tag{2.92}$$

The coefficients $\bar{A}$ and $\bar{B}$ are found from the properties of the vector wave functions to be

$$\bar{A} = \frac{(2 - \delta_{mn})\kappa}{\pi ab(k_m^2 + k_n^2)}\bar{N}'_{oo}(k_x, k_y, -k_z) \tag{2.93}$$

$$\bar{B} = \frac{(2 - \delta_{mn})\kappa}{\pi ab(k_m^2 + k_n^2)}\bar{M}'_{ee}(k_x, k_y, -k_z) \tag{2.94}$$

where the Kronecker delta function δ_{mn} is equal to 1 for $m = 0$ or $n = 0$ and 0 otherwise (the case where both $m = 0$ and $n = 0$ is the trivial, zero field solution for this case). Thus,

Equation (2.92) can be written as

$$\nabla \times [\bar{\bar{I}}\delta(\bar{R}-\bar{R}')] = \int_{-\infty}^{\infty} dk_z \sum_{m=0}^{\infty}\sum_{n=0}^{\infty} \frac{(2-\delta_{mn})\kappa}{\pi ab(k_m^2+k_n^2)} \cdot \left[\bar{M}_{oo}(k_x,k_y,k_z)\bar{N}'_{oo}(k_x,k_y,-k_z) + \bar{N}_{ee}(k_x,k_y,k_z)\bar{M}'_{ee}(k_x,k_y,-k_z)\right] \quad (2.95)$$

To find $\bar{\bar{G}}_{mJ}^{(W)}$ we let

$$\bar{\bar{G}}_{mJ}^{(W)} = \int_{-\infty}^{\infty} dk_z \sum_{m=0}^{\infty}\sum_{n=0}^{\infty} \frac{(2-\delta_{mn})\kappa}{\pi ab(k_m^2+k_n^2)} \cdot \left[a\bar{M}_{oo}(k_x,k_y,k_z)\bar{N}'_{oo}(k_x,k_y,-k_z) + b\bar{N}_{ee}(k_x,k_y,k_z)\bar{M}'_{ee}(k_x,k_y,-k_z)\right] \quad (2.96)$$

Substituting into Equation (2.88) we find as usual

$$a = b = \frac{1}{\kappa^2 - k_i^2} \quad (2.97)$$

so that

$$\bar{\bar{G}}_{mJ}^{(W)} = \int_{-\infty}^{\infty} dk_z \sum_{m=0}^{\infty}\sum_{n=0}^{\infty} \frac{(2-\delta_{mn})}{\pi ab(k_m^2+k_n^2)} \left[\frac{\kappa}{\kappa^2-k_i^2}\right] \cdot \left[\bar{M}_{oo}(k_x,k_y,k_z)\bar{N}'_{oo}(k_x,k_y,-k_z) + \bar{N}_{ee}(k_x,k_y,k_z)\bar{M}'_{ee}(k_x,k_y,-k_z)\right] \quad (2.98)$$

The Fourier integral can be evaluated in closed form by means of contour integration and the radiation condition leading to

$$\bar{\bar{G}}_{mJ}^{(W)} = -\sum_{m=0}^{\infty}\sum_{n=0}^{\infty} \frac{jk_i(2-\delta_{mn})}{abk_z(k_m^2+k_n^2)} \cdot \left[\bar{M}_{oo}(k_x,k_y,\pm k_z)\bar{N}'_{oo}(k_x,k_y,\mp k_z) + \bar{N}_{ee}(k_x,k_y,\pm k_z)\bar{M}'_{ee}(k_x,k_y,\mp k_z)\right]$$

$$\text{for } z \gtrless z' \quad (2.99)$$

where $k_z^2 = k_i^2 - (k_m^2 + k_n^2)$. Using Equation (1.15):

$$\bar{\bar{G}}_{eJ}^{(W)} = -\frac{1}{k_i^2}\hat{z}\hat{z}\delta(\bar{R}-\bar{R}') - \sum_{m=0}^{\infty}\sum_{n=0}^{\infty} \frac{j(2-\delta_{mn})}{abk_z(k_m^2+k_n^2)} \cdot \left[\bar{M}_{oo}(k_x,k_y,\pm k_z)\bar{N}'_{oo}(k_x,k_y,\mp k_z) + \bar{N}_{ee}(k_x,k_y,\pm k_z)\bar{M}'_{ee}(k_x,k_y,\mp k_z)\right]$$

$$\text{for } z \gtrless z' \quad (2.100)$$

2.4.2 Cavity with Opposing Impedance Walls: Electric Current

We now introduce impedance walls at $z = c$ and $z = d$ where the added boundary conditions given by Equation (2.1) are to be enforced. Using the method of scattering superposition we let

$$\bar{\bar{G}}_{mJ} = \bar{\bar{G}}^{(W)}_{mJ} + \bar{\bar{G}}^{(S)}_{mJ} \tag{2.101}$$

where

$$\bar{\bar{G}}^{(S)}_{mJ} = -\sum_{m=0}^{\infty}\sum_{n=0}^{\infty} \frac{jk_i(2-\delta_{mn})}{abk_z(k_m^2+k_n^2)}$$
$$\cdot\left[\bar{M}_{oo}(k_x,k_y,k_z)\,\bar{A}^{+} + \bar{M}_{oo}(k_x,k_y,-k_z)\,\bar{A}^{-} + \bar{N}_{ee}(k_x,k_y,k_z)\,\bar{B}^{+} + \bar{N}_{ee}(k_x,k_y,-k_z)\,\bar{B}^{+}\right] \tag{2.102}$$

Evaluating the boundary conditions given by Equations (2.1) we get the same system of equations as (2.33-2.35) except this time with

$$\bar{M}'(\pm k_z) \Longrightarrow \bar{M}'_{ee}(k_x,k_y,\pm k_z) \tag{2.103}$$

$$\bar{N}'(\pm k_z) \Longrightarrow \bar{N}'_{oo}(k_x,k_y,\pm k_z) \tag{2.104}$$

Again we already have the solutions for this set by changing the notation of the VWFs. With some algebraic manipulation and use of the relations in Appendix A the results are

$$\bar{\bar{G}}_{mJ} = \sum_{m=0}^{\infty}\sum_{n=0}^{\infty} \frac{2jk_i(2-\delta_{mn})}{abk_z(k_x^2+k_y^2)}$$
$$\cdot\left\{ \frac{\begin{pmatrix} \bar{\mathcal{M}}_{oo}[\tilde{\eta}_{mU};k_x,k_y,k_z(z-c)]\;\bar{\mathcal{N}}'_{oo}[\tilde{\eta}_{mL};k_x,k_y,k_z(z'-d)] \\ \bar{\mathcal{M}}_{oo}[\tilde{\eta}_{mL};k_x,k_y,k_z(z-d)]\;\bar{\mathcal{N}}'_{oo}[\tilde{\eta}_{mU};k_x,k_y,k_z(z'-c)] \end{pmatrix}}{(\tilde{\eta}_{mU}-\tilde{\eta}_{mL})\cos k_z(c-d) - j(\tilde{\eta}_{mU}\tilde{\eta}_{mL}-1)\sin k_z(c-d)} \right.$$
$$\left. + \frac{\begin{pmatrix} \bar{\mathcal{N}}_{ee}[\tilde{\eta}_{eU};k_x,k_y,k_z(z-c)]\;\bar{\mathcal{M}}'_{ee}[\tilde{\eta}_{eL};k_x,k_y,k_z(z'-d)] \\ \bar{\mathcal{N}}_{ee}[\tilde{\eta}_{eL};k_x,k_y,k_z(z-d)]\;\bar{\mathcal{M}}'_{ee}[\tilde{\eta}_{eU};k_x,k_y,k_z(z'-c)] \end{pmatrix}}{(\tilde{\eta}_{eU}-\tilde{\eta}_{eL})\cos k_z(c-d) - j(\tilde{\eta}_{eU}\tilde{\eta}_{eL}-1)\sin k_z(c-d)} \right\}$$
$$\text{for } z \gtrless z' \tag{2.105}$$

and

$$\bar{\bar{G}}_{eJ} = \frac{1}{k_i^2}\hat{z}\hat{z}\delta(\bar{R}-\bar{R}') + \sum_{m=0}^{\infty}\sum_{n=0}^{\infty}\frac{2j(2-\delta_{mn})}{abk_z(k_x^2+k_y^2)}$$
$$\cdot\left\{\frac{\begin{pmatrix}\bar{\mathcal{M}}_{ee}[\bar{\eta}_{eU};k_x,k_y,k_z(z-c)]\,\bar{\mathcal{M}}'_{ee}[\bar{\eta}_{eL};k_x,k_y,k_z(z'-d)]\\ \bar{\mathcal{M}}_{ee}[\bar{\eta}_{eL};k_x,k_y,k_z(z-d)]\,\bar{\mathcal{M}}'_{ee}[\bar{\eta}_{eU};k_x,k_y,k_z(z'-c)]\end{pmatrix}}{(\bar{\eta}_{eU}-\bar{\eta}_{eL})\cos k_z(c-d) - j(\bar{\eta}_{eU}\bar{\eta}_{eL}-1)\sin k_z(c-d)}\right.$$
$$\left.+\frac{\begin{pmatrix}\bar{\mathcal{N}}_{oo}[\bar{\eta}_{mU};k_x,k_y,k_z(z-c)]\,\bar{\mathcal{N}}'_{oo}[\bar{\eta}_{mL};k_x,k_y,k_z(z'-d)]\\ \bar{\mathcal{N}}_{oo}[\bar{\eta}_{mL};k_x,k_y,k_z(z-d)]\,\bar{\mathcal{N}}'_{oo}[\bar{\eta}_{mU};k_x,k_y,k_z(z'-c)]\end{pmatrix}}{(\bar{\eta}_{mU}-\bar{\eta}_{mL})\cos k_z(c-d) - j(\bar{\eta}_{mU}\bar{\eta}_{mL}-1)\sin k_z(c-d)}\right\}$$
$$\text{for } z\gtrless z' \quad (2.106)$$

The operator functions are defined by the relations

$$\bar{\mathcal{M}}_{oo}[\eta;\alpha] = \eta\bar{M}_{ooo}[\alpha] + j\bar{M}_{ooe}[\alpha] \quad (2.107)$$

$$\bar{\mathcal{M}}_{ee}[\eta;\alpha] = \eta\bar{M}_{eee}[\alpha] - j\bar{M}_{eeo}[\alpha] \quad (2.108)$$

$$\bar{\mathcal{N}}_{oo}[\eta;\alpha] = \eta\bar{N}_{ooo}[\alpha] + j\bar{N}_{ooe}[\alpha] \quad (2.109)$$

$$\bar{\mathcal{N}}_{ee}[\eta;\alpha] = \eta\bar{N}_{eee}[\alpha] - j\bar{N}_{eeo}[\alpha] \quad (2.110)$$

2.4.3 TE and TM Modes in Homogeneously Filled Rectangular Waveguide and Cavities with Opposing Impedance Walls: Magnetic Currents

To model the slots, we also need the cavity dyadic Green's functions of both types for magnetic currents. The derivation could follow the previous case explicitly, however, because of the way the functions have been defined, we can take advantage of the symmetry of the equations and write the solution by making simple notational replacements. (The only exception is the treatment of the $(2-\delta_{mn})$ term which here is expanded as $(2-\delta_m)(2-\delta_n)$ since the $m=n=0$ case may produce non-zero field components.) Using this approach we can write the TE and TM solutions for magnetic currents in rectangular

waveguide as

$$\bar{\bar{G}}_{eK}^{(W)} = -\sum_{m=0}^{\infty}\sum_{n=0}^{\infty}\frac{jk_i(2-\delta_m)(2-\delta_n)}{abk_z(k_m^2+k_n^2)}$$
$$\cdot\left[\bar{M}_{ee}(k_x,k_y,\pm k_z)\bar{N}'_{ee}(k_x,k_y,\mp k_z)+\bar{N}_{oo}(k_x,k_y,\pm k_z)\bar{M}'_{oo}(k_x,k_y,\mp k_z)\right] \quad z\gtrless z' \quad (2.111)$$

$$\bar{\bar{G}}_{mK}^{(W)} = -\frac{1}{k_i^2}\hat{z}\hat{z}\delta(\bar{R}-\bar{R}')-\sum_{m=0}^{\infty}\sum_{n=0}^{\infty}\frac{j(2-\delta_m)(2-\delta_n)}{abk_z(k_m^2+k_n^2)}$$
$$\cdot\left[\bar{M}_{oo}(k_x,k_y,\pm k_z)\bar{M}'_{oo}(k_x,k_y,\mp k_z)+\bar{N}_{ee}(k_x,k_y,\pm k_z)\bar{N}'_{ee}(k_x,k_y,\mp k_z)\right] \quad z\gtrless z' \quad (2.112)$$

The cavity solutions are

$$\bar{\bar{G}}_{eK} = \sum_{m=0}^{\infty}\sum_{n=0}^{\infty}\frac{2jk_i(2-\delta_m)(2-\delta_n)}{abk_z(k_m^2+k_n^2)}$$
$$\cdot\left\{\frac{\begin{pmatrix}\bar{\mathcal{M}}_{ee}[\tilde{\eta}_{eU};k_x,k_y,k_z(z-c)]\,\bar{\mathcal{N}}'_{ee}[\tilde{\eta}_{eL};k_x,k_y,k_z(z'-d)]\\ \bar{\mathcal{M}}_{ee}[\tilde{\eta}_{eL};k_x,k_y,k_z(z-d)]\,\bar{\mathcal{N}}'_{ee}[\tilde{\eta}_{eU};k_x,k_y,k_z(z'-c)]\end{pmatrix}}{(\tilde{\eta}_{eU}-\tilde{\eta}_{eL})\cos k_z(c-d)-j(\tilde{\eta}_{eU}\tilde{\eta}_{eL}-1)\sin k_z(c-d)}\right.$$
$$\left.+\frac{\begin{pmatrix}\bar{\mathcal{N}}_{oo}[\tilde{\eta}_{mU};k_x,k_y,k_z(z-c)]\,\bar{\mathcal{M}}'_{oo}[\tilde{\eta}_{mL};k_x,k_y,k_z(z'-d)]\\ \bar{\mathcal{N}}_{oo}[\tilde{\eta}_{mL};k_x,k_y,k_z(z-d)]\,\bar{\mathcal{M}}'_{oo}[\tilde{\eta}_{mU};k_x,k_y,k_z(z'-c)]\end{pmatrix}}{(\tilde{\eta}_{mU}-\tilde{\eta}_{mL})\cos k_z(c-d)-j(\tilde{\eta}_{mU}\tilde{\eta}_{mL}-1)\sin k_z(c-d)}\right\}$$
$$\text{for } z\gtrless z' \quad (2.113)$$

and

$$\bar{\bar{G}}_{mK} = \frac{1}{k_i^2}\hat{z}\hat{z}\delta(\bar{R}-\bar{R}')+\sum_{m=0}^{\infty}\sum_{n=0}^{\infty}\frac{2j(2-\delta_m)(2-\delta_n)}{abk_z(k_m^2+k_n^2)}$$
$$\cdot\left\{\frac{\begin{pmatrix}\bar{\mathcal{M}}_{oo}[\tilde{\eta}_{mU};k_x,k_y,k_z(z-c)]\,\bar{\mathcal{M}}'_{oo}[\tilde{\eta}_{mL};k_x,k_y,k_z(z'-d)]\\ \bar{\mathcal{M}}_{oo}[\tilde{\eta}_{mL};k_x,k_y,k_z(z-d)]\,\bar{\mathcal{M}}'_{oo}[\tilde{\eta}_{mU};k_x,k_y,k_z(z'-c)]\end{pmatrix}}{(\tilde{\eta}_{mU}-\tilde{\eta}_{mL})\cos k_z(c-d)-j(\tilde{\eta}_{mU}\tilde{\eta}_{mL}-1)\sin k_z(c-d)}\right.$$
$$\left.+\frac{\begin{pmatrix}\bar{\mathcal{N}}_{ee}[\tilde{\eta}_{eU};k_x,k_y,k_z(z-c)]\,\bar{\mathcal{N}}'_{ee}[\tilde{\eta}_{eL};k_x,k_y,k_z(z'-d)]\\ \bar{\mathcal{N}}_{ee}[\tilde{\eta}_{eL};k_x,k_y,k_z(z-d)]\,\bar{\mathcal{N}}'_{ee}[\tilde{\eta}_{eU};k_x,k_y,k_z(z'-c)]\end{pmatrix}}{(\tilde{\eta}_{eU}-\tilde{\eta}_{eL})\cos k_z(c-d)-j(\tilde{\eta}_{eU}\tilde{\eta}_{eL}-1)\sin k_z(c-d)}\right\}$$
$$\text{for } z\gtrless z' \quad (2.114)$$

We now have derived and specified the dyadic Green's functions for all types of structures to be treated in this work. The integral equations are therefore fully defined and the task remaining is to solve for the unknown currents in each case and interpret the results.

CHAPTER III

METHOD OF MOMENTS FORMULATION

A general methodology for application to the various problems treated will be presented in this chapter for the case where two components of current will be allowed on both the strips and slots. Later, we will restrict our attention to strips and slots which are narrow so that only the longitudinal component of current need be considered. This assumption is sufficient to yield accurate results for the experimental cases to be used for verification, and thus simplifies the numerical implementation without loss of generality.

The solutions to the presented integral equations can be found by choosing basis functions to approximate the various currents. The error in the approximation is minimized by applying the well known Method of Moments, resulting in highly accurate representations of the currents from which the electrical behavior of the structures can be deduced. Furthermore, the method of moments formulation will be discussed in the context of the radiating slot problem only, since this problem contains all the essential elements of the coupler problem as well.

3.1 Definition of Coordinate Systems and Basis Functions

Let us expand the current on the strip in the following manner. We first define a strip-fixed coordinate system as illustrated in Figure 3.1. The currents on the strip in this

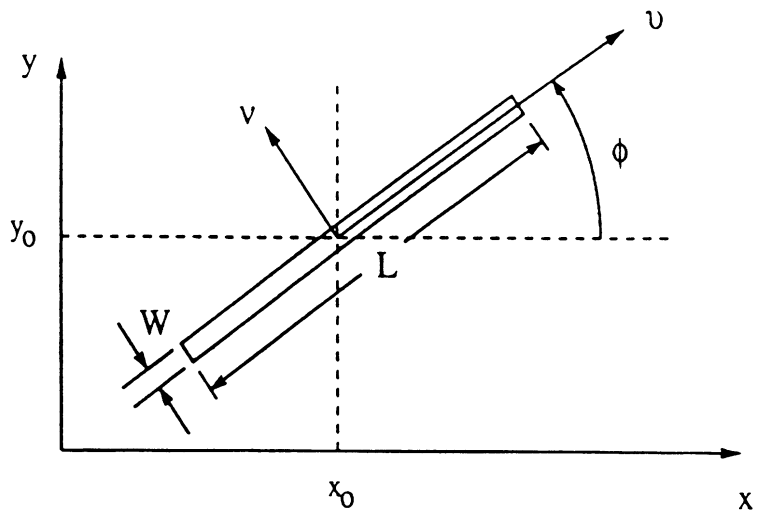

Figure 3.1: Cavity (x, y) and Strip-fixed (v, ν) Coordinate System.

coordinate system can now be expanded as

$$\bar{J}_s = J_v \hat{v} + J_\nu \hat{\nu} \tag{3.1}$$

$$J_v = \Psi(\nu) \sum_j \Phi(v_j) I_{vj} \tag{3.2}$$

$$J_\nu = \Phi(\nu) \sum_j I_{\nu j} \tag{3.3}$$

where Φ are piecewise sinusoidal basis functions defined by

$$\Phi(\alpha) = \frac{1}{\sin k_b l_\alpha} \begin{cases} \sin k_b(\alpha - \alpha_{q-1}) & \text{for} \quad -l_\alpha \le \alpha - \alpha_q \le 0 \\ \sin k_b(\alpha_{q+1} - \alpha) & \text{for} \quad 0 \le \alpha - \alpha_q \le l_\alpha \end{cases} \tag{3.4}$$

and l_α is half the subsection length defined by

$$l_\alpha = [\alpha_{q+1} - \alpha_{q-1}]/2 \tag{3.5}$$

The subscript q is an index identifying basis functions at various points along the strips and slots. Actually, k_b will always be chosen so that $k_b l_\alpha \ll \pi/2$, making the function basically a triangular pulse. This way, because the basis functions overlap, the current will essentially be approximated by piecewise 'linear' segments between sample points (see [32] for an introduction to the method of moments and basis functions). The sampling rate is determined by field phenomena, phase resolution requirements or numerical limitations, as

will be shown later. Typically, the sampling rate will be at least 20 samples per wavelength, often much higher, so we generally set $k_b \sim k_i$ which is more than sufficient to 'linearize' the basis functions. The motivation for the sinusoidal dependence is to simplify later integrations and evaluation of the resulting functions.

The Ψ function will be either a 'Maxwellian' distribution or a 'pulse' basis function defined as

$$\Psi(\beta) = \begin{cases} \Psi_{Maxwellian}(\beta) = \dfrac{1}{\pi l_\beta \sqrt{1-(\beta/l_\beta)^2}} & |\beta - \beta_q| \leq l_\beta \\ \Psi_{pulse} = 1 \end{cases} \tag{3.6}$$

The Maxwellian function is often used since it closely approximates the true solution for narrow strips or slots [52, 88]. These expansions are further illustrated by Figure 3.2 where the sinusoidal functions are exaggerated for clarity.

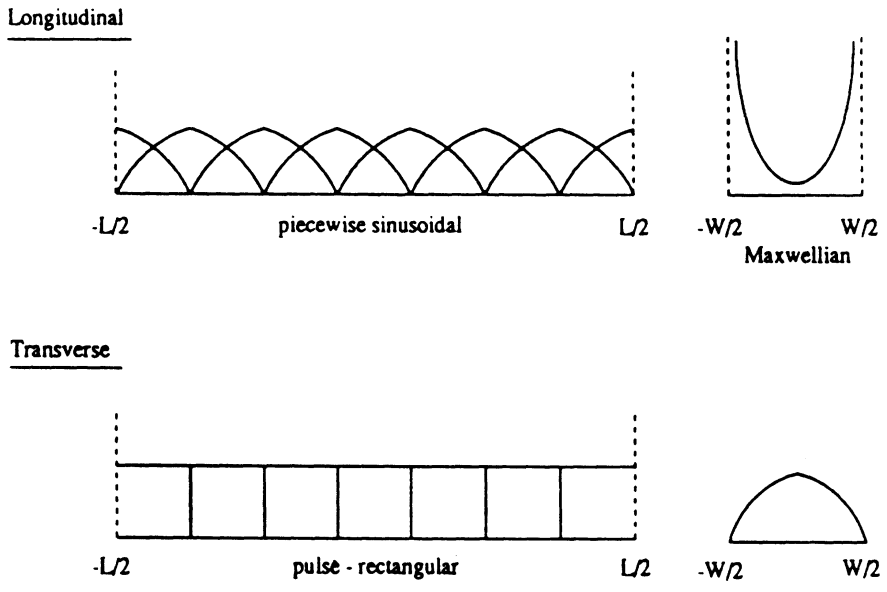

Figure 3.2: Current Expansion Functions.

In this work, we will deal exclusively with strips and slots which are narrow with respect to wavelength so that only one basis function will be used to represent the narrow dimension. For wider structures, rooftop functions are commonly used, involving similar overlapping basis functions in the direction of each component of current, but using the

pulse basis function for the transverse dependence. Because our strips and slots are narrow, we will typically only model the longitudinal component of current, however, both components are discussed here for generality and to form a basis for future efforts. The primary motivation for the use of piecewise functions is that they are very efficient in terms of changing strip or slot lengths as opposed to entire domain basis functions.

The strip-fixed system is related to the cavity coordinate system by

$$v = (x - x_o)\cos\phi + (y - y_o)\sin\phi \tag{3.7}$$

$$\nu = -(x - x_o)\sin\phi + (y - y_o)\cos\phi \tag{3.8}$$

We also define a slot-fixed coordinate system as illustrated in Figure 3.3 where

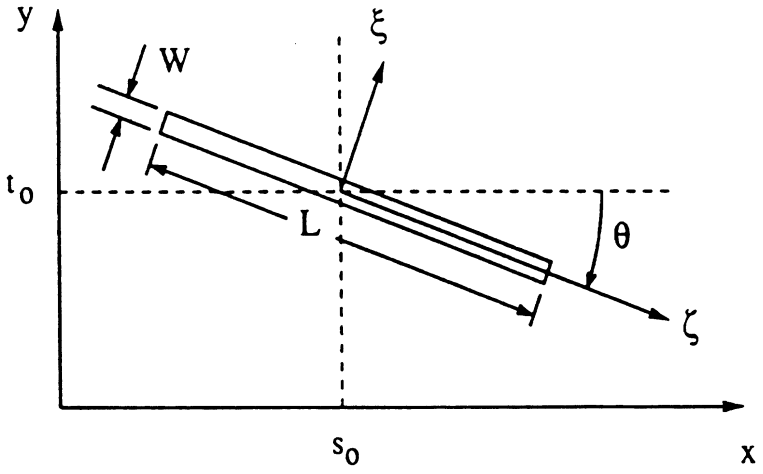

Figure 3.3: Slot-fixed Coordinate System (ζ, ξ).

$$\zeta = (x - s_o)\cos\theta + (y - t_o)\sin\theta \tag{3.9}$$

$$\xi = -(x - s_o)\sin\theta + (y - t_o)\cos\theta \tag{3.10}$$

The slot currents are now written as

$$\overline{K}_L = K_{L\zeta}\hat{\zeta} + K_{L\xi}\hat{\xi} \tag{3.11}$$

$$\overline{K}_U = K_{U\zeta}\hat{\zeta} + K_{U\xi}\hat{\xi} \tag{3.12}$$

where the 'L' subscript represents the slot opening to the cavity and the 'U' subscript represents the slot interfacing with the dielectric cover. Assuming similar expansions for these currents,

$$K_{L\zeta} = \Psi(\xi)\sum_j \Phi(\zeta_j)V_{L\zeta j} \tag{3.13}$$

$$K_{U\zeta} = \Psi(\xi)\sum_j \Phi(\zeta_j)V_{U\zeta j} \tag{3.14}$$

$$K_{L\xi} = \Phi(\xi)\sum_j V_{L\xi} \tag{3.15}$$

$$K_{U\xi} = \Phi(\xi)\sum_j V_{U\xi} \tag{3.16}$$

Equations (1.54–1.56) can be written in matrix form

$$\begin{bmatrix} \mathbf{Z}_{11} & \mathbf{Z}_{12} & \mathbf{Y}_{13} & \mathbf{Y}_{14} & \mathbf{0} & \mathbf{0} \\ \mathbf{Z}_{21} & \mathbf{Z}_{22} & \mathbf{Y}_{23} & \mathbf{Y}_{24} & \mathbf{0} & \mathbf{0} \\ \mathbf{Z}_{31} & \mathbf{Z}_{32} & \mathbf{Y}_{33} & \mathbf{Y}_{34} & \mathbf{Y}_{35} & \mathbf{Y}_{36} \\ \mathbf{Z}_{41} & \mathbf{Z}_{42} & \mathbf{Y}_{43} & \mathbf{Y}_{44} & \mathbf{Y}_{45} & \mathbf{Y}_{46} \\ \mathbf{0} & \mathbf{0} & \mathbf{Y}_{53} & \mathbf{Y}_{54} & \mathbf{Y}_{55} & \mathbf{Y}_{56} \\ \mathbf{0} & \mathbf{0} & \mathbf{Y}_{63} & \mathbf{Y}_{64} & \mathbf{Y}_{65} & \mathbf{Y}_{66} \end{bmatrix} \begin{bmatrix} \mathbf{I}_{vj} \\ \mathbf{I}_{\nu j} \\ \mathbf{V}_{L\zeta j} \\ \mathbf{V}_{L\xi j} \\ \mathbf{V}_{U\zeta j} \\ \mathbf{V}_{U\xi j} \end{bmatrix} = \begin{bmatrix} \mathcal{E} \\ \mathcal{E} \\ \mathcal{H} \\ \mathcal{H} \\ \mathcal{H} \\ \mathcal{H} \end{bmatrix} \tag{3.17}$$

where each term in bold face is a submatrix described by integrals such as

$$Z_{11}^j = \iint_{S_j} G_{vv}^{(11)}(x,y,x',y')\Psi(\nu)\Phi(v_j)dS_j$$

$$Z_{12}^j = \iint_{S_j} G_{v\nu}^{(12)}(x,y,x',y')\Psi(v_j)\Phi(\nu)dS_j$$

$$Y_{13}^j = \iint_{S_j} G_{v\zeta}^{(13)}(x,y,x',y')\Psi(\xi)\Phi(\zeta_j)dS_j$$

$$Y_{14}^j = \iint_{S_j} G_{v\xi}^{(14)}(x,y,x',y')\Psi(\zeta_j)\Phi(\xi)dS_j$$

•

•

•

or in a more compact form as

$$\iint_{S_j} \begin{bmatrix} G_{\upsilon\upsilon}^{(11)} & G_{\upsilon\nu}^{(12)} & G_{\upsilon\zeta}^{(13)} & G_{\upsilon\xi}^{(14)} & 0 & 0 \\ G_{\nu\upsilon}^{(21)} & G_{\nu\nu}^{(22)} & G_{\nu\zeta}^{(23)} & G_{\nu\xi}^{(24)} & 0 & 0 \\ G_{\zeta\upsilon}^{(31)} & G_{\zeta\nu}^{(32)} & G_{\zeta\zeta}^{(33)} & G_{\zeta\xi}^{(34)} & G_{\zeta\zeta}^{(35)} & G_{\zeta\xi}^{(36)} \\ G_{\xi\upsilon}^{(41)} & G_{\xi\nu}^{(42)} & G_{\xi\zeta}^{(43)} & G_{\xi\xi}^{(44)} & G_{\xi\zeta}^{(45)} & G_{\xi\xi}^{(46)} \\ 0 & 0 & G_{\zeta\zeta}^{(53)} & G_{\zeta\xi}^{(54)} & G_{\zeta\zeta}^{(55)} & G_{\zeta\xi}^{(56)} \\ 0 & 0 & G_{\xi\zeta}^{(63)} & G_{\xi\xi}^{(64)} & G_{\xi\zeta}^{(65)} & G_{\xi\xi}^{(66)} \end{bmatrix} \begin{bmatrix} \Psi(\nu)\Phi(\upsilon_j)I_{\upsilon j} \\ \Psi(\upsilon_j)\Phi(\nu)I_{\nu j} \\ \Psi(\xi)\Phi(\zeta_j)V_{L\zeta j} \\ \Psi(\zeta_j)\Phi(\xi)V_{L\xi j} \\ \Psi(\xi)\Phi(\zeta_j)V_{U\zeta j} \\ \Psi(\zeta_j)\Phi(\xi)V_{U\xi j} \end{bmatrix} \begin{matrix} dx'_j \\ dy'_j \end{matrix} = \begin{bmatrix} \mathcal{E} \\ \mathcal{E} \\ \mathcal{H} \\ \mathcal{H} \\ \mathcal{H} \\ \mathcal{H} \end{bmatrix} \tag{3.18}$$

The functions on the right hand sides of Equation (3.17) and (3.18) are discussed in Chapter I and are further defined in section 3.2.

Note that S_j is the $j^{\underline{th}}$ 'source' segment of the corresponding strip or slot. We also have a triply mixed coordinate system which must be accommodated using the transformations given by Equations (3.7–3.10). For example, computation of $G_{\upsilon\zeta}^{(13)}$ involves both $G_{\zeta\zeta}^{(13)}$ and $G_{\xi\zeta}^{(13)}$. In addition, the derived Green's functions are in the cavity-fixed coordinate system. Consequently, all terms must be transformed to a common coordinate system before the integrations can be performed. Treatment of these integrations and manipulation of the various G terms will be discussed in a later section.

The evaluation of the elements of the matrix at the positions where the boundary conditions are being imposed has not yet been discussed. Following the conventional method of moments formulation, we introduce a weighting function and impose an inner product to be evaluated at each subsection on the strips or slots. The inner product is defined as

$$\langle \bar{a}, \bar{b} \rangle = \iint \bar{a} \cdot \bar{b} \; dS \tag{3.19}$$

where $\bar{a} = \bar{w}$, the weighting function, and $\bar{b}$ will be the vectors represented by Equations (1.54–1.56). Note that the elements of Equation (1.54) are to be evaluated on the strip as indicated by (1.57) and (1.58). Similarly, Equation (1.55) is evaluated on the lower

slot as indicated by Equations (1.59–1.61) and Equation (1.56) on the upper slot as implied by (1.62) and (1.63).

Following Galerkin's method we can choose $\bar{w}$ to have the same form as the basis functions used in the expansions of the currents. Thus, for Equation (1.54)

$$\bar{w} = \Psi(\nu)\Phi(\upsilon)\hat{\upsilon} + \Psi(\upsilon)\Phi(\nu)\hat{\nu} \tag{3.20}$$

Similarly, for Equations (1.55) and (1.56)

$$\bar{w}_s = \Psi(\xi)\Phi(\zeta)\hat{\zeta} + \Psi(\zeta)\Phi(\xi)\hat{\xi} \tag{3.21}$$

The elements of the matrix in Equation (3.17) are then changed to

$$Z_{11}^{ij} = \iint_{S_i} \Psi(\nu)\Phi(\upsilon)Z_{11}^{j}dS_i$$
$$Z_{12}^{ij} = \iint_{S_i} \Psi(\upsilon)\Phi(\nu)Z_{12}^{j}dS_i$$
$$Y_{13}^{ij} = \iint_{S_i} \Psi(\xi)\Phi(\zeta)Y_{13}^{j}dS_i$$
$$\bullet$$
$$\bullet$$
$$\bullet$$

where the i index represents the 'field' point integration locations.

For certain cases we will use point matching on the slots driven by considerations in the evaluation of the Sommerfeld integrals of the half-space Green's function. In this case the weight function for the transverse dependence of the longitudinal component of magnetic current on the slot becomes a delta function resulting in the evaluation of the field at a point at the center of the slot.

3.2 Excitation Models

The final element to be discussed is the excitation vector represented by the right hand side of Equation (3.17). As mentioned previously (Section 1.3), the $\vec{\mathcal{E}}$ terms represent

non-zero values in the excitation vector corresponding to gap generator locations on the strips. Likewise, the $\bar{\mathcal{H}}$ terms will be non-zero for the incident $\overline{\mathrm{H}}$ field excitation used with the Reaction Method. In this case, the incident field must be weighted the same way as the left hand side so that the right hand side terms become

$$\mathcal{H}_i = \iint_{S_i} \bar{w} \cdot \overline{\mathrm{H}}^{inc} \, dS_i \tag{3.22}$$

For the gap generators, the corresponding field for the gap subsection can be designated $\overline{\mathrm{E}}_g$. Application of Galerkin's method then, results in the integral

$$\mathcal{E}_i = \iint_{S_g} \bar{w} \cdot \overline{\mathrm{E}}_g \, dS_g \tag{3.23}$$

on the right hand side of Equation (3.17). $\overline{\mathrm{E}}_g$ is an unknown caused by a source at that location on the microstrip. If we assume $\overline{\mathrm{E}}_g = E_{gv}\hat{v}$, then we can set $\bar{\mathcal{E}} \equiv 0$ in the second row of Equation (1.54).

In most cases, we can arbitrarily set the integral of (3.23) so that $\mathcal{E}$ of the first row of (3.17) becomes a zero column vector except for one element corresponding to the position of the gap generator of the form

$$\mathcal{E} = [\,0 \;\cdots\; 0 \;\; 1 \;\; 0 \;\cdots\; 0 \;\; 0\,]^T \tag{3.24}$$

where T denotes the transposition operator. Setting the magnitude of $\overline{\mathrm{E}}_g$ is arbitrary because the Standing Wave Method used with the gap generators uses relative interpretations of the resulting current, not absolute quantities.

For certain problems, however, we need the use of the gap generator model to determine absolute values of current on the lines. If we set the field in the gap such that the voltage over the gap given by

$$V_o = -\int_{gap} \overline{\mathrm{E}}_g \, dl \tag{3.25}$$

is equal to 1 Volt, the input impedance at the feed point is given by $Z_{in} = 1/I_g$ to first order. A similar model can be used for slots with a coaxial feed, as in [21, p.360] for example, by replacing the coaxial feed with a current source on the slot.

Before moving on, it is worthwhile to examine this process a little more closely in the context of some of the terminology and physical interpretations of gap generator models found in the literature. Restricting this discussion to one dimension, at the source our system of equations represents the enforcement of the boundary condition

$$\int_{source} w f(x)\ dx = K \tag{3.26}$$

where w is the weight function, $f(x)$ is the field quantity and K is the constant specified on the right hand side of the matrix equation row corresponding to the location of the source. It is clear that the only non-zero contribution to the integral can occur on the domain of w for which w is non-zero so that any physical interpretation is confined to that region. It should also be noted that there may be an infinite number of solutions $f(x)$ satisfying this equation and that this equation does not force further constraints on what $f(x)$ might be, i.e., the right hand side does not specify how $f(x)$ behaves on a scale smaller than the domain over which w is non-zero. We then also have no basis for a physical interpretation which imagines the terminals of the source within this domain, but rather we should interpret the terminals to be at the domain's endpoints. Obviously, K will depend on the nature of w. The physical interpretation of the nature of the source then also depends on w. For simple cases such as a pulse weight function, the delta-gap physical interpretation is appropriate since Equation (3.26) reduces to a form similar to Equation (3.25). The point match case, or delta-function source can be interpreted in the same manner by taking the limiting case of the pulse weight function, shrinking its width to an infinitesimal gap while keeping the area constant. For more complex weight functions, the physical interpretation is unclear except that we can consider the source to

be 'distributed' over the domain of the weight function.

The system of equations represented by Equation (3.17) is now fully specified. The unknown currents $\bar{J}_s$, $\overline{K}_L$ and $\overline{K}_U$ can now be found by solving for the matrix elements and inverting the matrix.

3.3 Expansion of the Dyadic Green's Functions for the Cavity

To evaluate the elements of the matrix, we need to expand the dyadic Green's functions into the components corresponding to the electric and magnetic currents which are in x-y planes. All of the required terms can be separated into trigonometric functions of x,x',y and y' multiplied by a complex coefficient which contains the z and z' dependence. The Green's functions can then be written in a condensed form as follows. Also, a constant complex coefficient C_{mn} can be factored out which appears in all Green's functions for the cavity and is defined by

$$C_{mn} = \frac{2j(2-\delta_o)}{abk_z(k_m^2+k_n^2)} \tag{3.27}$$

Cavity EFIE – Electric Currents $\bar{J}$

The electric field integral equation contribution of the electric currents involves the x-y components of $\bar{\bar{G}}_{eJ}$ which can be written in the form

$$\begin{aligned}
G_{eJxx} &= \sum_{m=0}^{\infty}\sum_{n=0}^{\infty} C_{mn}\mathcal{G}_{eJxx}\cos k_m x \sin k_n y \cos k_m x' \sin k_n y' \\
G_{eJyx} &= \sum_{m=0}^{\infty}\sum_{n=0}^{\infty} C_{mn}\mathcal{G}_{eJyx}\sin k_m x \cos k_n y \cos k_m x' \sin k_n y' \\
G_{eJxy} &= \sum_{m=0}^{\infty}\sum_{n=0}^{\infty} C_{mn}\mathcal{G}_{eJxy}\cos k_m x \sin k_n y \sin k_m x' \cos k_n y' \\
G_{eJyy} &= \sum_{m=0}^{\infty}\sum_{n=0}^{\infty} C_{mn}\mathcal{G}_{eJyy}\sin k_m x \cos k_n y \sin k_m x' \cos k_n y'
\end{aligned} \tag{3.28}$$

where $k_x = k_m = m\pi/a$, $k_y = k_n = n\pi/b$, and

$$\mathcal{G}_{eJxx} = \left[k_n^2 \mathcal{Z}_{ee}(\tilde{\eta}_e) + \left(\frac{k_m k_z}{k_i}\right)^2 \mathcal{Z}_{ee}(\tilde{\eta}_m)\right] \tag{3.29}$$

$$\mathcal{G}_{eJyy} = \left[k_m^2 \mathcal{Z}_{ee}(\tilde{\eta}_e) + \left(\frac{k_n k_z}{k_i}\right)^2 \mathcal{Z}_{ee}(\tilde{\eta}_m)\right] \tag{3.30}$$

$$\mathcal{G}_{eJyx} = \mathcal{G}_{eJxy} = -k_m k_n \left[\mathcal{Z}_{ee}(\tilde{\eta}_e) - \left(\frac{k_z}{k_i}\right)^2 \mathcal{Z}_{ee}(\tilde{\eta}_m)\right] \tag{3.31}$$

The z dependence of the Green's function is contained in the $\mathcal{Z}_{ee}$ function defined as

$$\mathcal{Z}_{ee}(\tilde{\eta}) = \left\{ \frac{\begin{array}{l}[\tilde{\eta}_U \cos k_z(z-c) - j \sin k_z(z-c)]\,[\tilde{\eta}_L \cos k_z(z'-d) - j \sin k_z(z'-d)] \\ [\tilde{\eta}_L \cos k_z(z-d) - j \sin k_z(z-d)]\,[\tilde{\eta}_U \cos k_z(z'-c) - j \sin k_z(z'-c)]\end{array}}{(\tilde{\eta}_U - \tilde{\eta}_L)\cos k_z(c-d) - j(\tilde{\eta}_U \tilde{\eta}_L - 1)\sin k_z(c-d)} \right\}$$

$$\text{for } z \gtrless z' \tag{3.32}$$

Here again we use the '*ee*' subscript notation to imply the trigonometric dependence of the function.

Cavity EFIE – Magnetic Currents $\overline{K}$

The contribution of the magnetic currents involves the components of $\bar{\bar{G}}_{eK}$ which can be written as

$$\begin{aligned}
G_{eKxx} &= \sum_{m=0}^{\infty}\sum_{n=0}^{\infty} C_{mn}\, \mathcal{G}_{eKxx} \cos k_m x \sin k_n y \sin k_m x' \cos k_n y' \\
G_{eKyx} &= \sum_{m=0}^{\infty}\sum_{n=0}^{\infty} C_{mn}\, \mathcal{G}_{eKyx} \sin k_m x \cos k_n y \sin k_m x' \cos k_n y' \\
G_{eKxy} &= \sum_{m=0}^{\infty}\sum_{n=0}^{\infty} C_{mn}\, \mathcal{G}_{eKxy} \cos k_m x \sin k_n y \cos k_m x' \sin k_n y' \\
G_{eKyy} &= \sum_{m=0}^{\infty}\sum_{n=0}^{\infty} C_{mn}\, \mathcal{G}_{eKyy} \sin k_m x \cos k_n y \cos k_m x' \sin k_n y'
\end{aligned} \tag{3.33}$$

with

$$\mathcal{G}_{eKyx} = -k_z \left[k_m^2 \mathcal{Z}_{eo}(\tilde{\eta}_e) + k_n^2 \mathcal{Z}_{eo}(\tilde{\eta}_m)\right] \tag{3.34}$$

$$\mathcal{G}_{eKxy} = k_z \left[k_n^2 \mathcal{Z}_{eo}(\tilde{\eta}_e) + k_m^2 \mathcal{Z}_{eo}(\tilde{\eta}_m)\right] \tag{3.35}$$

$$\mathcal{G}_{eKxx} = -\mathcal{G}_{eKyy} = k_m k_n k_z \left[\mathcal{Z}_{eo}(\tilde{\eta}_e) + \mathcal{Z}_{eo}(\tilde{\eta}_m)\right] \tag{3.36}$$

The $\mathcal{Z}_{eo}$ function is defined as

$$\mathcal{Z}_{eo} = \left\{ \frac{\begin{array}{l}[\tilde{\eta}_U \cos k_z(z-c) - j \sin k_z(z-c)]\,[\tilde{\eta}_L \sin k_z(z'-d) + j \cos k_z(z'-d)] \\ [\tilde{\eta}_L \cos k_z(z-d) - j \sin k_z(z-d)]\,[\tilde{\eta}_U \sin k_z(z'-c) + j \cos k_z(z'-c)]\end{array}}{(\tilde{\eta}_U - \tilde{\eta}_L)\cos k_z(c-d) - j(\tilde{\eta}_U\tilde{\eta}_L - 1)\sin k_z(c-d)} \right\} \quad \text{for } z \gtrless z' \qquad (3.37)$$

Cavity MFIE – Electric Currents $\bar{J}$

The magnetic field integral equation contribution of the electric currents involves the components of $\bar{\bar{G}}_{mJ}$ which can be written in the form

$$\begin{aligned} G_{mJxx} &= \sum_{m=0}^{\infty}\sum_{n=0}^{\infty} C_{mn}\, \mathcal{G}_{eKxx} \sin k_m x \cos k_n y \cos k_m x' \sin k_n y' \\ G_{mJyx} &= \sum_{m=0}^{\infty}\sum_{n=0}^{\infty} C_{mn}\, \mathcal{G}_{eKyx} \cos k_m x \sin k_n y \cos k_m x' \sin k_n y' \\ G_{mJxy} &= \sum_{m=0}^{\infty}\sum_{n=0}^{\infty} C_{mn}\, \mathcal{G}_{eKxy} \sin k_m x \cos k_n y \sin k_m x' \cos k_n y' \\ G_{mJyy} &= \sum_{m=0}^{\infty}\sum_{n=0}^{\infty} C_{mn}\, \mathcal{G}_{eKyy} \cos k_m x \sin k_n y \sin k_m x' \cos k_n y' \end{aligned} \qquad (3.38)$$

Notice that the coefficients are the same as for the $\bar{\bar{G}}_{eK}$ case. It is not difficult to show that upon application of Galerkin's method,

$$\left\langle \bar{K}, \bar{\bar{G}}_{mJ}, \bar{J} \right\rangle = \left\langle \bar{J}, \bar{\bar{G}}_{eK}, \bar{K} \right\rangle \qquad (3.39)$$

where the double inner product notation is defined by

$$\langle \bar{a}, \bar{\bar{c}}, \bar{b} \rangle = \iint \bar{a} \cdot \iint \bar{\bar{c}} \cdot \bar{b}\; dS'\, dS \qquad (3.40)$$

This implies, because of the signs of Equations (1.58–1.59), that the submatrix associated with the electric current contribution to the MFIE is the negative of the submatrix for the magnetic current contribution to the EFIE (diagonally opposite for the order given). This observation reduces the computational effort required since only one of these submatrices

needs to be calculated to fill their respective positions in the matrix. However, for the radiating slot problem when we use the Maxwellian transverse distribution, evaluation of the Sommerfeld integral has been accomplished through point matching which does not produce this symmetry. Hence, in that particular case, we cannot take advantage of this property.

It can also be shown that the electric current EFIE terms form a submatrix which is diagonally symmetric as are the terms in the diagonal submatrix representing the MFIE contribution of the magnetic currents. Therefore, these also can be formed by calculating only about half of the terms, however, as will be seen later, taking advantage of other mathematical relations for these terms produces far more significant improvements in the fill time for these submatrices.

Cavity MFIE - Magnetic Currents $\overline{K}$

The cavity magnetic current MFIE terms are associated with a Green's function which can be expressed as

$$\begin{aligned}
G_{\text{mKxx}} &= \sum_{m=0}^{\infty}\sum_{n=0}^{\infty} C_{mn}\, \mathcal{G}_{\text{mKxx}} \sin k_m x \cos k_n y \sin k_m x' \cos k_n y' \\
G_{\text{mKyx}} &= \sum_{m=0}^{\infty}\sum_{n=0}^{\infty} C_{mn}\, \mathcal{G}_{\text{mKyx}} \cos k_m x \sin k_n y \sin k_m x' \cos k_n y' \\
G_{\text{mKxy}} &= \sum_{m=0}^{\infty}\sum_{n=0}^{\infty} C_{mn}\, \mathcal{G}_{\text{mKxy}} \sin k_m x \cos k_n y \cos k_m x' \sin k_n y' \\
G_{\text{mKyy}} &= \sum_{m=0}^{\infty}\sum_{n=0}^{\infty} C_{mn}\, \mathcal{G}_{\text{mKyy}} \cos k_m x \sin k_n y \cos k_m x' \sin k_n y' \qquad (3.41)
\end{aligned}$$

where

$$\mathcal{G}_{\text{mKxx}} = \left[k_n^2 \mathcal{Z}_{oo}(\tilde{\eta}_e) + \left(\frac{k_m k_z}{k_i}\right)^2 \mathcal{Z}_{oo}(\tilde{\eta}_m)\right] \qquad (3.42)$$

$$\mathcal{G}_{\text{mKyy}} = \left[k_m^2 \mathcal{Z}_{oo}(\tilde{\eta}_e) + \left(\frac{k_n k_z}{k_i}\right)^2 \mathcal{Z}_{oo}(\tilde{\eta}_m)\right] \qquad (3.43)$$

$$\mathcal{G}_{\text{mKyx}} = \mathcal{G}_{\text{mKxy}} = -k_m k_n \left[\mathcal{Z}_{oo}(\tilde{\eta}_e) - \left(\frac{k_z}{k_i}\right)^2 \mathcal{Z}_{oo}(\tilde{\eta}_m)\right] \qquad (3.44)$$

The $\mathcal{Z}_{oo}$ function is defined as

$$\mathcal{Z}_{oo} = \left\{ \frac{\begin{array}{l}[\tilde{\eta}_U \sin k_z(z-c) + j\cos k_z(z-c)]\,[\tilde{\eta}_L \sin k_z(z'-d) + j\cos k_z(z'-d)] \\ [\tilde{\eta}_L \sin k_z(z-d) + j\cos k_z(z-d)]\,[\tilde{\eta}_U \sin k_z(z'-c) + j\cos k_z(z'-c)]\end{array}}{(\tilde{\eta}_U - \tilde{\eta}_L)\cos k_z(c-d) - j(\tilde{\eta}_U\tilde{\eta}_L - 1)\sin k_z(c-d)} \right\} \quad \text{for } z \gtrless z' \qquad (3.45)$$

Slot MFIE – Magnetic Currents $\overline{K}$

For the slot, the transverse components of $\bar{\bar{G}}_{mK}$ for a homogeneously filled cavity are needed which can be written in the forms:

$$\begin{aligned}
G_{mKxx} &= \sum_{m=0}^{\infty}\sum_{n=0}^{\infty} C_{mn}\,\mathcal{G}_{mKxx} \sin k_m x \cos k_n y \sin k_m x' \cos k_n y' \\
G_{mKyx} &= \sum_{m=0}^{\infty}\sum_{n=0}^{\infty} C_{mn}\,\mathcal{G}_{mKyx} \cos k_m x \sin k_n y \sin k_m x' \cos k_n y' \\
G_{mKxy} &= \sum_{m=0}^{\infty}\sum_{n=0}^{\infty} C_{mn}\,\mathcal{G}_{mKxy} \sin k_m x \cos k_n y \cos k_m x' \sin k_n y' \\
G_{mKyy} &= \sum_{m=0}^{\infty}\sum_{n=0}^{\infty} C_{mn}\,\mathcal{G}_{mKyy} \cos k_m x \sin k_n y \cos k_m x' \sin k_n y' \qquad (3.46)
\end{aligned}$$

where

$$\begin{aligned}
\mathcal{G}_{mKxx} &= \frac{\cos k_z(z'-d)}{\sin k_z(c-d)}\left[k_n^2 + \frac{k_m^2 k_z^2}{k_s^2}\right] \\
\mathcal{G}_{mKyy} &= \frac{\cos k_z(z'-d)}{\sin k_z(c-d)}\left[k_m^2 + \frac{k_n^2 k_z^2}{k_s^2}\right] \\
\mathcal{G}_{mKyx} &= = \mathcal{G}_{mKxy} = -k_m k_n \frac{\cos k_z(z'-d)}{\sin k_z(c-d)}\left[1 - \frac{k_z^2}{k_s^2}\right] \qquad (3.47)
\end{aligned}$$

These expression are valid for currents on one end of the slot coupling to field points on the opposite end when $z' = c$. For currents coupling to the same end, z' is set equal to d.

Half-Space MFIE – Magnetic Currents $\overline{K}$

Although the Green's function for the half-space was derived in Chapter II, the numerical treatment is quite involved and will not be detailed here. It consist of a real axis

Gaussian Quadrature scheme with singularity extraction of the branch point and surface wave poles and asymptotic evaluation of large arguments. The methodology has been outlined by Katehi and Alexopoulos in [36]. The numerical implementations used to evaluate the half-space admittance elements of the matrix were provided by Katehi for the Maxwellian transverse distributions and by Harokopus [31] for the rooftop functions.

3.4 Identification and Reduction of the Integrands

The elements of each of the submatrices of Equation (3.17) involve double surface integrals as shown earlier. The inner surface integrations are over 'source' regions defined by the current expansion basis functions. The outer surface integrals result from the application of the weighting functions and cover the 'observation' or 'field' regions of the problem where the boundary conditions represented by the integral equations (section 1.4) are being enforced.

Using the condensed notation we can now write expressions for the impedance elements in a general form which will identify the integrations to be performed for each term. To illustrate, only the EFIE expansions for the current on the strip will be presented. The MFIE for the strip and slot currents are handled in an exactly the same manner.

The EFIE:electric current terms can be written as follows:

$$
\begin{aligned}
Z_{11}^{ij} &= \sum_{m=0}^{\infty}\sum_{n=0}^{\infty} \iint_{S_i} \Psi(\nu)\Phi(v_i) \iint_{S_j} G_{vv}^{(11)} \Psi(\nu)\Phi(v_j)\, dS_j\, dS_i \\
Z_{21}^{ij} &= \sum_{m=0}^{\infty}\sum_{n=0}^{\infty} \iint_{S_i} \Psi(v_i)\Phi(\nu) \iint_{S_j} G_{\nu v}^{(21)} \Psi(\nu)\Phi(v_j)\, dS_j\, dS_i \\
Z_{12}^{ij} &= \sum_{m=0}^{\infty}\sum_{n=0}^{\infty} \iint_{S_i} \Psi(\nu)\Phi(v_i) \iint_{S_j} G_{v\nu}^{(12)} \Psi(v_j)\Phi(\nu)\, dS_j\, dS_i \\
Z_{22}^{ij} &= \sum_{m=0}^{\infty}\sum_{n=0}^{\infty} \iint_{S_i} \Psi(v_i)\Phi(\nu) \iint_{S_j} G_{\nu\nu}^{(22)} \Psi(v_j)\Phi(\nu)\, dS_j\, dS_i
\end{aligned}
\tag{3.48}
$$

As before, the superscripts i and j represent the $i^{\underline{th}}$ "field" subsection and the $j^{\underline{th}}$ 'source'

subsection. The Green's function terms can be transformed using the relations

$$\hat{x} = \hat{v}\cos\phi - \hat{\nu}\sin\phi \tag{3.49}$$

$$\hat{y} = \hat{v}\sin\phi + \hat{\nu}\cos\phi \tag{3.50}$$

The transverse Green's function,

$$\bar{\bar{G}}_{eJ} = G_{eJxx}\hat{x}\hat{x} + G_{eJyx}\hat{y}\hat{x} + G_{eJxy}\hat{x}\hat{y} + G_{eJyy}\hat{y}\hat{y} \tag{3.51}$$

can then be written for the strip-fixed coordinate system as

$$\bar{\bar{G}}_{eJ} = G_{eJvv}\hat{v}\hat{v} + G_{eJ\nu v}\hat{\nu}\hat{v} + G_{eJv\nu}\hat{v}\hat{\nu} + G_{eJ\nu\nu}\hat{\nu}\hat{\nu} \tag{3.52}$$

where

$$\begin{aligned}
G_{eJvv} &= G_{eJxx}\cos^2\phi + (G_{eJyx} + G_{eJxy})\sin\phi\cos\phi + G_{eJyy}\sin^2\phi \\
G_{eJ\nu v} &= -(G_{eJxx} - G_{eJyy})\sin\phi\cos\phi + G_{eJyx}\cos^2\phi - G_{eJxy}\sin^2\phi \\
G_{eJv\nu} &= -(G_{eJxx} - G_{eJyy})\sin\phi\cos\phi - G_{eJyx}\sin^2\phi + G_{eJxy}\cos^2\phi \\
G_{eJ\nu\nu} &= G_{eJxx}\sin^2\phi - (G_{eJyx} + G_{eJxy})\sin\phi\cos\phi + G_{eJyy}\cos^2\phi
\end{aligned} \tag{3.53}$$

When the coordinate systems are mixed, such as the case of the magnetic slot current contribution to the EFIE, the Green's function terms are also mixed. The relations for the slot-fixed coordinate system unit vectors are

$$\hat{x} = \hat{\zeta}\cos\theta - \hat{\xi}\sin\theta \tag{3.54}$$

$$\hat{y} = \hat{\zeta}\sin\theta + \hat{\xi}\cos\theta \tag{3.55}$$

Substituting these into the posterior positions of Equation (3.51) and (3.49,3.50) into the anterior positions, the Green's function terms for this case become

$$G_{eK\nu\zeta} = G_{eJxx}\cos\phi\cos\theta + G_{eJyx}\sin\phi\cos\theta + G_{eJxy}\cos\phi\sin\theta + G_{eJyy}\sin\phi\sin\theta$$

$$G_{eK\upsilon\xi} = -G_{eJxx}\cos\phi\sin\theta - G_{eJyx}\sin\phi\sin\theta + G_{eJxy}\cos\phi\cos\theta + G_{eJyy}\sin\phi\cos\theta$$

$$G_{eK\nu\zeta} = -G_{eJxx}\sin\phi\cos\theta + G_{eJyx}\cos\phi\cos\theta - G_{eJxy}\sin\phi\sin\theta + G_{eJyy}\cos\phi\sin\theta$$

$$G_{eK\nu\xi} = G_{eJxx}\sin\phi\sin\theta - G_{eJyx}\cos\phi\sin\theta - G_{eJxy}\sin\phi\cos\theta + G_{eJyy}\cos\phi\cos\theta \tag{3.56}$$

Returning to the EFIE:electric current case, we can now write the terms of the associated submatrix terms as (omitting the C_{mn} constant)

$$Z_{11}^{ij} = \sum_{m=0}^{\infty}\sum_{n=0}^{\infty} \mathcal{G}_{eJxx}\cos^2\phi I_{eo}(\upsilon_i,\nu_i)I_{eo}(\upsilon_j,\nu_j) + \mathcal{G}_{eJyx}\sin\phi\cos\phi I_{oe}(\upsilon_i,\nu_i)I_{eo}(\upsilon_j,\nu_j)$$
$$+ \mathcal{G}_{eJxy}\sin\phi\cos\phi I_{eo}(\upsilon_i,\nu_i)I_{oe}(\upsilon_j,\nu_j) + \mathcal{G}_{eJyy}\sin^2\phi I_{oe}(\upsilon_i,\nu_i)I_{oe}(\upsilon_j,\nu_j)$$

$$Z_{21}^{ij} = \sum_{m=0}^{\infty}\sum_{n=0}^{\infty} -\mathcal{G}_{eJxx}\sin\phi\cos\phi I_{eo}(\nu_i,\upsilon_i)I_{eo}(\upsilon_j,\nu_j) + \mathcal{G}_{eJyx}\cos^2\phi I_{oe}(\nu_i,\upsilon_i)I_{eo}(\upsilon_j,\nu_j)$$
$$- \mathcal{G}_{eJxy}\sin^2\phi I_{eo}(\nu_i,\upsilon_i)I_{oe}(\upsilon_j,\nu_j) + \mathcal{G}_{eJyy}\sin\phi\cos\phi I_{oe}(\nu_i,\upsilon_i)I_{oe}(\upsilon_j,\nu_j)$$

$$Z_{12}^{ij} = \sum_{m=0}^{\infty}\sum_{n=0}^{\infty} -\mathcal{G}_{eJxx}\sin\phi\cos\phi I_{eo}(\upsilon_i,\nu_i)I_{eo}(\nu_j,\upsilon_j) - \mathcal{G}_{eJyx}\sin^2\phi I_{oe}(\upsilon_i,\nu_i)I_{eo}(\nu_j,\upsilon_j)$$
$$+ \mathcal{G}_{eJxy}\cos^2\phi I_{eo}(\upsilon_i,\nu_i)I_{oe}(\nu_j,\upsilon_j) + \mathcal{G}_{eJyy}\sin\phi\cos\phi I_{oe}(\upsilon_i,\nu_i)I_{oe}(\nu_j,\upsilon_j)$$

$$Z_{22}^{ij} = \sum_{m=0}^{\infty}\sum_{n=0}^{\infty} \mathcal{G}_{eJxx}\sin^2\phi I_{eo}(\nu_i,\upsilon_i)I_{eo}(\nu_j,\upsilon_j) - \mathcal{G}_{eJyx}\sin\phi\cos\phi I_{oe}(\nu_i,\upsilon_i)I_{eo}(\nu_j,\upsilon_j)$$
$$- \mathcal{G}_{eJxy}\sin\phi\cos\phi I_{eo}(\nu_i,\upsilon_i)I_{oe}(\nu_j,\upsilon_j) + \mathcal{G}_{eJyy}\cos^2\phi I_{oe}(\nu_i,\upsilon_i)I_{oe}(\nu_j,\upsilon_j) \tag{3.57}$$

Now it can be seen that the only terms involved in the integration are of the form

$$I_{\substack{ee\\oe}}(\alpha_q,\beta_q) = \iint_{S_q}\begin{bmatrix}\cos k_m x\sin k_n y\\ \sin k_m x\cos k_n y\end{bmatrix}\Phi(\alpha_q)\Psi(\beta_q)\,dS_q \tag{3.58}$$

where (α_q,β_q) could be either (υ_q,ν_q) or (ν_q,υ_q) with $dS_q = d\upsilon d\nu$ for the strip or (α_q,β_q) would be replaced by (ζ_q,ξ_q) or (ξ_q,ζ_q) with $dS_q = d\zeta d\xi$ for the slots.

3.5 Integration

We will ultimately assume, as is commonly done, that the strip and slot are sufficiently narrow so that the longitudinal components of current are much greater in magnitude than the transverse components. The latter can then be neglected which, as will shortly become apparent, greatly simplifies the book-keeping required to keep track of various Green's function and current components, coordinate transformations, cross-coupled terms, etc. The assumption is further justified in that, at this point, there is no known advantage or requirement for the microstrip or slot structure to be more complex. For the moment, however, the complete expansion will be retained so that the numerical model can later be extended based on these expansions, by evaluating the additional terms of the matrix.

Now the $I_{\alpha\alpha}^{eo}(\alpha_q, \beta_q)$ function is still a mixed coordinate system function, therefore, to perform the integration the function must be transformed to a common system. The simplest approach is to transform the cavity-fixed coordinate system functions into the strip-fixed system by solving Equations (3.7–3.8) for x and y and substitute into Equation (3.58) giving

$$x = v\cos\phi - \nu\sin\phi + x_o \tag{3.59}$$

$$y = v\sin\phi + \nu\cos\phi + y_o \tag{3.60}$$

Equation (3.58) then becomes

$$I_{\alpha\alpha}^{eo}(\alpha_q, \beta_q) = \iint_{S_q} \left\{ \begin{matrix} \cos[k_m(v\cos\phi - \nu\sin\phi + x_o)]\sin[k_n(v\sin\phi + \nu\sin\phi + y_o)] \\ \sin[k_m(v\cos\phi - \nu\sin\phi + x_o)]\cos[k_n(v\sin\phi + \nu\sin\phi + y_o)] \end{matrix} \right\} \cdot\Phi(\alpha_q)\Psi_p(\beta_q)\, dv\, d\nu \tag{3.61}$$

By introducing the notation,

$$k_e^{\pm} = k_m\cos\phi \pm k_n\sin\phi \tag{3.62}$$

$$k_o^{\pm} = k_m\sin\phi \pm k_n\cos\phi \tag{3.63}$$

$$v_o = k_m x_o \tag{3.64}$$

$$\nu_o = k_n y_o \tag{3.65}$$

we can reduce these integrals to the form

$$\begin{aligned} I_{\substack{eo\\oe}}(\alpha_q, \beta_q) = \frac{1}{2}\iint_{S_q} &[\sin(k_e^+ v + v_o)\cos(k_o^- \nu - \nu_o) - \cos(k_e^+ v + v_o)\sin(k_o^- \nu - \nu_o) \\ &\mp \sin(k_e^- v + v_o)\cos(k_o^+ \nu + \nu_o) \pm \cos(k_e^- v + v_o)\sin(k_o^+ \nu + \nu_o)] \\ &\cdot \Phi(\alpha_q)\Psi(\beta_q)\, dv\, d\nu \end{aligned} \tag{3.66}$$

It is now clear that there are only two integral forms which must be evaluated:

$$\begin{aligned} &\iint \sin(k_\alpha \alpha + \alpha_o)\cos(k_\beta \beta + \beta_o)\Phi(\alpha)\Psi(\beta)\, d\alpha\, d\beta \\ &\iint \cos(k_\alpha \alpha + \alpha_o)\sin(k_\beta \beta + \beta_o)\Phi(\alpha)\Psi(\beta)\, d\alpha\, d\beta \end{aligned} \tag{3.67}$$

The integrals involving $\Phi(\alpha)$ are expanded and evaluated in straightforward fashion to give

$$\int \begin{bmatrix}\sin\\ \cos\end{bmatrix}(k\alpha \pm \alpha_o)\Phi(\alpha)\, d\alpha = \frac{k_b l_\alpha^2}{\sin k_b l_\alpha}\begin{bmatrix}\sin\\ \cos\end{bmatrix}(k\alpha_q \pm \alpha_o)\,\mathrm{sinc}\left[(k + k_b)\frac{l_\alpha}{2}\right]\mathrm{sinc}\left[(k - k_b)\frac{l_\alpha}{2}\right] \tag{3.68}$$

where $\mathrm{sinc}(x) = \sin(x)/x$.

For the case where $\Psi(\beta)$ is the Maxwellian distribution,

$$I_m^{\pm} = \int \begin{bmatrix}\sin\\ \cos\end{bmatrix}(k\beta \pm \beta_o)\Psi(\beta)d\beta = \frac{1}{\pi l_\beta}\int_{-l_\beta}^{l_\beta}\begin{bmatrix}\sin\\ \cos\end{bmatrix}(k\beta \pm \beta_o)\frac{d\beta}{\sqrt{1 - (\frac{\beta}{l_\beta})^2}} \tag{3.69}$$

Using the substitution $\frac{\beta}{l_\beta} = \sin\gamma$, we have

$$\begin{aligned} I_m^{\pm} &= \frac{1}{\pi}\int_{-\pi/2}^{\pi/2}\begin{bmatrix}\sin\\ \cos\end{bmatrix}(kl_\beta \sin\gamma \pm \beta_o)\, d\gamma \\ &= \frac{\cos(\beta_o)}{\pi}\int_{-\pi/2}^{\pi/2}\begin{bmatrix}\sin\\ \cos\end{bmatrix}(kl_\beta \sin\gamma)\, d\gamma \pm \frac{\sin(\pm\beta_o)}{\pi}\int_{-\pi/2}^{\pi/2}\begin{bmatrix}\cos\\ \sin\end{bmatrix}(kl_\beta \sin\gamma)\, d\gamma \end{aligned} \tag{3.70}$$

This form can be reduced to

$$I_m^{\pm} = \frac{2}{\pi}\begin{bmatrix}\sin\\ \cos\end{bmatrix}(\pm\beta_o)\int_0^{\pi/2}\cos(kl_\beta \sin\gamma)\, d\gamma = \begin{bmatrix}\sin\\ \cos\end{bmatrix}(\pm\beta_o)\, J_o(kl_\beta) \tag{3.71}$$

For the rooftop functions, the transverse weighting is $1/2l_\beta$ so that

$$\begin{aligned} I_r^{\pm} &= \int \begin{bmatrix} \sin \\ \cos \end{bmatrix} (k\beta \pm \beta_o) \Big] \Psi(\beta) d\beta = \frac{1}{2l_\beta} \int_{-l_\beta}^{l_\beta} \begin{bmatrix} \sin \\ \cos \end{bmatrix} (k\beta \pm \beta_o) \Big] d\beta \\ &= \begin{bmatrix} \sin \\ \cos \end{bmatrix} (\pm\beta_o) \Big] \operatorname{sinc}(k_b l_\beta) \end{aligned} \tag{3.72}$$

With these results, the integration of Equation (3.66) is fully specified and we can proceed to evaluate the terms of the matrix.

3.6 Numerical Evaluation Considerations

Before proceeding to the applications, some comments on the numerical implementation should be made. At this point we are in a position to go ahead and program the previous expressions to evaluate the matrix elements as they stand, however, just a brute force approach, without some consideration of the algorithms to be used, would undoubtedly result in a very inefficient program which takes much longer to run than need be. In this section, some 'common sense' features will be pointed out in addition to some mathematical identities which can be used to significantly improve the convergence rate of the summations involved.

3.6.1 Precomputation

By writing out the complete expression to be evaluated for the self-impedance on the strips, the main points can be illustrated which also apply to other elements of the matrix. Let us assume that the strip is oriented along the $\hat{x}$ axis in the cavity with a width of W and is centered at the point (x_o, y_o). A typical element of the $[\mathbf{Z}_{11}]$ can then be written as

$$\begin{aligned} Z_{ij}^{(11)} &= \sum_m \sum_n \iint_{S_i} \Phi(x)\Psi(y) \iint_{S_j} G_{xx}^{(11)} \Phi(x')\Psi(y') \; dx\, dy\, dx' dy' \\ &= \sum_m \sum_n C_{mn}\, \mathcal{G}_{\mathrm{eJxx}} I_{eo}(x_i, y_i) I_{eo}(x_j', y_j') \end{aligned} \tag{3.73}$$

Assuming the Maxwellian transverse dependence, the I_{eo} terms are evaluated as in the previous section and Z_{ij} becomes

$$Z_{ij}^{(11)} = -j\omega\mu \sum_m \sum_n \frac{C_{mn} k_b^2 l_x^4}{\sin^2 k_b l_x} \mathcal{G}_{eJxx} \cos[k_m(x_i + x_o)] \cos[k_m(x_j + x_o)] \sin^2 k_n y_o J_o^2(k_n l_y) \mathrm{sinc}^2[(k_m + k_b)l_x] \mathrm{sinc}^2[(k_m - k_b)l_x] \quad (3.74)$$

The most basic rule to optimize the speed of the computations is to perform any operation or function evaluation as few times as possible. Immediately we recognize then, that the constants should be factored out and the outer loop factors should be removed from the inner loop:

$$Z_{ij}^{(11)} = \frac{4f\mu k_b^2 l_x^4}{ab \sin^2 k_b l_x} \sum_m \frac{(2 - \delta_m)}{2} \cos[k_m(x_i + x_o)] \cos[k_m(x_j + x_o)] \mathrm{sinc}^2[(k_m + k_b)l_x] \mathrm{sinc}^2[(k_m - k_b)l_x] \cdot \left\{ \sum_n \mathcal{G}_{eJxx} \sin^2 k_n y_o J_o^2(k_n l_y) \right\} \quad (3.75)$$

Now in this expression, although evaluation of the sine and Bessel function J_o in each cycle of the loops is implied, in practice these are computed and multiplied external to both loops and stored as a vector dimensioned to include the maximum value of 'n' to be evaluated. Thus, these functions are evaluated only once per value of 'n'. Similarly, the $(2 - \delta_m)/2$ factor (= 1 for $m \neq 0$) appears only in the 'm' loop, since for $n = 0$ there is no contribution (note also that the conditional statement which tests for $m = 0$ can be eliminated by calculating the $m = 0$ terms separately).

3.6.2 Transformations

Finally it is noted that the 'm' loop implies $m \times N$ evaluations of the cosine terms and with the inner n loop implies $m \times n \times N^2$ products of these terms and the remaining terms where N is the number of basis functions on the line. This can be dramatically reduced

by making use of the relation

$$\cos A \cos B = \frac{1}{2}[\cos(A+B) + \cos(A-B)] \tag{3.76}$$

so that our expression becomes

$$Z_{ij}^{(11)} = \frac{2f\mu k_b^2 l_x^4}{ab \sin^2 k_b l_x} \sum_m \frac{(2-\delta_m)}{2} \langle \cos[k_m(x_i + x_j + 2x_o)] + \cos[k_m(x_i - x_j)] \rangle$$
$$\cdot \mathrm{sinc}^2[(k_m + k_b)l_x] \mathrm{sinc}^2[(k_m - k_b)l_x] \left\{ \sum_n \mathcal{G}_{\mathrm{eJxx}} \sin^2 k_n y_o J_o^2(k_n l_y) \right\} \tag{3.77}$$

We now need at most $m \times (3N-1)$ cosine evaluations, on the order of $m \times n \times N$ products and N^2 simple additions which greatly improves the computation time, especially as N increases. The sum resulting from the application of Equation (3.76) is performed *after* the m and n summations are complete. This is the key to the speedup since a factor of N is removed from the number of product evaluations. A factor of N^2 additions are added, however, this is inconsequential since the additions are simple (two complex numbers) whereas the previously required product evaluations also involve the calculation of other non-trivial coefficients. If the matrix elements are to be stored in data files, storage of the cosine sum and difference terms also greatly reduces the file size - now on the order of $(3N-1)$ rather than N^2.

This technique also applies to the slot self-impedance terms. For the coupling terms (slot-to-strip, etc.), the same principles are used except the sum and difference scheme no longer applies due to mixing of k_m and k_n wavenumbers. However, in these cases, due to the separation of the structures in the $\hat{z}$ direction, sine or cosine factors in the denominators become hyperbolic for large values of m and n and improve the convergence rate so that the upper limits of the summations can be reduced.

Other factors can be considered, however, the above points are thought to contribute the most significant improvements in program efficiency with minimal effort. Of course, there are other issues which have not been addressed since they often depend on the avail-

able facilities; memory limits for example. There are also schemes available to improve convergence through auxiliary series transformations, however, these are often only possible at the sacrifice of generality. For example, for uniformly filled cavities, e.g., stripline problems, techniques such as those found in [13, Appendix A.6] can be applied but then multi-layered cases would require separate treatment. Admittedly, the full extent of these possibilities have not been adequately explored and may offer further improvements in program efficiency. Rather, the emphasis has been focused on phenomenological exploration of the applications in the discussion to follow.

3.6.3 Convergence, Algorithms and Run-Time

As with other eigenfunction expansion methods, consideration of the convergence of the modal summations is an important process in establishing reliable results. For these types of solutions it would be desirable to analytically examine the expressions involved and derive formulas for acceptable upper limits of the summations. Ideally these formulas would be provided for each type of Green's function and would be functions of all the relevant geometric and electrical parameters and the desired accuracy. To develop such a system, however, is a major undertaking in itself and would really only be worthwhile after a more thorough investigation of possible series transformations alluded to above. In addition, convergence behavior generally varies depending on which output variable is sought, further complicating the situation.

Nevertheless, it was necessary to investigate some aspects of this question in order to produce reasonably efficient programs, the intention here then being to pass along some of the information gained to those who may extend the scope of this work. Also it should be recognized that although it has become common practice to discuss convergence by showing the behavior of particular parameters for the structure at hand as a function of the number

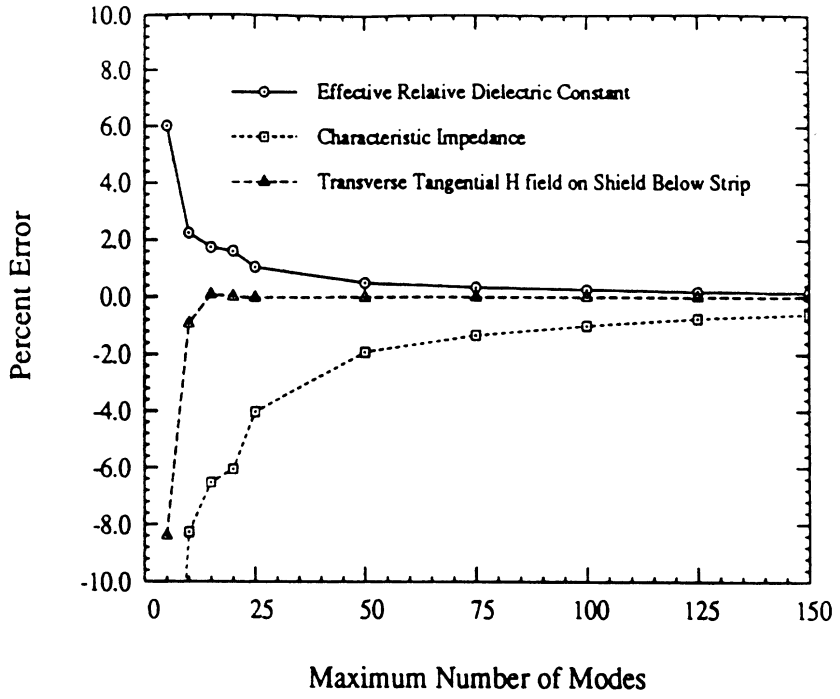

Figure 3.4: Convergence behavior for several parameters of a centered shielded microstrip transmission line. Dimensions a = b = .25, w = h = .025, ϵ_r = 9.7. Terminal values at 1000 modes were $Z_o = 49.63\Omega$, $\epsilon_{r,eff.} = 6.90$, $H_X = 12.45A/\lambda_o$.

of modes used in their calculation, this information is really of limited value since when the technique is applied to a different structure, there is usually no guarantee of similar results. The plots given here are therefore provided only to illustrate some intuitive points and to give the reader an 'order of magnitude' feeling for the required range of upper limits. Unless some analytical guidelines are developed and become available for these problems, similar numerical experiments must be performed for each new application.

To illustrate, let us first look at the convergence rates for several transmission line characteristics. The theory behind the calculations is presented in Chapter IV. Figure 3.4 shows the convergence behavior for three key transmission line parameters of a shielded microstrip line. As can be seen, the rate of convergence depends on which characteristic is to be computed. We re-emphasize that these features may vary as a function of the

geometric and electrical specifications. It should also be mentioned that this application does not present any practical difficulties since not only does the convergence appear to be quite rapid but these parameters are computed by a two-dimensional formulation involving only a single summation. The efficiency of evaluating the summation for this problem is not a significant issue given today's desktop computer capabilities. For example, the data in the figure were efficiently computed on an Apollo DN2500 workstation[1].

This brings us to the consideration of the two dimensional summations required in the analysis of three dimensional problems of the type discussed in Chapters V-VII. The required number of terms in the double summations depends on their behavior in the mn-plane, where m and n are the two parameters of summation. The real problem is in predicting or anticipating this behavior *a-priori* so that the corresponding limits can be set. Some progress in this direction can be achieved by recognizing that these summations are similar in many respects to the Fourier series. By drawing on our understanding of this topic, we can gain some intuitive understanding of how the modal summations behave. For example, it can easily be shown by numerical experiments that the closer two elements are in spatial coordinates, the greater will be the extent of the mode spectrum as in Fourier analysis. In addition, there may be no sign changes for the self coupling terms so that we can immediately conclude that these terms will display the slowest convergence. Thus, we could potentially monitor only the self coupling and nearby terms to determine whether the summations have converged or not. There is also a potential savings in time, if we can monitor the convergence of the series as a function of one direction (referred to as an 'eigendirection'), the direction of m say, while the other (n) is constant. Thereby we can potentially eliminate significant fractions of individual rows or even entire rows, depending

[1]The Apollo DN2500 is quite slow relative to most other engineering workstations, perhaps comparable in speed to standard Intel 80386 based personal computers. The above data was computed at a rate of approximately one minute cpu time per 1000 modes. The relation is approximately linear since there is only a single summation.

on the behavior of the functions involved.

While these ideas have an attractive generality to them in that we might be able to develop an algorithm for monitoring the convergence of the sum, making the convergence question invisible to the user, there are serious difficulties when we try to put it into practice. Most significant of the pitfalls involved include the fact that the final result is not known *a-priori* so it is quite difficult to establish a criteria for convergence. To illustrate, consider what happens if a 'percent change' criterion is used. Suppose some of the terms of series at the early stages of summation contribute very large values which are later canceled by similar terms of the opposite sign. At the early stages then, the sum will be large and a fixed percentage of the current sum may be quite large compared to the final result. Thus, truncating the local contributions to the series based on the current percent change may prevent important terms from making their contributions which in the end leaves a significant error. Another problem is that, as with Fourier analysis, the mode spectrum may have extended gaps along the eigendirections so that a summation in that direction may appear to be converged when in fact there are addition terms farther along which are needed.

Some time was invested in pursuing an algorithm which takes these factors into account based on observations of the spectra of various cases. In the end, however, it was found that while some progress could be made by instituting various monitoring schemes, the final conclusion was that the overhead required for keeping track of the progress of the sum and the periodic testing of sum's status, more or less offsets the gains made in reducing the number of actual terms added to produce the result. However, one scheme that emerged does bear mention here since it is straightforward. It should be recognized that the cancellation of terms generally occurs along both eigendirections and also the largest terms occur near the origin. Then, one can readily accumulate the bulk of the sum by making sure

to sum the low index terms near the origin at the onset, thus providing a good estimate of the final result and alleviating the problem of not having a good estimate of the final result in advance. A very simple algorithm accomplishes this scheme by simultaneously incrementing either m or n while decrementing the other and successively moving away from the origin, thereby summing in a direction normal to the diagonal of the mn-plane. However, because of the tradeoff mentioned, the final versions did not use any of the developed schemes but simply scanned the mn-plane in a straightforward, raster-like fashion with terminating conditions set by experience.

Generally, to avoid any question of convergence while other investigations were underway and because sufficient processing power was available, far more terms than necessary were used anyway, typically on the order of 1000-1500 modes in the eigendirection associated with the directions of the lines or slots, and half as many in the other direction. For the cases studied here, not nearly as many modes in the one eigendirection are needed as in the other. This is due to the fact that in the particular cases studied for comparison to experiments, the strips and slots were always parallel to the side walls of the cavities so that one coordinate describing the position of the basis functions is constant. This tends to cause the spectral variations in the corresponding eigenvalue to be similar for all basis functions, although the variation of the other coordinate prevents this from being strictly true. If, for example, the y coordinate is constant for all basis functions and n is the associated eigenvalue, the spectra in n at a fixed value of m will be identical except for a constant scale factor which depends on x. Truncation error in n then tends to get averaged out by the variation in x. To illustrate, let the aspect ratio in this example be defined by N/M, i.e., the denominator is the maximum eigenvalue corresponding to the coordinate which varies and N is the maximum of the other eigenvalue ($N \leq M$). Figures 3.5 and 3.6 demonstrate a typical convergence experiment in which the aspect ratio has been fixed

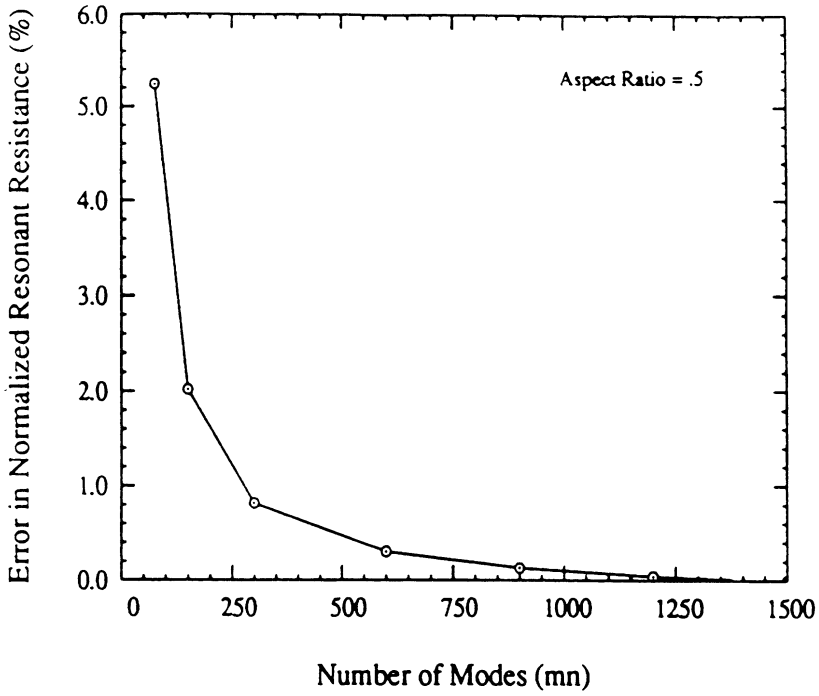

Figure 3.5: Convergence behavior for peak normalized resistance versus maximum mode number.

at 0.5. The quantities examined are key parameters to be introduced in Chapter VI. As always, other parameters may converge at different rates and the rates may vary as geometric or electrical parameters change. The key point here is that at least for this case, when the maximum m value is set to M = 600, the changes which occur as N/M is reduced from 1.0 to 0.25 are less than 0.1% for the resistance and 0.03% for the resonant length. Thus, far fewer modes are needed in the n direction.

For subsectional basis functions, the spatial sampling rate also requires convergence criteria. Since the quantities we are dealing with, e.g., impedance, are typically highly sensitive to the behavior of the near-field and also often depend only on the fields in a small region, the required spatial sampling rate is generally substantially higher than what is required for far-field type problems (or non-uniform sampling is needed which is more complex to implement). Again, the actual requirements depend on the circumstances

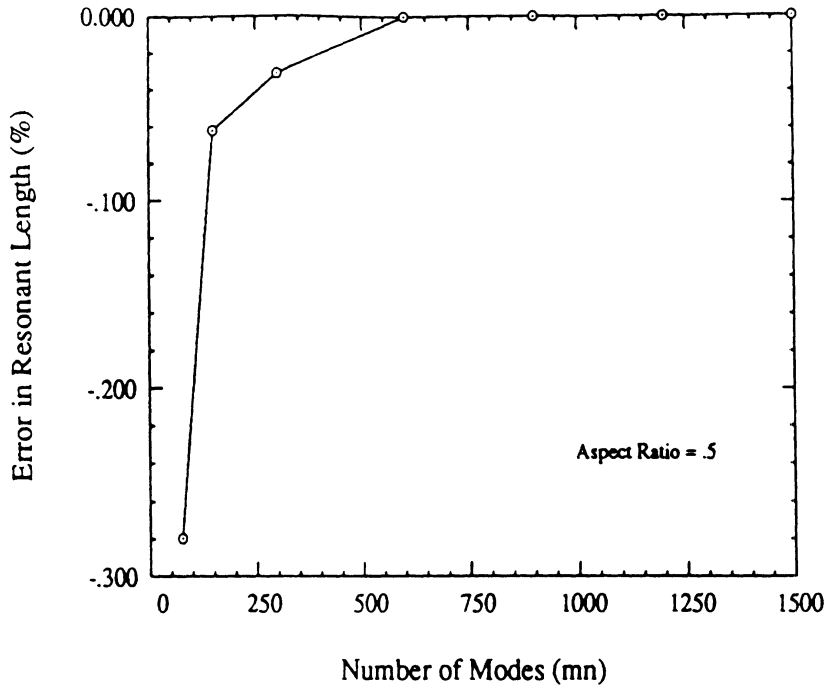

Figure 3.6: Convergence of resonant slot length as a function of the number of modes.

and techniques used so it is difficult to provide general statements on these requirements. Twenty samples per material wavelength is often used as a 'rule of thumb' for far-field problems which we generally increase to the 30-40 samples/wavelength range for sampling on strips or non-resonant slots. For the resonant slots, we often increase the sampling to 100-125 samples per wavelength making sure to overestimate the resonant length of the slot by a significant amount. This practice is not driven so much by convergence criterion as it is by practical matters. It takes far longer to generate the matrix elements than it does to invert and process the cases studied here. Changes in length or the relative positions of slots and lines for example, can easily be accomplished by loading a matrix with longer than needed lengths and scanning the behavior of the structure as a function of lengths or distances by successively removing the appropriate rows and columns; inverting and solving for the appropriate parameters at each stage. Thus, the matrix elements

need to be generated only once for a given frequency, allowing a wide variety of geometric variations to be studied as long as the cavity dimensions are not changed. We also use this technique to provide greater resolution of lengths and relative distances without requiring a regeneration of the matrix. The upper limit of the spatial sampling rate when the elements of the matrix are computed with double precision seems to be on the order of about 250 samples per material wavelength. This number, attributable to round-off and truncation error, is machine and algorithm dependent which brings us to the final point on this subject.

For problems of these types, it is common practice to quote run times typical for certain machines, often not very well identified. It is common knowledge that machines vary widely in their ability to execute codes, especially from machines of one type to another, but even for the same type of machine with different hardware configurations. In addition, the information provided can quickly become dated and irrelevant since available computing facilities are changing rapidly. Not only this, but also the execution time of the same analysis implemented with different algorithms and different degrees of generality can vary widely (easily on the order of a 10 to 1 variation, depending on both the abilities and knowledge of the programmer as well as the time spent in optimizing the algorithms for speed). Undoubtedly, there are techniques which can be used, in addition to those discussed above, to improve the run time of codes developed for this analysis. The real issue comes down to a tradeoff between time spent on optimizing codes versus producing and examining results. Of course, the outcome of this tradeoff depends on available resources, the objective in producing the codes, and their intended end use. Suffice it to say that the key element in the current approach is the generation of the matrix, which for a typical three dimensional structure at a single frequency, can be generated in 45-60 minutes or less on a $\sim$ 25 million instructions per second machine such as the IBM RS6000/320. This amount of processing time has been sufficient for our needs.

CHAPTER IV

ANALYSIS OF TWO-DIMENSIONAL STRUCTURES

The treatment of multiple layers can be illustrated in greater detail by presenting the methods used to analyze structures which are uniform in one dimension. Complex three-dimensional problems are often treated initially in this manner by analyzing their more fundamental elements - two dimensional transmission lines - with lumped elements added to represent discontinuities. The total problem can then be treated by network analysis if the basic properties of the individual structures are known.

The objective here is to show how these fundamental properties can be obtained, for instance, the propagation constants and characteristic impedances of transmission lines. These quantities are directly tied to the solutions for the fields in the structure which thus becomes the main objective of this chapter, that is, to demonstrate the procedure for matching field components through multiple substrate and superstrate layers as applied to two-dimensional problems. The presentation also serves to illustrate how the technique can be applied to more general three-dimensional problems since the procedure is the same. Some examples of field solutions are given to demonstrate the utility of the approach. The work in this chapter is also needed in later chapters which deal with the microstrip-fed slot antenna elements.

The scattering of waveguide modes by vertical wires is also studied in this chapter. This problem reduces to two dimensions for the homogeneously-filled waveguide case which

is relevant to the experimental work on stripline to be discussed later. The problem is unique in this work in that the currents are normal to directions of the other currents discussed. The treatment of wires inserted through multiple layers cannot be reduced to a two-dimensional problem and will not be discussed although, as will be seen, the solution to this problem would be needed to complete the general analysis of waveguides and especially cavities formed by inserting wires through the ground planes of multi-layered parallel plate waveguides. It is also noted that even for the homogeneously-filled case, the problem of vertical posts or wires has not been extensively treated in the literature, especially for parallel plate structures, even though they are often used in practice for the suppression of unwanted higher-order modes.

4.1 Application to General Multi-layered Shielded Microstrip Structures

The objective of this section is to show how the fields in the various levels can be calculated from a known form of current density on a single microstrip line in a straightforward way. Also, although to this point we have considered multiple components of current, the applications to be discussed will be restricted to narrow strips with one current component to minimize the complexity of the presentation. There is no restriction on the placement of the current or the number of strips which can be used, however, a simple case here will better serve to outline the method. The procedure for the treatment of more complex multi-layer coupled strips can be found in [83], which serves as an example of the use of potential theory with impedance boundary conditions to generalize multiple layers in a way similar to what has been done here. This reference also addresses the modelling of strip conductor loss. In additon, we compare to a much earlier work on this type of analysis by Yamashita [90], whose method of non-uniform discretization would be appropriate for wider strips where the form of the current density cannot be assumed.

In order to calculate the characteristic impedance, the definition $Z = P/I^2$ is used where P is the time average of power propagating along the guide. Thus, if we set $I = 1$, the characteristic impedance is simply $Z = P$ which can be computed analytically by integration of the average Poynting vector on the cross section of the waveguide. Also, in some cases, the reaction of the fields (R) on the waveguide cross section is needed which can be computed in the same way.

For our purposes, let us assume a geometry such as shown in Figure 4.1 with a longi-

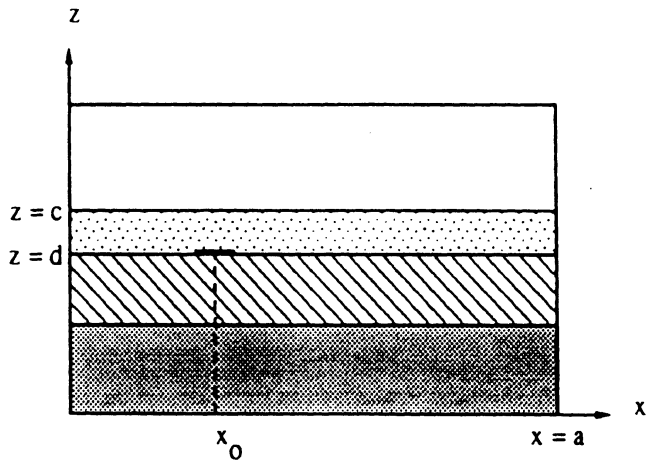

Figure 4.1: A shielded stripline, uniform in the $\hat{y}$ direction with multi-layered substrate and superstrate.

tudinal current component on a single narrow strip of the form

$$\bar{J}(x', y', z') = \hat{y} \frac{2\delta(z' - d)}{\pi W \sqrt{1 - 4\left(\frac{x' - x_o}{W}\right)^2}} e^{-jk_g y'} \quad |x' - x_o| < W/2 \tag{4.1}$$

i.e., a Maxwellian transverse variation of the current density which satisfies the edge conditions on an infinitesimally thin narrow strip. The propagation constant k_g represents the set of characteristic complex phase constants associated with shielded microstrip modes.

These complex constants are the eigenvalues of the equation

$$\bar{E}_t = -j\omega\mu \iiint \hat{n} \times \bar{\bar{G}}_{eJ} \cdot \bar{J}\, dV' = \hat{n} \times \bar{\bar{Z}}_s \cdot \bar{J} \tag{4.2}$$

which enforces the appropriate boundary conditions on the surface of the microstrip line [83]. A particular value for k_g must be found first, before the fields of a particular mode can be calculated.

Using Equation (4.1) in (4.2); the $\hat{y}\hat{y}$ component of $\bar{\bar{G}}_{eJ}$ as derived for layered rectangular waveguide in Chapter II; and the integral representation of the delta function,

$$\int_{-\infty}^{+\infty} e^{-j(k_g - k_y)y'} dy' = 2\pi\delta(k_g - k_y) \tag{4.3}$$

we find that the $\hat{y}$ component of the electric field can be written as

$$\begin{aligned} E_{yy} = \frac{\omega\mu}{a} \int_{-\infty}^{+\infty} dk_y \sum_{m=0}^{\infty} \frac{(2-\delta_m)\delta(k_g - k_y)}{k_z(k_x^2 + k_y^2)} \sin k_x x \sin k_x x_o J_o(k_x W/2) \\ \cdot \left\{ k_x^2 \left[\frac{\tilde{\eta}_{eL}[\tilde{\eta}_{eU} \cos k_z(c-z) + j \sin k_z(c-z)]}{(\tilde{\eta}_{eU} - \tilde{\eta}_{eL}) \cos k_z(c-d) - j(\tilde{\eta}_{eU}\tilde{\eta}_{eL} - 1) \sin k_z(c-d)} \right] \right. \\ \left. + \frac{k_y^2 k_z^2}{k_i^2} \left[\frac{\tilde{\eta}_{mL}[\tilde{\eta}_{mU} \cos k_z(c-z) + j \sin k_z(c-z)]}{(\tilde{\eta}_{mU} - \tilde{\eta}_{mL}) \cos k_z(c-d) - j(\tilde{\eta}_{mU}\tilde{\eta}_{mL} - 1) \sin k_z(c-d)} \right] \right\} \end{aligned} \tag{4.4}$$

where the Fourier integral can be eliminated using the sifting property of the δ function. Then, using Galerkin's procedure to enforce the boundary condition given by Equation (4.2), we can write

$$\begin{aligned} E_{yy} = \frac{\omega\mu}{a} \sum_{m=0}^{\infty} \frac{(2-\delta_m)}{k_z(k_x^2 + k_g^2)} \sin^2 k_x x_o J_o^2\left(\frac{k_x W}{2}\right) \\ \cdot \left\{ k_x^2 \left[\frac{\tilde{\eta}_{eL}[\tilde{\eta}_{eU} \cos k_z(c-d) + j \sin k_z(c-d)]}{(\tilde{\eta}_{eU} - \tilde{\eta}_{eL}) \cos k_z(c-d) - j(\tilde{\eta}_{eU}\tilde{\eta}_{eL} - 1) \sin k_z(c-d)} \right] \right. \\ \left. + \frac{k_z^2 k_g^2}{k_i^2} \left[\frac{\tilde{\eta}_{mL}[\tilde{\eta}_{mU} \cos k_z(c-d) + j \sin k_z(c-d)]}{(\tilde{\eta}_{mU} - \tilde{\eta}_{mL}) \cos k_z(c-d) - j(\tilde{\eta}_{mU}\tilde{\eta}_{mL} - 1) \sin k_z(c-d)} \right] \right\} \end{aligned} \tag{4.5}$$

We now numerically search, using Muller's method for example [60, p.262], to find the values of k_g which satisfy Equation (4.2) and thus correspond to microstrip modes.

With the propagation constants known, the fields in the i^{th} layer can be easily found. By inspection of Equations (2.80) and (2.85), the fields can be written in a general form

in terms of the homogeneous solutions to Equations (1.10) and (1.12). Thus, the fields in the i^{th} layer can be written as

$$\begin{aligned}\overline{\mathrm{H}}_J &= -\sum_{m=0}^{\infty} \frac{j(2-\delta_m)k_i}{2\pi a k_z(k_x^2+k_y^2)} \\ &\left\{ B_i \left(\begin{bmatrix} \tilde{\eta}_{mU}\bar{\mathrm{M}}_{oo}[k_x,k_z(z-c)] + j\bar{\mathrm{M}}_{oe}[k_x,k_z(z-c)] \\ \tilde{\eta}_{mL}\bar{\mathrm{M}}_{oo}[k_x,k_z(z-d)] + j\bar{\mathrm{M}}_{oe}[k_x,k_z(z-d)] \end{bmatrix} \right) \right. \\ &\left. + A_i \left(\begin{bmatrix} \tilde{\eta}_{eU}\bar{\mathrm{N}}_{ee}[k_x,k_z(z-c)] - j\bar{\mathrm{N}}_{eo}[k_x,k_z(z-c)] \\ \tilde{\eta}_{eL}\bar{\mathrm{N}}_{ee}[k_x,k_z(z-d)] - j\bar{\mathrm{N}}_{eo}[k_x,k_z(z-d)] \end{bmatrix} \right) \right\} \end{aligned} \tag{4.6}$$

and

$$\begin{aligned}\overline{\mathrm{E}}_J &= -\sum_{m=0}^{\infty} \frac{j(2-\delta_m)}{2\pi a k_z(k_x^2+k_y^2)} \\ &\left\{ A_i \left(\begin{bmatrix} \tilde{\eta}_{eU}\bar{\mathrm{M}}_{ee}[k_x,k_z(z-c)] - j\bar{\mathrm{M}}_{eo}[k_x,k_z(z-c)] \\ \tilde{\eta}_{eL}\bar{\mathrm{M}}_{ee}[k_x,k_z(z-d)] - j\bar{\mathrm{M}}_{eo}[k_x,k_z(z-d)] \end{bmatrix} \right) \right. \\ &\left. + B_i \left(\begin{bmatrix} \tilde{\eta}_{mU}\bar{\mathrm{N}}_{oo}[k_x,k_z(z-c)] + j\bar{\mathrm{N}}_{oe}[k_x,k_z(z-c)] \\ \tilde{\eta}_{mL}\bar{\mathrm{N}}_{oo}[k_x,k_z(z-d)] + j\bar{\mathrm{N}}_{oe}[k_x,k_z(z-d)] \end{bmatrix} \right) \right\} \end{aligned} \tag{4.7}$$

which are valid for all layers except the source layer. Some of the leading constants are preserved for convenience in later notation.

4.1.1 LSE Modes

Expanding the VWFs we then find that the LSE mode fields in each layer can be written in the form

$$\begin{aligned}\overline{\mathrm{E}}_{LSE} &= A_i \left[\frac{2\omega\mu_o}{a k_{zi}(k_x^2+k_y^2)} \right] \left[\hat{x}\hat{y} j k_x k_y \cos k_x x \sin k_x x' - \hat{y}\hat{y} k_x^2 \sin k_x x \sin k_x x' \right] \\ &\cdot \frac{1}{\cos k_{zi}(c_i-d_i)} \begin{cases} \cos k_{zi}(c_i-z)\left[\tilde{\eta}_{eUi} + j\tan k_{zi}(c_i-z)\right] & (i \le 0) \\ \cos k_{zi}(z-d_i)\left[\tilde{\eta}_{eLi} - j\tan k_{zi}(z-d_i)\right] & (i > 0) \end{cases} \end{aligned} \tag{4.8}$$

$$\overline{H}_{LSE} = \mp A_i \left[\frac{2j}{a(k_x^2+k_y^2)}\right]\left[\hat{x}\hat{y}k_x^2 \sin k_x x \sin k_x x' + \hat{y}\hat{y}jk_x k_y \cos k_x x \sin k_x x'\right]$$
$$\cdot\frac{1}{\cos k_{zi}(c_i-d_i)}\begin{cases}\cos k_{zi}(c_i-z)\left[\tilde{\eta}_{eUi}\tan k_{zi}(c_i-z)-j\right] & (i\le 0)\\ \cos k_{zi}(z-d_i)\left[\tilde{\eta}_{eLi}\tan k_{zi}(z-d_i)+j\right] & (i>0)\end{cases}$$

$$+A_i\left[\frac{2j}{ak_{zi}}\right]\left[\hat{z}\hat{y}k_x\cos k_x x \sin k_x x'\right]$$
$$\cdot\frac{1}{\cos k_{zi}(c_i-d_i)}\begin{cases}\cos k_{zi}(c_i-z)\left[\tilde{\eta}_{eUi}+j\tan k_{zi}(c_i-z)\right] & (i\le 0)\\ \cos k_{zi}(z-d_i)\left[\tilde{\eta}_{eLi}-j\tan k_{zi}(z-d_i)\right] & (i>0)\end{cases} \tag{4.9}$$

where $i=0$ for the layer containing the strip and

$$A_0 = \frac{-\tilde{\eta}_{eL0}}{(\tilde{\eta}_{eU0}-\tilde{\eta}_{eL0})\cos k_z(c_0-d_0) - j(\tilde{\eta}_{eU0}\tilde{\eta}_{eL0}-1)\sin k_z(c_0-d_0)} \tag{4.10}$$

By matching the tangential components of the field at the interfaces above and below the strip layer the remaining coupling coefficients are found to be

$$A_1 = A_0\frac{k_{z1}}{k_{z0}}\left[\frac{\tilde{\eta}_{eU0}+j\tan k_{z0}(c_0-d_0)}{\tilde{\eta}_{eL1}-j\tan k_{z1}(c_1-d_1)}\right] \tag{4.11}$$

$$A_i = \begin{cases}\dfrac{A_{i-1}k_{zi}\tilde{\eta}_{eL(i-1)}}{k_{z(i-1)}\cos k_{z(i-1)}(c_{i-1}-d_{i-1})[\tilde{\eta}_{eLi}-j\tan k_{zi}(c_i-d_i)]} & (i>1)\\ \dfrac{A_{i+1}k_{zi}\tilde{\eta}_{eU(i+1)}}{k_{z(i+1)}\cos k_{z(i+1)}(c_{i+1}-d_{i+1})[\tilde{\eta}_{eUi}+j\tan k_{zi}(c_i-d_i)]} & (i<0)\end{cases} \tag{4.12}$$

For computation of power (P), the needed component of Poynting vector is $\hat{y}\cdot\frac{1}{2}\overline{E}\times\overline{H}^*$ while for reaction (R) we need $\hat{y}\cdot\overline{E}(k_y)\times\overline{H}(-k_y)$. For the case of LSE modes, power density and reaction are given by

$$P = E_x H_z^* = \frac{2\omega\mu}{a^2}\left[\frac{A_i k_x k_y}{k_{zi}(k_x^2+k_y^2)}\right]\left[\frac{A_i^* k_x}{k_{zi}^*}\right]\frac{\cos^2 k_x x\left[\int \sin k_x x'\right]^2}{|\cos k_{zi}(c_i-d_i)|^2}$$
$$\cdot\begin{cases}|\tilde{\eta}_{eUi}\cos k_{zi}(c_i-z)+j\sin k_{zi}(c_i-z)|^2 & (i\le 0)\\ |\tilde{\eta}_{eLi}\cos k_{zi}(z-d_i)-j\sin k_{zi}(z-d_i)|^2 & (i>0)\end{cases} \tag{4.13}$$

$$R = E_x(k_y)H_z(-k_y) = \frac{4\omega\mu}{a^2}\left[\frac{jA_ik_xk_y}{k_{zi}(k_x^2+k_y^2)}\right]\left[\frac{jA_ik_x}{k_{zi}}\right]\frac{\cos^2 k_x x\,[\int \sin k_x x']^2}{\cos^2 k_{zi}(c_i-d_i)} \cdot \begin{cases} [\tilde{\eta}_{eUi}\cos k_{zi}(c_i-z) + j\sin k_{zi}(c_i-z)]^2 & (i\le 0) \\ [\tilde{\eta}_{eLi}\cos k_{zi}(z-d_i) - j\sin k_{zi}(z-d_i)]^2 & (i>0) \end{cases} \tag{4.14}$$

4.1.2 LSM Modes

Similarly, the LSM mode fields can be written as

$$\begin{aligned} \overline{\mathrm{E}}_{LSM} &= -B_i\left[\frac{2j\omega\mu k_{zi}}{ak_i^2(k_x^2+k_y^2)}\right]\left[\hat{x}\hat{y}jk_xk_y\cos k_x x\sin k_x x' + \hat{y}\hat{y}k_y^2\sin k_x x\sin k_x x'\right] \\ &\quad \cdot\frac{1}{\cos k_{zi}(c_i-d_i)}\begin{cases} \cos k_{zi}(c_i-z)\,[\tilde{\eta}_{mUi} + j\tan k_{zi}(c_i-z)] & (i\le 0) \\ \cos k_{zi}(z-d_i)\,[\tilde{\eta}_{mLi} - j\tan k_{zi}(z-d_i)] & (i>0) \end{cases} \\ &\quad \pm B_i\left[\frac{2j\omega\mu}{ak_i^2}\right]\left[\hat{z}\hat{y}jk_y\sin k_x x\sin k_x x'\right] \\ &\quad \cdot\frac{1}{\cos k_{zi}(c_i-d_i)}\begin{cases} \cos k_{zi}(c_i-z)\,[\tilde{\eta}_{mUi}\tan k_{zi}(c_i-z) - j] & (i\le 0) \\ \cos k_{zi}(z-d_i)\,[\tilde{\eta}_{mLi}\tan k_{zi}(z-d_i) + j] & (i>0) \end{cases} \end{aligned} \tag{4.15}$$

$$\begin{aligned} \overline{\mathrm{H}}_{LSM} &= \mp B_i\left[\frac{2j}{a(k_x^2+k_y^2)}\right]\left[\hat{x}\hat{y}k_y^2\sin k_x x\sin k_x x' - \hat{y}\hat{y}jk_xk_y\cos k_x x\sin k_x x'\right] \\ &\quad \cdot\frac{1}{\cos k_{zi}(c_i-d_i)}\begin{cases} \cos k_{zi}(c_i-z)\,[\tilde{\eta}_{mUi}\tan k_{zi}(c_i-z) - j] & (i\le 0) \\ \cos k_{zi}(z-d_i)\,[\tilde{\eta}_{mLi}\tan k_{zi}(z-d_i) + j] & (i>0) \end{cases} \end{aligned} \tag{4.16}$$

where the coefficients are defined by

$$B_0 = \frac{-\tilde{\eta}_{mL0}}{(\tilde{\eta}_{mU0}-\tilde{\eta}_{mL0})\cos k_z(c_0-d_0) - j(\tilde{\eta}_{mU0}\tilde{\eta}_{mL0}-1)\sin k_z(c_0-d_0)} \tag{4.17}$$

$$B_1 = B_0\frac{k_{z0}k_1^2}{k_{z1}k_0^2}\left[\frac{\tilde{\eta}_{mU0} + j\tan k_{z0}(c_0-d_0)}{\tilde{\eta}_{mL1} - j\tan k_{z1}(c_1-d_1)}\right] \tag{4.18}$$

$$B_i = \begin{cases} \dfrac{B_{i-1}k_{z(i-1)}k_i^2\tilde{\eta}_{mL(i-1)}}{k_{zi}k_{(i-1)}^2\cos k_{z(i-1)}(c_{i-1}-d_{i-1})[\tilde{\eta}_{mLi} - j\tan k_{zi}(c_i-d_i)]} & (i>1) \\ \dfrac{B_{i+1}k_{z(i+1)}k_i^2\tilde{\eta}_{mU(i+1)}}{k_{zi}k_{(i+1)}^2\cos k_{z(i+1)}(c_{i+1}-d_{i+1})[\tilde{\eta}_{eUi} + j\tan k_{zi}(c_i-d_i)]} & (i<0) \end{cases} \tag{4.19}$$

To calculate the field at a particular point in the $i^{\underline{th}}$ layer, we then calculate only the coupling coefficients $(A_0 \ldots A_i)$ and $(B_0 \ldots B_i)$ while evaluating Equations (4.8,4.9) and (4.15,4.16).

For the LSM modes the required terms for calculating power density and reaction are given by

$$P = -E_z H_x^* = \frac{2\omega\mu}{a^2}\left[\frac{B_i k_y}{k_i^2}\right]\left[\frac{B_i^*(k_y^*)^2}{(k_x^2+k_y^2)^*}\right]\frac{\sin^2 k_x x\,[\int \sin k_x x']^2}{|\cos k_{zi}(c_i-d_i)|^2} \cdot \begin{cases} |\tilde{\eta}_{mUi}\sin k_{zi}(c_i-z) - j\cos k_{zi}(c_i-z)|^2 & (i \le 0) \\ |\tilde{\eta}_{mLi}\sin k_{zi}(z-d_i) + j\cos k_{zi}(z-d_i)|^2 & (i > 0) \end{cases} \tag{4.20}$$

$$R = -E_z(k_y)H_x(-k_y) = -\frac{4\omega\mu}{a^2}\left[\frac{jB_i k_y}{k_i^2}\right]\left[\frac{-jB_i k_y^2}{(k_x^2+k_y^2)}\right]\frac{\sin^2 k_x x\,[\int \sin k_x x']^2}{\cos^2 k_{zi}(c_i-d_i)} \cdot \begin{cases} [\tilde{\eta}_{mUi}\sin k_{zi}(c_i-z) - j\cos k_{zi}(c_i-z)]^2 & (i \le 0) \\ [\tilde{\eta}_{mLi}\sin k_{zi}(z-d_i) + j\cos k_{zi}(z-d_i)]^2 & (i > 0) \end{cases} \tag{4.21}$$

4.1.3 Cross Terms

There are also two sets of cross-terms from the $\overline{\mathrm{E}}_{LSM} \times \overline{\mathrm{H}}_{LSE}$ product. The power terms are

$$P = E_x H_z^* = -\frac{2\omega\mu}{a^2}\left[\frac{B_i k_x k_y k_{zi}}{k_i^2(k_x^2+k_y^2)}\right]\left[\frac{A_i^* k_x}{k_{zi}^*}\right]\frac{\cos^2 k_x x\,[\int \sin k_x x']^2}{|\cos k_{zi}(c_i-d_i)|^2} \cdot \begin{cases} [\tilde{\eta}_{mUi}\cos k_{zi}(c_i-z) + j\sin k_{zi}(c_i-z)]\,[\tilde{\eta}_{eUi}\cos k_{zi}(c_i-z) + j\sin k_{zi}(c_i-z)]^* & (i \le 0) \\ [\tilde{\eta}_{mLi}\cos k_{zi}(z-d_i) - j\sin k_{zi}(z-d_i)]\,[\tilde{\eta}_{eLi}\cos k_{zi}(z-d_i) - j\sin k_{zi}(z-d_i)]^* & (i > 0) \end{cases} \tag{4.22}$$

$$P = -E_z H_x = \frac{2\omega\mu}{a^2}\left[\frac{B_i k_y}{k_i^2}\right]\left[\frac{A_i^* k_x^2}{(k_x^2+k_y^2)^*}\right]\frac{\sin^2 k_x x\,[\int \sin k_x x']^2}{|\cos k_{zi}(c_i-d_i)|^2} \cdot \begin{cases} [\tilde{\eta}_{mUi}\sin k_{zi}(c_i-z) - j\cos k_{zi}(c_i-z)]\,[\tilde{\eta}_{eUi}\sin k_{zi}(c_i-z) - j\cos k_{zi}(c_i-z)]^* & (i \le 0) \\ [\tilde{\eta}_{mLi}\sin k_{zi}(z-d_i) + j\cos k_{zi}(z-d_i)]\,[\tilde{\eta}_{eLi}\sin k_{zi}(z-d_i) + j\cos k_{zi}(z-d_i)]^* & (i > 0) \end{cases} \tag{4.23}$$

For the reaction we have

$$R = E_x(k_y)H_z(-k_y) = \frac{4\omega\mu}{a^2}\left[\frac{-jB_i k_x k_y k_{zi}}{k_i^2(k_x^2+k_y^2)}\right]\left[\frac{jA_i k_x}{k_{zi}}\right]\frac{\cos^2 k_x x\,[\int \sin k_x x']^2}{\cos^2 k_{zi}(c_i-d_i)}$$
$$\cdot\begin{cases}[\tilde{\eta}_{mUi}\cos k_{zi}(c_i-z)+j\sin k_{zi}(c_i-z)][\tilde{\eta}_{eUi}\cos k_{zi}(c_i-z)+j\sin k_{zi}(c_i-z)] & (i\le 0)\\ [\tilde{\eta}_{mLi}\cos k_{zi}(z-d_i)-j\sin k_{zi}(z-d_i)][\tilde{\eta}_{eLi}\cos k_{zi}(z-d_i)-j\sin k_{zi}(z-d_i)] & (i>0)\end{cases} \tag{4.24}$$

$$R = -E_z(k_y)H_x(-k_y) = -\frac{4\omega\mu}{a^2}\left[\frac{jB_i k_y}{k_i^2}\right]\left[\frac{-jA_i k_x^2}{(k_x^2+k_y^2)}\right]\frac{\sin^2 k_x x\,[\int \sin k_x x']^2}{\cos^2 k_{zi}(c_i-d_i)}$$
$$\cdot\begin{cases}[\tilde{\eta}_{mUi}\sin k_{zi}(c_i-z)-j\cos k_{zi}(c_i-z)][\tilde{\eta}_{eUi}\sin k_{zi}(c_i-z)-j\cos k_{zi}(c_i-z)] & (i\le 0)\\ [\tilde{\eta}_{mLi}\sin k_{zi}(z-d_i)+j\cos k_{zi}(z-d_i)][\tilde{\eta}_{eLi}\sin k_{zi}(z-d_i)+j\cos k_{zi}(z-d_i)] & (i>0)\end{cases} \tag{4.25}$$

4.1.4 Integration of Power and Reaction terms

The evaluation of total power can be done analytically by integrating the power density on the waveguide cross-section. Integration of the x dependence is trivial and has been indicated in the previous expressions. The z dependence appears in two forms, the first of which is

$$\begin{aligned} I_{PM} &= \int_d^c \begin{cases}[\eta_1\cos k(c-z)+j\sin k(c-z)][\eta_2\cos k(c-z)+j\sin k(c-z)]^* \\ [\eta_1\cos k(z-d)-j\sin k(z-d)][\eta_2\cos k(z-d)-j\sin k(z-d)]^*\end{cases} dz \\ &= \frac{\eta_1\eta_2^*-1}{4\Re e(k)}\sin 2\Re e(k)(c-d) \mp j\frac{\eta_1-\eta_2^*}{2\Re e(k)}\sin^2\Re e(k)(c-d) \\ &\quad + \frac{\eta_1\eta_2^*+1}{4\Im m(k)}\sinh 2\Im m(k)(c-d) \mp \frac{\eta_1+\eta_2^*}{2\Im m(k)}\sinh^2\Im m(k)(c-d) \end{aligned} \tag{4.26}$$

where $\Re e(k)$ and $\Im m(k)$ symbolize the real and imaginary parts of k respectively. The second form is

$$\begin{aligned} I_{PN} &= \int_d^c \begin{cases}[\eta_1\sin k(c-z)-j\cos k(c-z)][\eta_2\sin k(c-z)-j\cos k(c-z)]^* \\ [\eta_1\sin k(z-d)+j\cos k(z-d)][\eta_2\sin k(z-d)+j\cos k(z-d)]^*\end{cases} dz \\ &= -\frac{\eta_1\eta_2^*-1}{4\Re e(k)}\sin 2\Re e(k)(c-d) \pm j\frac{\eta_1-\eta_2^*}{2\Re e(k)}\sin^2\Re e(k)(c-d) \\ &\quad + \frac{\eta_1\eta_2^*+1}{4\Im m(k)}\sinh 2\Im m(k)(c-d) \mp \frac{\eta_1+\eta_2^*}{2\Im m(k)}\sinh^2\Im m(k)(c-d) \end{aligned} \tag{4.27}$$

For reaction we also have two types of integrations to perform. The first is

$$I_{RM} = \int_d^c \left\{ \begin{array}{l} [\eta_1 \cos k(c-z) + j \sin k(c-z)][\eta_2 \cos k(c-z) + j \sin k(c-z)] \\ [\eta_1 \cos k(z-d) - j \sin k(z-d)][\eta_2 \cos k(z-d) - j \sin k(z-d)] \end{array} \right\} dz$$

$$= \frac{\eta_1\eta_2 - 1}{2}(c-b) + \frac{\eta_1\eta_2 + 1}{4k} \sin 2k(c-b) \pm j\frac{\eta_1 + \eta_2}{2k} \sin^2 k(c-b) \qquad (4.28)$$

Similarly,

$$I_{RN} = \int_d^c \left\{ \begin{array}{l} [\eta_1 \sin k(c-z) - j \cos k(c-z)][\eta_2 \sin k(c-z) - j \cos k(c-z)] \\ [\eta_1 \sin k(z-d) + j \cos k(z-d)][\eta_2 \sin k(z-d) + j \cos k(z-d)] \end{array} \right\} dz$$

$$= \frac{\eta_1\eta_2 - 1}{2}(c-d) - \frac{\eta_1\eta_2 + 1}{4k} \sin 2k(c-d) \mp j\frac{\eta_1 + \eta_2}{2k} \sin^2 k(c-d) \qquad (4.29)$$

4.1.5 Applications

With these analytical results, the fields, power flow and reaction, characteristic impedance and propagation constants can be readily found for shielded strips with any combination of layered substrates and superstrates. An example is shown in Figure 4.2 where results of the present technique are compared to a commercial CAD package (*Touchstone* [20]) and experimental measurements provided by Dunleavy [19]. The relatively large error bars provided by Dunleavy for this case do not provide for any conclusion on the comparative accuracy of the full-wave approach since the agreement is excellent. The corresponding characteristic impedance is shown in Figure 4.3.

We conclude that the accuracy of the full-wave implementation is excellent since the accuracy of *Touchstone* is well established and has been further verified by Dunleavy for this case. One can argue that the full-wave implementation with its greater complexity is not needed, however, most CAD packages, including *Touchstone*, are based on approximate formulas which, although they can be quickly evaluated, generally decrease in accuracy as frequency is increased. Also they deal almost exclusively with the dominant propagating

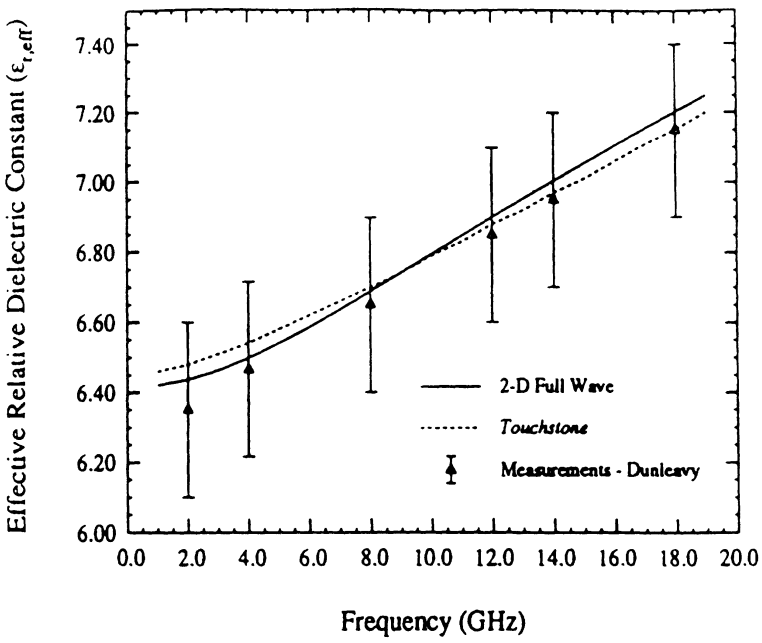

Figure 4.2: Effective relative dielectric constant for shielded microstrip on alumina (a = b = 250 mils, W = 25 mils, ϵ_r = 9.7) compared to measurements [19] and *Touchstone* [20].

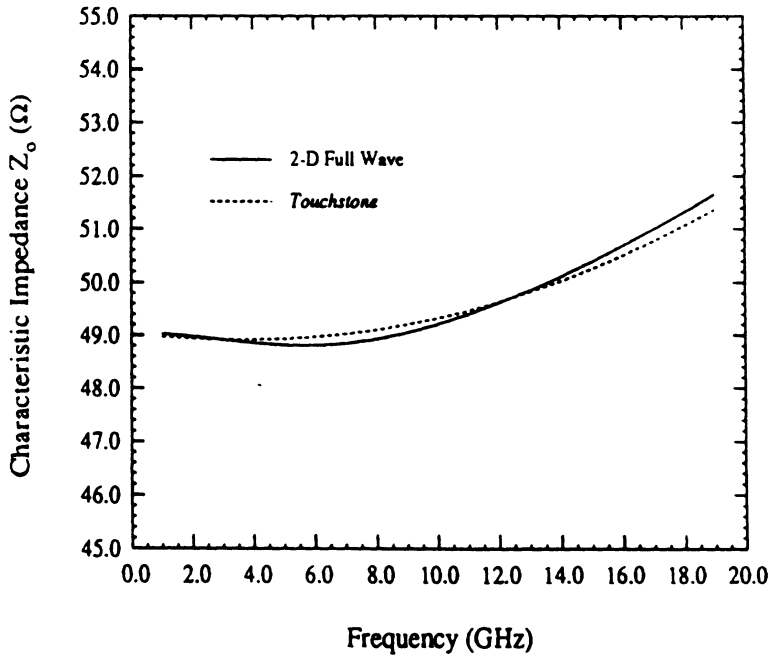

Figure 4.3: Characteristic impedance for shielded microstrip on alumina (a = b = 250 mils, W = 25 mils, ϵ_r = 9.7) compared to *Touchstone*.

modes which sometimes is insufficient. These features are similar to the behavior of "quasi-static" analyses although today's CAD packages generally go beyond "quasi-statics" by employing higher-order, albeit still approximate techniques. The results, of course, are very efficient routines for each component in a microwave circuit which make these packages very powerful and efficient for circuit design.

Full-wave techniques have their greatest promise where the other methods fail, for example, analysis of high frequencies components, systems with multi-mode interactions, radiation problems and applications with geometries and accuracy requirements not amenable to simpler analytical techniques, i.e., the type of structures studied here. For instance, Figure 4.4 shows the multi-mode propagation constants for the even modes on a shielded microstrip line produced by a program generalized to handle arbitrary layered structures as discussed. The simple case of microstrip is shown since there is available data for comparison and verification. The curves overlay the data supplied by Yamashita [90] with the exception of the dominant mode. *Touchstone* results are also shown for the dominant mode which are in exact agreement with the present method. It is presumed that the *Touchstone* results are correct for this mode since the dimensions are not extreme in terms of wavelengths; thus, quasi-TEM assumptions, as used by *Touchstone*, should be adequate. Most likely, the discrepancy for Yamashita's approach is attributable to the use of pulse basis functions at the strip edge which do not satisfy the edge conditions, although his discretization over the strip improves the capability to approximate the true current. Nevertheless, the form of current assumed with the present method is the exact form for the static case which should be very close to the true solution and therefore is more likely to give better accuracy. Since the exact details of the discretization are not supplied in [90], it is difficult to make a judgement, however, the real point here is the ability to model the higher order modes. (To represent the odd modes, a higher order expansion of the current

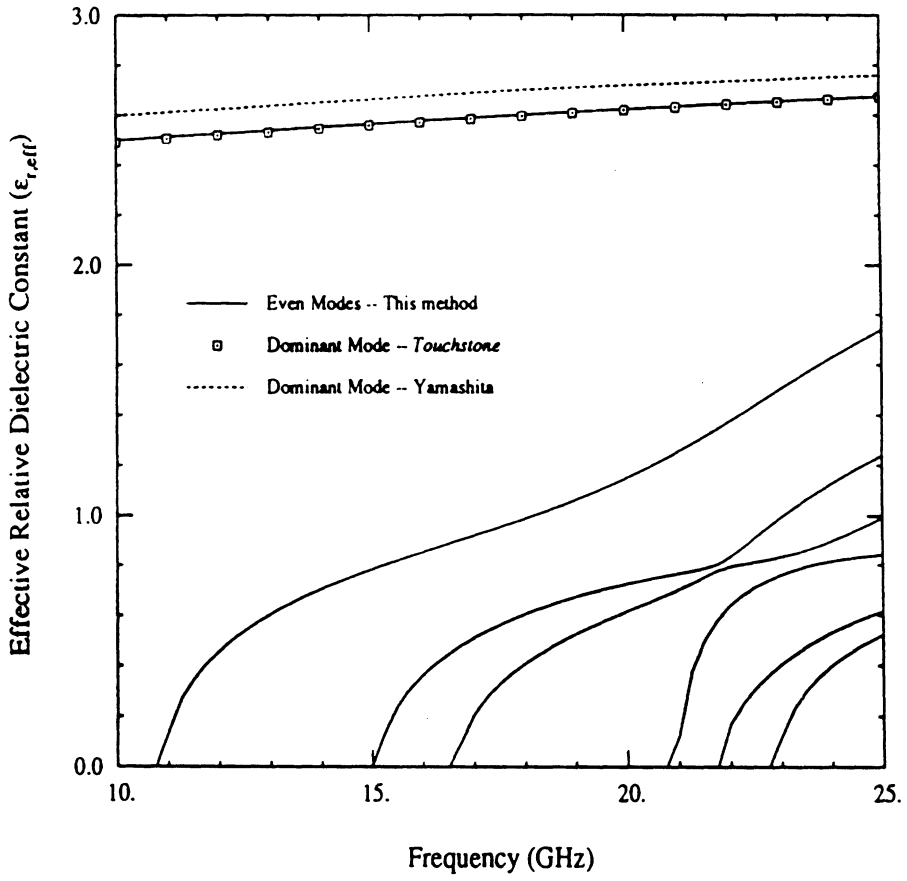

Figure 4.4: Multi-mode propagation constants for the even modes in shielded microstrip (a = b = 12.7 mm, h = 1.27 mm, w = .635 mm ϵ_r = 8.875).

is needed such as Yamashita's approach or possibly, expansion by Chebyshev polynomials as in [83].)

Besides the obvious utility of this type of information for circuit design and the need for these quantities to be demonstrated in later chapters, the ability to visualize the field or power distribution often provides important insights into why certain structures behave as they do, and also, how the behavior might change when the structure is modified. For example, we later will extensively discuss the special case of a stripline (homogeneously filled shielded strip) which passes through an aperture in the wall of a cavity. The field distribution in the vicinity of the strip as shown in Figure 4.5 gives a clear indication of the constraints which must be placed on the size of the aperture. One can see that the larger

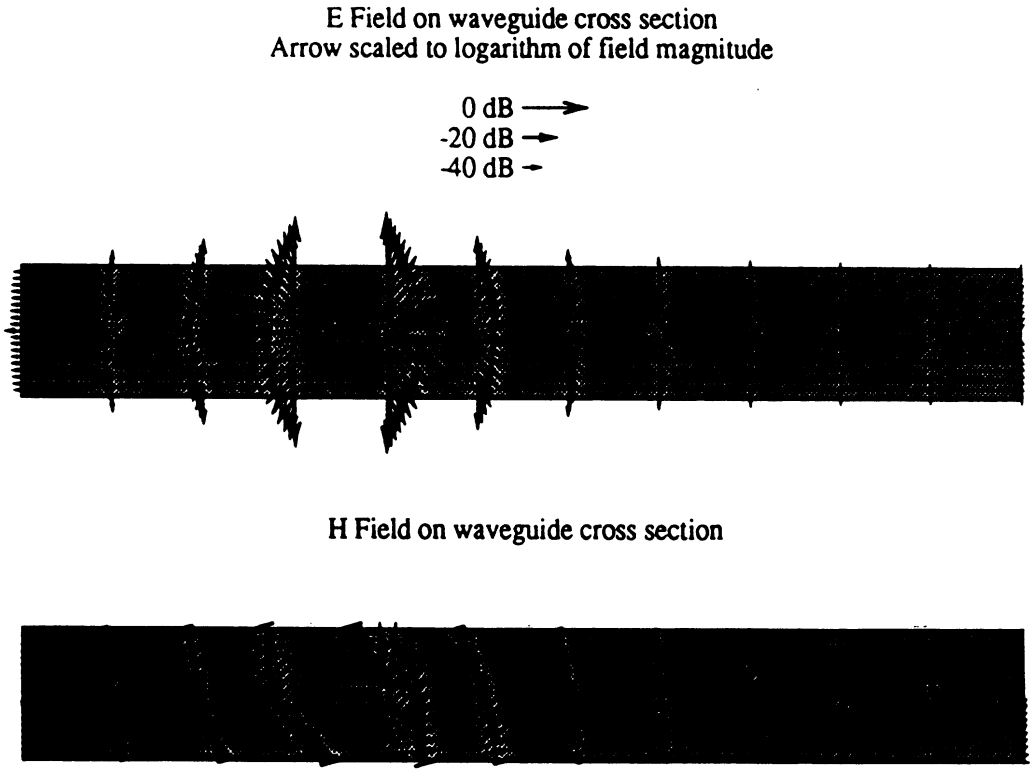

Figure 4.5: Stripline field distribution for the dominant propagating mode.

field magnitudes are tightly confined to the immediate vicinity of the strip as expected (the tails of the arrows are the field points). For a 'pass-thru' aperture then, the opening

in the wall should be sufficiently large so that minimal energy (proportional to the field) is intercepted by the wall. From the numerical data, quantitative criteria can easily be established.

Similar examples for microstrip and suspended microstrip can be found in Figures 4.6 and 4.7, respectively. The upper part of the structure in Figure 4.7 has the same dimen-

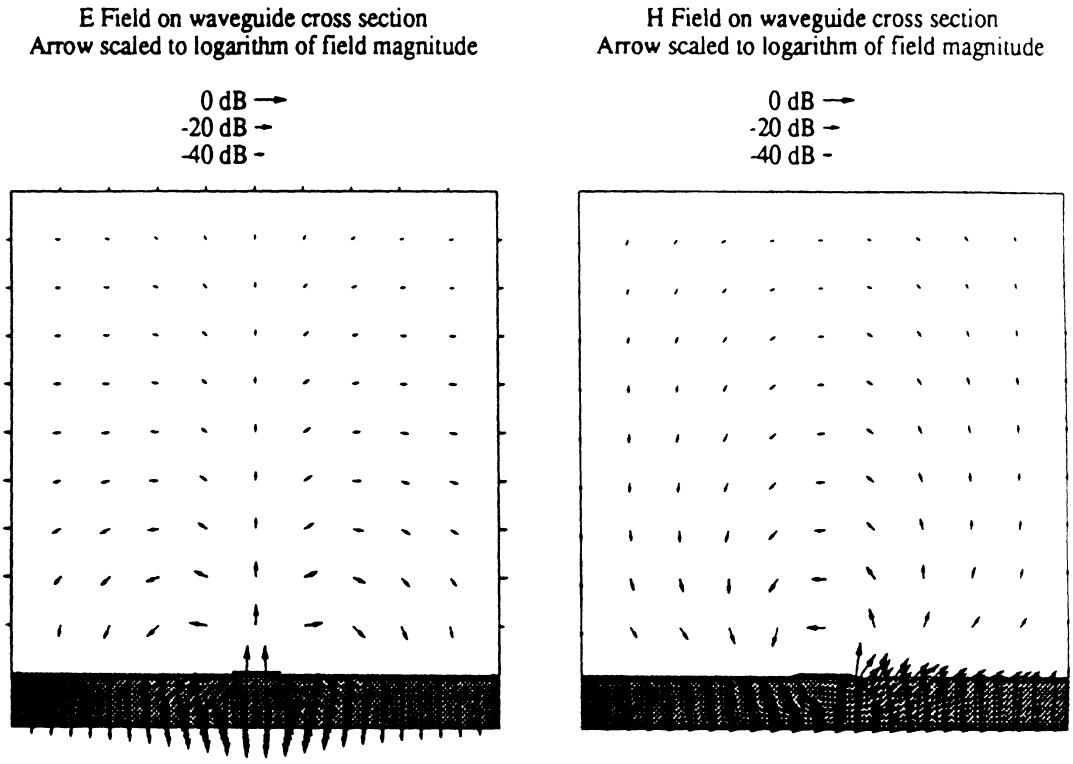

Figure 4.6: Microstrip field distribution for the dominant propagating mode.

sions as the structure in Figure 4.6. By comparing the fields in these two cases, especially in the substrates, one can appreciate how one structure behaves quite differently from the other. Consider for example, what would happen if another strip is introduced on the substrate in these two cases. Clearly, the suspended microstrip field distribution would be more greatly disturbed than the conventional shielded microstrip, and therefore the coupling between strips would likewise be greater. This type of argument is a 'visual' application of the Reaction Theorem. Such an ability to visualize the field demonstrates

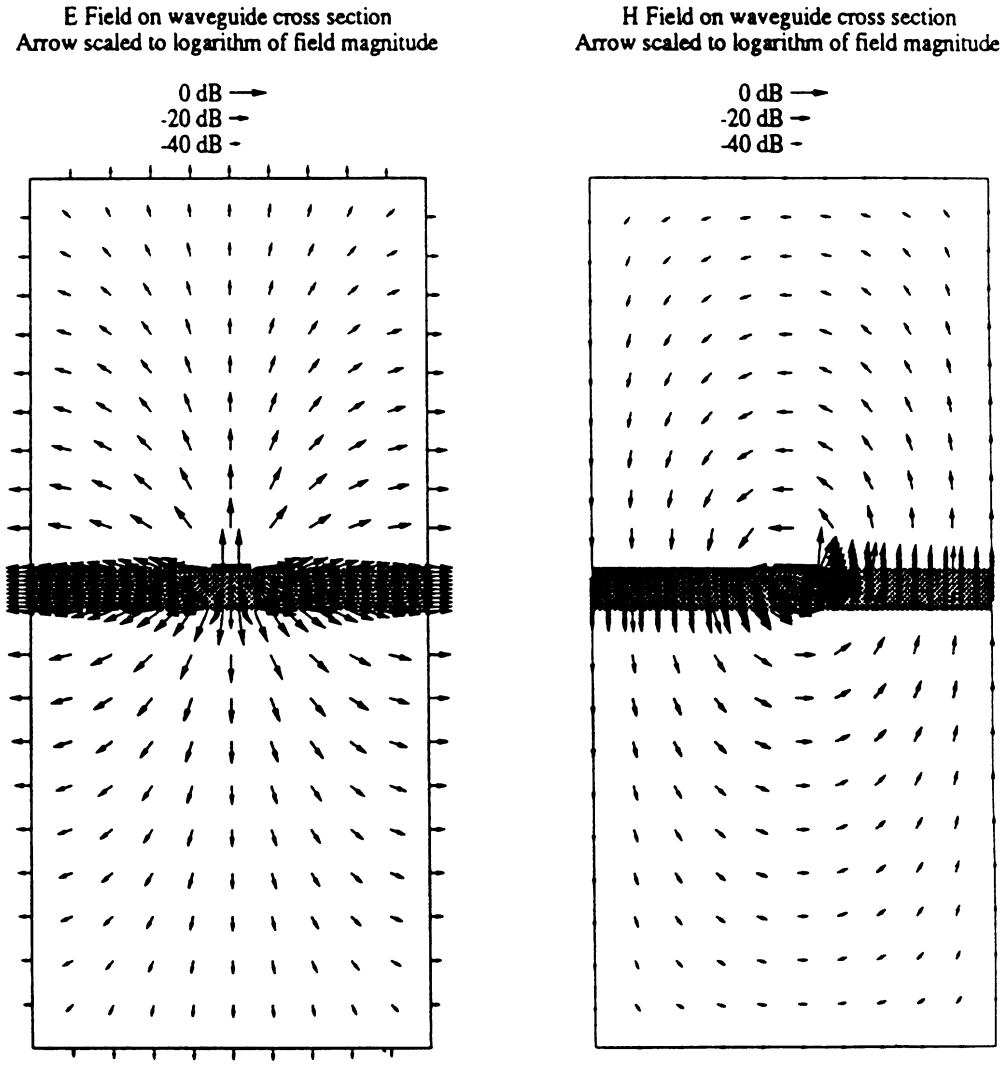

Figure 4.7: Suspended microstrip field distribution for the dominant propagating mode.

one of the benefits of this type of analysis: enhancing our intuitive understanding of the behavior of these structures as well as providing quantitative information.

4.2 Application to Multi-layered Slotline

A similar process can be used to evaluate slotlines or coplanar waveguide. Since coplanar waveguide can be treated as coupled slotlines by a simple extension of the method, only the single slot case will be discussed here. We assume the magnetic current is of the same form as in the electric current case which then is valid for narrow slots:

$$\overline{\mathrm{K}}(x',y',z') = \hat{y}\frac{2\delta(z'-d)}{\pi W\sqrt{1-4\left(\frac{x'-x_o}{W}\right)^2}}e^{-jk_g y'} \quad |x'-x_o| < W/2 \tag{4.30}$$

The variable k_g here represents the set of characteristic complex phase constants associated with shielded slotline modes. They are the eigenvalues of the boundary condition equation:

$$\overline{\mathrm{H}}_t^+ - \overline{\mathrm{H}}_t^- = -j\omega\epsilon\iiint\left[\bar{\bar{\mathrm{G}}}_{\mathrm{mK}}^+ - \bar{\bar{\mathrm{G}}}_{\mathrm{mK}}^-\right]\cdot\overline{\mathrm{K}}\,dV' = 0 \tag{4.31}$$

which enforces continuity of the tangential magnetic field ($\overline{\mathrm{H}}_t$) in the slot. As before, a particular value for k_g is found first, before the fields of a particular mode are calculated. The procedure is the same as before except that the field expressions are changed to reflect the change in the source terms and complementary boundary conditions for the dual fields.

4.2.1 LSE Modes

Expanding the VWFs we then find that the LSE mode fields in each layer can be written in the forms:

$$\begin{aligned}\overline{\mathrm{E}}_{LSE} &= A_i\frac{1}{\epsilon_i}\left[\frac{(2-\delta_m)}{a(k_x^2+k_y^2)}\right]\left[\hat{x}\hat{y}k_y^2\cos k_x x\cos k_x x' + \hat{y}\hat{y}jk_x k_y\sin k_x x\cos k_x x'\right] \\ &\quad\cdot\frac{1}{\cos k_{zi}(c_i-d_i)}\begin{cases}\cos k_{zi}(c_i-z)\left[\tilde{\eta}_{eUi}+j\tan k_{zi}(c_i-z)\right] & (i\le 0)\\ \cos k_{zi}(z-d_i)\left[\tilde{\eta}_{eLi}-j\tan k_{zi}(z-d_i)\right] & (i>0)\end{cases}\end{aligned} \tag{4.32}$$

$$\overline{\mathrm{H}}_{LSE} = \pm A_i \left[\frac{(2-\delta_m)\omega\epsilon_o k_{zi}}{a k_i^2 (k_x^2+k_y^2)}\right] \left[\hat{x}\hat{y} k_x k_y \sin k_x x \cos k_x x' + \hat{y}\hat{y} j k_y^2 \cos k_x x \cos k_x x'\right]$$
$$\cdot \frac{1}{\cos k_{zi}(c_i - d_i)} \begin{cases} \cos k_{zi}(c_i - z)\,[\tilde{\eta}_{eUi} \tan k_{zi}(c_i - z) - j] & (i \le 0) \\ \cos k_{zi}(z - d_i)\,[\tilde{\eta}_{eLi} \tan k_{zi}(z - d_i) + j] & (i > 0) \end{cases}$$

$$-A_i \left[\frac{(2-\delta_m)\omega\epsilon_o}{a k_i^2}\right] \left[\hat{z}\hat{y} k_y \cos k_x x \cos k_x x'\right]$$
$$\cdot \frac{1}{\cos k_{zi}(c_i - d_i)} \begin{cases} \cos k_{zi}(c_i - z)\,[\tilde{\eta}_{eUi} + j \tan k_{zi}(c_i - z)] & (i \le 0) \\ \cos k_{zi}(z - d_i)\,[\tilde{\eta}_{eLi} - j \tan k_{zi}(z - d_i)] & (i > 0) \end{cases} \tag{4.33}$$

where $i = 0$ for the layer with the slot so that

$$A_0 = \frac{-\epsilon_0}{\tilde{\eta}_{eU0} + j \tan k_{z0}(c_0 - d_0)} \tag{4.34}$$

$$A_1 = \frac{\epsilon_1}{\tilde{\eta}_{eL1} - j \tan k_{z1}(c_1 - d_1)} \tag{4.35}$$

By matching the tangential components of the field at the interfaces above and below the strip layer the remaining coupling coefficients are found to be

$$A_i = \begin{cases} j A_{i-1} \dfrac{k_{z(i-1)} k_i^2}{k_{zi} k_{(i-1)}^2 \cos k_{z(i-1)}(c_{i-1} - d_{i-1})[\tilde{\eta}_{eLi} \tan k_{zi}(c_i - d_i) + j]} & (i > 1) \\ -j A_{i+1} \dfrac{k_{z(i+1)} k_i^2}{k_{zi} k_{(i+1)}^2 \cos k_{z(i+1)}(c_{i+1} - d_{i+1})[\tilde{\eta}_{eUi} \tan k_{zi}(c_i - d_i) - j]} & (i < 0) \end{cases} \tag{4.36}$$

The expressions for power density and reaction of the LSE modes are

$$P = E_x H_z^* = |A_i|^2 \frac{(2-\delta_m)^2 \omega\epsilon_o}{2a^2} \left[\frac{k_y^2}{(k_x^2+k_y^2)\epsilon_i}\right] \left[\frac{k_y^*}{(k_i^*)^2}\right] \frac{\cos k_x x \left[\int \cos k_x x'\right]^2}{|\cos k_{zi}(c_i - d_i)|^2}$$
$$\cdot \begin{cases} |\tilde{\eta}_{eUi} \cos k_{zi}(c_i - z) + j \sin k_{zi}(c_i - z)|^2 & (i \le 0) \\ |\tilde{\eta}_{eLi} \cos k_{zi}(z - d_i) - j \sin k_{zi}(z - d_i)|^2 & (i > 0) \end{cases} \tag{4.37}$$

$$R = E_x(k_y) H_z(-k_y) = A_i^2 \frac{(2-\delta_m)^2 \omega\epsilon_o}{a^2} \left[\frac{k_y^2}{(k_x^2+k_y^2)\epsilon_i}\right] \left[\frac{k_y}{k_i^2}\right] \frac{\cos^2 k_x x \left[\int \cos k_x x'\right]^2}{\cos^2 k_{zi}(c_i - d_i)}$$
$$\cdot \begin{cases} [\tilde{\eta}_{eUi} \cos k_{zi}(c_i - z) + j \sin k_{zi}(c_i - z)]^2 & (i \le 0) \\ [\tilde{\eta}_{eLi} \cos k_{zi}(z - d_i) - j \sin k_{zi}(z - d_i)]^2 & (i > 0) \end{cases} \tag{4.38}$$

4.2.2 LSM Modes

Similarly, the LSM mode fields can be written as

$$\begin{aligned}
\overline{\mathrm{E}}_{LSM} &= -B_i \left[\frac{(2-\delta_m)}{a(k_x^2+k_y^2)\epsilon_i}\right] \left[\hat{x}\hat{y}k_x^2 \cos k_x x \cos k_x x' - \hat{y}\hat{y}jk_xk_y \sin k_x x \cos k_x x'\right] \\
&\quad \cdot \frac{1}{\cos k_{zi}(c_i - d_i)} \begin{cases} \cos k_{zi}(c_i - z)\left[\tilde{\eta}_{mUi} + j \tan k_{zi}(c_i - z)\right] & (i \le 0) \\ \cos k_{zi}(z - d_i)\left[\tilde{\eta}_{mLi} - j \tan k_{zi}(z - d_i)\right] & (i > 0) \end{cases} \\
&\quad \pm B_i \left[\frac{(2-\delta_m)}{a\epsilon_i k_{zi}}\right] \left[\hat{z}\hat{y}k_x \sin k_x x \cos k_x x'\right] \\
&\quad \cdot \frac{1}{\cos k_{zi}(c_i - d_i)} \begin{cases} \cos k_{zi}(c_i - z)\left[\tilde{\eta}_{mUi} \tan k_{zi}(c_i - z) - j\right] & (i \le 0) \\ \cos k_{zi}(z - d_i)\left[\tilde{\eta}_{mLi} \tan k_{zi}(z - d_i) + j\right] & (i > 0) \end{cases}
\end{aligned} \tag{4.39}$$

$$\begin{aligned}
\overline{\mathrm{H}}_{LSM} &= \mp B_i \left[\frac{(2-\delta_m)\omega\epsilon_o}{ak_{zi}(k_x^2+k_y^2)}\right] \left[\hat{x}\hat{y}k_xk_y \sin k_x x \cos k_x x' - \hat{y}\hat{y}jk_x^2 \cos k_x x \cos k_x x'\right] \\
&\quad \cdot \frac{1}{\cos k_{zi}(c_i - d_i)} \begin{cases} \cos k_{zi}(c_i - z)\left[\tilde{\eta}_{mUi} \tan k_{zi}(c_i - z) - j\right] & (i \le 0) \\ \cos k_{zi}(z - d_i)\left[\tilde{\eta}_{mLi} \tan k_{zi}(z - d_i) + j\right] & (i > 0) \end{cases}
\end{aligned} \tag{4.40}$$

where

$$B_0 = \frac{-\epsilon_0}{\tilde{\eta}_{mU0} + j \tan k_{z0}(c_0 - d_0)} \tag{4.41}$$

$$B_1 = \frac{\epsilon_1}{\tilde{\eta}_{mL1} - j \tan k_{z1}(c_1 - d_1)} \tag{4.42}$$

$$B_i = \begin{cases} B_{i-1} \dfrac{jk_{zi}}{k_{z(i-1)} \cos k_{z(i-1)}(c_{i-1} - d_{i-1})[\tilde{\eta}_{mLi} \tan k_{zi}(c_i - d_i) + j]} & (i > 1) \\ -B_{i+1} \dfrac{jk_{zi}}{k_{z(i+1)} \cos k_{z(i+1)}(c_{i+1} - d_{i+1})[\tilde{\eta}_{mUi} \tan k_{zi}(c_i - d_i) - j]} & (i < 0) \end{cases} \tag{4.43}$$

For the LSM modes the required terms for calculating power and reaction are

$$\begin{aligned}
P = -E_z H_x^* &= |B_i|^2 \frac{(2-\delta_m)^2 \omega\epsilon_o}{2a^2(k_x^2+k_y^2)} \left[\frac{k_x}{\epsilon_i k_{zi}}\right] \left[\frac{k_x k_y^*}{k_{zi}^*}\right] \frac{\sin^2 k_x x \left[\int \cos k_x x'\right]^2}{|\cos k_{zi}(c_i - d_i)|^2} \\
&\quad \cdot \begin{cases} |\tilde{\eta}_{mUi} \sin k_{zi}(c_i - z) - j \cos k_{zi}(c_i - z)|^2 & (i \le 0) \\ |\tilde{\eta}_{mLi} \sin k_{zi}(z - d_i) + j \cos k_{zi}(z - d_i)|^2 & (i > 0) \end{cases}
\end{aligned} \tag{4.44}$$

$$R = -E_z(k_y)H_x(-k_y) = -B_i^2\frac{(2-\delta_m)^2\omega\epsilon_o}{a^2}\left[\frac{k_x}{\epsilon_i k_{zi}}\right]\left[\frac{k_x k_y}{k_{zi}(k_x^2+k_y^2)}\right]\frac{\sin^2 k_x x\,[\int\cos k_x x']^2}{\cos^2 k_{zi}(c_i-d_i)}$$
$$\cdot\begin{cases}[\tilde{\eta}_{mUi}\sin k_{zi}(c_i-z) - j\cos k_{zi}(c_i-z)]^2 & (i\le 0)\\ [\tilde{\eta}_{mLi}\sin k_{zi}(z-d_i) + j\cos k_{zi}(z-d_i)]^2 & (i>0)\end{cases} \tag{4.45}$$

4.2.3 Cross Terms

There are also two sets of cross-terms from the $\overline{E}_{LSM} \times \overline{H}_{LSE}$ product. The power terms are

$$P = E_x H_z^* = B_i A_i^*\frac{(2-\delta_m)^2\omega\epsilon_o}{2a^2}\left[\frac{k_x^2}{(k_x^2+k_y^2)\epsilon_i}\right]\left[\frac{k_y^*}{(k_i^*)^2}\right]\frac{\cos^2 k_x x\,[\int\cos k_x x']^2}{|\cos k_{zi}(c_i-d_i)|^2}$$
$$\cdot\begin{cases}[\tilde{\eta}_{mUi}\cos k_{zi}(c_i-z) + j\sin k_{zi}(c_i-z)][\tilde{\eta}_{eUi}\cos k_{zi}(c_i-z) + j\sin k_{zi}(c_i-z)]^* & (i\le 0)\\ [\tilde{\eta}_{mLi}\cos k_{zi}(z-d_i) - j\sin k_{zi}(z-d_i)][\tilde{\eta}_{eLi}\cos k_{zi}(z-d_i) - j\sin k_{zi}(z-d_i)]^* & (i>0)\end{cases} \tag{4.46}$$

$$P = -E_z H_x = B_i A_i^*\frac{(2-\delta_m)^2\omega\epsilon_o}{a^2}\left[\frac{k_x}{k_{zi}\epsilon_i}\right]\left[\frac{k_x k_y^*}{k_{zi}^*(k_x^2+(k_y^*)^2)}\right]\frac{\sin^2 k_x x\,[\int\cos k_x x']^2}{|\cos k_{zi}(c_i-d_i)|^2}$$
$$\cdot\begin{cases}[\tilde{\eta}_{mUi}\sin k_{zi}(c_i-z) - j\cos k_{zi}(c_i-z)][\tilde{\eta}_{eUi}\sin k_{zi}(c_i-z) - j\cos k_{zi}(c_i-z)]^* & (i\le 0)\\ [\tilde{\eta}_{mLi}\sin k_{zi}(z-d_i) + j\cos k_{zi}(z-d_i)][\tilde{\eta}_{eLi}\sin k_{zi}(z-d_i) + j\cos k_{zi}(z-d_i)]^* & (i>0)\end{cases} \tag{4.47}$$

Similarly, for the reaction we have

$$R = E_x(k_y)H_z(-k_y) = B_i A_i\frac{(2-\delta_m)^2\omega\epsilon_o}{a^2}\left[\frac{k_x^2}{(k_x^2+k_y^2)\epsilon_i}\right]\left[\frac{k_y}{k_i^2}\right]\frac{\cos^2 k_x x\,[\int\cos k_x x']^2}{\cos^2 k_{zi}(c_i-d_i)}$$
$$\cdot\begin{cases}[\tilde{\eta}_{mUi}\cos k_{zi}(c_i-z) + j\sin k_{zi}(c_i-z)][\tilde{\eta}_{eUi}\cos k_{zi}(c_i-z) + j\sin k_{zi}(c_i-z)] & (i\le 0)\\ [\tilde{\eta}_{mLi}\cos k_{zi}(z-d_i) - j\sin k_{zi}(z-d_i)][\tilde{\eta}_{eLi}\cos k_{zi}(z-d_i) - j\sin k_{zi}(z-d_i)] & (i>0)\end{cases} \tag{4.48}$$

$$R = -E_z(k_y)H_x(-k_y) = B_i A_i\frac{(2-\delta_m)^2\omega\epsilon_o}{a^2}\left[\frac{k_x}{k_{zi}\epsilon_i}\right]\left[\frac{k_x k_y}{k_{zi}(k_x^2+k_y^2)}\right]\frac{\sin^2 k_x x\,[\int\cos k_x x']^2}{\cos^2 k_{zi}(c_i-d_i)}$$
$$\cdot\begin{cases}[\tilde{\eta}_{mUi}\sin k_{zi}(c_i-z) - j\cos k_{zi}(c_i-z)][\tilde{\eta}_{eUi}\sin k_{zi}(c_i-z) - j\cos k_{zi}(c_i-z)] & (i\le 0)\\ [\tilde{\eta}_{mLi}\sin k_{zi}(z-d_i) + j\cos k_{zi}(z-d_i)][\tilde{\eta}_{eLi}\sin k_{zi}(z-d_i) + j\cos k_{zi}(z-d_i)] & (i>0)\end{cases} \tag{4.49}$$

The integration of these terms on the cross section involves the same forms as for the

electric currents which have already been given.

4.2.4 Application to Finline and Suspended Finline

As with strips, the distribution of the field provides insight into the behavior of the structures. Two examples illustrate by showing the change in the field structure for finline without a substrate compared to the case where a dielectric substrate ($\epsilon_r = 2.2$) is added. These cases are shown in Figures 4.8 and 4.9

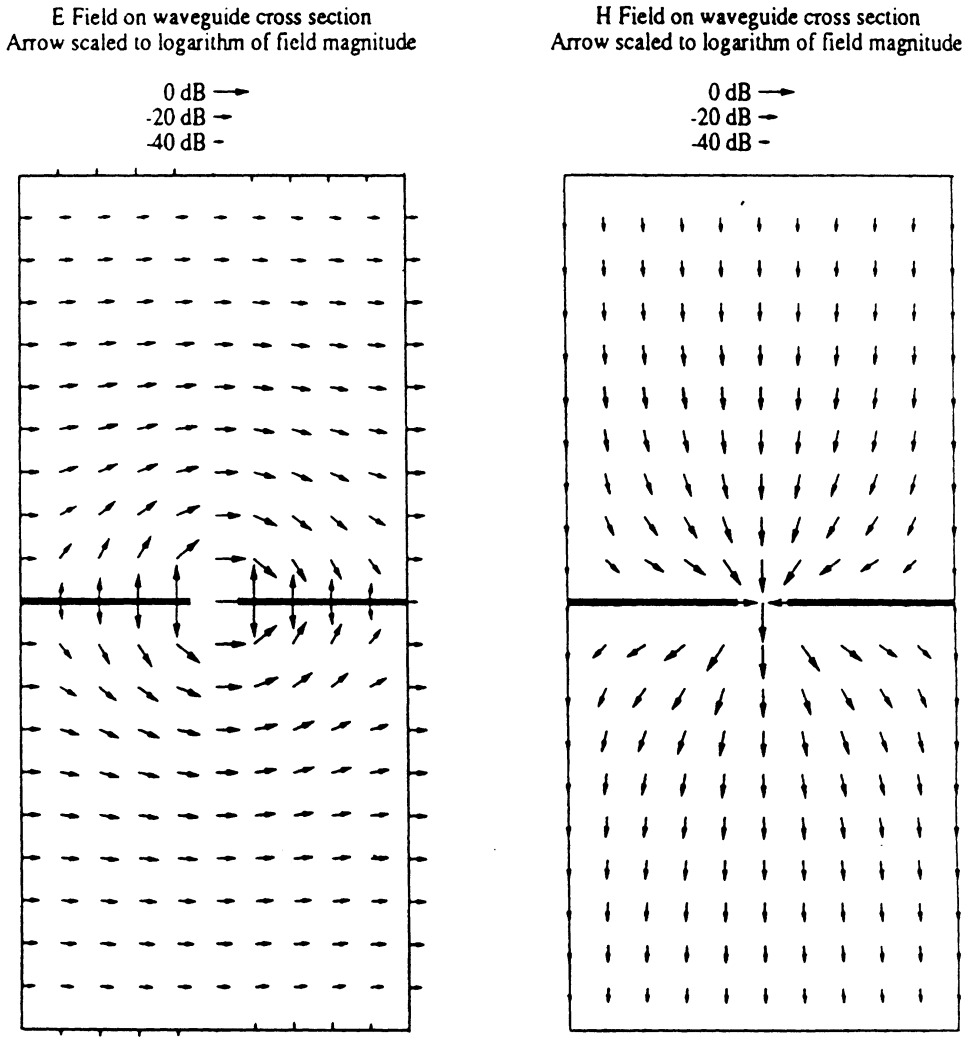

Figure 4.8: Finline field distribution for the dominant mode.

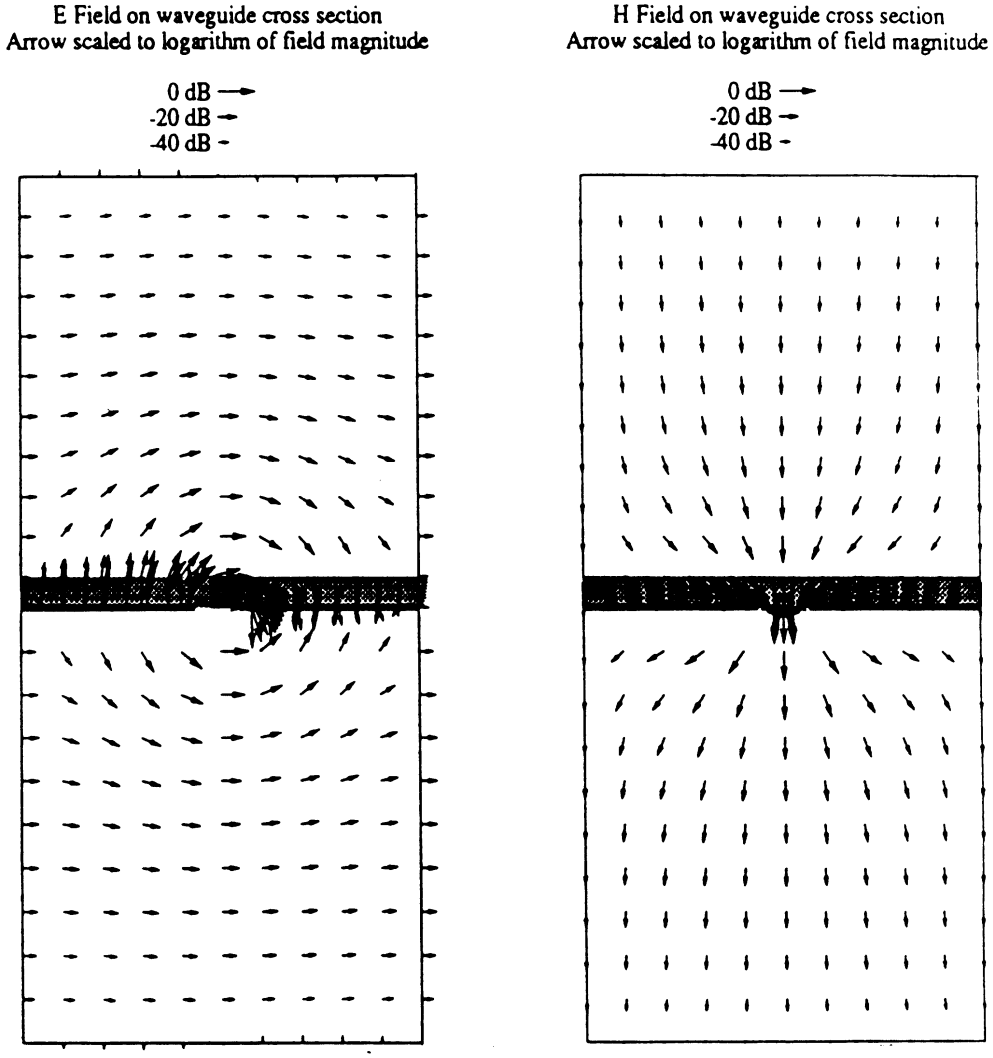

Figure 4.9: Suspended finline field distribution for the dominant mode.

4.3 Scattering from Pins in Rectangular Waveguide

The insertion of wires or pins through the ground planes is a technique used for many years to suppress parallel plate waveguide modes in stripline and for structural support. It is also a convenient way to form waveguides, cavities or isolation walls in stripline circuits. The experimental work discussed in Chapter VI is an example of the formation of a cavity where our particular need for this analysis will become evident. Other applications include the use of posts (or strips) in a rectangular waveguide as reactive elements in filter and matching networks [9, 10, 68] and for active device mounts and tuning elements [7, 24]. These types of applications have been the focus of most of the theoretical and experimental work appearing in the literature. In contrast, what we are interested in here is the effectiveness of a 'wall of wires' as a short circuit.

Analytical techniques in early works are primarily based on variational methods [54, 48, 45]. These approaches, however, become impractical for more than a few posts or posts with irregular spacings and are limited in accuracy at high frequencies. Even later works focussed primarily the study of three posts at most with emphasis on accuracy for post of relatively large diameter [43, 44, 3]. The emphasis on a limited number of larger posts is the opposite of what we require here where we will tend to use wires of small diameter and of greater number (and density). It is also evident that larger posts require more complex formulations and numerical treatments than is desirable for our situation[1]. Image theory or grating formulations as in [29] or especially [46] would seem to be appropriate for this problem but appear to be excessively complex and have limited potential for combination with other structures. The approach developed here will therefore be in spirit of the approach given in [43] which offers a good balance of simplicity and flexibility. In addition,

[1] Unless one already has a numerical code to treat the problem at hand, it is always desirable to use the simplest formulations which can produce results of sufficient accuracy and therefore can be quickly implemented. Another consideration is whether the resulting numerical model can be efficiently evaluated which usually, but not always, favors the simpler formulations.

the method will be even further simplified for wires of small diameter.

4.3.1 Reflection Coefficient Formula Derived from the Reciprocity Theorem

Consider a grid of wires appearing in the cross section of a rectangular waveguide as illustrated in Figure 4.10. Let us assume that the diameters of the wires are sufficiently

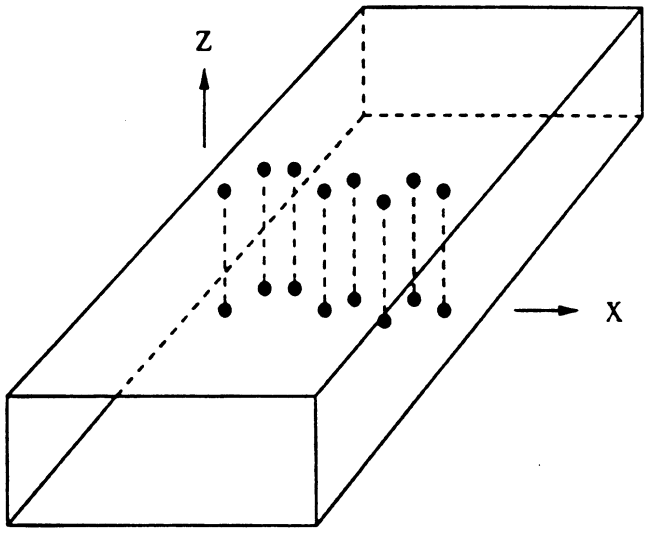

Figure 4.10: A grid of vertical wires in rectangular waveguide.

small to allow us to represent the current on the wire as an infinitesimal filament located at the center of the wire, i.e.,

$$\bar{J} = \hat{z} I_j \delta(x - x_j)\delta(y - y_j) \tag{4.50}$$

Furthermore, the waveguide dimensions are deemed to be such that all modes but the dominant one are cut-off. The current on the wires is also assumed to be excited by the dominant mode field which has no z variation. This fact justifies our assumption that the current also has no z variation. For multilayered structures this assumption would no longer be valid and the formulation must be made more general, however, it is sufficient here since the present need for this effort is restricted to stripline in support of Chapter VI.

We can derive a reflection coefficient representing the scattering of the dominant mode by an application of the Reciprocity Theorem [33] in the form

$$\iint \left[\bar{E}_a \times \bar{H}_b - \bar{E}_b \times \bar{H}_a\right] \cdot \hat{n}\, dS = \iiint \left[\bar{E}_b \cdot \bar{J}_a - \bar{E}_a \cdot \bar{J}_b\right] dV \qquad (4.51)$$

The locations of the surfaces defining the volume of integration are coincident with the side walls of the waveguide and two transverse planes on either side of the grid of wires. The transverse planes are assumed to be far enough away from the grid wires so that only the dominant mode has significant field strength. Now let the $\bar{E}_a$ and $\bar{H}_a$ fields represent the normalized fields of the dominant mode, incident from along the $-y$ axis, having no source terms within the volume of integration, i.e., $\bar{J}_a = 0$. Then these fields are given by

$$\bar{E}_a = \bar{E}_{10} = \hat{z} \sin(k_m x) e^{-jk_y y} \qquad (4.52)$$

$$\bar{H}_a = \bar{H}_{10} = -\hat{x} \frac{k_y}{\omega\mu} \sin(k_m x) e^{-jk_y y} \qquad (4.53)$$

where $k_m = m\pi/a$, $m = 1$ for the dominant mode and $k_y = \sqrt{k^2 - k_m^2}$. The $\bar{E}_b$ and $\bar{H}_b$ fields will be produced by the currents on the wires and radiate in both the $+\hat{y}$ and $-\hat{y}$ directions. If the currents on the wires, I_j, are those which are excited by the above incident field, then we can write

$$\bar{E}_b = \Gamma \bar{E}_{10} = \hat{z}\, \Gamma \sin(k_m x) e^{\pm jk_y y} \qquad (4.54)$$

$$\bar{H}_b = \Gamma \bar{H}_{10} = \pm\hat{x}\, \Gamma \frac{k_y}{\omega\mu} \sin(k_m x) e^{\pm jk_y y} \qquad (4.55)$$

where the top sign is for $y < y'$ and the bottom sign for $y > y'$. Equation (4.51) now reduces to

$$\Gamma = -\frac{\iiint \bar{E}_{10} \cdot \bar{J}\, dV}{2 \iint \bar{E}_{10} \times \bar{H}_{10} \cdot \hat{y}\, dx dz} \qquad (4.56)$$

Note that to obtain this result, the surface integrations over the walls of the waveguide were found to be zero, since the tangential $\bar{E}$ fields are zero there for perfectly conducting

walls and also the surface integral over the waveguide cross section on the $+y$ side of the wires evaluates to zero. The remaining integrations are readily performed to give

$$\Gamma = -\frac{2\pi f\mu_o}{a\sqrt{k^2-(\pi/a)^2}}\sum_j I_j \sin(\pi x_j/a) \tag{4.57}$$

We thus need only determine the unknown currents from which the reflection coefficient is produced by this simple summation.

4.3.2 Method of Moments Formulation

In the previous section, the assumption of constant current on the z dimension has already been stated. In the parlance of the Method of Moments this is a 'pulse' basis function which in effect has reduced the problem from three dimensions to two. For small diameter wires as treated here, the problem can be further reduced to one dimension, if the grid of wires are all contained in a transverse plane, however, this produces no significant advantage.

Since we have previously found the dyadic Green's functions for homogeneously filled rectangular waveguide (section 2.4), we can use Equation (1.33) to derive the electric fields in the waveguide. With the current as stated by Equation (4.50), the z component of the $\overline{\mathrm{E}}$ field produced by the j^{th} current filament is given by:

$$E_z = -\frac{\omega\mu_o}{a} I_j \sum_{m=1}^{\infty} \frac{1}{k_y} \sin(k_m x)\sin(k_m x_j) e^{-jk_y|y-y_j|} \tag{4.58}$$

It remains then, to find the set of I_j's which produce a total electric field that satisfies the boundary conditions on the wires, specifically $E_z + \hat{z}\cdot\overline{\mathrm{E}}_{10} = 0$. The simplest way to enforce this condition is to use point matching on the surface of the wires which is to use a delta weight function. Although found to produce identical results, a two point matching scheme was used to provide symmetry balance in which the field is taken as the average

over two points of the wire surface. The resulting expression for the field is

$$E_{zi} = -\frac{\omega\mu_o}{a} I_j \sum_{m=1}^{\infty} \frac{1}{k_y} \sin[k_m(x_i \pm r_i)] \sin(k_m x_j) e^{-jk_y|y_i - y_j|} \tag{4.59}$$

where i is an index indicating the field evaluation points and r_i is the radius of the i^{th} wire. The $\pm r_i$ notation is taken to imply the averaging of the field contributions at these points. The combined field expression can be written in matrix form as

$$[\mathbf{Z}_{ij}][\mathbf{I}_j] = [-\mathbf{E}_{10,i}] \tag{4.60}$$

which is solved by matrix inversion for the unknown currents.

4.3.3 Validation

In order to investigate the validity of this formulation we first compare to the data of Marcuvitz [48] for single posts. The accuracy of this data is well established for diameter to waveguide width ratios (d/a) of up to 0.25. The equivalent circuit for the single post is as shown in Figure 4.11. From this equivalent circuit we can convert the values given

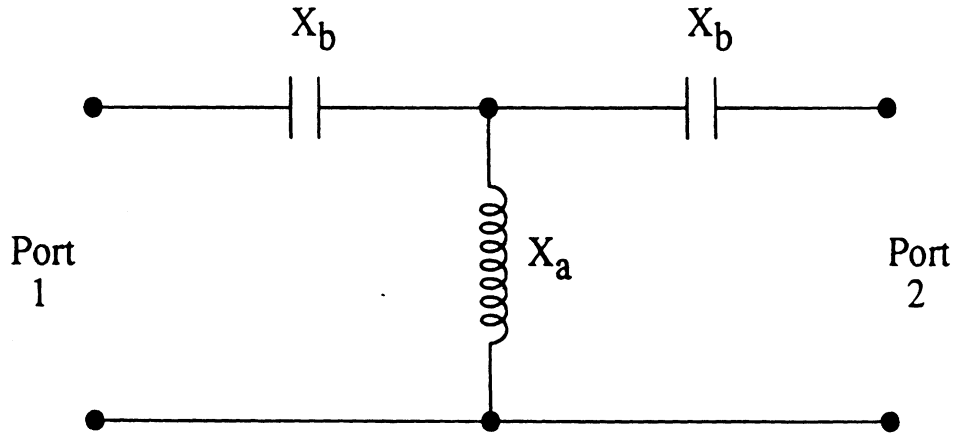

Figure 4.11: Equivalent circuit for single post in rectangular waveguide.

by the formula in [48] to a reflection coefficient which can be compared to the results of Equation (4.57). Since our formulation is a simplified version of the method found in [43],

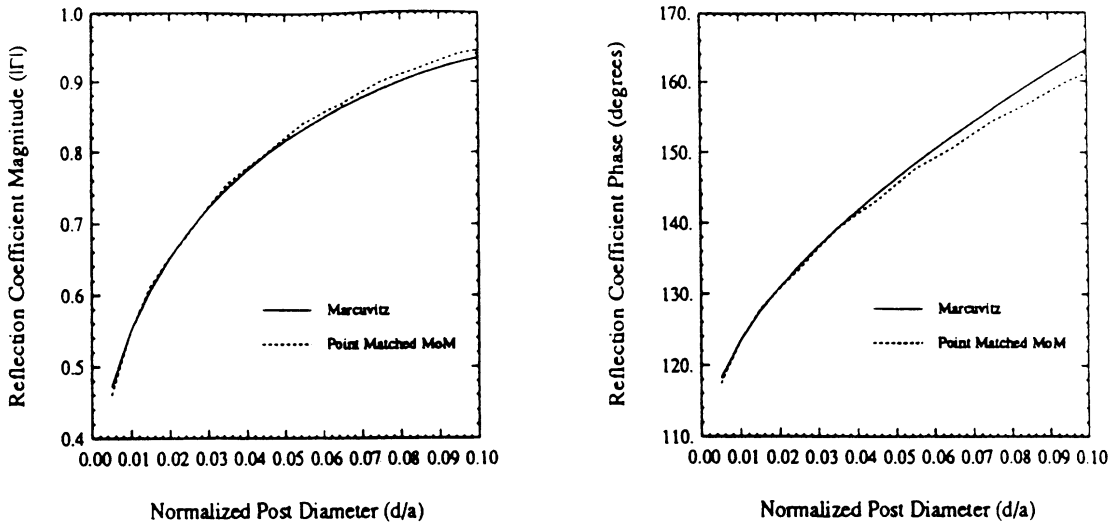

Figure 4.12: Magnitude and phase of reflection coefficient for a single conducting post in rectangular waveguide. Point match Method of Moments (MoM) results compared to the data of Marcuvitz [48] ($\lambda/a = 1.4$).

we would not expect the range of its accuracy to extend as far; thus, we will limit the range of our discussion to $d/a < 0.1$. Moreover, we are specifically interested in thin wires with diameters (d) much smaller $0.1a$, on the order of $0.02a$, the approximate value to be used later in Chapter VI. The results over this range is given in Figure 4.12 which shows the magnitude and phase of the reflection coefficient of a single post in rectangular waveguide as compared to Marcuvitz's data. As can be seen, the comparison is excellent with a maximum phase error of less than four degrees for the largest wire diameter. Thus, we have a first indication of the accuracy of the method.

Before proceeding to further results, it is instructive to further examine the single post case. The behavior of the element values of the equivalent circuit follow the curves illustrated in Figure 4.13. By evaluating the input impedance for one of the ports with the second port matched and plotting it on the Smith Chart as in Figure 4.14, we see that the input impedance progresses from inductive to capacitive as the diameter is increased. We also note that the single post makes a surprisingly good short circuit at a diameter as

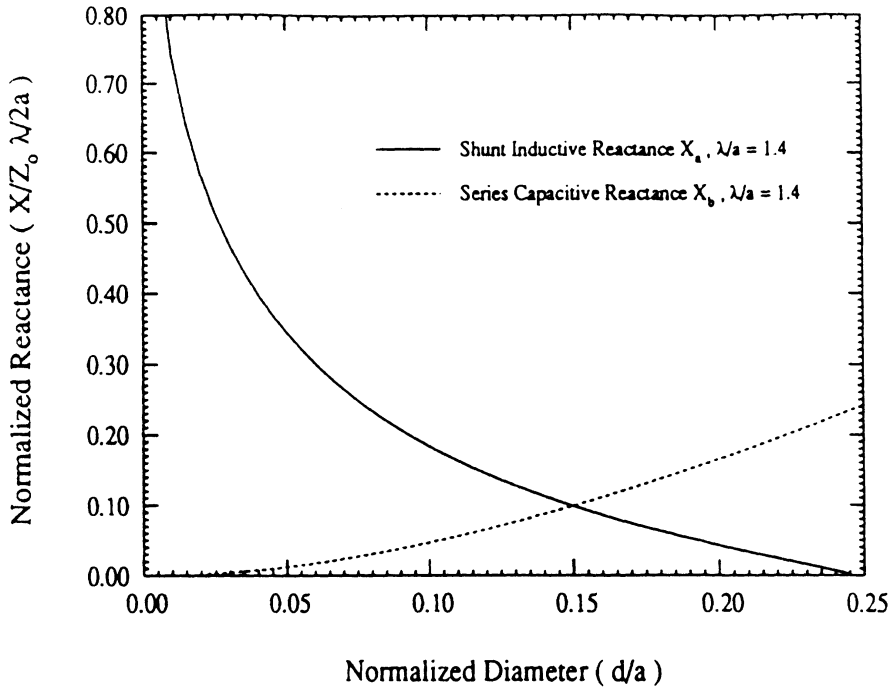

Figure 4.13: Behavior of element values for the equivalent circuit given by Marcuvitz [48] ($\lambda/a = 1.4$).

small as $d/a = 0.15$, the diameter at the 180° phase shift point.

Not surprisingly, as more pins are added the wires form an even better short circuit producing ever higher shunt susceptance values. For example, Figure 4.15 shows how the shunt susceptance value increases rapidly as the number of equally spaced wires is increased. In this case we have lumped the reactive behavior of the grid into a single shunt element on the transmission line, i.e., replace the series capacitors of the equivalent circuit of Figure 4.11 with shorts and the shunt inductor with a general reactive element. (Note also that all wires in this investigation will be located in the same transverse plane of the waveguide which is the reference plane for the equivalent circuits.) It is interesting to observe that the normalized pin diameter (d/a), where the susceptance crosses over from inductive to capacitive, depends on the number of wires and generally moves toward smaller post diameters as the number of posts increases. This suggests that for a given

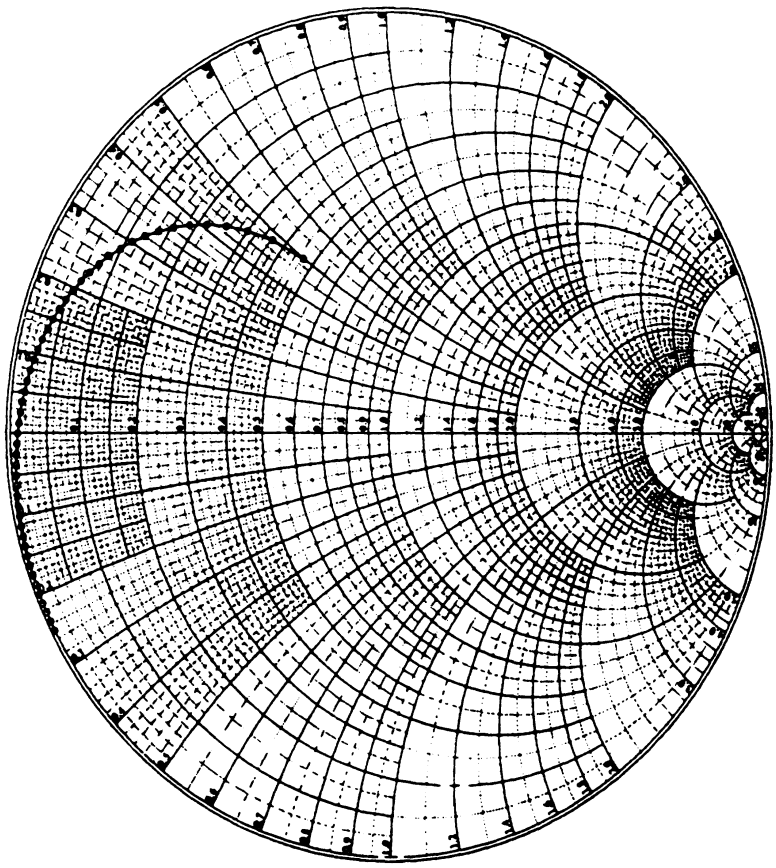

Figure 4.14: Input impedance as a function of post diameter with a matched load port. Post diameter increases in the counter-clockwise direction from $d/a = .005$ to $d/a = .25$ in .005 steps, demonstrating the transition of the input impedance from inductive to capacitive.

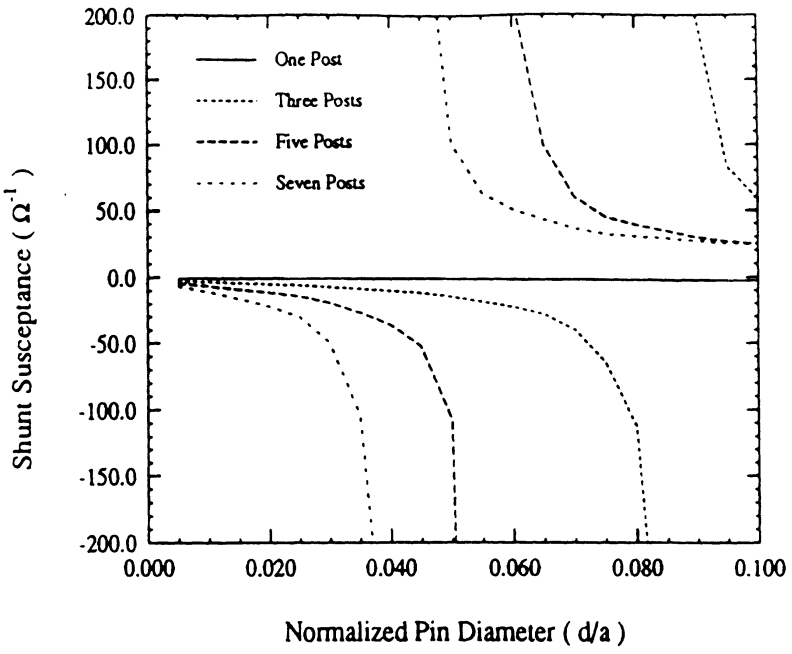

Figure 4.15: Shunt susceptance behavior for up to seven wires placed evenly spaced across waveguide cross section.

number of wires equally spaced across the guide, there is an optimum post diameter which most nearly produces an effective short circuit. Similarly, it implies that additional posts do not necessarily improve the capability to simulate a true short circuit at the reference plane.

With these large shunt susceptance values, the real part of the input impedance becomes negligible so that the network can be treated as a one port terminated with this reactive element. As such, the one port can also be modelled as a true short circuit located at a distance from the reference plane determined by the calculated value of susceptance and the transmission line equation:

$$B = \cot(\beta l) \tag{4.61}$$

where B is the susceptance, l is the distance from a true short to the reference plane and $\beta = 2\pi/\lambda_g$, with λ_g the guided mode wavelength. The argument βl is the phase angle of the reflection coefficient for the line. The accuracy with which we can determine this angle

is a measure of how well the grid of wires is treated by the simplified model, thus becoming the focus of the experimental results and comparisons to follow.

To further confirm the accuracy of this method, measurements were made with an HP8510 Network Analyzer on various combinations of wires in X-band waveguide (0.4×0.9 inches) at 12 GHz. A series of seven equally spaced holes where drilled in a line on the broad wall, transverse to the axis of a section of waveguide. The holes themselves were small enough in diameter and sufficiently spaced so that they did not significantly perturb the propagation of the fundamental mode, a fact verified by subsequent measurements. The reference plane was established and the fixturing de-embedded by performing a one-port calibration with two short circuited waveguide sections of different lengths and a precision waveguide load. To make the measurements, different patterns of wires were inserted through selected holes and the reflection coefficients recorded. The patterns used will be denoted by a series of ones and zeroes, for example the case of the single centered post would be designated by the pattern '0001000'.

The results of one set of measurements are shown in Figure 4.16. In this and the following charts, data marks correspond to the three wire diameters used ($d = .025, .033, .039$ in.), the filled-in marks representing the corresponding measured points. As can be seen by drawing a line from the center of the chart through the various points, the accuracy of the predicted phase angle is quite good. Similar results are found for wires in pairs as shown in Figure 4.17.

Figure 4.18 is an experimental demonstration of the case discussed above where the number of pins is progressively increased. This is perhaps the worst case where errors in phase angle are on the order of five degrees for some points. Some of these errors are attributable to experimental error due to variables such as mis-alignment in the transverse plane and tilting of the wires in the holes, which necessarily must be larger to accommodate

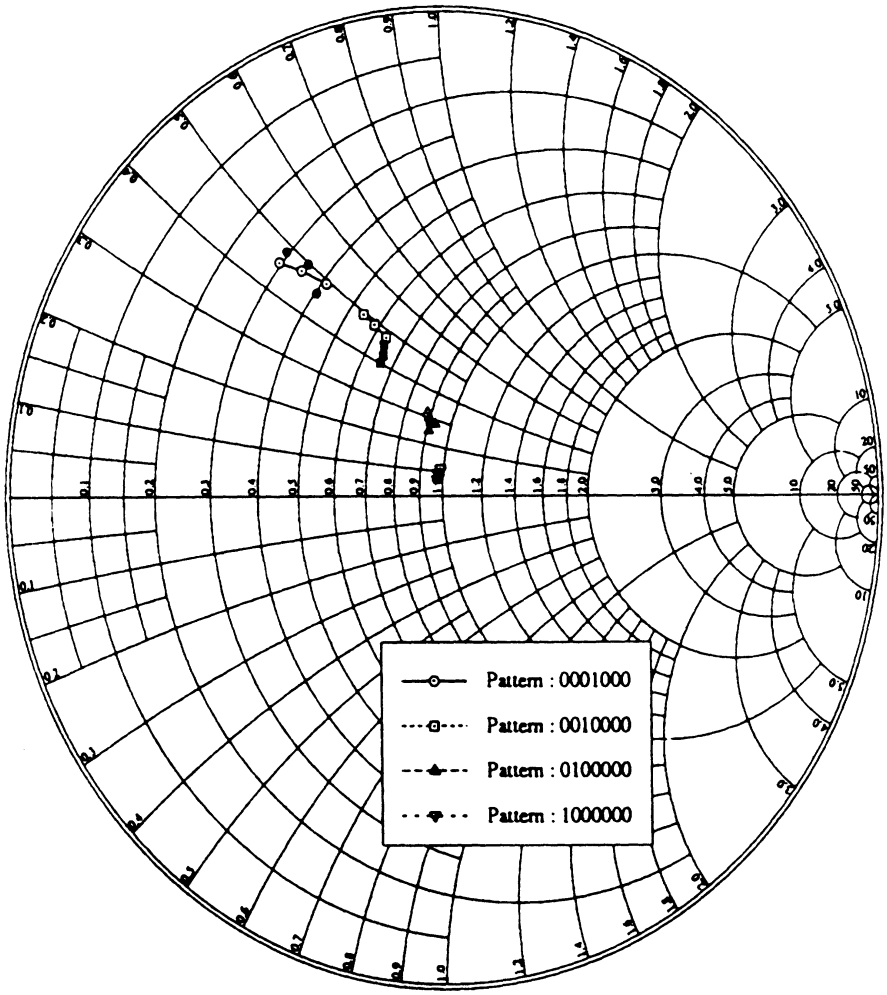

Figure 4.16: Reflection coefficient measurements for a single post at various offsets from the centerline compared to predictions from the simplified model. Wire diameters (d = .025, .033, .039 in.) increase in the counter-clockwise direction.

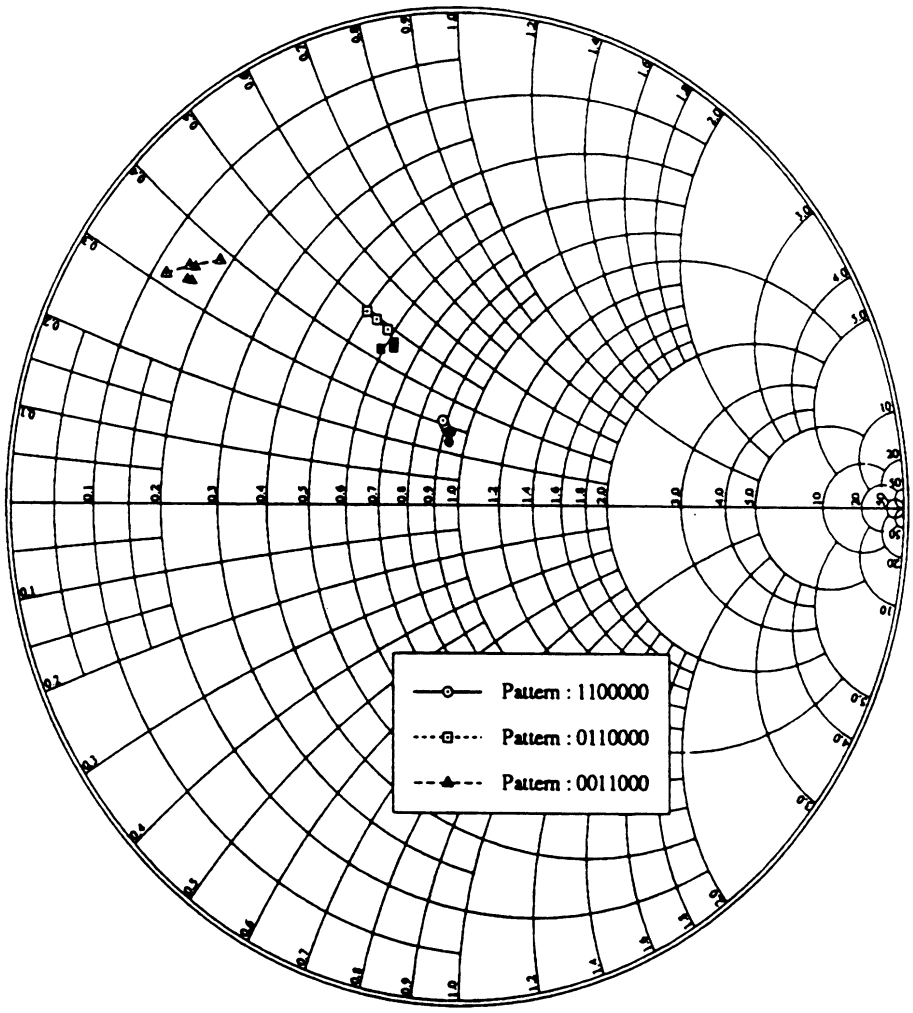

Figure 4.17: Reflection coefficient measurements for pairs of wires at various offsets from the centerline compared to predicted values. Wire diameters (d = .025, .033, .039 in.) increase in the counter-clockwise direction.

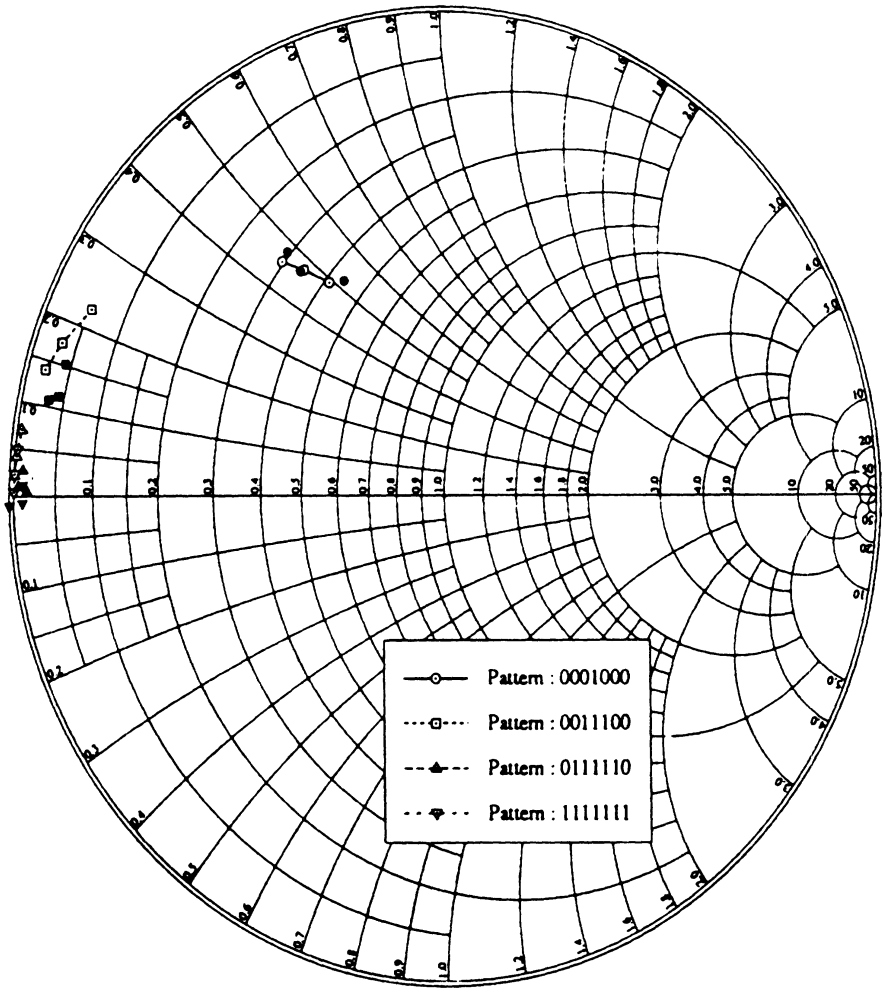

Figure 4.18: Measured reflection coefficients for centered wire grids of equal spacing and increasing number. Wire diameters (d = .025, .033, .039 in.) increase in the counter-clockwise direction.

different diameters. Nevertheless, the overall results suggest that the method is capable of predicting the phase to within a few degrees.

The final plot, Figure 4.19, is an illustration of a case very similar to one which will

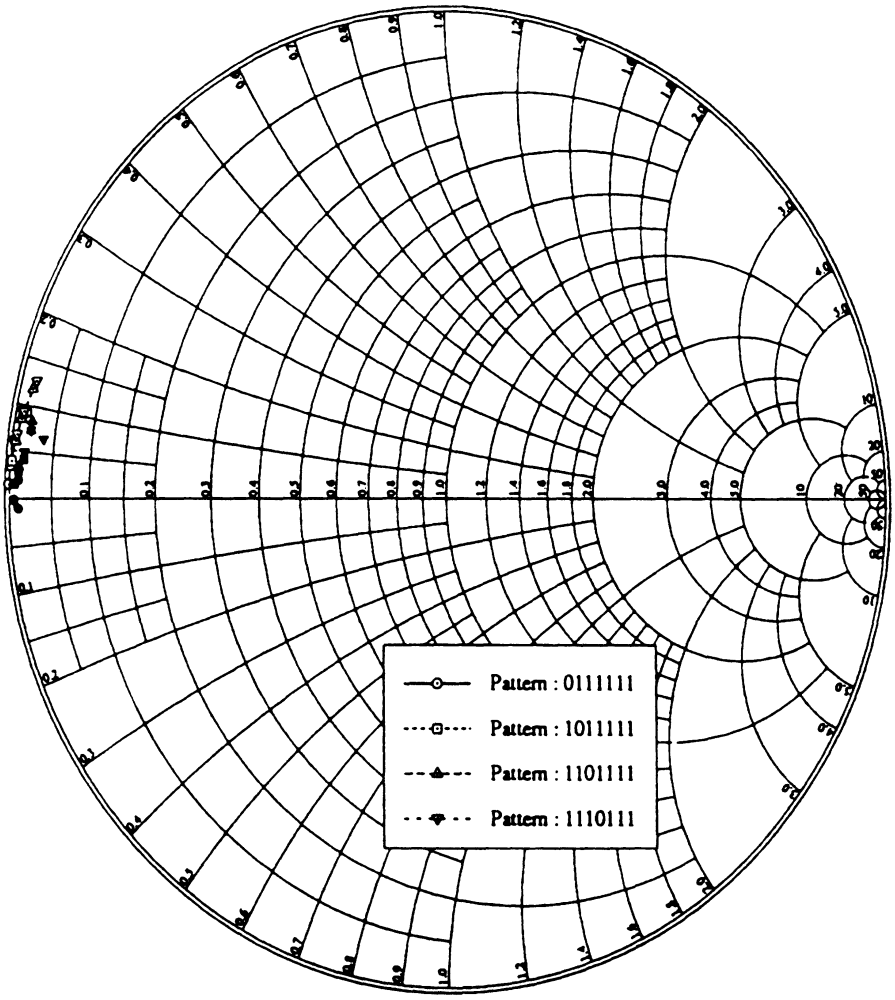

Figure 4.19: Measured and predicted reflection coefficients for wire grids with a single pin missing in the sequence. Wire diameters (d = .025, .033, .039 in.) increase in the counter-clockwise direction.

be encountered later. In this instance, an evenly spaced row of wires were installed across the waveguide cross-section, however, one pin was removed at various locations in the sequence. As will be seen in Chapter VI, this type of approach is used to allow a strip to pass through the pin curtain. The ability to predict the reflection coefficient for this case

is very important for certain situations as will be seen. Although the comparison for this case looks reasonable, it is pushing the limits of the experimental errors involved with the fixture. However, a consideration of the previous results leads to the conclusion that the results are reliable.

4.4 Summary and Conclusions

In summary, we have seen how problems with uniformity in one dimension can be analyzed with a high degree of accuracy. The uniformity allows the structure to be represented by a single modal series which can be numerically evaluated efficiently.

The use of impedance boundary conditions and a LSE and LSM expansion of the fields greatly simplifies the modelling of multilayer substrates and superstrates. This particularly facilitates the computation of fields throughout the structure since most of the evaluation can be done analytically. Application to shielded strip and slot geometries yields both reliable quantitative information as well as visual representations of the fields providing insight into the behavior of the structure.

A simple model for scattering from wires in rectangular waveguide has also been developed. The simplicity of the model is in contrast to methods discussed in the literature which are oriented towards fewer posts with relatively large diameters. The present method, however, emphasizes posts of greater number and smaller diameter. Experimental results were obtained to verify the modelling ability of the technique. The need for this model in the context of the present work appears in Chapter VI.

CHAPTER V

COUPLING THROUGH STRIP-FED SLOTS

A class of structures which couple from one guiding structure to another through an aperture is important in microwave circuits, aside from the radiating slot. In fact, for antennas, the coupling of waveguide to waveguide through a narrow slot in a common wall has been used for many years in the design of corporate feed networks for slotted waveguide arrays. As discussed in Chapter I, the case of coupling between shielded strips in a similar manner is becoming equally important in current and future systems, including similar feed networks. In this chapter, the analysis of these types of couplers will be presented along with experimental verification of the numerical results to demonstrate the applicability of these techniques to microwave and millimeter wave devices.

5.1 Network Analysis

The basic structure of the coupler to be discussed is as shown in Figure 5.1. Variations on this geometry include cases with microstrip lines on the same side of the slot; multi-layered substrates/superstrates; reverse couplers where the lines exit on the same wall; additional parallel slots and lines; and 3- and 4-port networks, among others, but all can be analyzed using the same approach.

Integral equations have been formulated for this problem in Chapter I and are solved as outlined in Chapter III for currents on the slot and strips. Therefore, in this chapter

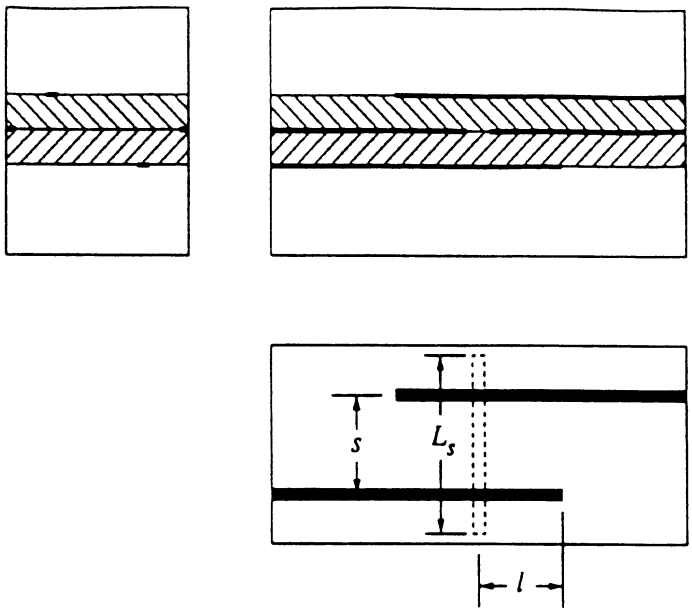

Figure 5.1: Geometry of basic coupler.

we need only discuss the interpretation of these currents in order to extract the network parameters which characterize the coupler's behavior.

Solutions for the currents are found with even and odd gap generator excitations at the line ends. These are sufficient to characterize the two-port problem since all excitations can be decomposed into even and odd components. The approach can be generalized using N-port network analysis [14, pp. 157-158] but this aspect is beyond the focus of this work.

From the even and odd currents on the microstrip lines, even and odd impedances are found by measuring the relative distance (d) from a standing wave maximum to the location of the slot as illustrated in Figure 5.2. We can also estimate the guided wavelength for the even and odd modes from the standing wave patterns by measuring the spacings between minima or maxima. If the materials are lossless, as we typically can assume for most microwave circuit applications[1], the expression for the reflection coefficient referenced

[1] For slightly lossy structures, the estimation of the attenuation constant can be easily determined from the ratios of successive current maxima or minima[55]. For larger losses the situation is more complex, since not only the envelope of the standing wave current but also the spacing between maxima and minima vary along the line [27, sec. 5.4]. In this case one must resort to a parameter estimation scheme to find the

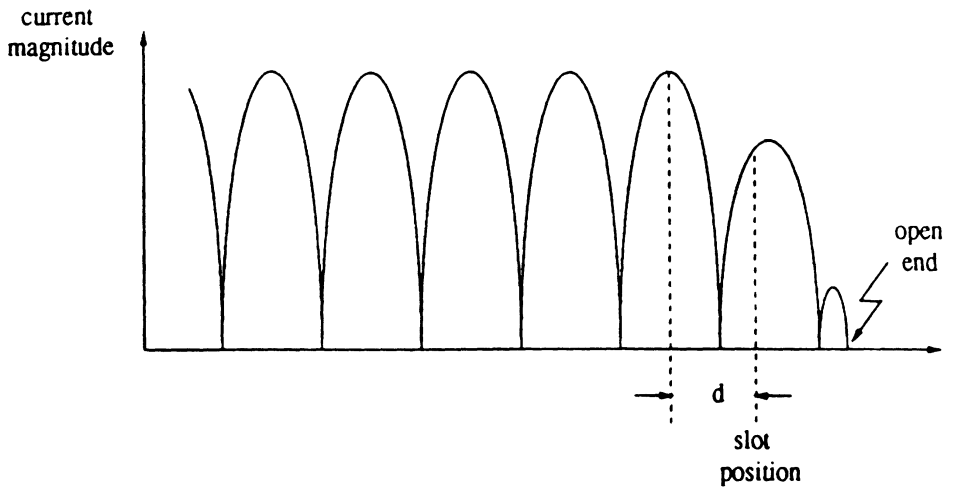

Figure 5.2: Measurement of location of current peak relative to the slot for standing wave calculation.

to the slot reduces to

$$\Gamma = -e^{j4\pi d/\lambda_g} \tag{5.1}$$

which produces an impedance according to

$$Z = \frac{1+\Gamma}{1-\Gamma} \tag{5.2}$$

The even and odd impedances are then combined to form the Z-parameters which, in the symmetric case studied here, are given by the simple expressions:

$$Z_{11} = \frac{Z_o + Z_e}{2} = Z_{22} \tag{5.3}$$

$$Z_{21} = \frac{Z_o - Z_e}{2} = Z_{12} \tag{5.4}$$

Finally, the even and odd impedances may be combined to produce S-parameters through the transformations:

$$S_{11} = \frac{Z_{11}^2 - Z_{21}^2 - 1}{Z_{11}^2 + 2Z_{11} - Z_{21}^2 + 1} = S_{22} \tag{5.5}$$

$$S_{21} = \frac{2Z_{21}}{Z_{11}^2 + 2Z_{11} - Z_{21}^2 + 1} = S_{12} \tag{5.6}$$

optimum fit to the current with the attenuation and propagation constants as parameters.

which are used to characterize the coupling behavior.

Before proceeding, the limitations of this technique should be noted. Transmission line analysis of the current in this way assumes that there is only one propagating mode on the line at some distance from the discontinuities. For the shielded structures treated here, this requires that the cross-sectional dimensions of the feeding microstrip lines be such that all higher-order modes are cut-off or, looked at another way, a given cross-section restricts the maximum frequency for which circuit parameters can be reliably produced with this technique. Also, in order to estimate the phase constant, the line must have a minimum length, typically on the order of the wavelength. Moreover, for good numerical stability of the results over a wide range of parameters, it has been found useful to average a number of estimates on a line approximately three wavelength long, discarding the maximum and minimum values. This restriction demands more unknowns and hence greater computation time, however, the results are quite reliable. The alternative method based on the Reciprocity Theorem developed in Chapter VI, overcomes these limitations at the expense of a more complex formulation.

5.2 Fixture Design

To verify the results, we have designed and constructed the fixture shown in Figure 5.3. Sample substrates with various line and slot dimensions are installed in the fixture in different combinations to allow frequency response measurements. A number of circuit boards were made: One set of boards was double-sided with a microstrip line etched to a certain length relative to a slot etched in the ground plane on the opposite side. The second set was one-sided boards designed to be held against the boards of the first set by the fixture, with microstrip lines of corresponding lengths. The lines are excited by Eisenhart connectors which provide a reasonable match over a broad frequency range, even when the contrast in ϵ_r is high ($\epsilon_r = 1$ for the connector, $\epsilon_r = 10.6$ for the substrates). In our case

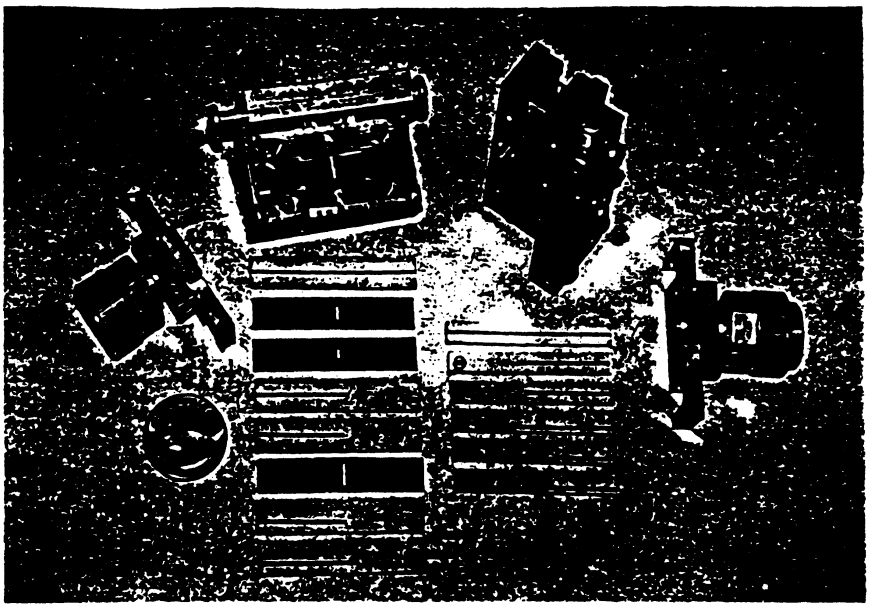

Figure 5.3: Photograph of coupler fixture assembly.

this is partly a result of the good match in dimensions between the boards and the tip to outer conductor spacing of the connector. Another critical factor is the transition from the outer conductor of the connectors to the ground planes of the boards which must be carefully designed. The match at the connectors was optimized to minimize the launching discontinuity, allowing us to avoid the necessity for TRL [34] or similar de-embedding schemes which require additional and more complex fixturing.

5.3 Numerical and Experimental Results

A coupler with the geometry of Figure 5.1 was analyzed using the above techniques. The parameters which can be varied in this design are numerous, consequently, only a few variations will be presented here. In all cases, although not required in general, symmetric geometry was maintained to simplify the even and odd mode analysis, as discussed above. Also, in all cases the cross-section for the cavity was 0.25×0.25 inches; the substrates were 0.025 inches thick with $\epsilon_r = 10.6$; and the slot and line widths were 0.025 inches. The

cavity length was fixed at 2.0 inches for the measurements and varied for the numerical results to allow an approximately constant 3λ feed-line length. This dimension does not affect the results since for all frequencies considered here, the cavity is below the cutoff frequency of the higher order microstrip modes and the reference plane was fixed at the location of the slot.

To illustrate the behavior of the coupler, we first examine the influence of various parameters at fixed operating frequencies. The effect of the line stub length (l) is shown in Figure 5.4. It can be seen that the stub is initially too long for an ideal match at this

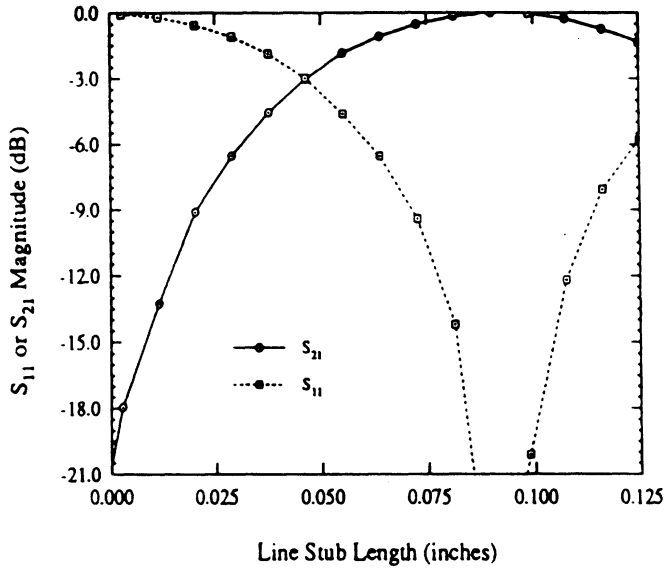

Figure 5.4: Effect of the line stub length (l) on S_{21} and S_{11} magnitudes ($s = 0, L_s = 0.25$ inches and $f = 12.0$ GHz).

frequency. However, as the stub is progressively shortened, a certain length "matches" the two port coupler and with further shortening the match gets progressively worse. We can interpret this effect by examining the equivalent circuit shown in Figure 5.5. Variation of the stub length has the effect of changing the position of the current maxima (virtual shorts) and minima (virtual opens) on the lines relative to the slot, thus varying the degree of coupling through the slot represented by the coupling transformers. Consequently, the

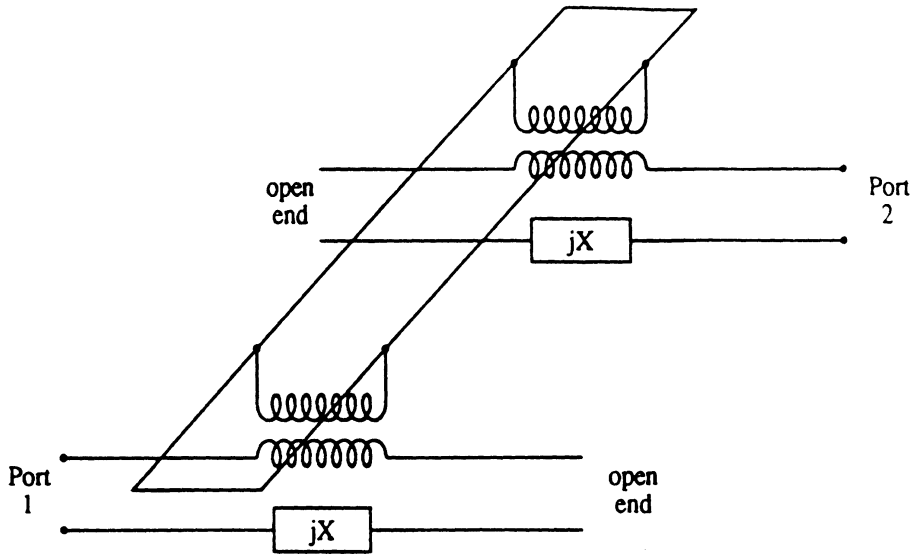

Figure 5.5: Equivalent circuit for a 2-port coupler.

peak coupling occurs when line stub length places a current maximum below the slot or lengths in odd multiples of $\sim \lambda/4$. The opposite effect occurs when the line stub is approximately in multiples of $\lambda/2$ in length so that there is a virtual open circuit beneath the slot, in which case there would be very little coupling between the line and slot.

A similar effect is observed for variations in slot length (L_s) as illustrated in Figure 5.6. Again using the transmission line analogy, one can interpret this effect by transforming the impedances at the ends of the slot to the center. These end impedances are nearly short circuits, the difference being due to fringing fields which extend beyond the ends of the slot line, fully accounted for by the full-wave analysis. At the matching length, the resulting transformed reactances at the center cancel the reactance associated with the junction, thereby matching the two ports. As the slot becomes very short, the field in the slot is effectively "short circuited"; thus, coupling is reduced. S_{21} then tends to zero while S_{11} approaches unity (since the structure is closed and assumed lossless). All of these effects would be expected to repeat as the slot length increases in multiples of λ, however, for the case studied here, the maximum slot length is limited by the dimensions of the shielding

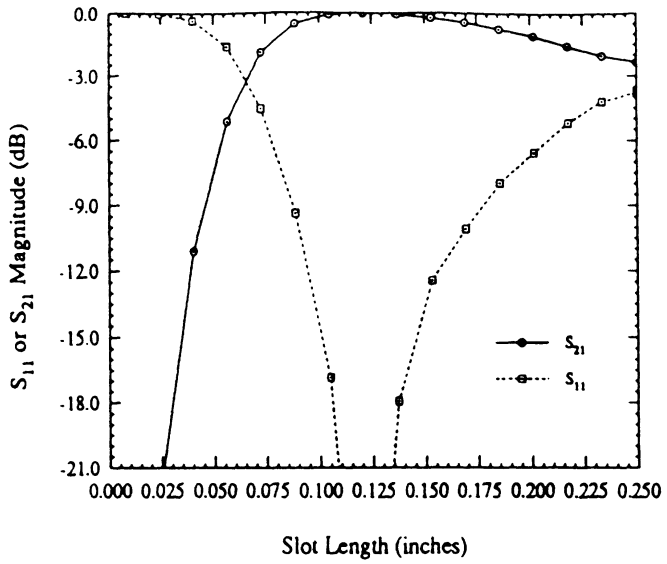

Figure 5.6: Effect of the slot length on S_{21} and S_{11} magnitudes ($s = 0, l = 0.049$ inches and $f = 18.0$ GHz).

package which have been chosen to allow propagation of only the dominant microstrip mode.

To generate a frequency response, the programs are run at each frequency of interest and the slot and line lengths are varied to form a parametric database. The database is then scanned and interpolated to assemble frequency response plots as functions of the geometric parameters. Measurement of one of the assemblies is shown in Figure 5.7 in comparison to corresponding numerical results for a stub length of $l = 0.115$ inches. The position of the high frequency corner of the response was found to be very sensitive to the length of the line stub. As discussed above, this corner is controlled by the length at which the stub is approximately $\lambda/2$. Since the effective dielectric constant for the microstrip is approximately $\epsilon_{r,eff} = 7.8$ at 17.0 GHz, a null is predicted in the coupler response for that neighborhood, in good agreement with the results shown. The error bar on the high end indicates the sensitivity of the high frequency corner to a ± 5 mil error in line stub length which is well within the expected tolerance errors for positioning the stubs relative

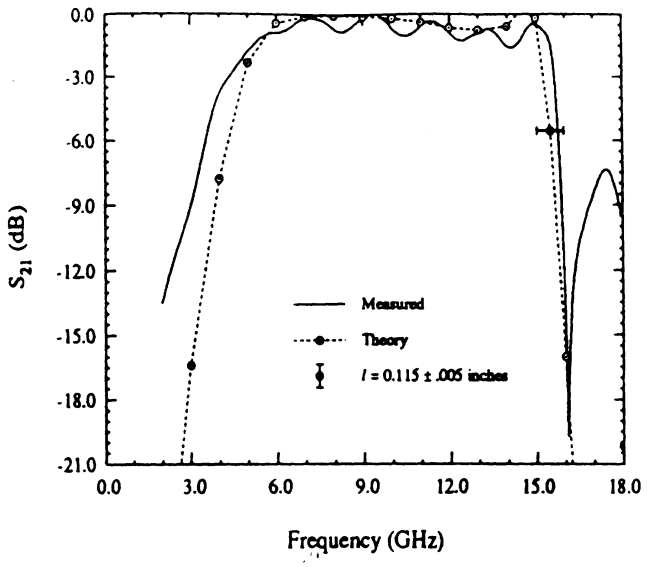

Figure 5.7: Comparison of theory and experiment for S_{21} magnitudes with $s = 0, l = 0.115$ in., $L_s = 0.250$ inches. The error bar indicates the influence on the high frequency corner of a $\pm.005$ inch change in stub length.

to the slot. In view of the above, we conclude that the theoretical results are in excellent agreement with the experimental data. In fact, we were able to move the upper board slightly toward the slot to extend the stub length somewhat, shifting the high corner to a lower frequency as expected. However, this also created problems with the match at the Eisenhart microstrip launchers so these results are not shown.

The 'sidelobe' which can be seen at the high frequency end, is also attributed to tolerance errors for the line stub lengths. A difference in lengths would produce multiple nulls in the response at the high end resulting in undesirable sidelobes in between. Because of the high sensitivity to line length, owing in part to the high dielectric constant, the amplitude and span of the sidelobe is a strong function of the relative line stub lengths, a fact which can be observed when the boards are slightly shifted as described above. The sidelobes do not appear in the theoretical result since a difference in stub lengths between the upper and lower lines introduces an asymmetry which has not been included in the

current numerical model and contradicts some of the assumptions stated for the network analysis. A more general model can be produced by extending the network analysis to the non-symmetric case.

The ripple in all the measurements can be shown to result from mismatch at the microstrip launchers. The measurements are particularly sensitive to this connection because of the high dielectric constant of the substrate. Ripple occurs to various degrees throughout the measurements and is also influenced by small air gaps between the connector assembly, fixture and substrates. It could be removed by more sophisticated de-embedding techniques, however, this requires additional fixtures. Nevertheless, the ripple shown in the results presented here is not substantial and does not significantly interfere with the fundamental behavior of the devices. Also, the broadening of the low frequency response is typical in the measurements. We were not able to identify a direct cause for this effect, however, we suspect that it is related to the fixture/connector interface, since we have not de-embedded these transitions. We also postulated that some of the anomalies might be caused by the side-wall grooves in the fixture which hold the double-sided board in place. This possibility was eliminated, however, by installing movable side-wall shorts which are visible in Figure 5.3.

The remaining discrepancy is perhaps a slight additional loss found in some of the measured results. To de-embed the losses for the structure, a through line was measured and the remaining measurements were post-processed to compensate for conductor and dielectric losses on the microstrip lines. This process does not correct for losses associated with the slot including both conductor and dielectric losses, additional losses on the cavity walls, and losses due to the added line lengths. The remaining differences are attributed to these factors together with measurement errors and are judged to be within acceptable limits.

Measurements on a different line stub length are shown in Figure 5.8 again showing

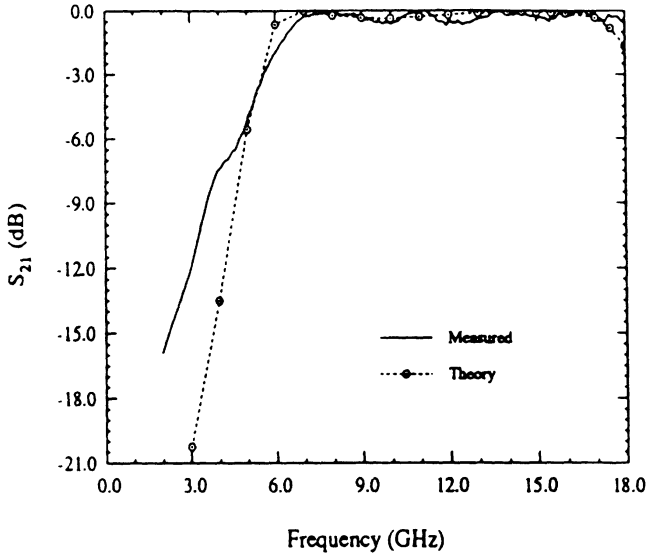

Figure 5.8: Comparison of experiment and theory for S_{21} magnitudes with $s = 0, l = 0.080$ in., $L_s = 0.250$ inches, illustrating the control of the high frequency corner with the line stub length by comparison to Figure 5.7.

good agreement with the theoretical results. In this case, the shortening of the stub length has moved the high frequency corner out of the range of the measurements. What is interesting to note about this case is that the low frequency corner of the response is quite insensitive to this change in stub length. Also of particular interest is the wide bandwidth of this transition.

Figure 5.9 illustrates the effect of shortening the slot length. One consequence is reduced coupling in the passband which was also demonstrated in Figure 5.6. We also see in this result, some movement of the high frequency null due to a shortening of the line stub length.

The final plots, Figures 5.10 and 5.11, show the influence of the line separation parameter (s) on the frequency response. These figures are to be compared to Figures 5.7 and 5.8, respectively, and in general show a narrowing of the frequency passband as

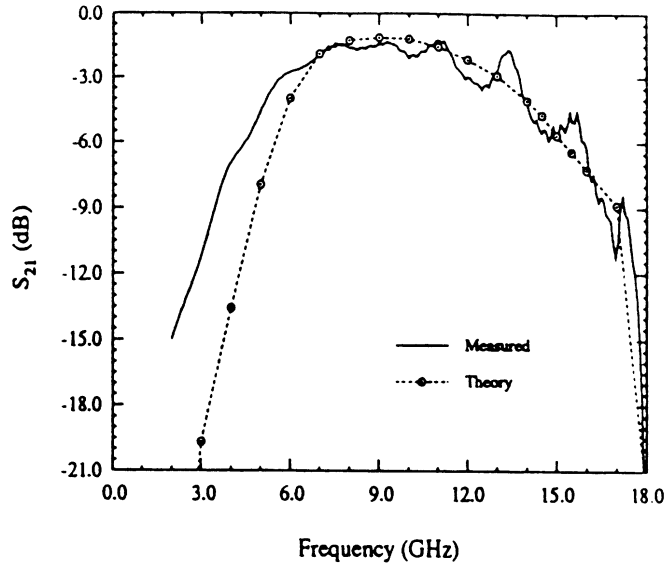

Figure 5.9: Experiment and theory for S_{21} magnitudes with $s = 0, l = 0.110$ in., $L_s = 0.153$ inches, showing the effect of shortening the slot length.

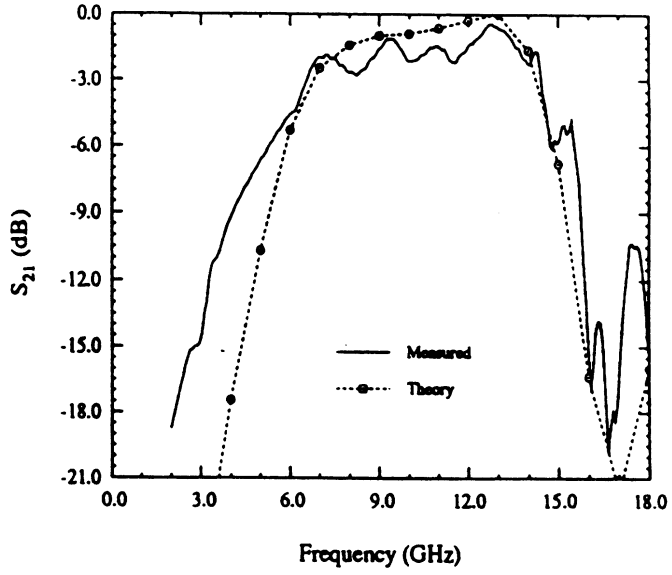

Figure 5.10: Comparison showing the effect of line separation with $l = 0.115$ in., $L_s = 0.250$ in. and $s = 0.125$ inches.

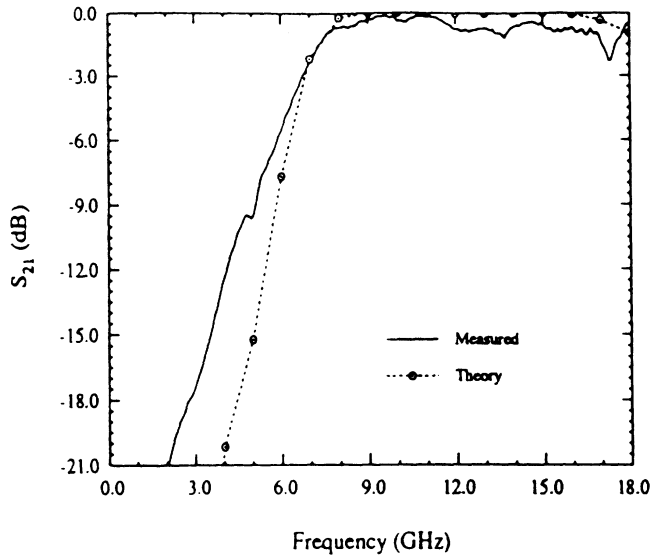

Figure 5.11: The effect of line separation with shorter line stub length; l = 0.080 in., L_s = 0.250 in. and s = 0.125 inches.

is increased. This is to be expected, since we have now introduced an additional length parameter which can influence the response through its relationship to wavelength. Here again, the numerical model is judged to have correctly predicted the coupler behavior after the experimental artifacts are considered.

5.4 Summary

The frequency response plots shown demonstrate the utility of the structure as an interconnect. With proper selection of the geometric parameters such as line and slot widths, lengths, line separation, substrate heights and materials, the frequency response can be tailored to give the required center frequency, bandwidth, shape, etc. As has been shown, very wide bandwidths can be achieved which makes the structure very versatile. Avoidance of via-hole transitions and their inherent limitations by the use of planar structures to form vertical interconnects, together with the ability of the model to accurately predict the coupler behavior as demonstrated by experimental results, are especially important

considerations for design of monolithic circuits. In addition, although the approach discussed here uses certain simplifying assumptions about the symmetry of the structures, the technique can be readily adapted to the general case.

CHAPTER VI

ANALYSIS OF STRIP-FED RADIATING SLOTS

Arrays of slots have been widely used in antenna design for nearly fifty years. The most common approach has been to cut slots in the walls of rectangular waveguide forming a linear array. An arrangement of linear arrays, fed by additional slotted waveguides, has frequently been used for two-dimensional arrays. The design and analysis of these approaches has proceeded over many years to the point where accurate numerical techniques are now available so that costly, time-consuming empirical techniques can be bypassed [23, 61].

More recently, complex systems have imposed new antenna requirements with demands for compact conformability, reduced weight, and higher order antenna functions such as electronic beam steering, polarization control and power generation. A suitable approach employing stripline-fed series slots isolated from higher order modes by shorting pins, has been analyzed by Shavit and Elliott [67]. Their approach, together with an alternative coupler feed arrangement, is illustrated in Figure 6.1. The isolation of the slots by the cavity walls, in addition to simplifying the design, has been shown to provide significant advantages for phase steerable antennas [47]. Other variations on this approach may be adapted to fit system requirements including the incorporation of active elements and vertical integration of more complex circuits on multi-layered substrates.

As indicated in earlier chapters, we extend the analysis to include strips on multi-layered substrates and superstrates, as well as to include the effect of a dielectric cover on

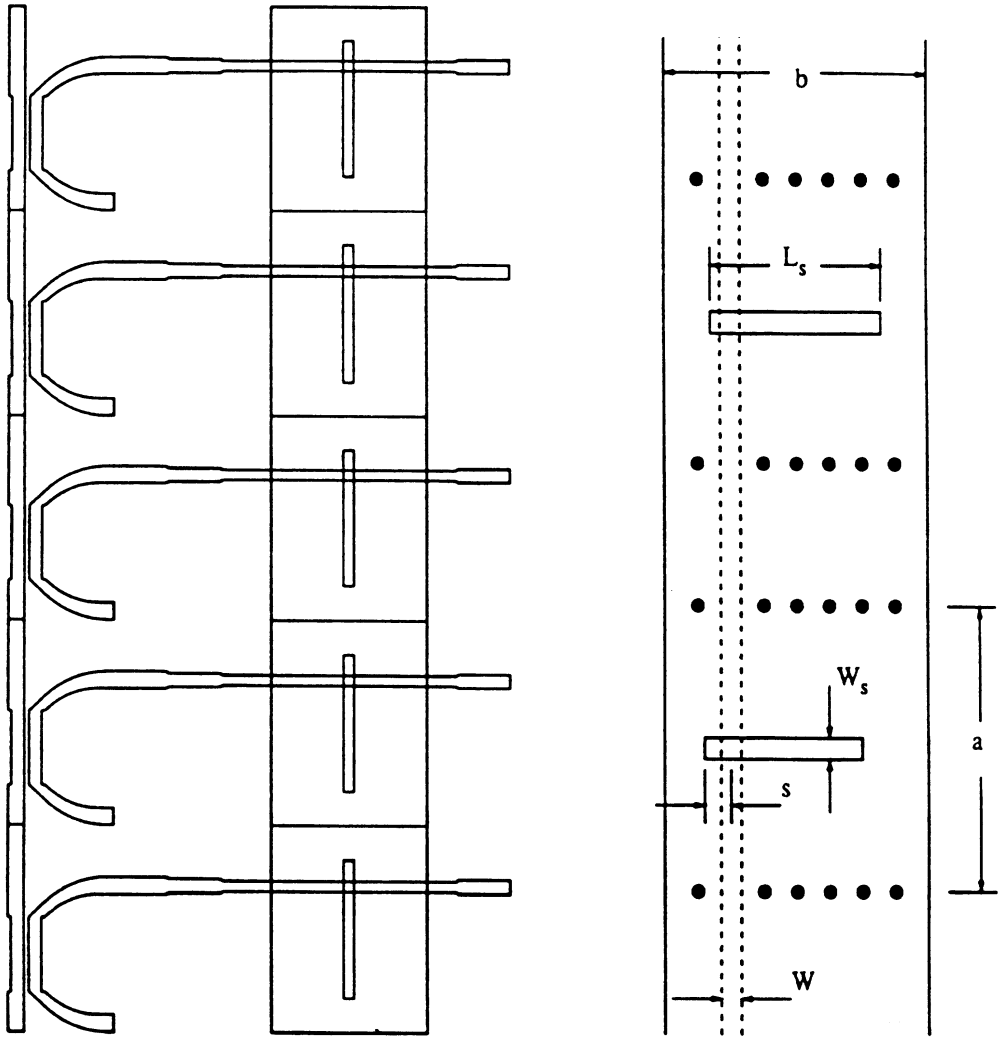

Figure 6.1: Strip-fed cavity-backed slots with coupler-fed and series-fed corporate feed arrangements.

the slots. As will be seen the present formulation substantially improves accuracy, to the point where one could expect to perform the design without empirical methods.

6.1 Equivalent Slot Impedance

In order to produce a slot whose resonant length is less than the width of the cavity, the cavity dimensions must be such that the first higher order mode in the cavity cross-section – the TE_{10} mode – is not cut-off. In this case, since more than one mode can propagate on the microstrip line, the method used to extract circuit parameters in Chapter V cannot be used. In addition, these cavities are typically on the order of one-half wavelength in length so that the lines would probably not be long enough to get reliable circuit parameters using the Standing Wave Method. The scattering parameters for the slot can, however, be derived through application of the Reciprocity Theorem [33] to the cases illustrated in Figure 6.2, resulting in

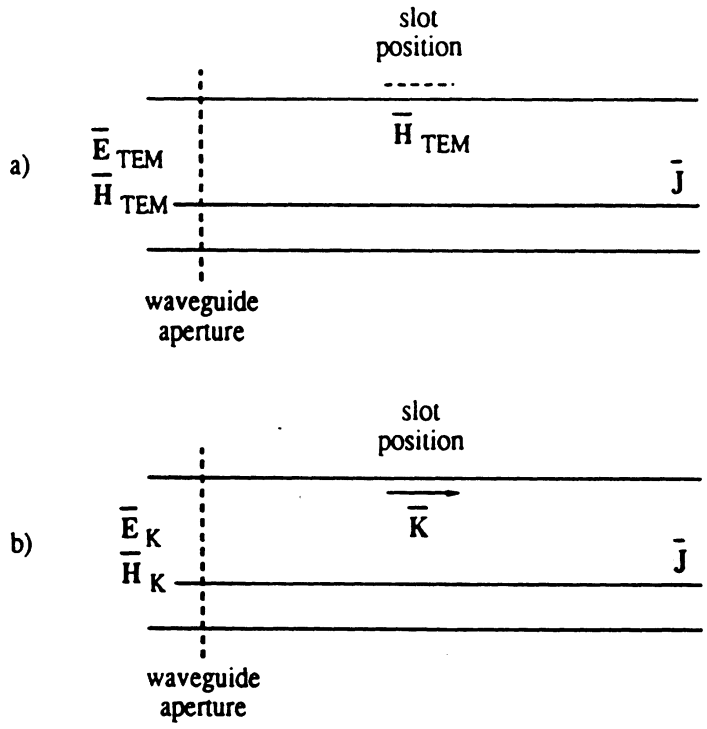

Figure 6.2: Two cases for application of the Reciprocity Theorem.

$$\iint_{waveguide} \left[\overline{E}_{TEM} \times \overline{H}_K - \overline{E}_K \times \overline{H}_{TEM} \right] dS = \iint_{slot} \overline{H}_{TEM} \cdot \overline{K}\, dS \qquad (6.1)$$

where we have assumed the incident wave is the dominant TEM-like mode on the microstrip line. The pins forming the walls of the cavity are sufficiently spaced at the microstrip line so that they do not disturb the dominant mode fields. In this manner, the dominant microstrip mode can pass through the wall unperturbed, while the higher order modes are reflected by effectively, a perfectly conducting wall. The fields for the reflected mode, external to the cavity are then given by

$$\overline{E}_K = \Gamma \left(\bar{e}_{TEM} - \hat{l} \cdot \overline{E}_{TEM} \right) e^{j\beta l} \qquad (6.2)$$

$$\overline{H}_K = -\Gamma \left(\bar{h}_{TEM} - \hat{l} \cdot \overline{H}_{TEM} \right) e^{j\beta l} \qquad (6.3)$$

where $\bar{e}$ and $\bar{h}$ are the field components transverse to the propagation direction, $\hat{l}$.

Rearranging Equation (6.1) we find the reflection coefficient to be

$$\Gamma = -\frac{1}{2} \frac{\iint_{slot} \overline{H}_{TEM} \cdot \overline{K}\, dS}{\iint_{waveguide} \left(\overline{E}_{TEM} \times \overline{H}_{TEM} \right) \cdot (-\hat{l})\, dS} \qquad (6.4)$$

This is the central equation needed to produce the equivalent impedance of the slot from which the equivalent scattering parameters can be derived. In order to evaluate this expression, we note that field components from the solutions to the two problems illustrated in Figure 6.2 are required. The first case - which will be referred to as 'the waveguide problem' - is a shielded microstrip line with layers matching the cavity structure, and provides the transverse components of the field on the entire cross-section. From these we can calculate the reaction integral in the denominator of Equation (6.4) which, for the lossless case, is twice the characteristic impedance of the line. Additionally, we will have the $\overline{H}_{TEM}$ term in the numerator at the location of the slot which is used as the excitation for the second case; 'the cavity problem'. In this case we need to find $\overline{K}$, a conductor-backed, equivalent magnetic current, which replaces the tangential electric field in the slot through the Equivalence Principle [33].

With assumptions on the symmetry of the field in the slot as in [67], the cavity-backed slot can be treated as a two-port series impedance element. Once Γ is known, we can determine the equivalent slot impedance (normalized to the microstrip line impedance);

$$\tilde{Z}_s = \frac{2\Gamma}{1-\Gamma} \tag{6.5}$$

from which the equivalent circuit scattering parameters can be derived by standard network theory. The integral equation formulations for these problems and the solutions for the currents by means of the method of moments has been described in the previous chapters. We therefore can proceed to the verification of the theory and numerical model by presenting the experimental results.

6.2 Numerical Results and Measurements

The solutions for the waveguide problem are obtained as outlined in Chapter IV. The cavity problem is solved using conventional Method of Moments techniques, as outlined in Chapter III with the $\overline{H}_{TEM}$ field from the waveguide problem as the incident field on the slot. Both the strip and the slot are assumed to be sufficiently narrow so that the transverse components of current can be neglected. The longitudinal components on the strip are expanded in terms of piecewise sinusoidal basis functions with the Maxwellian transverse distribution as used for the waveguide problem. Galerkin's method is used to enforce the boundary conditions on the strip. For the slot, we have investigated the use of both the Maxwellian and uniform (rooftop) transverse dependence, using Galerkin's method for the rooftop functions and point matching for the Maxwellian case. In the latter case, point matching is required due to numerical considerations in the evaluation of the Sommerfeld integrals for the half-space. This requires additional computation since the matrix loses its symmetry. We would expect the Maxwellian results for narrow slots to be more accurate since the edge conditions are satisfied, however, in the end the differences

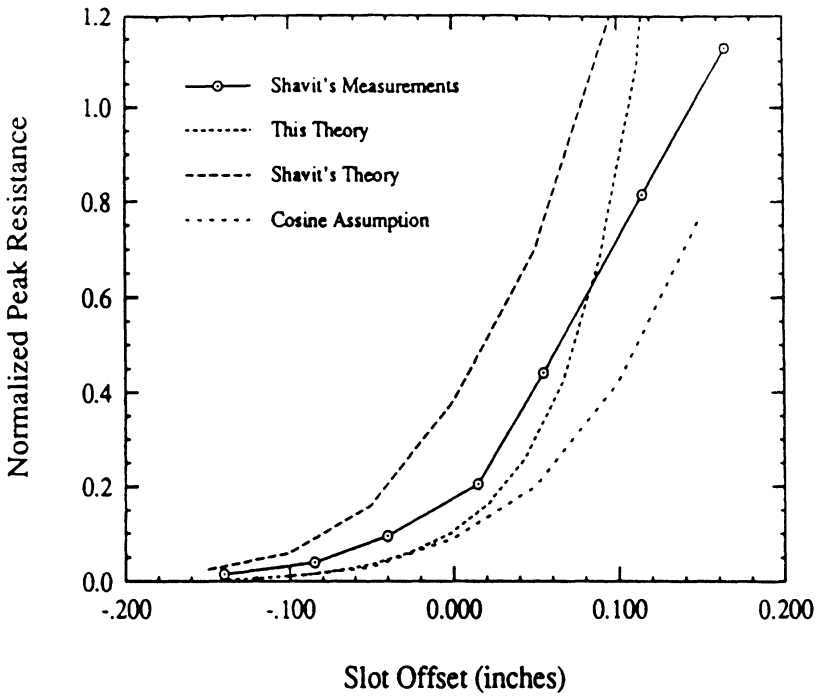

Figure 6.3: Normalized resistance as a function of slot offset compared to Shavit's measurements [67].

are minimal. Therefore, the rooftop functions are preferred and will be used throughout, with the added benefit of their greater flexibility in modelling wider or more complex slots. With this discretization of the integral equations, the resulting system of linear equations is solved for the unknown current distributions by matrix inversion.

To verify the accuracy of the model, we first compare with the theoretical results and measurements of Shavit [67] shown in Figures 6.3 and 6.4. Figure 6.4 shows the results of calculations of resonant length which is a key parameter in the design of high performance antenna arrays. This is a special case involving stripline and no dielectric cover and shows significantly improved agreement between this work and the experimental measurements. The reason for the larger discrepancy in Shavit's theory is uncertain, since there are some similarities with the present method. The most likely factor may be his use of approximate Green's functions, which also restricts application of his method to stripline only. This

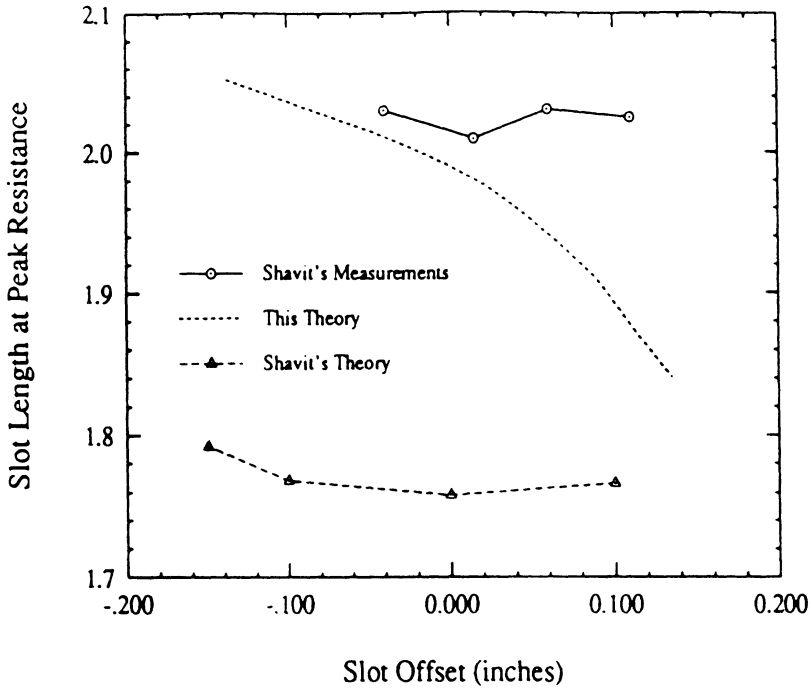

Figure 6.4: Resonant length as a function of slot offset compared to measurements [67].

leads to certain assumptions about the enforcement of the boundary conditions on the strip, whereas we have used the exact expressions and enforced the boundary condition explicitly. The number of modes used in the summations (convergence) can also be an important factor. High mode numbers are needed, especially since the critical field behavior occurs in the region where the strip and slot are most closely spaced.

Since making accurate measurements for these types of slots is quite difficult and considering that these measurements were made almost a decade ago, we have performed extensive measurements on a new set of slots, with and without dielectric covers. In the process, we have uncovered new factors not previously recognized which can significantly influence the results. Individual test pieces for several combinations of slot lengths and offsets have been built. The pieces were constructed using two copper-clad dielectric boards (31 mil thick 2 inch square Duroid 5880 $\epsilon_r = 2.2$ with 0.7 mil thick copper-cladding). The

size of the boards is small enough to minimize material and fixturing costs but large enough to provide an adequate ground plane and reduce the effects of reflections from the board edges. The slots and transmission lines for each sample were produced by removing copper from the top planes of the top and bottom boards, respectively. The slot length (L_S) and offset of the transmission line from the end of the slot (s) were varied from circuit to circuit with the slot always in the center of the board. The top and bottom boards were then bonded together by placing 3M 6700 2 mil thick thermoplastic bonding film at their interface and subjecting them to the heat and pressure profiles specified by the manufacturer. In addition, to improve accuracy, calibration standards were constructed for de-embedding of the fixtures using the TRL method [34]. Dielectric covers were made from 125 mil Duroid (ϵ_r = 2.2) bonded to the circuits with Ablebond 550 thermoset in a bonding press at 230°F for approximately 3 hours. Recessed tracks were milled in the covers to accommodate the soldered shorting pins which protrude slightly above the top surface of the circuits. Other dimensions were held constant to the extent possible throughout the experiment and were: a = 0.425, b = 0.516, W = 0.0279 and W_S = 0.0315 inches. A sample slot is shown in Figure 6.5 at various stages of fabrication.

Once calibration is established which places the reference plane at the center of the slot, the S-parameters were measured for each slot. The equivalent impedance of the slot as a series element can be determined from

$$Z = 2Z_o\left(\frac{1}{S_{21}} - 1\right) \tag{6.6}$$

or

$$Z = \frac{2Z_oS_{11}}{1 - S_{11}} \tag{6.7}$$

The extent to which Equations (6.6) and (6.7) agree provides a measure of the accuracy of calibration. In general, however, Equation (6.7) was found to be more accurate for resonant lengths because the calibration of S_{21} is more sensitive to dielectric constant and length

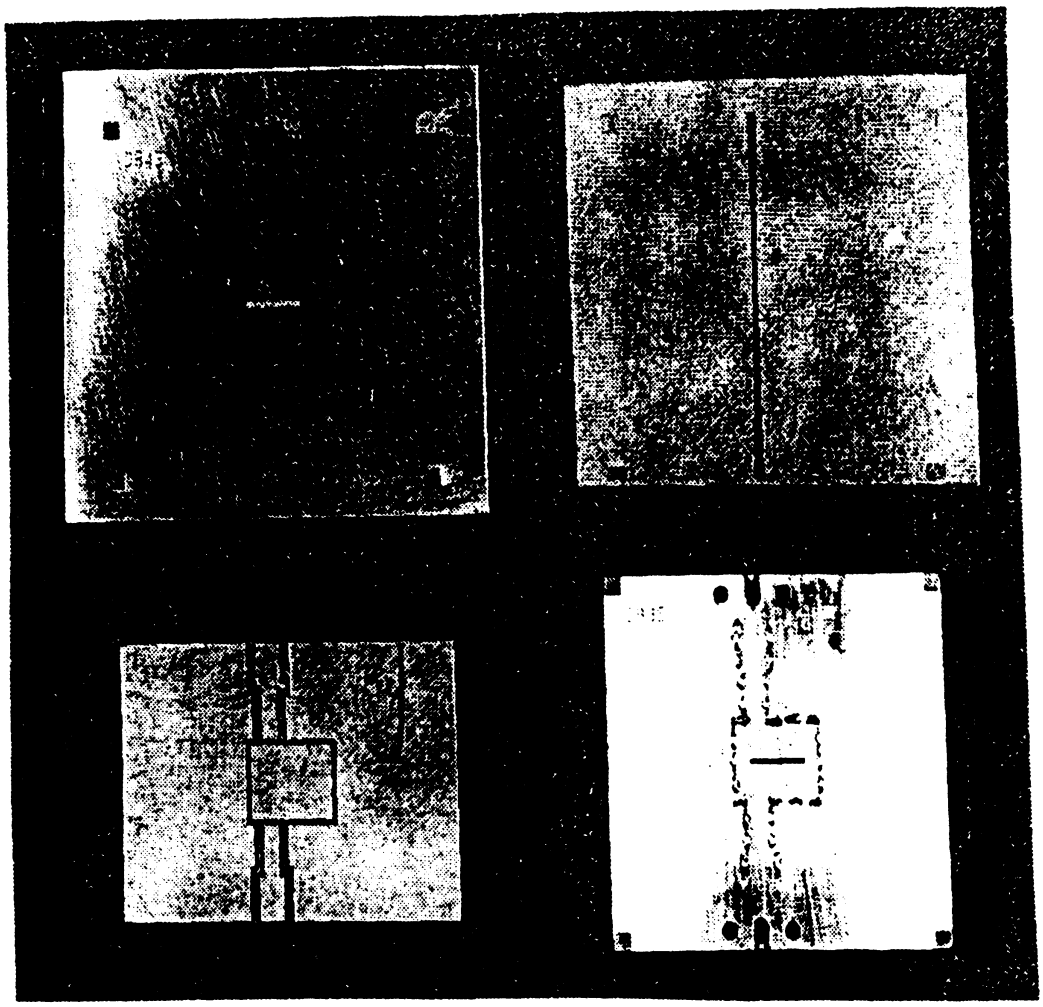

Figure 6.5: Photograph of slot assembly pieces in various stages of fabrication.

variations. In contrast, Equation (6.6) was judged to be more reliable for estimations of the peak resistance values based on the behavior of S_{11} with frequency in the few cases where the results of Equations (6.6) and (6.7) differed. We have also defined resonant length as corresponding to the peak in the resistance curve, since this definition is less sensitive to measurement and calibration errors and is more consistent when constant parasitic reactances are present.

Figure 6.6 shows an example of a comparison between the calculated resistance at

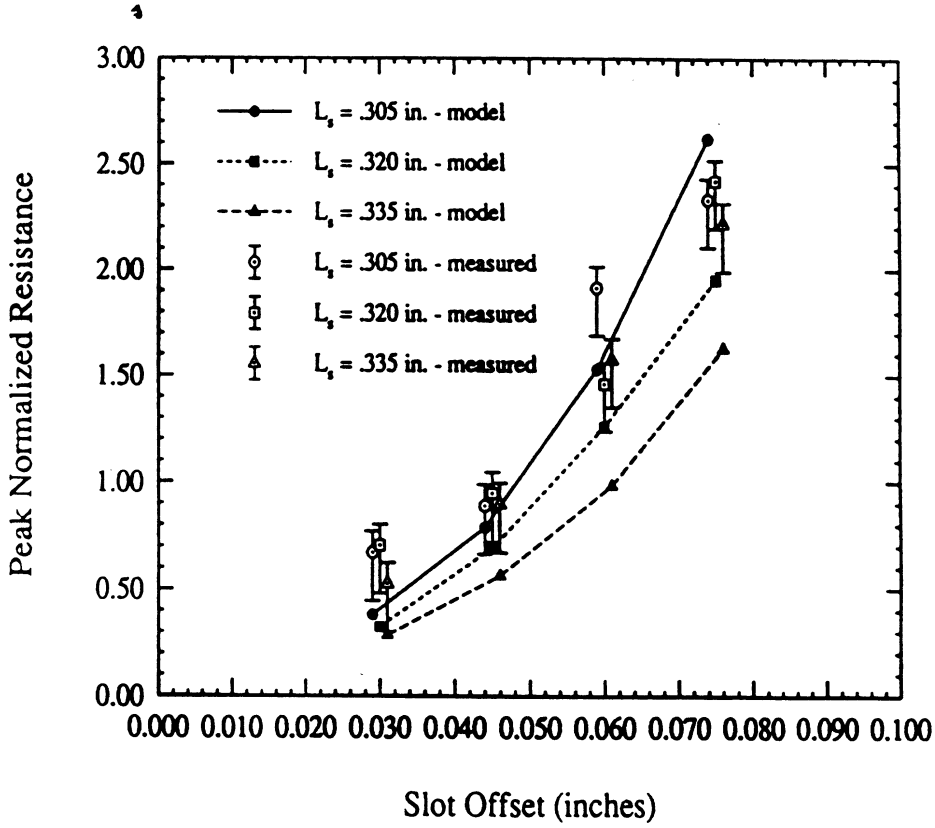

Figure 6.6: Uncompensated peak normalized resistance as a function of slot offset compared to measurements for uncovered slots.

resonance and the measured values, normalized to the impedance of the line. The curves represent the resistance versus offset, the distance from the end of the slot to the centerline of the strip, at the measured resonant frequencies. The data points shown are the measured values with error bars indicating the uncertainty due to a combination of repeatability tests

and an estimate of potential systematic calibration error due to variation in the substrates. By comparing the measured resistance values with the corresponding points predicted by the numerical model, it can be seen that virtually all predicted resistance values are low. Furthermore, it should be noted that the error bars are conservative, since they do not account for slot and dielectric cover losses which cannot be calibrated out, or variations in fabrication such as dimension changes. Also, the plotted offsets have been artificially staggered ±1 mil for clarity and do not indicate an error estimate. Fabrication variations are blamed for points which deviate from the trend of the data, for example in this Figure, the case where s = 0.075 and L_S = 0.305 inches is particularly suspect.

Figure 6.7 displays the predicted resonant lengths for the same frequency range. Here the crosses indicate the physical parameters for the measured slots. One can then estimate the error in either resonant length or frequency by correlating the measured resonant frequencies listed in the table with the curves. A comparison of the resonant lengths shows that the predicted lengths are all too long. (Equivalently, predicted resonant frequencies for a given slot length are too high.)

These comparisons, together with other observations made in making the measurements and numerical parametric studies, led to the important realization that a compensation must be made for the aperture in the wall which allows the strip to pass through. In the past it has been assumed that if the pins are sufficiently far from the strip, the dominant mode can pass through the wall unperturbed. At the same time, it has been assumed that if the pin spacing is sufficiently dense, the higher order modes - particularly the TE_{10} mode - will effectively encounter a perfectly conducting wall allowing us to use the closed cavity Green's function to model the walls. Although the first assumption is valid, the second may not be and is of crucial importance because the behavior of the slot is strongly influenced by the TE_{10} mode, leading to the above discrepancies.

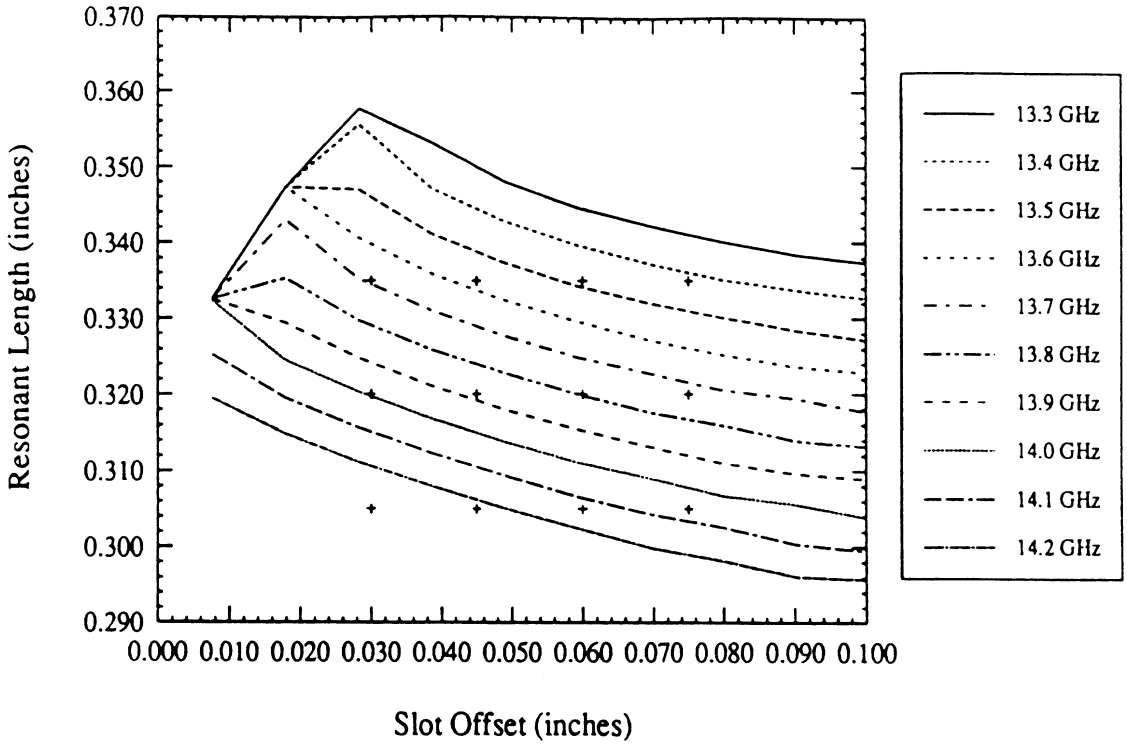

MEASURED RESONANT FREQUENCIES (GHz)

Slot Offset (inches)	Slot Length (inches)		
	L_s = .305	L_s = .320	L_s = .335
s = .030	14.165	13.74	13.39
s = .045	14.145	13.845	13.38
s = .060	14.17	13.80	13.31
s = .075	14.045	13.61	13.285

Figure 6.7: Predicted resonant length as a function of slot offset for uncovered slots. Crosses indicate actual test piece dimensions to be compared with the frequency curve corresponding to the measured resonant frequencies listed in the table.

The sensitivity of the slot's behavior to the relative position of the walls parallel to the slot is demonstrated in Figure 6.8. We see that the resonant slot length for the uncovered

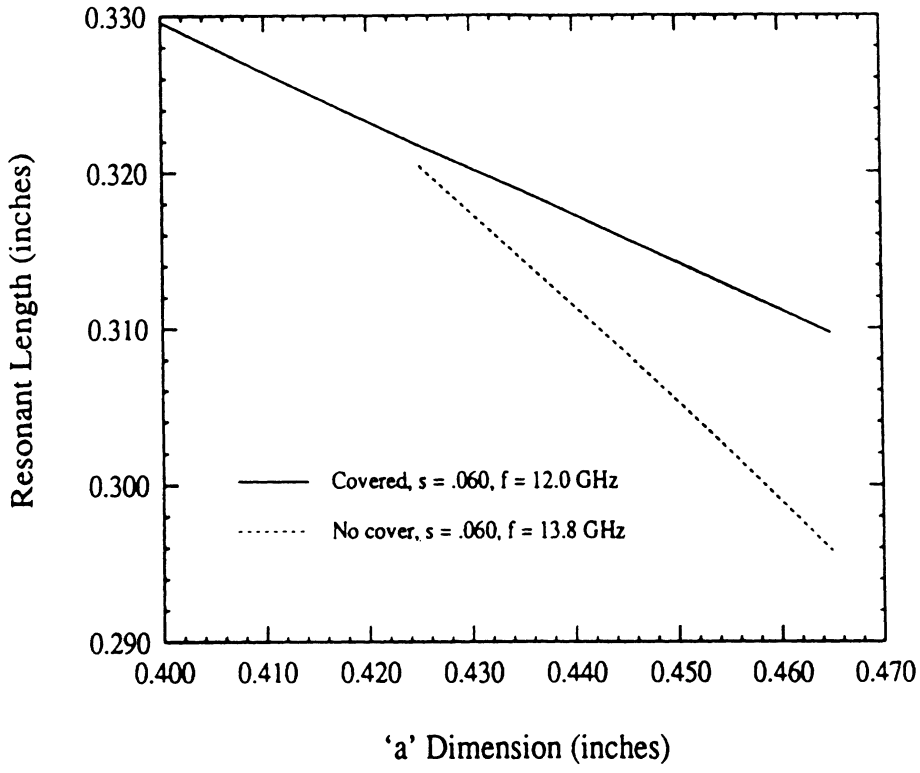

Figure 6.8: Sensitivity of resonant length to cavity length dimension 'a'.

case depends on the position of these walls on a nearly one-to-one basis. Thus, a 1% error in the position of the walls will produce approximately a 1% error in the resonant length. Assuming that our average fabrication tolerances are better than that, implying that we should emphasize the trend of the data, the discrepancy between theory and experiment can be traced to ignoring the apertures in the walls for the TE_{10} mode. (Note, however, that just the diameter of the wire used to construct the walls of the cavity - 10 mils - is on the order of 1.5% of the electrical length of the cavity.) It is observed that the covered case is less sensitive to this dimension because the magnitude of the slot field in the covered case is not as large, implying a smaller excitation of the TE_{10} mode relative to the other

mechanisms.

In a rectangular waveguide, wall apertures of the type used here can be represented by a shunt inductance. For a one-port, a shunt inductance can be replaced by an equivalent length of shorted transmission line. Since for stripline and rectangular waveguide the TE_{10} modes are identical, variational formulas for calculating this inductance in rectangular waveguide such as found in [54, pp.165] can be used to estimate a correction to the length of the cavity, compensating for the affect of the aperture. It is also desirable to suppress the propagation of energy in this mode through the aperture, by lining the stripline with shorting pins to cut off all higher order modes outside the cavity as shown in Figure 6.5. In addition, by modelling the wires explicitly after a manner similar to [43] as discussed in Chapter IV, and using the 'rule-of-thumb' from [54, pp.188–189] to account for the change in width, we have found that the correction may be somewhat smaller than indicated by variational formulas and has less sensitivity to frequency. The end result, in this case, is an estimated correction of 12.5 mils for the length of the cavity. The other walls of the cavity are also made with wires but the slot characteristics are quite insensitive to this dimension.

The model is now re-evaluated with the compensated dimension and the predicted resistance and resonant lengths are compared to the measured resistance and actual slot lengths at the measured resonant frequencies. In Shavit's case, the dimensions used result in only a 16 mil correction which, for his operating frequency, has minimal influence on the results shown previously. For our measurements the compensated coupling (resistance) results are shown in Figure 6.9 and the predicted resonant lengths are listed in Table 6.1. Parametric curves for resonant lengths for this and all remaining cases are similar to Figure 6.7 except the family of curves are shifted downward and therefore will not be shown. When the dielectric cover is introduced the same general features are observed. Using the same length compensation as in the uncovered cases because the cavities are the same, the comparison

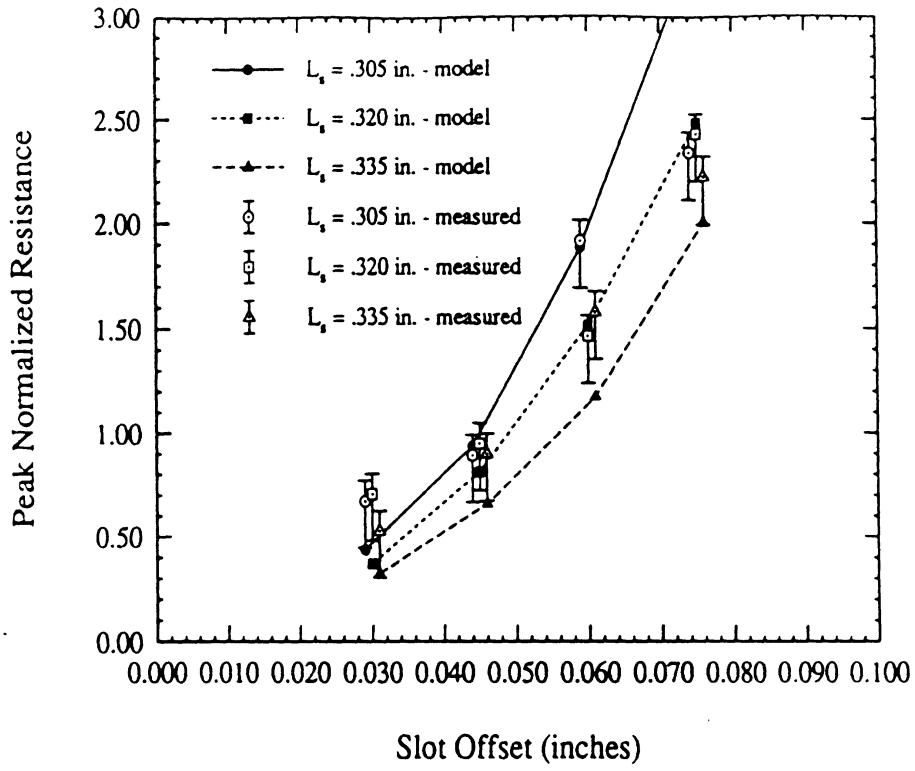

Figure 6.9: Compensated peak normalized resistance as a function of slot offset compared to measurements for uncovered slots.

Slot Offset (inches)	Slot Length (inches)					
	L_s(actual) = .305		L_s(actual) = .320		L_s(actual) = .335	
	f_{res}	L_s (model)	f_{res}	L_s (model)	f_{res}	L_s (model)
s = .030	14.165	.3045 (-0.2%)	13.74	.3234 (+1.1%)	13.39	.3409 (+1.8%)
s = .045	14.145	.3009 (-1.3%)	13.845	.3139 (-1.9%)	13.38	.3361 (+0.3%)
s = .060	14.17	.2957 (-3.0%)	13.80	.3120 (-2.5%)	13.31	.3351 (+0.0%)
s = .075	14.045	.2976 (-2.4%)	13.61	.3175 (-0.8%)	13.285	.3331 (-0.6%)

Table 6.1: Measured resonant frequencies (GHz) and predicted resonant slot lengths for uncovered slots with compensated cavity length. (Deviation from actual slot length listed in parenthesis in percent.)

between theory and experiment for the covered cases can be found in Figure 6.10 and

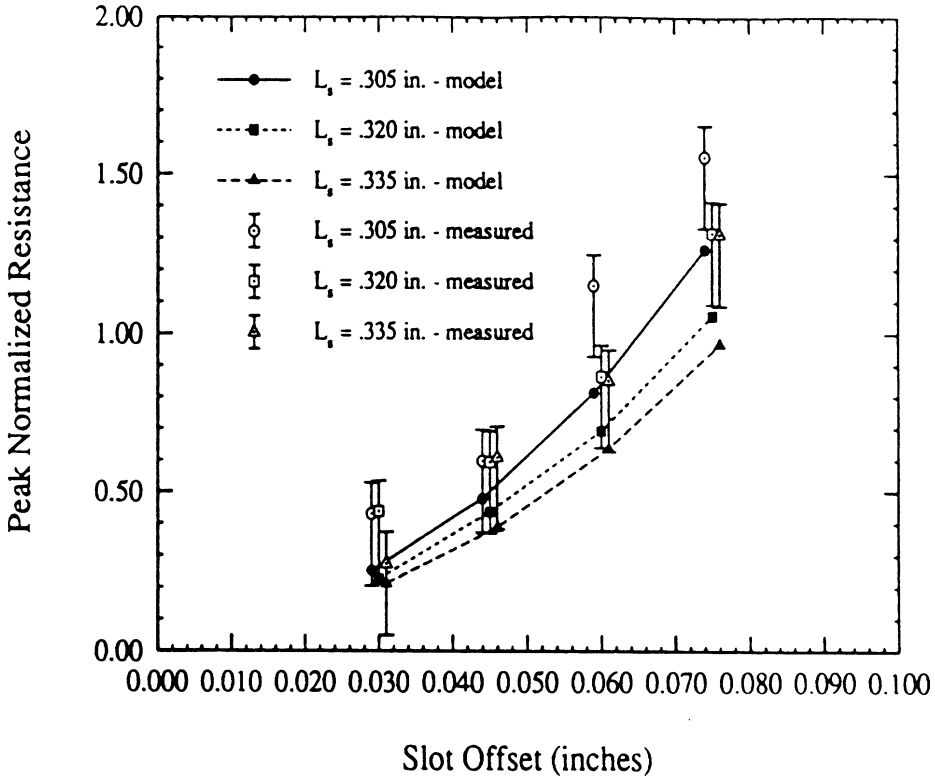

Figure 6.10: Compensated peak normalized resistance as a function of slot offset compared to measurements for covered slots.

Table 6.2.

The variation of the errors in these tables is attributed primarily to variations in fabrication. It can be seen that the average error for the uncovered slots is on the order of -0.8% which is considered to be excellent. For the covered cases, the average error is approximately 3.3%, however, in this case we would expect an increased uncertainty due to additional factors including: variations in cover dielectric constants and bonding; a potential increase in the influence of the finite ground plane due to the introduction of surface waves; and the affect of the milled recesses in the covers, although very shallow, which are not included in the model. The latter two factors are of particular interest considering the sensitivity of the resonant length to the position of the internal walls of the cavity parallel

Slot Offset (inches)	Slot Length (inches)					
	L_s(actual) = .305		L_s(actual) = .320		L_s(actual) = .335	
	f_{res}	L_s (model)	f_{res}	L_s (model)	f_{res}	L_s (model)
s = .030	12.40	.3123 (+2.4%)	12.00	.3318 (+3.7%)	11.75	.3453 (+3.1%)
s = .045	12.35	.3125 (+2.4%)	12.03	.3274 (+2.3%)	11.61	.3489 (+4.1%)
s = .060	12.35	.3107 (+1.9%)	11.83	.3353 (+4.8%)	11.56	.3493 (+4.3%)
s = .075	12.35	.3092 (+1.4%)	11.81	.3348 (+4.6%)	11.54	.3487 (+4.1%)

Table 6.2: Measured resonant frequencies (GHz) and predicted resonant slot lengths for covered slots with compensated cavity length. (Deviation from the actual slot length listed in parenthesis in percent.)

to the slot. It should also be noted that because the resonant length of the slot is controlled by factors which do not scale identically with frequency, these errors do not indicate the expected error of predicted resonant frequencies. In fact, for the geometry studied here, the expected error in resonant frequency for a given slot length, is roughly half of the prediction error for resonant lengths. This feature can be deduced from Figure 6.7 for the uncovered slots, and similar parametric plots for the covered case, by calculating the slope of length over frequency. The case for resonant lengths has been shown in the tables, since these errors are more relevant to initial antenna designs.

Finally, we point out that the fixtures were built by varying the position of the strip to achieve different slot offsets while in the numerical model it is more efficient to vary the slot position relative to the strip. A comparison of numerical results for the actual dimensions has shown that the relative positions of the strip and slot in the cavity have some influence on the slot characteristics, however, the variations are within the bounds of the experiment, indicating the true accuracy of the approach is at least as good as suggested above. In fact,

to some extent there is coupling between errors in frequency and resistance values so that variation of a parameter tends to improve the agreement with experiment for one while degrading the comparison for the other. For example, in the covered case, evaluating the numerical model at the measured resonant frequency tends to reduce the error in predicted resonant length while increasing the discrepancy in resistance values. For the uncovered slots, the resonant length (frequency) and resistance values are more stable, suggesting not only that the compensation length is likely to be correct, but also that the introduction of the covers has introduced an error in the experiment. Nevertheless, the overall agreement with the experimental data is considered to be excellent to the extent that the variations can be controlled for this type of construction.

6.3 Summary

In summary, we have presented a full-wave integral equation approach for the analysis of strip-fed cavity-backed slots. The formulation involves the application of the Reciprocity Theorem which requires the field solutions to two distinct situations; the infinite shielded line (the 'waveguide problem') and the cavity problem. Methods for deriving the exact Green's functions for these problems have been described including the incorporation of multi-layered substrate and superstrate capability. Solutions to the integral equations are then found by the Method of Moments.

Modelling of the strip itself, and accounting for the effect of the openings in the cavity walls, were found to be a key factors not previously recognized for accurate modelling of these types of strip-fed slots. Comparison with measurements for the special case of stripline has demonstrated that solutions using the exact Green's functions and compensation for the strip aperture lead to significant improvements in accuracy over previous methods. The analysis described is also exact for more general structures involving multiple layered substrates and superstrates with the exception of determining the compensating

length for the feed-through aperture. This can be found by extension of the 'waveguide problem' approach as described above with wires or apertures modelled in a manner similar to [43] or [3].

For the type of fabrication techniques described in this experiment, it was found that the numerical model produces accuracies on the order of that for the experiments. This suggests the method has sufficient accuracy to replace many of the empirical steps used in the design of antenna arrays, which can significantly reduce design and development costs.

CHAPTER VII

MODELLING OF THICK-SLOTS

It has been suggested that strip-fed radiating slots may play an important role in the recent trend towards more complex antenna systems. This is particularly true for monolithic phased array applications where active devices are integrated with the radiating elements for phase control and in some cases, to generate power. One of the practical difficulties which arises with the introduction of active devices is the dissipation of heat. One solution is to increase the thickness of the antenna face for use as a heat sink, which also adds the possibility of cooling channels. This has an influence on the electrical design, however, since the slots may no longer be considered infinitely thin as is commonly done. On the other hand, we can take advantage of the thickness to improve bandwidth, which has traditionally been a fundamental limitation of slot arrays. This possibility is the primary topic for this chapter.

While semi-empirical and approximate correction factors for finite thickness slots have been introduced and may be adequate and appropriate in some circumstances [39], it is desirable to develop exact methods to improve the accuracy and generality of numerical design tools. The full-wave integral equation technique which has been presented is also applicable to this class of antennas, allowing not only the analysis of thick slots [84, 85], but also slots which couple through a section of waveguide as shown in Figure 7.1. This latter case also provides the mechanism for improved performance. By adjusting the slots

on the ends of the waveguide section to different lengths, we can essentially 'stagger tune' each slot to a different frequency, increasing the overall bandwidth.

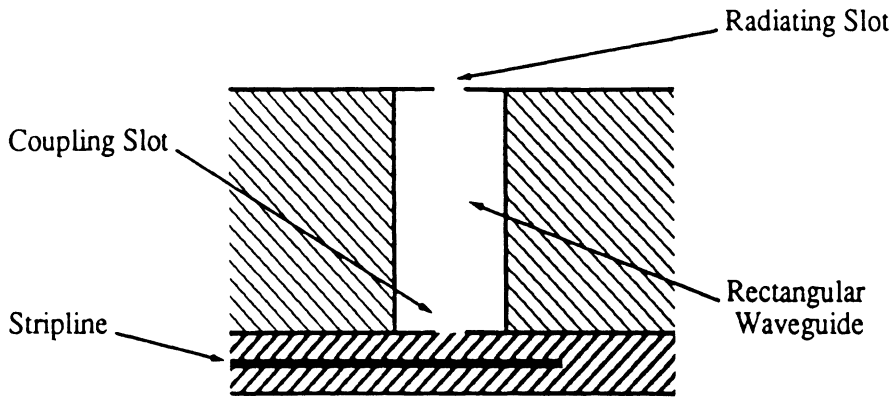

Figure 7.1: Stripline excitation of waveguide-coupled slots.

7.1 Numerical Results for Waveguide Coupled Slots

To illustrate the behavior of the structure, a particular case at 9.7 GHz is presented with a 0.60 x 0.60 inch cavity (ϵ_r = 2.2) fed by stripline with a ground spacing of 0.125 inches. A strip width of 0.1 inches was assumed which results in a 50Ω line and the slot is of the same width and is assumed to be covered by an ϵ_r = 2.2, 0.0625 inches thick dielectric sheet. The coupling to the slot can be represented by an equivalent series impedance. As will be seen, its value is controlled primarily by the length of the waveguide section (L_W) and the slot offset (s), the distance between the end of the slot and the centerline of the strip. Note that the waveguide must be dimensioned above cutoff, if substantial lengths are to be used. Thus, we have assumed half-height X-band waveguide with transverse dimensions of 0.900 x 0.225 inches.

Figures 7.2 and 7.3 indicate typical impedance behaviors as functions of the slot length. Figure 7.2 shows the influence of the slot offset for the case of a conventional 'thin' slot as treated in Chapter VI which also applies to the 'thick' slot case. Figure 7.3 demonstrates

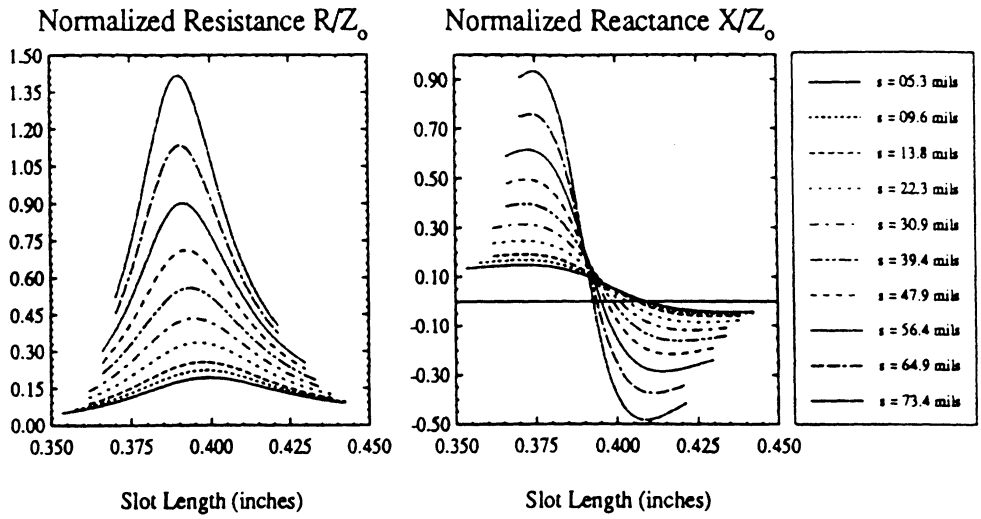

Figure 7.2: Typical variation of impedance as a function of slot length for a conventional 'thin' slot with slot offset as a parameter.

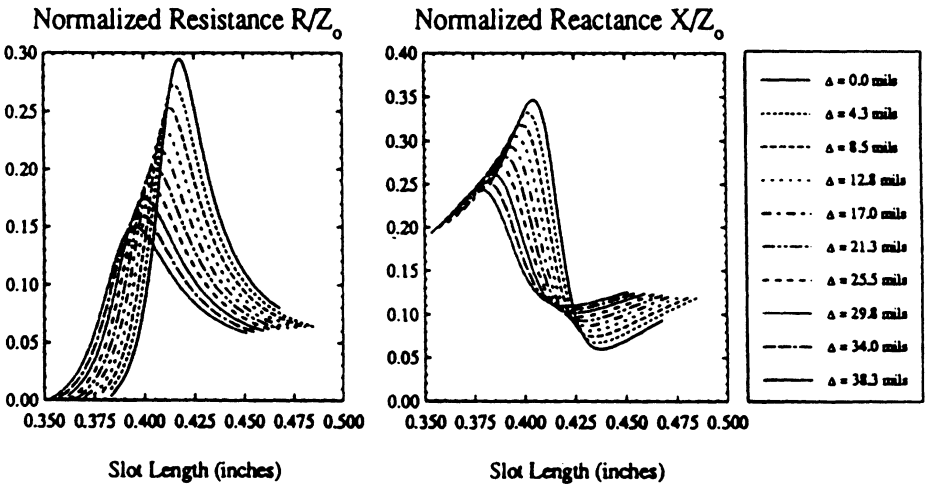

Figure 7.3: Variation of impedance as a function of slot length with the difference in top and bottom slot lengths as a parameter.

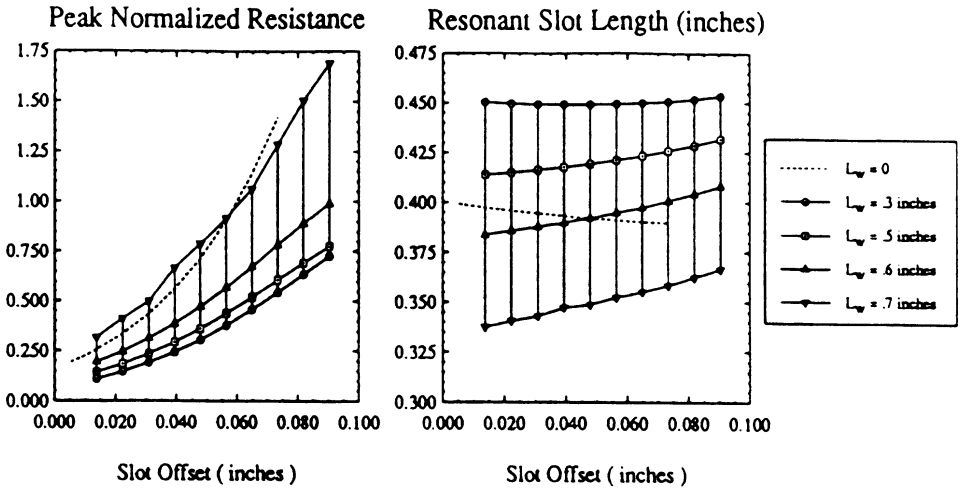

Figure 7.4: Slot coupling (resistance) and resonant length dependence on offset and waveguide length (L_W).

similar behavior for the 'thick' slot case when the difference in length between the top and bottom slots (Δ) is used as a parameter and the slot offset fixed. Notably, the reactive part does not necessarily cross through zero. This is due to parasitic reactive discontinuities in the geometry which are not strong functions of slot length; for example, the step discontinuities in the slot-to-waveguide transitions. Nevertheless, a resonant behavior is clearly indicated and we will define resonant length by the peak in the resistance curve. We also see an affect on resonant length which is typical. The influence of slot offset and waveguide length are summarized in Figure 7.4. In this case the top and bottom slots are identical in length.

Frequency response can be inferred from the impedance behavior with respect to slot length, through its relationship to wavelength. Therefore, we can use this parameter as an indication of apparent bandwidth. Using length as a parameter is preferred because this data is more easily obtained than direct frequency data. Returning to Figure 7.3 we see that as the difference in length (Δ) increases with slot offset held constant, the

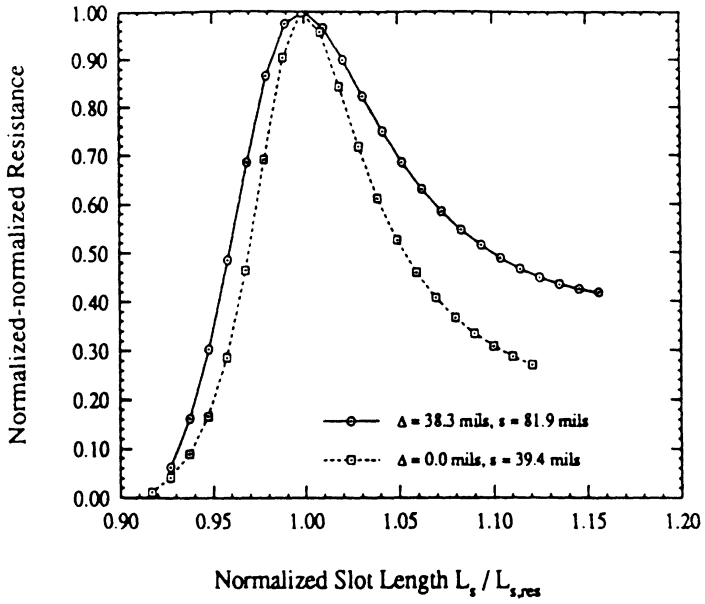

Figure 7.5: Apparent bandwidth comparison for identical slots versus slots with different lengths based on an interpretation of the relationship of slot length to wavelength.

apparent bandwidth is increased together with a change in resonant length, but the coupling resistance is simultaneously reduced. Since the resistance is normally a fixed value dictated by the feed design, we can compensate for this either by increasing the slot offset or adjusting the waveguide length as indicated by Figure 7.4. However, because apparent bandwidth reduces in a similar way with increased offset, it is difficult to judge whether any gains in bandwidth can be produced. To evaluate the improvement in bandwidth for the largest slot length difference of Figure 7.3, the offset was varied while the waveguide length was fixed at L_W = 0.5 inches. The normalized resistance curves were then re-normalized to the peak value to remove any remaining discrepancy (R/Z_o = 0.294 vs. 0.295). Slot lengths were also normalized to the resonant lengths to remove variations. A suggestion of an increase in bandwidth is now obvious as illustrated in Figure 7.5.

The apparent bandwidth interpretations so far have been based on the slot length. As

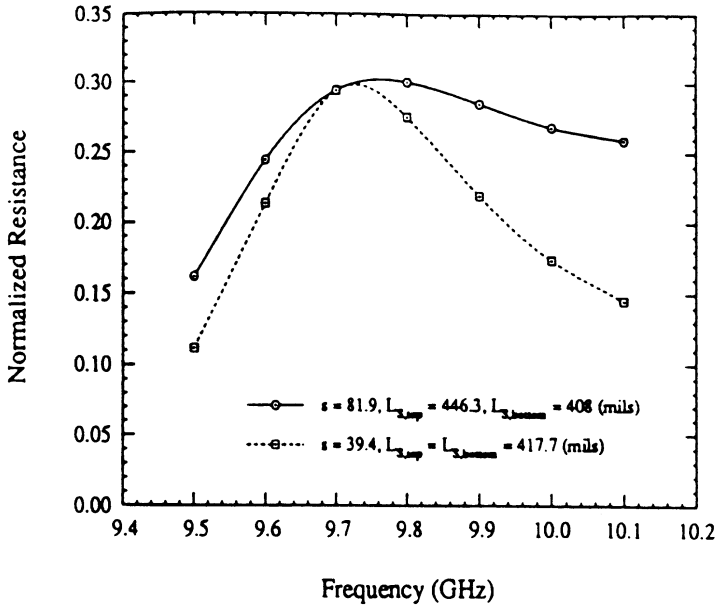

Figure 7.6: Apparent bandwidth comparison for identical slots versus slots with different lengths based on calculations at selected frequencies.

indicated earlier, however, each transition in the structure may have parasitics impedances which are independent of slot length. These are unlikely to be constant or have the same variation with frequency, therefore, to rigorously translate the previous figures into a frequency response, it is necessary to run each geometry at an ensemble of frequencies. The plot in Figure 7.6 shows a comparison of the two cases over a sample of frequencies. It is evident that the previous estimates based on length calculations were conservative, so that we may be justified in a preference for the length-based results, at least for a parametric study of the structure. Comparing Figure 7.6 with Figure 7.5 also suggests that although, strictly speaking, scaling cannot be applied to the length data to derive the frequency response, it does provide a reasonable estimation of the actual response, at least in this case. Scaling length data could then be used in the initial design stages to increase the efficiency of the design process.

7.2 Summary and Conclusions

In conclusion, the thick slot has been modelled by treating the slot apertures as separate slots coupled through a section of rectangular waveguide. It has been shown through a parametric study that, based on the theoretical model developed, the apparent bandwidth of the element can be enhanced by stagger-tuning the coupled slots. Although this part of the analysis has not been verified by experimental evidence, the concept is a simple extension of the models verified previously and the behavior of the structure follows intuitive expectations.

Within the limited range of parameter variations used here, apparent bandwidth increases of 50% are possible. The true bandwidth would depend on the external circuits actually used to feed and load the slot. It seems likely that with a more detailed study of the influence of various parameters on the impedance characteristics, even greater improvements in bandwidth could be obtained.

CHAPTER VIII

CONCLUSIONS AND RECOMMENDATIONS FOR FUTURE WORK

The class of structures treated in this work involves rectangularly shielded microstrip and slot lines. An integral equation formulation for the analysis of these structures in various combinations has been shown to provide accurate characterizations of a variety of elements. The capability to analyze multi-layered substrates and superstrates has been included through the use of impedance boundary conditions and provides an exact representation by modal analysis of the geometries involved.

Solutions to the integral equations require the specification of Green's functions for each case. A number of Green's functions of different types have been derived by a extending and generalizing a dyadic analysis technique to incorporate the impedance boundary conditions. This approach greatly simplifies the treatment of multilayered structures through the use of transmission line analysis. The impedance boundary conditions have thus been incorporated into the exact dyadic Green's functions making the analysis "full-wave", therefore all electromagnetic interactions are taken into account. For all structures treated, the derivation of the Green's functions reduces to a straightforward procedure producing all components of both the electric and magnetic field dyads in one exercise. Because of the normalization of the functions used for the expansions of the fields, the approach also produces the dual Green's functions by a simple change in notation, similar to the application

of the Duality Principle.

The integral equations have been solved through a conventional application of the Method of Moments. The treatment of basis functions in general coordinate systems has been shown to reduce to straightforward coordinate transformations. This reduces the required integrations over source and weight functions to simple forms which have been evaluated for piecewise sinusoidal basis functions with both constant and Maxwellian transverse dependence. These results lay a foundation for the treatment of coupling between strips and slots with arbitrary planar orientations within a rectangular cavity.

The remainder of the work is a study of special cases of current interest. Overall, the method has been shown to produce numerical models with excellent accuracy such that one could expect to design devices involving these elements with little or no empirical work or adjustments. This conclusion is evidenced by extensive experimental data provided throughout. The remainder of this chapter is devoted to discussion of specific findings for the various applications studied and recommendations for further development of these techniques.

8.1 Summary of Achievements

8.1.1 Two-Dimensional Analysis

A number of geometries have been considered in Chapter IV which can be treated by a two-dimensional analysis. The primary motivation for the studies in Chapter IV was to support the work in later chapters, particularly Chapter VI. However, the results of this chapter have some significance themselves.

The benefits of using LSE and LSM modes for the expansion of fields in connection with a transmission line representation of impedance boundary conditions was demonstrated. It has been shown that in order to find the propagation constants of microstrip or slot lines,

we first need only consider the boundary conditions in the region of the strip or slot. The remaining layers are represented by the impedance conditions, simplifying the numerical implementation. Once the propagation constant for a particular mode is known, the fields in the remaining layers, and hence the characteristic impedance of the line, can be found by a summation of modes with coefficients specified by analytically matching the modes across layer interfaces. The matching procedure results in simple expressions as a result of the use of the LSE and LSM modes. The fields throughout all layers can be efficiently found in the same manner, allowing a visual representation of the field structure which is useful for intuitive as well a quantitative information. Comparisons with available data were made to verify reliability. The presentation also serves as an illustration of the technique when applied to other structures such as cavities, parallel plate waveguides, or open structures.

We also developed a simple technique for the evaluation of scattering from vertical wires or pins in a rectangular waveguide. The method is a simplification of more complex routines discussed in the literature, allowable in our case since we are concerned with wires of small diameter. This work was needed in support of Chapter VI but also led to certain observations which have not been widely discussed. The validity of the results was verified by experimental results and published data. The specialization of this problem to homogeneously filled rectangular waveguides allows it to be treated as a two dimensional problem which precludes its use with multilayered structures; however, the extension to the three dimensions is not difficult.

8.1.2 Couplers

Chapter V contains a study of coupling from microstrip to microstrip through a narrow slot aperture. The unique feature of the treatment of this problem is the use of the Standing Wave method with even and odd excitation analysis to extract the circuit parameters. This

method has been used by others and thus is only briefly discussed, however, some of its key limitations are pointed out.

The primary significance of this topic is in the numerical and experimental results. It has been shown that this structure enables one to make very wide band transitions from one line to the other. The particular structure studied, a transition from one substrate level to another, has significant implications for vertical interconnects in monolithic circuits since no via-hole is required. Qualitative explanations for the behavior of the structure, as a function of various parameters, were provided in connection with an equivalent circuit to develop an intuitive understanding of the device. The numerical analysis has been shown to produce highly accurate results by comparison with experimental data.

8.1.3 Radiating Slots

The modelling of microstrip-fed radiating slots is one of the principle topics of this work. The fundamental results for this element are discussed in Chapter VI. The limitations of the Standing Wave method developed for the coupler require a different technique to derive circuit parameters. An alternative method, applied earlier by Shavit [67], was developed for our use and is here referred to as the 'Reaction Method'. The technique is based on the Reciprocity Theorem and is applied in a manner similar to that used for waveguide-fed slots developed many years ago. However, due to the presence of the strip, the method is somewhat more complex and required the development of techniques described in Chapter IV. The explicit treatment of the strip for this type of antenna element, was shown to be the likely cause for discrepancies found in earlier work.

Here it has been shown that the numerical model is capable of producing accuracies on the order of experimental work. The model demonstrates much better performance than earlier work on this type of slot. One of the key discoveries in this area is that the

openings in the cavity wall which allow access for the strip cannot necessarily be ignored as has previously been assumed. A technique has been developed, supported by the models discussed in Chapter IV, which compensates for the effect of the opening. The resulting data shows excellent agreement with an extensive experiment.

8.1.4 Modelling of Thick Slots

The motivation for making a thick slot may be for structural purposes or to act as a heat sink for active devices. The original formulation in Chapter I outlines the modelling of thick slots by replacing them with a closed cavity and equivalent magnetic currents on the slots. Thus, the cavity dimensions do no have to correspond to the dimensions of the slot, allowing greater flexibility in applying the model to different applications.

In Chapter VII, we numerically investigate the behavior of a structure in which the strip-fed slot couples to the radiating slot through an intervening section of rectangular waveguide, dimensioned to allow the dominant waveguide mode to propagate. The most significant feature of this chapter is the study of the effect of allowing the strip-fed slot and radiating slot to have different lengths. This detunes the structure by stagger tuning each slot to a slightly different frequency, resulting in an apparent increase in bandwidth. In order to achieve a constant slot impedance, the strip offset and/or waveguide length must be adjusted simultaneously with the alteration of slot lengths to compensate for a change in resonant resistance. This is significant, since bandwidth is one of the primary limiting factors for these types of antenna elements.

Experimental verification of this result is left for later work. However, it is expected to be correct since it is a relatively straightforward extension of the remainder of the model which has been validated by experiment. The result is also appealing from our intuitive understanding of the slot behavior.

8.2 Model Limitations

Aside from resource issues such as the matters discussed in section 3.6.3, there are several technical limitations of the methods used in this work which should be pointed out. Some have already been discussed regarding the Standing Wave method, however, the stated limitations of this technique could potentially be circumvented. For example, it has been stated that this method requires a minimum of about one wavelength of line away from the discontinuities in order to estimate the guided wavelength. In some cases, this information can be derived from other methods similar to the two-dimensional analyses derived in Chapter IV. Another restriction is the requirement of only one propagating mode on the line. This constraint, however, is a result of our simple interpretation of the standing wave pattern by locating the relative positions of the peaks or nulls. It is possible, by more sophisticated parameter estimation schemes, to derive the required information even when more modes are present. Of course, these variations may introduce their own requirements which may or may not be beneficial.

A more serious limitation involves the two-port microstrip-fed slots discussed in Chapter VI. It has been shown that the feed-through apertures, which allow the strip access to the cavity, can have a significant influence on the behavior of the slot. While we have demonstrated that this effect can be effectively compensated for in the cases studied, numerical experiments have shown that this technique is limited to strips which are significantly offset from the cavity centerline (perhaps 25% or more). It is suspected that this is due to certain assumptions made about the behavior of the higher order modes at the feed-through apertures. Specifically, the first-order correction technique we have applied does not account for potential interactions between the wall aperture, the strip and the reactive fields of higher order modes. This interaction may have a profound influence on the amplitude and phase of the TE_{10} mode, as well as the dominant mode, which in turn

may significantly alter the field on the slot. The effect would be enhanced for a centered strip since, not only is the TE_{10} mode more strongly excited at the slot, but also it is more strongly coupled to the feed-through aperture. Thus, the field on the slot may not be correctly determined under these conditions and will lead to incorrect slot impedance values. The rectification of the situation is, of course, to expand the model to include an explicit representation of the feed-through apertures, which would fully account for their influence.

Other limitations of the models are not unique to this particular approach and need not be discussed in detail. For example, all numerical models involve finite approximations to reality and therefore involve some errors in their representations. Nevertheless, full-wave integral equation techniques such as used here, have been proven to provide some of the most accurate and reliable models available for the simulation of a wide variety of problems.

8.3 Recommendation for Future Work

Several applications should be further investigated based on the formulations presented and form the basis for extensions to this work. The first instance would employ the transformations derived in Chapter III to study the case discussed in [62]. This case is of interest because the sensitivity of the impedance to the strip offset for the geometry of Chapter VI may place unduly stringent tolerance requirements on the fabrications process. The application of the full-wave techniques to this problem may make possible the elimination of the semi-empirical factors used in [62]. Since the feed-through apertures could be significantly offset from the cavity centerline, the apparent problem with their neglect in the present model may be avoided.

Another case to consider is the 'T-Bar' fed slot which has the geometry illustrated in Figure 8.1. The formulation for extracting the impedance of the equivalent impedance could follow the Reaction Method used in Chapter VI by applying the Reciprocity Theorem

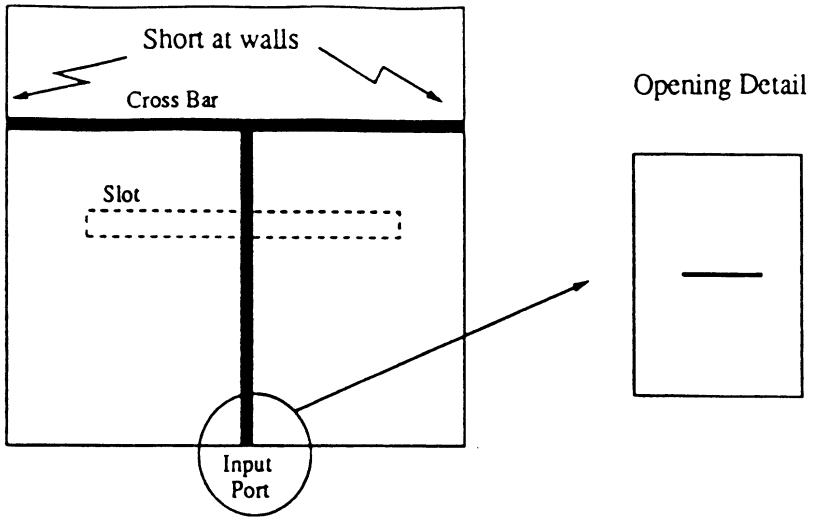

Figure 8.1: T-Bar fed slot geometry.

to the two cases shown in Figure 8.2. Here, in both cases, the strip feed line is terminated by the cross-bar within the cavity. We now identify the reflected fields supported by the currents on the strip in the cavity, case 'b', as

$$\overline{E}_K = \Gamma_S \left(\overline{e}_{TEM} - \hat{l} \cdot \overline{E}_{TEM}\right) e^{j\beta l} \tag{8.1}$$

$$\overline{H}_K = -\Gamma_S \left(\overline{h}_{TEM} - \hat{l} \cdot \overline{H}_{TEM}\right) e^{j\beta l} \tag{8.2}$$

These are the fields associated with the dominant stripline mode produced by the scattering of the slot as before, and it is still assumed that the dominant mode is unaffected by the required aperture in the cavity wall. The fields supported by the currents in the 'a' case, however, are now given by

$$\overline{E}_L = (e^{-j\beta l} + \Gamma_L e^{j\beta l})\overline{e}_{TEM} + (e^{-j\beta l} - \Gamma_L e^{j\beta l})\, \hat{l} \cdot \overline{E}_{TEM} \tag{8.3}$$

$$\overline{H}_L = (e^{-j\beta l} - \Gamma_L e^{j\beta l})\overline{h}_{TEM} + (e^{-j\beta l} + \Gamma_L e^{j\beta l})\, \hat{l} \cdot \overline{H}_{TEM} \tag{8.4}$$

where Γ_L is the reflection coefficient of the T-bar line without the slot present, referenced to the location of the slot on the line, or the reference point for the slot, if not at the plane

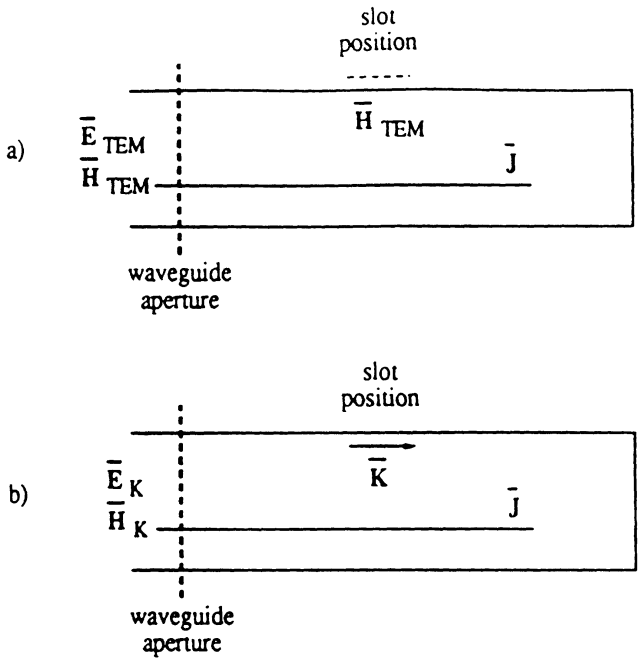

Figure 8.2: Two cases for application of the Reciprocity Theorem for the T-bar fed case.

of the slot. The reflection coefficient on the line is now given by

$$\Gamma_S = -\frac{1}{2}\frac{\iint_{slot} \bar{H}^a_{TEM} \cdot \bar{K}\, dS}{\iint_{waveguide} (\bar{E}_{TEM} \times \bar{H}_{TEM}) \cdot (-\hat{l})\, dS} - \Gamma_L \qquad (8.5)$$

We now also need to know Γ_L from which we can find $\bar{H}^a_{TEM}$ which we then use as an excitation for the cavity problem to find $\bar{K}$, as before. Accurately knowing all these terms, we should be able to produce the reflection coefficient for the slot from which the slot impedance and circuit parameters can be derived. One difficulty in this approach is forseen to be the determination of Γ_L. This problem would be straightforward except for the fact that for the dimensions of the cavity, more than one mode can propagate on the line. To derive Γ_L for the dominant mode on such a line would require further development as discussed above. Also the question of the effect of the feed-through aperture needs to be resolved which by itself can be viewed as an extension of the treatment of wires in Chapter IV.

Another topic which should be further developed for application to the radiating slots is the use of a power balance formulation. If we assume that the walls and materials in the cavity are loss-less, which we have done throughout, then the resistive part of the impedance for the T-bar fed slot is directly proportional to the total radiated power from the slot. This can be determined by integrating the radiation pattern of the slot field over the entire half space which can be done in the far field, given the field on the slot. For uncovered slots, this is a straightforward procedure since the Equivalence Principle can be used to replace the slot magnetic current by an equivalent magnetic dipole current in free space for which the total radiated power can easily be derived. For the covered slots, the situation is a little more complicated, due to the presence of surface waves in the dielectric; however, the integration can be performed in the far-field, in which case asymptotic expressions can be used with steepest descent path integration techniques. This method has been applied to other problems in the past where the slot voltage distribution has an assumed form at resonance [21, 58, 67, 62], but should be equally applicable with the present technique where we can determine the actual distribution at resonance.

Finally, it is suggested that the model could be extended to allow arbitrarily shaped slots and stripline configurations. It is well known that a wider slot has a broader bandwidth and that loading of the slot ends with different shapes also has some influence. This capability could be achieved by using rooftop basis functions which approximate the current in a piecewise fashion in the two planar slot dimensions. As the slot is made wider, however, one would likely need to model both directions of current as described in Chapter III.

APPENDICES

APPENDIX A

Vector Wave Function Expansions and Relations

By convention, $\bar{L}$, $\bar{M}$ and $\bar{N}$ are used throughout the text to denote the Vector Wave Functions (VWFs) defined by

$$\bar{L} = \nabla\Psi \tag{A.1}$$

$$\bar{M} = \nabla \times \Psi\hat{x}_i = \frac{1}{\kappa}\nabla \times \bar{N} \tag{A.2}$$

$$\bar{N} = \frac{1}{\kappa}\nabla \times \nabla \times \Psi\hat{x}_i = \frac{1}{\kappa}\nabla \times \bar{M} \tag{A.3}$$

These form a complete set of solutions to the homogeneous wave equation $\nabla \times \nabla \times \overline{F} - K^2\overline{F} = 0$ when Ψ is the scalar function solution to the equation $\nabla^2\Psi + \kappa^2\Psi = 0$. The particular solution for Ψ is chosen to satisfy the boundary conditions of the problem. The $\hat{x}_i$ unit vector is called the 'piloting vector' which determines the forms of $\bar{L}$, $\bar{M}$ and $\bar{N}$ and κ is the separation constant $\kappa^2 = k_x^2 + k_y^2 + k_z^2$. In this appendix, the expansions of various vector wave functions (VWFs) used throughout the text are provided as a convenient reference. In addition, some identities used to reduce some of the derived expressions to simpler forms are provided.

By convention, $\bar{L}$, $\bar{M}$ and $\bar{N}$ are assumed throughout to be formed from the generating function $\Psi = e^{-j(k_x x + k_y y + k_z z)}$ with $\hat{z}$ as the piloting vector unless indicated otherwise by additional subscripts, superscripts or in the text. A common superscript to be used will be a prime ($'$) which will imply both that the x, y and z dependence will be x', y' and z' corre-

sponding to source coordinates, and that the wavenumbers k_x, k_y and k_z will be led by a j instead of a $-j$ if the functional dependence is the exponential, e.g., $\bar{M}' \sim e^{j(k_x x' + k_y y' + k_z z')}$. Also, a notational convention has been established which should eliminate ambiguity when subscripts are used to imply trigonometric dependence. Specifically, subscripts 'o' and 'e' are used to indicate sine and cosine variation of the generating function, respectively. When these are used, the arguments will be provided in one-to-one correspondence to indicate the variable to which the trigonometric function applies. For example, the function $\bar{M}_{eo}[k_x, k_y, k_z(z-c)]$ implies that the generating function is $\Psi_{eo}[k_x, k_y, k_z(z-c)]$. Ψ_{eo} must then have the form $[\cos k_x x \sin k_y y e^{jk_z(z-c)}]$, since the first two arguments are k_x and k_y, corresponding to the 'e' and 'o' subscripts, respectively. This example also illustrates the additional specification of spatial coordinate dependencies as in $(z-c)$ instead of just z.

Parallel Plate:

$$\Psi_e(k_x) = \cos k_x x e^{-j(k_y y + k_z z)} \tag{A.4}$$

$$\begin{aligned} \bar{M}_e(k_x) &= \nabla \times \Psi_{ee}(k_x)\hat{z} \\ &= [-\hat{x} j k_y \cos k_x x + \hat{y} k_x \sin k_x x] e^{-j(k_y y + k_z z)} \end{aligned} \tag{A.5}$$

$$\begin{aligned} \bar{N}_e(k_x) &= \frac{1}{\kappa} \nabla \times \nabla \times \Psi_{ee}(k_x)\hat{z} \\ &= \frac{1}{\kappa} [\hat{x} j k_x k_z \sin k_x x - \hat{y} k_y k_z \cos k_x x + \hat{z}(k_x^2 + k_y^2) \cos k_x x] e^{-j(k_y y + k_z z)} \end{aligned} \tag{A.6}$$

$$\Psi_o(k_x) = \sin k_x x e^{-j(k_y y + k_z z)} \tag{A.7}$$

$$\begin{aligned} \bar{M}_o(k_x) &= \nabla \times \Psi_{oo}(k_x)\hat{z} \\ &= [-\hat{x} j k_y \sin k_x x + \hat{y} k_x \cos k_x x] e^{-j(k_y y + k_z z)} \end{aligned} \tag{A.8}$$

$$\begin{aligned} \bar{N}_o(k_x) &= \frac{1}{\kappa} \nabla \times \nabla \times \Psi_o(k_x)\hat{z} \\ &= \frac{1}{\kappa} [\hat{x} j k_x k_z \cos k_x x - \hat{y} k_y k_z \sin k_x x - \hat{z}\,(k_x^2 + k_y^2) \sin k_x x] e^{-j(k_y y + k_z z)} \end{aligned} \tag{A.9}$$

Rectangular Waveguide:

$$\Psi_{ee}(k_x, k_y) = \cos k_x x \cos k_y y e^{-jk_z z} \tag{A.10}$$

$$\begin{aligned}\bar{M}_{ee}(k_x, k_y) &= \nabla \times \Psi_{ee}(k_x, k_y)\hat{z} \\ &= [-\hat{x}\, k_y \cos k_x x \sin k_y y + \hat{y}\, k_x \sin k_x x \cos k_y y]e^{-jk_z z}\end{aligned} \tag{A.11}$$

$$\begin{aligned}\bar{N}_{ee}(k_x, k_y) &= \frac{1}{\kappa}\nabla \times \nabla \times \Psi_{ee}(k_x, k_y)\hat{z} \\ &= \frac{1}{\kappa}[\hat{x}\, jk_x k \sin k_x x \cos k_y y + \hat{y}\, jk_y k \cos k_x x \sin k_y y \\ &\qquad + \hat{z}\,(k_x^2 + k_y^2)\cos k_x x \cos k_y y]e^{-jk_z z}\end{aligned} \tag{A.12}$$

$$\Psi_{oo}(k_x, k_y) = \sin k_x x \sin k_y y e^{-jk_z z} \tag{A.13}$$

$$\begin{aligned}\bar{M}_{oo}(k_x, k_y) &= \nabla \times \Psi_{oo}(k_x, k_y)\hat{z} \\ &= [\hat{x}\, k_y \sin k_x x \cos k_y y - \hat{y} k_x \cos k_x x \sin k_y y]e^{-jk_z z}\end{aligned} \tag{A.14}$$

$$\begin{aligned}\bar{N}_{oo}(k_x, k_y) &= \frac{1}{\kappa}\nabla \times \bar{M}_{oo}(k_x, k_y) \\ &= \frac{1}{\kappa}[-\hat{x}\, jk_x k \cos k_x x \sin k_y y - \hat{y}\, jk_y k \sin k_x x \cos k_y y \\ &\qquad + \hat{z}\,(k_x^2 + k_y^2)\sin k_x x \sin k_y y]e^{-jk_z z}\end{aligned} \tag{A.15}$$

$$\Psi_{eo}(k_x, k_y) = \cos k_x x \sin k_y y e^{-jk_z z} \tag{A.16}$$

$$\begin{aligned}\bar{M}_{eo}(k_x, k_y) &= \nabla \times \Psi_{eo}(k_x, k_y)\hat{z} \\ &= [\hat{x} k_x \cos k_x x \cos k_y y + \hat{y}\, k_x \sin k_x x \sin k_y y]e^{-jk_z z}\end{aligned} \tag{A.17}$$

$$\begin{aligned}\bar{N}_{eo}(k_x, k_y) &= \frac{1}{\kappa}\nabla \times \nabla \times \Psi_{eo}(k_x, k_y)\hat{z} \\ &= \frac{1}{\kappa}[\hat{x} jk_x k_z \sin k_x x \sin k_y y - \hat{y} jk_y k_z \cos k_x x \cos k_y y \\ &\qquad + \hat{z}(k_x^2 + k_y^2)\sin k_x x \sin k_y y]e^{-jk_z z}\end{aligned} \tag{A.18}$$

$$\Psi_{oe}(k_x, k_y) = \sin k_x x \cos k_y y e^{-jk_z z} \tag{A.19}$$

$$\bar{M}_{oe}(k_x, k_y) = \nabla \times \Psi_{oe}(k_x, k_y)\hat{z}$$

$$= [-\hat{x}k_y \sin k_x x \sin k_y y - \hat{y}k_x \cos k_x x \cos k_y y]e^{-jk_z z} \quad (A.20)$$

$$\bar{N}_{oe}(k_x, k_y) = \frac{1}{\kappa}\nabla \times \bar{M}_{oe}(k_x, k_y)$$

$$= \frac{1}{\kappa}[-\hat{x}jk_x k_z \cos k_x x \cos k_y y + \hat{y}jk_y k_z \sin k_x x \sin k_y y$$

$$+\hat{z}(k_x^2 + k_y^2) \sin k_x x \cos k_y y]e^{-jk_z z} \quad (A.21)$$

Rectangular Cavities:

$$\bar{M}_{eee}(k_x, k_y, k_z) = \nabla \times [\hat{z} \cos k_x x \cos k_y y \cos k_z z]$$

$$+ \quad -\hat{x}\ k_y \cos k_x x \sin k_y y \cos k_z z + \hat{y}\ k_x \sin k_x x \cos k_y y \cos k_z z \quad (A.22)$$

$$\bar{M}_{eeo}(k_x, k_y, k_z) = \nabla \times [\hat{z} \cos k_x x \cos k_y y \sin k_z z]$$

$$= -\hat{x}\ k_y \cos k_x x \sin k_y y \sin k_z z + \hat{y}\ k_x \sin k_x x \cos k_y y \sin k_z z \quad (A.23)$$

$$\bar{M}_{ooo}(k_x, k_y, k_z) = \nabla \times [\hat{z} \sin k_x x \sin k_y y \sin k_z z]$$

$$= +\hat{x}\ k_y \sin k_x x \cos k_y y \sin k_z z - \hat{y}\ k_x \cos k_x x \sin k_y y \sin k_z z \quad (A.24)$$

$$\bar{M}_{ooe}(k_x, k_y, k_z) = \nabla \times [\hat{z} \sin k_x x \sin k_y y \cos k_z z]$$

$$= +\hat{x}\ k_y \sin k_x x \cos k_y y \cos k_z z - \hat{y}\ k_x \cos k_x x \sin k_y y \cos k_z z \quad (A.25)$$

$$\bar{N}_{eee}(k_x, k_y, k_z) = \frac{1}{\kappa}\nabla \times \bar{M}_{eee}(k_x, k_y, k_z)$$

$$= \frac{1}{\kappa}[+\hat{x}\ k_x k_z \sin k_x x \cos k_y y \sin k_z z + \hat{y}\ k_y k_z \cos k_x x \sin k_y y \sin k_z z$$

$$+\hat{z}\ (k_x^2 + k_y^2) \cos k_x x \cos k_y y \cos k_z z] \quad (A.26)$$

$$\bar{N}_{eeo}(k_x, k_y, k_z) = \frac{1}{\kappa}\nabla \times \bar{M}_{eeo}(k_x, k_y, k_z)$$

$$\frac{1}{\kappa}[-\hat{x}\ k_x k_z \sin k_x x \cos k_y y \cos k_z z - \hat{y}\ k_y k_z \cos k_x x \sin k_y y \cos k_z z$$

$$+\hat{z}\ (k_x^2 + k_y^2) \cos k_x x \cos k_y y \sin k_z z] \quad (A.27)$$

$$\bar{N}_{ooo}(k_x, k_y, k_z) = \frac{1}{\kappa}\nabla \times \bar{M}_{ooo}(k_x, k_y, k_z)$$

$$\frac{1}{\kappa}[+\hat{x}\ k_x k_z \cos k_x x \sin k_y y \cos k_z z + \hat{y}\ k_y k_z \sin k_x x \cos k_y y \cos k_z z$$

$$+\hat{z}\ (k_x^2 + k_y^2) \sin k_x x \sin k_y y \sin k_z z] \quad (A.28)$$

$$\bar{N}_{ooe}(k_x,k_y,k_z) = \frac{1}{\kappa}\nabla \times \bar{M}_{ooe}(k_x,k_y,k_z)$$

$$\frac{1}{\kappa}[-\hat{x}\ k_x k_z \cos k_x x \sin k_y y \sin k_z z - \hat{y}\ k_y k_z \sin k_x x \cos k_y y \sin k_z z$$

$$+\hat{z}\ (k_x^2+k_y^2)\sin k_x x \sin k_y y \cos k_z z] \qquad \text{(A.29)}$$

Identities:

$$e^{jk_zc}\bar{M}(k_z) \pm e^{-jk_zc}\bar{M}(-k_z) = \bar{M}[k_z(z-c)] \pm \bar{M}[-k_z(z-c)]$$

$$= \begin{cases} +2\bar{M}_e[k_z(z-c)] \\ -2j\bar{M}_o[k_z(z-c)] \end{cases} \qquad \text{(A.30)}$$

$$e^{jk_zc}\bar{M}(k_z) \pm e^{-jk_zc}\bar{M}(-k_z) = \bar{M}[k_z(z-c)] \pm \bar{M}[-k_z(z-c)]$$

$$= \begin{cases} +2\bar{M}_e[k_z(z-c)] \\ -2j\bar{M}_o[k_z(z-c)] \end{cases} \qquad \text{(A.31)}$$

$$e^{jk_zc}\bar{N}(k_z) \pm e^{-jk_zc}\bar{N}(-k_z) = \bar{N}[k_z(z-c)] \pm \bar{N}[-k_z(z-c)]$$

$$= \begin{cases} +2\bar{N}_e[k_z(z-c)] \\ -2j\bar{N}_o[k_z(z-c)] \end{cases} \qquad \text{(A.32)}$$

$$e^{jk_zc}\bar{N}(k_z) \pm e^{-jk_zc}\bar{N}(-k_z) = \bar{N}[k_z(z-c)] \pm \bar{N}[-k_z(z-c)]$$

$$= \begin{cases} +2\bar{N}_e[k_z(z-c)] \\ -2j\bar{N}_o[k_z(z-c)] \end{cases} \qquad \text{(A.33)}$$

$$e^{jk_zc}\bar{M}_e(k_x,k_z) \pm e^{-jk_zc}\bar{M}_e(k_x,-k_z) = \bar{M}_e[k_x,k_z(z-c)] \pm \bar{M}_e[k_x,-k_z(z-c)]$$

$$= \begin{cases} +2\bar{M}_{ee}[k_x,k_z(z-c)] \\ -2j\bar{M}_{eo}[k_x,k_z(z-c)] \end{cases} \qquad \text{(A.34)}$$

$$e^{jk_zc}\bar{M}_o(k_x,k_z) \pm e^{-jk_zc}\bar{M}_o(k_x,-k_z) = \bar{M}_o[k_x,k_z(z-c)] \pm \bar{M}_o[k_x,-k_z(z-c)]$$

$$= \begin{cases} +2\bar{M}_{oe}[k_x,k_z(z-c)] \\ -2j\bar{M}_{oo}[k_x,k_z(z-c)] \end{cases} \qquad \text{(A.35)}$$

$$e^{jk_zc}\bar{N}_e(k_x,k_z) \pm e^{-jk_zc}\bar{N}_e(k_x,-k_z) = \bar{N}_e[k_x,k_z(z-c)] \pm \bar{N}_e[k_x,-k_z(z-c)]$$

$$= \begin{cases} +2\bar{N}_{ee}[k_x,k_z(z-c)] \\ -2j\bar{N}_{eo}[k_x,k_z(z-c)] \end{cases} \qquad \text{(A.36)}$$

$$e^{jk_zc}\bar{N}_o(k_x,k_z) \pm e^{-jk_zc}\bar{N}_o(k_x,-k_z) = \bar{N}_o[k_x,k_z(z-c)] \pm \bar{N}_o[k_x,-k_z(z-c)]$$

$$= \begin{cases} +2\bar{N}_{oe}[k_x,k_z(z-c)] \\ -2j\bar{N}_{oo}[k_x,k_z(z-c)] \end{cases} \qquad \text{(A.37)}$$

$$e^{jk_zc}\bar{\mathrm{M}}_{\mathrm{ee}}(k_x,k_y,k_z)\pm e^{-jk_zc}\bar{\mathrm{M}}_{\mathrm{ee}}(k_x,k_y,-k_z)$$

$$\begin{aligned}&=\bar{\mathrm{M}}_{\mathrm{ee}}[k_x,k_y,k_z(z-c)]\pm\bar{\mathrm{M}}_{\mathrm{ee}}[k_x,k_y,-k_z(z-c)]\\&=\begin{cases}+2\bar{\mathrm{M}}_{\mathrm{eee}}[k_x,k_y,k_z(z-c)]\\-2j\bar{\mathrm{M}}_{\mathrm{eeo}}[k_x,k_y,k_z(z-c)]\end{cases}\end{aligned}\tag{A.38}$$

$$e^{jk_zc}\bar{\mathrm{M}}_{\mathrm{oo}}(k_x,k_y,k_z)\pm e^{-jk_zc}\bar{\mathrm{M}}_{\mathrm{oo}}(k_x,k_y,-k_z)$$

$$\begin{aligned}&=\bar{\mathrm{M}}_{\mathrm{oo}}[k_x,k_y,k_z(z-c)]\pm\bar{\mathrm{M}}_{\mathrm{oo}}[k_x,k_y,-k_z(z-c)]\\&=\begin{cases}+2\bar{\mathrm{M}}_{\mathrm{ooe}}[k_x,k_y,k_z(z-c)]\\-2j\bar{\mathrm{M}}_{\mathrm{ooo}}[k_x,k_y,k_z(z-c)]\end{cases}\end{aligned}\tag{A.39}$$

$$e^{jk_zc}\bar{\mathrm{N}}_{\mathrm{ee}}(k_x,k_y,k_z)\pm e^{-jk_zc}\bar{\mathrm{N}}_{\mathrm{ee}}(k_x,k_y,-k_z)$$

$$\begin{aligned}&=\bar{\mathrm{N}}_{\mathrm{ee}}[k_x,k_y,k_z(z-c)]\pm\bar{\mathrm{N}}_{\mathrm{ee}}[k_x,k_y,-k_z(z-c)]\\&=\begin{cases}+2\bar{\mathrm{N}}_{\mathrm{eee}}[k_x,k_y,k_z(z-c)]\\-2j\bar{\mathrm{N}}_{\mathrm{eeo}}[k_x,k_y,k_z(z-c)]\end{cases}\end{aligned}\tag{A.40}$$

$$e^{jk_zc}\bar{\mathrm{N}}_{\mathrm{oo}}(k_x,k_y,k_z)\pm e^{-jk_zc}\bar{\mathrm{N}}_{\mathrm{oo}}(k_x,k_y,-k_z)$$

$$\begin{aligned}&=\bar{\mathrm{N}}_{\mathrm{oo}}[k_x,k_y,k_z(z-c)]\pm\bar{\mathrm{N}}_{\mathrm{oo}}[k_x,k_y,-k_z(z-c)]\\&=\begin{cases}+2\bar{\mathrm{N}}_{\mathrm{ooe}}[k_x,k_y,k_z(z-c)]\\-2j\bar{\mathrm{N}}_{\mathrm{ooo}}[k_x,k_y,k_z(z-c)]\end{cases}\end{aligned}\tag{A.41}$$

APPENDIX B

On the Use of Vector Potential Functions for the Derivation of Green's Functions

In previous literature there has been considerable discussion on the treatment of sources in waveguides or cavities, particularly the problem of a longitudinal slot in the broad wall of a rectangular guide. It has been stated and generally accepted that an additional "mode" needs to be included in the Green's function for the waveguide to accurately represent the currents at the slot [86]. However, the origin and derivation of this mode is somewhat unclear.

The difficulty arises from an incomplete treatment of the potential theory in the source region for these problems. It is identical to the difficulty associated with the vector wave function or direct field expansion formulations for which the problem has been adequately resolved after much discussion in the literature over an extended period of time [81, 65, 42, 15, 77, 11]. Because the use of vector wave functions as used in this work is perhaps somewhat unfamiliar and since the difficulties for the vector potential method are very closely related, this appendix presents a discussion of the use of potential theory for source regions to demonstrate the origin of the required 'additional' terms.

B.1 Potential Theory Solutions for Electric Currents

To examine the method, we will first consider the fields in a rectangular waveguide excited by a point source of longitudinally directed electric current. The waveguide axis is

assumed to lie along the $\hat{z}$ direction.

We must find solutions to Maxwell's equations as follows:

$$\nabla \times \overline{\mathrm{E}} = -j\omega\mu\,\overline{\mathrm{H}} \tag{B.1}$$

$$\nabla \times \overline{\mathrm{H}} = j\omega\epsilon\,\overline{\mathrm{E}} + \hat{z}\delta(x-x')\delta(y-y')\delta(z-z') \tag{B.2}$$

where the assumptions stated in section 1.3.1 are employed and in which we have introduced the current source

$$\bar{\mathrm{J}} = \hat{z}\delta(x-x')\delta(y-y')\delta(z-z') \tag{B.3}$$

Since $\nabla \cdot \overline{\mathrm{H}} = 0$ we can represent $\overline{\mathrm{H}}$ by

$$\overline{\mathrm{H}} = \frac{1}{\mu}\nabla \times \overline{\mathrm{A}} \tag{B.4}$$

where $\overline{\mathrm{A}}$ is, as yet, an arbitrary unknown vector function. Using Equation (B.4) in (B.1) we find

$$\nabla \times \overline{\mathrm{E}} = -j\omega\nabla \times \overline{\mathrm{A}} \tag{B.5}$$

which we can integrate to get

$$\overline{\mathrm{E}} = -j\omega\,\overline{\mathrm{A}} + \nabla\Phi \tag{B.6}$$

where Φ is a scalar function representing the constant of integration.

Using Equation (B.6) in (B.2) we find the relationship between $\overline{\mathrm{A}}$ and Φ must satisfy

$$\nabla \times \nabla \times \overline{\mathrm{A}} - k^2\,\overline{\mathrm{A}} - j\omega\epsilon\mu\nabla\Phi = \mu\bar{\mathrm{J}} \tag{B.7}$$

As $\overline{\mathrm{A}}$ is arbitrary, its specification determines Φ through Equation (B.7), to within an incidental constant. Equivalently, Φ may be arbitrarily specified which in turn defines $\overline{\mathrm{A}}$. Both, of course, are not entirely arbitrary since we must consider the resulting boundary conditions on the $\overline{\mathrm{E}}$ and $\overline{\mathrm{H}}$ fields. Thus, we are free to choose Φ in order to simplify

Equation (B.7) to a form for which the solution is either known or may be readily found. This step is really the quintessential motivation for the use of the vector potential method, since the overall problem is reduced to the solution of a single, presumably simple, equation.

The selection of two conditions which specify $\overline{A}$ or Φ may be familiar. The first is the Coulomb condition, or Coulomb 'gauge', in which $\overline{A}$ is assumed to satisfy $\nabla \cdot \overline{A} = 0$. From Equation (B.7) it can then be shown that Φ satisfies Poisson's equation:

$$\nabla^2 \Phi = -\frac{j}{\omega \epsilon} \nabla \cdot \bar{J} \tag{B.8}$$

however, this does not lead to a simple equation for $\overline{A}$. Thus, this approach is not generally used [53].

The Lorenz gauge [82] is by far more commonly used in which it is assumed that $\nabla \cdot \overline{A} = j\omega\mu\epsilon\Phi$. This reduces Equation (B.7) to ($\nabla^2 = -\nabla \times \nabla \times \quad + \nabla\nabla\cdot$)

$$\nabla^2 \overline{A} + k^2 \overline{A} = -\mu \bar{J} \tag{B.9}$$

To satisfy this *vector* equation *requires* that we choose $\bar{A}$ with a component in the same direction as $\bar{J}$, reducing it to a *scalar* equation. In our case, for example, we set $\overline{A} = A_z \hat{z}$ reducing Equation (B.9) to

$$\nabla^2 A_z + k^2 A_z = -\mu\delta(\bar{R} - \bar{R}') \tag{B.10}$$

the solution of which can be found by separation of variables and is the primary topic for much of the remainder of this appendix.

Before proceeding however, we must pause to distinguish this approach with other approaches involving potential functions. It is widely recognized that the fields in waveguide can be expressed in terms of a variety of combinations of potential functions, most notably in this context, the $\overline{A}$ and $\overline{F}$ potentials. For example, the complete set of homogeneous solutions for rectangular waveguide can be written in terms of $\overline{A} = A_z \hat{z}$ and $\overline{F} = F_z \hat{z}$

where $\overline{H} = \frac{1}{\mu}\nabla \times \overline{A}$ and $\overline{E} = \frac{1}{\epsilon}\nabla \times \overline{F}$ yielding the TM and TE waveguide modes respectively. Similarly, if we use $\overline{A} = A_x\hat{x}$ and $\overline{F} = F_x\hat{x}$, we produce the LSM and LSE modes which are TM and TE to the $\hat{x}$ direction respectively. Various other combinations are possible, not restricted to the rectangular waveguide problem, as noted in [25] for the dielectric half space. We should recognize that these potentials do not proceed from an attempt to solve the inhomogeneous field equations through the use of potentials, as above, but rather are solutions to the homogeneous (source-free) equations which allow a great deal more flexibility. Solving the inhomogeneous case by expanding the fields in terms of homogeneous potentials and enforcing the boundary conditions at the source, amounts to a field expansion method closely related to the vector wave function method employed in the main body of this work. As such, they perhaps should not properly be referred to as 'Potential Theory' methods as is often done. It is in these cases that the functions themselves can truly be called 'auxiliary potentials', since they are not directly solved for, but rather are only a vehicle to express the field in a simple way. It is also noted that these methods often introduce the radiation condition into the potentials which prevents them from being truly homogeneous solutions as will become evident.

Returning to the solution of Equation (B.10), the particular solution to this inhomogeneous equation can be constructed from the general homogeneous solutions. Once A_z has been found, the fields will be given by

$$\begin{aligned} \overline{H} &= \frac{1}{\mu}\nabla \times (A_z\hat{z}) \\ &= \frac{1}{\mu}\frac{\partial A_z}{\partial y}\hat{x} - \frac{1}{\mu}\frac{\partial A_z}{\partial x}\hat{y} \end{aligned} \tag{B.11}$$

$$\begin{aligned} \overline{E} &= -j\omega A_z\hat{z} + \frac{\nabla\nabla\cdot(A_z\hat{z})}{j\omega\mu\epsilon} \\ &= \frac{1}{j\omega\mu\epsilon}\left[\frac{\partial^2 A_z}{\partial x\partial z}\hat{x} + \frac{\partial^2 A_z}{\partial y\partial z}\hat{y}\right] + \left[\frac{1}{j\omega\mu\epsilon}\frac{\partial^2 A_z}{\partial z^2} - j\omega A_z\right]\hat{z} \end{aligned} \tag{B.12}$$

The homogeneous solutions are readily found by separation of variables and can be

written in the form

$$A_z = [A_1 \cos k_x x + A_2 \sin k_x x][B_1 \cos k_y y + B_2 \sin k_y y][C_1 e^{+jk_z(z-z')} + C_2 e^{-jk_z(z-z')}] \tag{B.13}$$

where $k^2 = k_x^2 + k_y^2 + k_z^2$. Applying the boundary condition $\hat{n} \times \overline{\mathrm{E}} = 0$ at the walls of the waveguide reduces (B.13) to

$$A_z = \sin k_x x \sin k_y y[C_1 e^{+jk_z(z-z')} + C_2 e^{-jk_z(z-z')}] \tag{B.14}$$

where $k_m = m\pi/a$, $k_n = n\pi/b$, and (m, n) are any integers. The eigenvalues k_m and k_n are thus infinite discrete sets while k_z has a continuous spectrum.

Before proceeding, it is instructional to verify that this solution satisfies the homogeneous form of Equation (B.10) which can be readily done by direct differentiation. In rectangular coordinates the ∇^2 operator is $\nabla^2 = \frac{\partial^2}{\partial x^2} + \frac{\partial^2}{\partial y^2} + \frac{\partial^2}{\partial z^2}$ which allows the x and y partial derivatives to be performed by inspection leaving

$$-k_m^2 A_z - k_n^2 A_z + \frac{\partial^2 A_z}{\partial z^2} + k^2 A_z = 0 \tag{B.15}$$

Since $k^2 = k_m^2 + k_m^2 + k_z^2$, Equation (B.15) reduces to

$$\frac{\partial^2 A_z}{\partial z^2} + k_z^2 A_z = 0 \tag{B.16}$$

Since A_z is continuous in z, the second derivative can be performed without difficulty so it is obvious that (B.16) is satisfied and (B.14) is confirmed as a solution to the homogeneous equation.

We now proceed as usual and impose the 'radiation condition' on the solution; that is,

$$\overline{\mathrm{E}} \to 0, \ \overline{\mathrm{H}} \to 0, \ \text{as} \ |z| \to \infty \tag{B.17}$$

with finite losses. (Or equivalently, require outward travelling waves outside of all source regions.) Of course we have anticipated this condition in the form of the solution's z

dependence and we now set

$$A_z = \sin k_m x \sin k_n y \begin{cases} C_1 e^{-jk_z(z-z')} & z \geq z' \\ C_2 e^{jk_z(z-z')} & z < z' \end{cases} \tag{B.18}$$

Notice the implications of imposing the radiation condition. Applying the left hand side of the scalar wave equation (B.10) we can immediately see that the solution (B.18) remains homogeneous in the entire domain with respect to the x and y dependence. Applying the remaining operations - left hand side of Equation (B.16) - we find

$$\frac{\partial A_z}{\partial z} = \sin k_m x \sin k_n y \begin{cases} -jk_z C_1 e^{-jk_z(z-z')} & z > z' \\ jk_z C_2 e^{jk_z(z-z')} & z < z' \end{cases} + [C_1 - C_2]\, \delta(z - z') \tag{B.19}$$

Note that the term involving $\delta(z - z')$ comes from the discontinuity in A_z that may exist if $C_1 \neq C_2$. We have performed the derivative by noting that for a function as shown in Figure B.1 a singularity appears at the discontinuity. Note also that the singularity may appear and be defined in the sense of a generalized function at $z = z'$ *whether or not the original function is defined at that point* [26, pp. 21-22].

We can eliminate the singularity in the first derivative by requiring

$$C_1 = C_2 = C \tag{B.20}$$

This is a boundary condition is based on the argument that the potential must approach the same value from either direction at $z = z'$, i.e., it is continuous [13, p. 160]. Then Equation (B.19) becomes

$$\frac{\partial A_z}{\partial z} = jk_z C \sin k_m x \sin k_n y \begin{cases} -e^{-jk_z(z-z')} & z > z' \\ e^{jk_z(z-z')} & z < z' \end{cases} \tag{B.21}$$

However, Equation (B.21) is discontinuous at $z = z'$ and the second derivative is

$$\frac{\partial A_z^2}{\partial z^2} = -k_z^2 C \sin k_m x \sin k_n y \begin{cases} e^{-jk_z(z-z')} & z > z' \\ e^{jk_z(z-z')} & z < z' \end{cases} - 2jk_z C \sin k_m x \sin k_n y\, \delta(z - z') \tag{B.22}$$

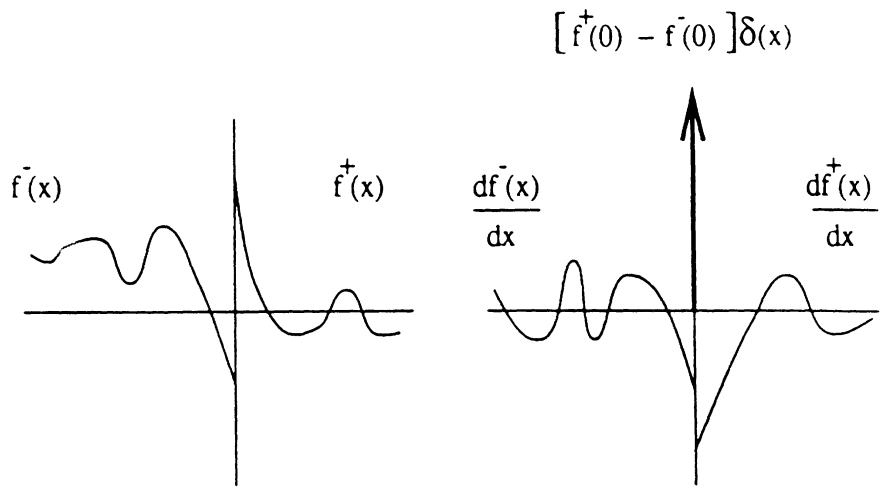

$$\frac{df(x)}{dx} = \begin{cases} \dfrac{df^+(x)}{dx} & x > x' \\ \dfrac{df^-(x)}{dx} & x < x' \end{cases} + [f^+(x) - f^-(x)]\delta(x - x')$$

Figure B.1: The derivative of an arbitrary discontinuous function.

Using Equation (B.22) in (B.16) we find that Equation (B.18) is indeed a homogeneous solution for A_z except at the point $z = z'$. Notice that this result was obtained by imposing the radiation condition alone. The continuity condition was also used but effects only the nature of the singularity in the second derivative at $z = z'$, that is, whether the delta function is produced or its first derivative. Thus, as is intuitively obvious, imposing the radiation condition dictates that the potential must satisfy an inhomogeneous equation with a driving function (source) located at some location between $-\infty < z' < \infty$. Notice that we arbitrarily chose the form of the z dependence so that the discontinuity would fall at $z = z'$. This is, of course, the most reasonable choice, since we ultimately are attempting to solve the source problem and we do not expect discontinuities in the fields in the source-free regions. However, we have not yet attempted to satisfy the original nonhomogeneous equation given by Equation (B.10).

Equation (B.22) suggests that we can take (B.18) as the homogeneous solutions for Equation (B.10) if we *exclude* the point $z = z'$ from the homogeneous solution's domain. We thus avoid the inhomogeneous contribution of the singular term in the second derivative. The complete set of homogeneous solutions of this type (TM) are then

$$A_z = \int_{-\infty}^{\infty} dk_z \sum_{m,n} C_{mn} \sin k_m x \sin k_n y \begin{cases} e^{-jk_z(z-z')} & z > z' \\ e^{jk_z(z-z')} & z < z' \end{cases} \tag{B.23}$$

The homogeneous solutions can be added to the particular solution with arbitrary coefficients without violating Equation (B.10) as long as the the exclusion of the point $z = z'$ is observed, even (especially) for derivatives of A_z. Specifically, this means that the fields arising from the homogeneous solutions are valid everywhere but the $z = z'$ point. Homogeneous solutions are often added, for example, to satisfy new boundary conditions introduced by adding obstacles to the waveguide. In fact, this is the basis for the method of scattering superposition used extensively in this work.

The form of the particular solution is suggested immediately by the singularity encountered in Equation (B.22). Therefore, we assume the particular solution has the form

$$A_z = \sum_{m,n} C_{mn} \sin k_m x \sin k_n y \begin{cases} e^{-jk_z(z-z')} & z > z' \\ e^{jk_z(z-z')} & z < z' \end{cases} \tag{B.24}$$

Note the exclusion of $z = z'$. In this case, however, *we do not exclude $z = z'$ from the solution domain.* As will be seen, this allows the discontinuity to contribute only when the second derivative at $z = z'$ is evaluated and allows the particular solution to be found. This type of exclusion is allowed since this potential is a Green's function which is always defined in the sense of a generalized function. Generally, this means that the function itself has no useful meaning except in the context of an integral, in which case, non-singular isolated points can be removed without effecting the result. However, the point is an *essential* point at which the derivatives must be allowed to exist (in the generalized function sense) in order to satisfy the differential equation.

On applying Equation (B.22) then, we are left to find C_{mn} such that (B.10) is satisfied, that is,

$$-2j\sum_{m,n} C_{mn}k_z \sin k_m x \sin k_n y\, \delta(z-z') = -\mu\delta(x-x')\delta(y-y')\delta(z-z') \quad \text{(B.25)}$$

or

$$\sum_{m,n} C_{mn} \sin k_m x \sin k_n y = \frac{-j\mu}{2k_z}\delta(x-x')\delta(y-y') \quad \text{(B.26)}$$

We can find C_{mn} by multiplying Equation (B.26) by $\sin k_m x \sin k_n y$ and integrating over the cross section of the waveguide getting

$$C_{mn} = \frac{-j2\mu}{k_z ab} \sin k_m x' \sin k_n y' \quad \text{(B.27)}$$

Equation (B.26) thus implies

$$\sum_{m,n} \frac{4}{ab} \sin k_m x \sin k_n y \sin k_m x' \sin k_n y' = \delta(x-x')\delta(y-y') \quad \text{(B.28)}$$

or

$$\sum_{m} \frac{2}{a} \sin k_m x \sin k_m x' = \delta(x-x') \quad \text{(B.29)}$$

$$\sum_{n} \frac{2}{b} \sin k_n y \sin k_n y' = \delta(y-y') \quad \text{(B.30)}$$

which can be shown independently. The particular solution is then

$$A_z = -\sum_{m,n} \frac{j2\mu}{abk_z} \sin k_m x \sin k_n y \sin k_m x' \sin k_n y' \begin{cases} e^{-jk_z(z-z')} & z > z' \\ e^{jk_z(z-z')} & z < z' \end{cases} \quad \text{(B.31)}$$

B.2 Field Behavior – Electric Current

Now that we have the particular solution for the potential, our interest turns to the behavior of the fields, particularly near the source. The $\overline{H}$ field is determined by evaluating Equation (B.4) which yields

$$H_x = -\sum_{m,n} \frac{j2k_n}{abk_z} \sin k_m x \cos k_n y \sin k_m x' \sin k_n y' \begin{cases} e^{-jk_z(z-z')} & z > z' \\ e^{jk_z(z-z')} & z < z' \end{cases} \quad \text{(B.32)}$$

$$H_y = \sum_{m,n} \frac{j2k_m}{abk_z} \cos k_m x \sin k_n y \sin k_m x' \sin k_n y' \begin{cases} e^{-jk_z(z-z')} & z > z' \\ e^{jk_z(z-z')} & z < z' \end{cases} \tag{B.33}$$

$$H_z = 0 \tag{B.34}$$

The $\bar{E}$ field can be found from (B.12) with the Lorenz condition and is

$$E_x = -\sum_{m,n} \frac{j2k_m}{ab\omega\epsilon} \cos k_m x \sin k_n y \sin k_m x' \sin k_n y' \begin{cases} -e^{-jk_z(z-z')} & z > z' \\ e^{jk_z(z-z')} & z < z' \end{cases} \tag{B.35}$$

$$E_y = -\sum_{m,n} \frac{j2k_n}{ab\omega\epsilon} \sin k_m x \cos k_n y \sin k_m x' \sin k_n y' \begin{cases} -e^{-jk_z(z-z')} & z > z' \\ e^{jk_z(z-z')} & z < z' \end{cases} \tag{B.36}$$

$$\begin{aligned} E_z &= \left[\frac{1}{j\omega\mu\epsilon} \frac{\partial^2 A_z}{\partial z^2} - j\omega A_z \right] \\ &= -\sum_{m,n} \frac{j2\mu}{abk_z} \left(\frac{-k_z^2}{j\omega\mu\epsilon} - j\omega \right) \sin k_m x \sin k_n y \sin k_m x' \sin k_n y' \begin{cases} e^{-jk_z(z-z')} & z > z' \\ e^{jk_z(z-z')} & z < z' \end{cases} \\ &\quad -\frac{1}{j\omega\mu\epsilon} \sum_{m,n} \frac{4\mu}{ab} \sin k_m x \sin k_n y \sin k_m x' \sin k_n y' \, \delta(z - z') \\ &= -\sum_{m,n} \frac{2}{ab} \left(\frac{k_m^2 + k_n^2}{\omega\epsilon k_z} \right) \sin k_m x \sin k_n y \sin k_m x' \sin k_n y' \begin{cases} e^{-jk_z(z-z')} & z > z' \\ e^{jk_z(z-z')} & z < z' \end{cases} \\ &\quad -\frac{\delta(x - x')\delta(y - y')\delta(z - z')}{j\omega\epsilon} \end{aligned} \tag{B.37}$$

Thus, we find that the particular solution contains not only the normal (TM) waveguide modes but also a singular term in the $\hat{z}$ component of the $\bar{E}$ field, that is, the addition of the term

$$\bar{E} = -\hat{z} \frac{\delta(x - x')\delta(y - y')\delta(z - z')}{j\omega\epsilon} \tag{B.38}$$

This addition corresponds exactly to the singular term previously found by the vector wave function formulations discussed by many authors (see especially [78]). This term corresponds to the $\hat{z}\hat{z}$ term associated with a dyadic representation.

As was previously pointed out, the function is normally applied to the problem of an unknown current source with an integral of the type:

$$\bar{F}(\bar{R}) = \iiint \bar{\bar{G}}_F(\bar{R}, \bar{R}') \cdot \bar{J}(\bar{R}') dV' \tag{B.39}$$

where $\overline{F}$ is a field or potential and $\bar{\bar{G}}_F$ is a dyadic Green's function of the appropriate type. In the case where $\overline{F}$ is to be a potential, the singular term does not appear directly but should appear when the $\overline{E}$ is found by carefully performing the second derivatives indicated by the $\nabla\nabla \cdot \bar{A}$ operation. Similarly, if $\overline{F}$ is to be the $\overline{E}$ field, the correctly constructed dyadic Green's function will be of the electric field type and, in this case, will have the form

$$\bar{\bar{G}}_E = -\hat{z}\hat{z}\frac{\delta(x-x')\delta(y-y')\delta(z-z')}{j\omega\epsilon} + \bar{\bar{G}}_o \tag{B.40}$$

where $\bar{\bar{G}}_o$ is a modal expression.

Finally, we note that the solution found is the complete solution for $\bar{J} = \hat{z}\delta(\bar{R} - \bar{R}')$ in rectangular waveguide which can be seen to excite only the TM modes. The TE modes can be found by assuming $\overline{E} = \frac{1}{\epsilon}\nabla \times \overline{F}$ which are excited by currents in the other two directions. The point also illustrates the benefit of the vector wave function approach with dyadic analysis. Both the vector potential method and field expansion methods employing auxiliary potentials, when performed on a vector level, require each component of current to be considered separately. In contrast, the dyadic analysis produces the entire Green's function at once. Since all of these methods contain the same pitfalls when the derivatives at discontinuities are not carefully performed, this is the only fundamental difference. Of course, depending on the structures involved, when other beneficial techniques such as the use of impedance boundary conditions and scattering superposition are not employed, the difficulty of the various derivations may increase dramatically.

B.3 Potential Theory Solutions for Magnetic Currents

The necessity of the singular term is particularly evident in the literature pertaining to the analysis of apertures in rectangular waveguides and cavities. In these cases, the problem has a 'dual' nature in that we usually represent the apertures with magnetic currents. The

dual problem can then be handled in exactly the same manner as follows.

We take as the dual form of Maxwell's equations:

$$\nabla \times \overline{\mathrm{E}} = -j\omega\mu\,\overline{\mathrm{H}} - \hat{z}\delta(x-x')\delta(y-y')\delta(z-z') \tag{B.41}$$

$$\nabla \times \overline{\mathrm{H}} = j\omega\epsilon\,\overline{\mathrm{E}} \tag{B.42}$$

where we have introduced the magnetic current source

$$\overline{\mathrm{K}} = \hat{z}\delta(x-x')\delta(y-y')\delta(z-z') \tag{B.43}$$

Since $\nabla \cdot \overline{\mathrm{E}} = 0$ for the dual case, we set

$$\overline{\mathrm{E}} = \frac{1}{\epsilon}\nabla \times \overline{\mathrm{F}} \tag{B.44}$$

and search for solutions to

$$\nabla^2 \overline{\mathrm{F}} + k^2 \overline{\mathrm{F}} = \epsilon\,\overline{\mathrm{K}} \tag{B.45}$$

Because $\overline{\mathrm{K}}$ has only a $\hat{z}$ component we set

$$\overline{\mathrm{F}} = F_z\hat{z} \tag{B.46}$$

reducing Equation (B.45) to

$$\nabla^2 F_z + k^2 F_z = \epsilon\delta(x-x')\delta(y-y')\delta(z-z') \tag{B.47}$$

When F_z has been found, the fields will be given by

$$\begin{aligned}
\overline{\mathrm{E}} &= \frac{1}{\epsilon}\nabla \times (F_z\hat{z}) \\
&= \frac{1}{\epsilon}\frac{\partial F_z}{\partial y}\hat{x} - \frac{1}{\epsilon}\frac{\partial F_z}{\partial x}\hat{y} \qquad \text{(B.48)} \\
\overline{\mathrm{H}} &= j\omega F_z\hat{z} - \frac{\nabla\nabla\cdot(F_z\hat{z})}{j\omega\mu\epsilon} \\
&= -\frac{1}{j\omega\mu\epsilon}\left[\frac{\partial^2 F_z}{\partial x\partial z}\hat{x} + \frac{\partial^2 F_z}{\partial y\partial z}\hat{y}\right] - \left[\frac{1}{j\omega\mu\epsilon}\frac{\partial^2 F_z}{\partial z^2} - j\omega F_z\right]\hat{z} \qquad \text{(B.49)}
\end{aligned}$$

Following a procedure identical to the previous case, the particular solution is found to be

$$F_z = \frac{j\epsilon}{2ab}\sum_{m,n}\frac{\epsilon_m\epsilon_n}{k_z}\cos k_m x\cos k_n y\cos k_m x'\cos k_n y'\begin{cases} e^{-jk_z(z-z')} & z>z' \\ e^{jk_z(z-z')} & z<z' \end{cases} \tag{B.50}$$

where ϵ_m and ϵ_n are the Neumann numbers defined as

$$\epsilon_i = \begin{cases} 2 & i \neq 0 \\ 1 & i = 0 \end{cases} \tag{B.51}$$

Note particularly in this case that for $m = 0$ and $n = 0$, the potential function is non-zero, unlike the previous case, and is the term referred to as the $(0,0)$ 'mode' in [86]. However, as can be seen from the field expansion below, this mode does not make the key contribution at the source, but rather, the additional contribution comes from the singular term.

B.4 Field Behavior – Magnetic Current

The fields produced by the infinitesimal magnetic current source are the following: The $\overline{\mathrm{E}}$ field is determined by evaluating Equation (B.48) which yields

$$E_x = -\sum_{m,n}\frac{j\epsilon_m\epsilon_n k_n}{2k_z ab}\cos k_m x\sin k_n y\cos k_m x'\cos k_n y'\begin{cases} e^{-jk_z(z-z')} & z>z' \\ e^{jk_z(z-z')} & z<z' \end{cases} \tag{B.52}$$

$$E_y = \sum_{m,n}\frac{j\epsilon_m\epsilon_n k_m}{2k_z ab}\sin k_m x\cos k_n y\cos k_m x'\cos k_n y'\begin{cases} e^{-jk_z(z-z')} & z>z' \\ e^{jk_z(z-z')} & z<z' \end{cases} \tag{B.53}$$

$$E_z = 0 \tag{B.54}$$

The $\overline{\mathrm{H}}$ field can be found from Equation (B.49) and is

$$H_x = \sum_{m,n}\frac{j\epsilon_m\epsilon_n k_m}{2\omega\mu ab}\sin k_m x\cos k_n y\cos k_m x'\cos k_n y'\begin{cases} -e^{-jk_z(z-z')} & z>z' \\ e^{jk_z(z-z')} & z<z' \end{cases} \tag{B.55}$$

$$H_y = \sum_{m,n}\frac{j\epsilon_m\epsilon_n k_n}{2\omega\mu ab}\cos k_m x\sin k_n y\cos k_m x'\cos k_n y'\begin{cases} -e^{-jk_z(z-z')} & z>z' \\ e^{jk_z(z-z')} & z<z' \end{cases} \tag{B.56}$$

$$\begin{aligned} H_z &= -\left[\frac{1}{j\omega\mu\epsilon}\frac{\partial^2 F_z}{\partial z^2} - j\omega F_z\right] \\ &= -\sum_{m,n}\left(\frac{-k_z^2}{j\omega\mu\epsilon} - j\omega\right)\frac{j\epsilon_m\epsilon_n\epsilon}{2k_z ab}\cos k_m x\cos k_n y\cos k_m x'\cos k_n y'\begin{cases} e^{-jk_z(z-z')} & z>z' \\ e^{jk_z(z-z')} & z<z' \end{cases} \\ &\quad + \frac{1}{j\omega\mu\epsilon}\sum_{m,n}\frac{\epsilon_m\epsilon_n\epsilon}{ab}\cos k_m x\cos k_n y\cos k_m x'\cos k_n y'\delta(z-z') \end{aligned}$$

$$= -\sum_{m,n}\left(\frac{k_m^2+k_n^2}{\omega\mu k_z}\right)\frac{\epsilon_m\epsilon_n}{2ab}\cos k_m x\cos k_n y\cos k_m x'\cos k_n y'\begin{cases} e^{-jk_z(z-z')} & z>z' \\ e^{jk_z(z-z')} & z<z' \end{cases}$$
$$-\frac{\delta(x-x')\delta(y-y')\delta(z-z')}{j\omega\mu} \qquad (B.57)$$

Again note that these solutions are complete for the $\hat{z}$ component of current which excites only the TE modes in the waveguide. The remaining modes may here be found by setting $\overline{H} = \frac{1}{\mu}\nabla \times \bar{A}$ with $\overline{A} = A_z\hat{z}$ in a manner similar to the electric current case.

For the problem of a slotted waveguide, the singular component which appears in the $\hat{z}$ component of the $\overline{H}$ field has the form

$$\overline{H} = -\hat{z}\frac{\delta(x-x')\delta(y-y')\delta(z-z')}{j\omega\mu} \qquad (B.58)$$

An integral of the type

$$\overline{H}(\bar{R}) = \iiint \bar{\bar{G}}_H(\bar{R},\bar{R}')\cdot\overline{K}(\bar{R}')dV' \qquad (B.59)$$

is typically applied to find the $\overline{H}$ field in the guide for which $\bar{\bar{G}}_H(\bar{R},\bar{R}')$ has the form

$$\bar{\bar{G}}_H = -\hat{z}\hat{z}\frac{\delta(x-x')\delta(y-y')\delta(z-z')}{j\omega\mu} + \bar{\bar{G}}_o \qquad (B.60)$$

It is obvious that the singular term will significantly alter the numerical value of the 'self-cell' and neighboring cells (with overlapping basis functions) in a Method of Moments solution to a problem of this type and therefore causes serious consequences when overlooked.

B.5 Partitioning

It has been observed that the singular term appears above in the $\hat{z}$ component of the field as a result of partitioning the field about $z = z'$ when we applied the radiation condition. In fact, the occurrence of this term also depends on the choice of modes used to expand the field. For example, for the multilayered shielded microstrip problem discussed

in Chapter IV, it is far more convenient to express the Green's function in terms of LSE and LSM modes and partition the problem parallel to the planes of the dielectric interfaces. Although the radiation condition was not imposed on that solution, the singular term appeared for the component of current normal to the interface for the normal field. Imposing the radiation condition in that case, amounts to choosing a contour for the Fourier integral which does not produce additional singularities. It can thus be seen that the singularity does not depend soley on the imposition of the radiation condition, but moreso on the combination of partitions and the manner in which the fields are expressed. Therefore, we can avoid the appearance of the singularity in certain components if necessary, by careful formulation, now that we understand the origin of the singularity.

These observations, however, raise a possibility which has not been addressed. Throughout this work we have emphasized the simplicity in the application of boundary conditions which results from the use of the LSE and LSM modes to expand the fields in various structures. This practice also avoids the singular term in the Green's function, since it appears in a component which is not needed for the planar circuits treated here. However, it is not clear that this is necessarily the most desirable form from the point of view of convergence for the modal sums. It may be that the explicit extraction of the singularity may improve the convergence of the remaining modal sums for that direction. If this is the case, it may be more desirable to retain the singularity in the direction of the current being modelled, even though enforcing the boundary conditions becomes significantly more difficult analytically. This question should be considered for future work.

APPENDIX C

On the Use of Vector Potentials with the Method of Scattering Superposition

For a magnetic source Maxwell's equations take the form

$$\nabla \times \overline{E} = -j\omega\mu \overline{H} - \overline{K} \tag{C.1}$$

$$\nabla \times \overline{H} = j\omega\epsilon \overline{E} \tag{C.2}$$

where the constitutive relations $\overline{D} = \epsilon \overline{E}$ and $\overline{B} = \mu \overline{H}$ have been assumed. Since from Equation (C.2) $\nabla \cdot \overline{E} = 0$, $\overline{E}$ can be expressed in terms of a vector potential function $\overline{F}$ as

$$\overline{E} = \frac{1}{\epsilon} \nabla \times \overline{F} \tag{C.3}$$

Using Equation (C.3) in Equation (C.2) and the usual Lorenz condition [82], $\overline{F}$ must satisfy

$$\nabla^2 \overline{F} + k^2 \overline{F} = \epsilon \overline{K} \tag{C.4}$$

and consequently,

$$\overline{H} = j\omega \overline{F} + \frac{j}{\omega\epsilon\mu} \nabla\nabla \cdot \overline{F} \tag{C.5}$$

For an $\hat{x}$ directected infinitesimal magnetic current in a homogeneously filled infinite space,

$$\overline{K} = \hat{x}\delta(\bar{R} - \bar{R}') \tag{C.6}$$

so that Equation C.4 becomes

$$\nabla^2 \overline{F} + k^2 \overline{F} = \hat{x}\epsilon\delta(x - x')\delta(y - y')\delta(z - z') \tag{C.7}$$

The particular solution in this case is known to be

$$\overline{\mathrm{F}}^{(P)} = -\hat{x}\frac{\epsilon}{4\pi R}e^{-jkR} \tag{C.8}$$

where $R = \sqrt{(x-x')^2+(y-y')^2+(z-z')^2}$. Sommerfeld has derived an integral form for this solution [69, Ch. 6] which is

$$\frac{e^{-jkR}}{R} = \int_0^\infty J_o(\lambda\rho)e^{-u|z-z'|}\frac{\lambda d\lambda}{u} = \int_0^\infty J_o(\lambda\rho)e^{\mp u(z-z')}\frac{\lambda d\lambda}{u} \quad z\gtrless z' \tag{C.9}$$

where $u = \sqrt{\lambda^2-k^2}$ and $k^2 = \omega^2\mu\epsilon$.

We now divide the space by introducing an infinite, perfectly conducting ground plane below the source and a dielectric interface above. This introduces new boundary conditions which must be satisfied. To accomplish this, we are free to add solutions of the homogeneous form of Equation (C.5) (i.e., 'source free'). These are taken to be in the forms:

$$F_x^+ = -\frac{\epsilon}{4\pi}\int_0^\infty A_x^+(\lambda)J_o(\lambda\rho)e^{-uz}\frac{\lambda d\lambda}{u} \qquad z<h \tag{C.10}$$

$$F_x^- = -\frac{\epsilon}{4\pi}\int_0^\infty A_x^-(\lambda)J_o(\lambda\rho)e^{uz}\frac{\lambda d\lambda}{u} \qquad z<h \tag{C.11}$$

$$F_x^o = -\frac{\epsilon_o}{4\pi}\int_0^\infty A_x^o(\lambda)J_o(\lambda\rho)e^{-u_o z}\frac{\lambda d\lambda}{u_o} \qquad z>h \tag{C.12}$$

in which $A_x^\pm$ and A_x^o are to be determined so that the new boundary conditions are satisfied. These terms can be interpreted as producing plane waves scattered from the ground plane and interface with components travelling in the $\pm\hat{z}$ directions within the slab. The terms with superscript 'o' corresponding to fields above the interface. Sommerfeld has shown that we must also include scattered potential functions having $\hat{z}$ components in order to satisfy the boundary conditions[1]. These are taken as

$$F_z^+ = -\frac{\epsilon}{4\pi}\cos\phi\int_0^\infty A_z^+(\lambda)J_1(\lambda\rho)e^{-uz}\frac{\lambda^2 d\lambda}{u} \tag{C.13}$$

$$F_z^- = -\frac{\epsilon}{4\pi}\cos\phi\int_0^\infty A_z^-(\lambda)J_1(\lambda\rho)e^{uz}\frac{\lambda^2 d\lambda}{u} \tag{C.14}$$

$$F_z^o = -\frac{\epsilon_o}{4\pi}\cos\phi\int_0^\infty A_z^o(\lambda)J_1(\lambda\rho)e^{-u_o z}\frac{\lambda^2 d\lambda}{u_o} \tag{C.15}$$

[1]This choice is not unique as noted in [25]

where $u_o = \sqrt{\lambda^2 - k_o^2}$, $k^2 = \omega^2 \mu_o \epsilon_o$ and ϕ is the angle $\hat{\rho}$ makes with the $\hat{x}$ axis. It should be noted that the functional forms have been chosen in anticipation of derivative operators which will be applied when the fields are evaluated at the boundaries. The solution in the slab then is

$$\overline{\mathrm{F}} = \overline{\mathrm{F}}^{(P)} + \hat{x}(F_x^+ + F_x^-) + \hat{z}(F_z^+ + F_z^-) \tag{C.16}$$

while in the infinite space above

$$\overline{\mathrm{F}} = \hat{x} F_x^o + \hat{z} F_z^o \tag{C.17}$$

In view of the expansions of Equations (C.3) and (C.5),

$$\overline{\mathrm{E}} = \frac{\hat{x}}{\epsilon}\frac{\partial F_z}{\partial y} - \frac{\hat{y}}{\epsilon}\left(\frac{\partial F_z}{\partial x} - \frac{\partial F_x}{\partial z}\right) - \frac{\hat{z}}{\epsilon}\frac{\partial F_x}{\partial y} \tag{C.18}$$

$$\overline{\mathrm{H}} = \frac{j}{\omega\mu\epsilon}\left[\hat{x}\left(kF_x + \frac{\partial}{\partial x}\nabla\cdot\overline{\mathrm{F}}\right) + \hat{y}\frac{\partial}{\partial y}\nabla\cdot\overline{\mathrm{F}} + \hat{z}\left(kF_z + \frac{\partial}{\partial z}\nabla\cdot\overline{\mathrm{F}}\right)\right] \tag{C.19}$$

We apply the following boundary conditions at the interfaces:

$$\hat{z} \times \overline{\mathrm{E}} = 0 \quad \text{at} \quad z = 0 \tag{C.20}$$

$$\hat{z} \times \overline{\mathrm{E}}^+ = \hat{z} \times \overline{\mathrm{E}}^- \quad \text{at} \quad z = h \tag{C.21}$$

$$\hat{z} \times \overline{\mathrm{H}}^+ = \hat{z} \times \overline{\mathrm{H}}^- \quad \text{at} \quad z = h \tag{C.22}$$

Here the $\pm$ superscripts imply evaluation of the field on either side of the interface (not to be confused with the $\pm$ waves used earlier). No additional boundary condition is needed at the source plane, since the particular solution already satisfies the source conditions and the scattered potentials are solutions to the homogeneous equation.

This leads to the following system of equations:

$$A_z^+ + A_z^- = 0 \tag{C.23}$$

$$A_x^+ - A_x^- = e^{-uz'} \tag{C.24}$$

$$\frac{1}{u}[A_z^+ e^{-uh} + A_z^- e^{uh}] = \frac{1}{u_o} A_z^o e^{-u_o h} \tag{C.25}$$

$$A_x^+ e^{-uh} - A_x^- e^{uh} = A_x^o e^{-u_o h} - e^{-u(h-z')} \tag{C.26}$$

$$\frac{\epsilon}{u}[A_x^+ e^{-uh} + A_x^- e^{uh}] = \frac{\epsilon_o}{u_o} A_x^o e^{-u_o h} - \frac{\epsilon}{u} e^{-u(h-z')} \tag{C.27}$$

$$\frac{1}{u}[A_x^+ e^{-uh} + A_x^- e^{uh}] + [A_z^+ e^{-uh} - A_z^- e^{uh}] = \frac{1}{u_o} A_x^o e^{-u_o h} + A_z^o e^{-u_o h} - \frac{1}{u} e^{-u(h-z')} \tag{C.28}$$

which when solved produce

$$A_x^+ = \left[\frac{\epsilon_r u_o \sinh[u(h-z')] + u\cosh[u(h-z')]}{f_1(\epsilon_r, u, u_o, h)}\right] \tag{C.29}$$

$$A_x^+ = \left[\frac{\epsilon_r u_o \sinh[u(h-z')] + u\cosh[u(h-z')]}{f_1(\epsilon_r, u, u_o, h)}\right] - e^{-uz'} \tag{C.30}$$

$$A_z^+ = -A_z^- = \frac{u(\epsilon_r - 1)\cosh(uz')}{f_1(\epsilon_r, u, u_o, h) f_2(u, u_o, h)} \tag{C.31}$$

$$A_x^o = e^{u_o h} \frac{2\epsilon_r u_o \cosh(uz')}{f_1(\epsilon_r, u, u_o, h)} \tag{C.32}$$

$$A_z^o = -e^{u_o h} \frac{2u_o(\epsilon_r - 1)\sinh(uh)\cosh(uz')}{f_1(\epsilon_r, u, u_o, h) f_2(u, u_o, h)} \tag{C.33}$$

where

$$f_1(\epsilon_r, u, u_o, h) = \epsilon_r u_o \cosh(uh) + u\sinh(uh) \tag{C.34}$$

$$f_2(u, u_o, h) = u\cosh(uh) + u_o \sinh(uh) \tag{C.35}$$

We then find that

$$F_x = -\frac{\epsilon}{2\pi}\int_0^\infty \frac{\lambda}{u} J_o(\lambda\rho) \frac{\left\{\begin{array}{l} \cosh(uz')\left[\epsilon_r u_o \sinh[u(h-z)] + u\cosh[u(h-z)]\right] \\ \cosh(uz)\left[\epsilon_r u_o \sinh[u(h-z')] + u\cosh[u(h-z')]\right] \end{array}\right\}}{f_1(\epsilon_r, u, u_o, h)} d\lambda$$

$$z \gtrless z' \tag{C.36}$$

$$F_x = -\frac{\epsilon_r \epsilon_o}{2\pi}\int_0^\infty \frac{\lambda J_o(\lambda\rho)\cosh(uz')}{f_1(\epsilon_r, u, u_o, h)} e^{-u_o(z-h)} d\lambda \qquad z > h \tag{C.37}$$

$$F_z = \frac{(\epsilon_r - 1)\epsilon}{2\pi}\cos\phi \int_0^\infty \frac{\lambda^2 J_1(\lambda\rho)\sinh(uz)\cosh(uz')}{f_1(\epsilon_r, u, u_o, h) f_2(u, u_o, h)} d\lambda \qquad z < h \tag{C.38}$$

$$F_z = \frac{(\epsilon_r - 1)\epsilon_o}{2\pi}\cos\phi \int_0^\infty \frac{\lambda^2 J_1(\lambda\rho)\sinh(uh)\cosh(uz')}{f_1(\epsilon_r, u, u_o, h) f_2(u, u_o, h)} e^{-u_o(z-h)} d\lambda \qquad z > h \tag{C.39}$$

These expressions are identical to the results in [37] from which the fields can be found by applying Equations (C.3) and (C.5). The fields correspond to the $\hat{x}\hat{x}$, $\hat{y}\hat{x}$, $\hat{z}\hat{x}$ components of the dyadic Green's functions. For $\hat{y}$ and $\hat{z}$ directed currents, the process must be repeated (although the $\hat{y}$ terms can be obtained by a coordinate rotation due to symmetry).

BIBLIOGRAPHY

BIBLIOGRAPHY

[1] M. Abramowitz and I. A. Stegun,Handbook of Mathematical Functions, Dover Publications, Inc., New York, 1965.

[2] M. Aikawa and H. Ogawa, "Double-sided MIC's and their applications," *IEEE Transactions on Microwave Theory and Techniques*, vol. MTT-37, pp. 406-413, February 1989.

[3] H. Auda and R. F. Harrington, "Inductive posts and diaphragms of arbitrary shape and number in a rectangular waveguide," *IEEE Transactions on Microwave Theory and Techniques*, vol. MTT-32, pp. 606-613, June 1984.

[4] M. C. Bailey, "Design of dielectric-covered resonant slots in a rectangular waveguide," *IEEE Transactions on Antennas and Propagation*, vol. AP-15, pp. 594-598, September 1967.

[5] M. C. Bailey, "The impedance properties of dielectric-covered narrow radiating slots in the broad face of a rectangular waveguide," *IEEE Transactions on Antennas and Propagation*, vol. AP-18, pp. 596-603, September 1970.

[6] C. A. Ballanis, Advanced Engineering Electromagnetics, John Wiley and Sons, New York, 1989.

[7] J. A. Bradshaw, "Scattering from a round metal post and gap," *IEEE Transactions on Microwave Theory and Techniques*, vol. MTT-21, pp. 313-322, May 1973.

[8] N. Camilleri and T. Itoh, "A quasi-optical multiplying slot array," *IEEE Transactions on Microwave Theory and Techniques*, vol. MTT-33, pp. 1189-1195, November 1985.

[9] K. Chang and P. J. Khan, "Coupling between narro transverse inductive strips in waveguide," *IEEE Transactions on Microwave Theory and Techniques*, vol. MTT-24, pp. 101-105, February 1976.

[10] K. Chang, "Impedance calculation of three narrow resonant strips on the transverse plane of rectangular waveguide," *IEEE Transactions on Microwave Theory and Techniques*, vol. MTT-32, pp. 126-130, January 1984.

[11] W. C. Chew, "Some observations on the spatial an eigenfunction representation of dyadic Green's functions," *IEEE Transactions on Antennas and Propagation*, vol. AP-37, pp. 1322-1327, October 1989.

[12] S. B. Cohn, "Slot line on a dielectric substrate," *IEEE Transactions on Microwave Theory and Techniques*, vol. MTT-17, pp. 768-778, October 1969.

[13] R. E. Collin, Field Theory of Guided Waves, McGraw-Hill Book Company, Inc., New York, 1960.

[14] R. E. Collin, Foundations for Microwave Engineering, McGraw-Hill Book Company, Inc., New York, 1966.

[15] R. E. Collin, "On the incompleteness of E and H modes in wave guides," *Canadian Journal of Physics*, vol. 51, pp. 1135-1140, 1973.

[16] B. N. Das and K. V. S. V. R. Prasad, "Impedance of a transverse slot in the ground plane of an offset stripline," *IEEE Transactions on Antennas and Propagation*, vol. AP-32, pp. 1245-1248, November 1984.

[17] G. Dubost and A. Rabbaa, "Analysis of a slot microstrip antenna," *IEEE Transactions on Antennas and Propagation*, vol. AP-34, pp. 155-163, February 1986.

[18] G. F. D. Duff and D. Naylor, Differential Equations of Applied Mathematics, John Wiley & Sons, Inc., New York, 1966, p.199.

[19] L. P. Dunleavy and P. B. Katehi, "Shielding effects in microstrip discontinuities," *IEEE Transactions on Microwave Theory and Techniques*, vol. MTT-36, pp. 1767-1774, December 1988.

[20] EESOF Inc., Westlake Village, CA. 91362.

[21] R. S. Elliott, Antenna Design and Analysis, Prentice-Hall, Inc., Englewood Cliffs, New Jersey, 1981.

[22] R. S. Elliott and L. A. Kurtz, "The design of small slot arrays," *IEEE Transactions on Antennas and Propagation*, vol. AP-26, pp. 214-219, March 1978.

[23] R. S. Elliott, "An improved design procedure for small arrays of shunt slots," *IEEE Transactions on Antennas and Propagation*, vol. AP-31, pp. 48-53, January 1981.

[24] O. L. El-Sayed, "Impedance characterization of a two-post mounting structure for varacter-tuned Gunn oscillators," *IEEE Transactions on Microwave Theory and Techniques*, vol. MTT-22, pp. 769-776, August 1974.

[25] A. Erteza and B. K. Park, "Nonuniqueness of resolution of Hertz vector in presence of a boundary, and the horizontal dipole problem," *IEEE Transactions on Antennas and Propagation*, vol. AP-17, pp. 376-378, May 1969.

[26] I. M. Gel'fand and G. E. Shilov, Generalized Functions, Vol. I., Academic Press, New York, 1964 (translated to English from Russian by E. Saletan).

[27] R. N. Ghose, Principles of Microwave Circuits, McGraw-Hill Book Company, New York, 1963.

[28] I. S. Gradshteyn and I. M. Ryzhik, Table of Integrals, Series, and Products, Academic Press, Inc., New York, 1980.

[29] R. B. Green, "A grating formulation for some problems involving cylindrical discontinuities in rectangular waveguide," *IEEE Transactions on Microwave Theory and Techniques*, vol. MTT-17, pp. 760-763, October 1969.

[30] K. G. Gupta, R. Garg and I. J. Bahl, Microstrip Lines and Slotlines, Artech House, Dedham, MA, 1979.

[31] W. P. Harokopus, "High frequency characterization of open microstrip discontinuities," *Ph.D. Dissertation*, The University of Michigan, 1991.

[32] R. F. Harrington, Field Computation by Moment Methods, The Macmillan Company, New York, 1968.

[33] R. F. Harrington, Time-Harmonic Electromagnetic Fields, McGraw Hill Book Company, 1961.

[34] Hewlett-Packard HP8510-8 Product Note, "Applying the HP 8510B TRL calibration for non-coaxial measurements," October 1987.

[35] R. H. Jansen, R. G. Arnold and I. G. Eddison, "A comprehensive CAD approach to the design of MMIC's up to MM-wave frequencies," *IEEE Transactions on Microwave Theory and Techniques*, vol. MTT-36, pp. 208-219, February 1988.

[36] P. B. Katehi and N. G. Alexopoulos, "Real axis integration of Sommerfeld integrals with applications to printed circuit antennas," *Journal of Mathematical Physics*, vol. 24, pp. 527-533, March 1983.

[37] P. B. Katehi, "The Green's function for a slot on the ground of a dielectric slab," *Radiation Lab Report RL-841*, EECS Dept., Univ. of Michigan, Ann Arbor, June 1987.

[38] P. B. Katehi, "A space domain integral equation approach in the analysis of dielectric-covered slots," *Radio Science*, vol. 24, pp. 253-260, 1989.

[39] P. B. Katehi, "Dielectric-Covered Waveguide Longitudinal Slots with Finite Wall Thickness," *IEEE Transactions on Antennas and Propagation* vol. AP-38, pp. 1039-1045, July 1990.

[40] D. Y. Kim and R. S. Elliot, "A design procedure for slot arrays fed by single-ridge waveguide," *IEEE Transactions on Antennas and Propagation*, vol. AP-36, pp. 1531-1536, November 1988.

[41] J. B. Knorr, "Slot-line transitions," *IEEE Transactions on Microwave Theory and Techniques*, vol. MTT-22, pp. 548-554, May 1974.

[42] K. Kurokawa, "The expansions of electromagnetic fields in cavities," *IRE Transactions on Microwave Theory and Techniques*, pp. 178-187, April 1958.

[43] Y. Leviatan, P. G. Li, A. T. Adams and J. Perini, "Single post inductive obstacle in rectangular waveguide," *IEEE Transactions on Microwave Theory and Techniques*, vol. MTT-31, pp. 806-812, October 1983.

[44] Y. Leviatan, D-H. Shau and A. T. Adams, "Numerical study of the current distribution on a post in rectangular waveguide," *IEEE Transactions on Microwave Theory and Techniques*, vol. MTT-32, pp. 1411-1415, October 1984.

[45] L. Lewin, Advanced Theory of Waveguides, Iliffe & Sons, Ltd., London, England, 1951.

[46] P. G. Li, A. T. Adams, Y. Leviatan and J. Perini, "Multiple-post inductive obstacles in rectangular waveguide," *IEEE Transactions on Microwave Theory and Techniques*, vol. MTT-32, pp. 365-373, April 1984.

[47] R. J. Mailloux, "On the use of metallized cavities in printed slot arrays with dielectric substrates," *IEEE Transactions on Antennas and Propagation*, vol. AP-35, pp. 477-487, May 1987.

[48] N. Marcuvitz, Waveguide Handbook, Boston Technical Publishers, Lexington, Massachusetts, 1964.

[49] E. A. Mariani, C. P. Heinzman, J. P. Agrios and S. B. Cohn, "Slot line characteristics," *IEEE Transactions on Microwave Theory and Techniques*, vol. MTT-17, pp. 1091-1096, December 1969.

[50] E. A. Mariani and J. P. Agrios, "Slot-line filters and couplers," *IEEE Transactions on Microwave Theory and Techniques*, vol. MTT-18, pp. 1089-1095, December 1970.

[51] B. J. Maxum, "Resonant slots with independent control of amplitude and phase," *IRE Transactions on Antennas and Propagation*, pp. 384-389, July 1960.

[52] J. Meixner, "The behaviour of electromagnetic fields at edges," *IEEE Transactions on Antennas and Propagation*, vol. AP-20, pp. 442-446, July 1972.

[53] K. A. Michalski and R. D. Nevels, "On the use of the Coulomb gauge in solving source-excited boundary value problems of electromagnetics," *IEEE Transactions on Microwave Theory and Techniques*, vol. MTT-36, pp. 1328-1333, September 1988.

[54] C. G. Montgomery, R. H. Dicke and E. M. Purcell, Principles of Microwave Circuits, Boston Technical Publishers, Lexington, Massachusetts, 1964.

[55] R. K. Moore, Traveling-wave Engineering, McGraw-Hill Book Company, New York, 1960.

[56] H. Ogawa, T. Hirota and M. Aikawa, "New MIC power dividers using coupled microstrip-slot lines: Two-sided MIC power dividers," *IEEE Transactions on Microwave Theory and Techniques*, vol. MTT-33, pp. 1155-1164, November 1985.

[57] A. A. Oliner, "The impedance properties of narrow radiating slots in the broad face of rectangular waveguide," *IRE Transactions on Antennas and Propagation*, pp. 4-20, January 1957.

[58] P. K. Park and R. S. Elliott, "Design of collinear longitudinal slot arrays fed by boxed stripline," *IEEE Transactions on Antennas and Propagation*, vol. AP-29, pp. 135-140, January 1981.

[59] P. K. Park, G. J. Stern and R. S. Elliott, "An improved technique for the evalution of transverse slot discontinuities in rectangular waveguide," *IEEE Transactions on Antennas and Propagation*, vol. AP-35, pp. 252-257, March 1987.

[60] W. H. Press, B. P. Flannery, S. A. Teukolsky and W. T. Vetterling, Numerical Recipes, Cambridge University Press, Cambridge, 1986.

[61] S. R. Rengarajan, "Compound radiating slots in a broad wall of a rectangular waveguide," *IEEE Transactions on Antennas and Propagation*, vol. 37, pp. 1116-1123, September 1989.

[62] R. S. Robertson and R. S. Elliott, "The design of transverse slot arrays fed by the meandering strip of a boxed stripline," *IEEE Transactions on Antennas and Propagation*, vol. AP-31, pp. 148-154, January 1983.

[63] T. B. A. Senior, "Approximate boundary conditions," *IEEE Transactions on Antennas and Propagation*, vol. AP-29, pp. 826-829, September 1981.

[64] T. B. A. Senior and J. L. Volakis, "Derivation and application of a class of generalized boundary conditions," *IEEE Transactions on Antennas and Propagation*, vol. AP-37, pp. 1566-1572, December 1989.

[65] S. A. Schelkunoff, "On representations of electromagnetic fields in cavities in terms of natural modes of oscillation," *Journal of Applied Physics*, vol. 26, pp. 1231-1234, October 1955.

[66] B. Schüppert, "Microstrip/slotline transitions: Modeling and experimental investigation," *IEEE Transactions on Microwave Theory and Techniques*, vol. MTT-36, pp. 1272-1282, August 1988.

[67] R. Shavit and R. S. Elliott, "Design of transverse slot arrays fed by a boxed stripline," *IEEE Transactions on Antennas and Propagation*, vol. AP-31, pp. 545-552, July 1983.

[68] S. N. Sinha, "Analysis of multi-strip discontinuity in a rectangular waveguide," *IEEE Transactions on Microwave Theory and Techniques*, vol. MTT-34, pp. 696-700, June 1986.

[69] A. Sommerfeld, Partial Differential Equations in Physics, Academic Press, 1964.

[70] G. J. Stern and R. S. Elliott, "Resonant length of longitudinal slots and validity of circuit representation: Theory and experiment," *IEEE Transactions on Antennas and Propagation*, vol. AP-33, pp. 1264-1271, November 1985.

[71] A. F. Stevenson, "Theory of slots in rectangular waveguides," *Journal of Applied Physics*, vol. 19, pp. 24-38, January 1948.

[72] C. T. Tai, Dyadic Green's Functions in Electromagnetic Theory, International Textbook Company, Scranton, Pennsylvania, 1971.

[73] C. T. Tai, "Dyadic Green's functions for a coaxial line," *IEEE Transactions on Antennas and Propagation*, vol. AP-31, pp. 355-358, March 1983.

[74] C. T. Tai, "Different representations of dyadic Green's functions for a rectangular cavity," *IEEE Transactions on Microwave Theory and Techniques*, vol. MTT-24, pp. 597-601, September 1976.

[75] C. T. Tai, "Eigenfunction expansion of dyadic Green's functions," Math Note 28, Weapons Systems Laboratory, Kirtland Air Force Base, Albuquerque, NM, July 1973.

[76] C. T. Tai, "Some essential formulas in dyadic analysis and their applications," *Radio Science*, vol. 22, pp. 1283-1288, December 1987.

[77] C. T. Tai, "On the eigenfunction expansion of dyadic Green's functions," *Proceedings of the IEEE* , pp. 480-481, April 1973.

[78] C. T. Tai, "Equivalent layers of surface charge, current sheet, and polarization in the eigenfunction expansions of Green's functions in electromagnetic theory," *IEEE Transactions on Antennas and Propagation*, vol. AP-29, pp. 733-739, September 1981.

[79] C. T. Tai, "Dyadic Green's function for a rectangular waveguide filled with two dielectrics," *Journal of Electromagnetic Waves and Applications*, vol. 2, no. 3/4, pp. 245-253, 1988.

[80] T. Tanaka, K. Tsunoda and M. Aikawa, "Slot-coupled directional couplers between double-sided substrate microstrip lines and their applications," *IEEE Transactions on Microwave Theory and Techniques*, vol. MTT-36, pp. 1752-1757, December 1988.

[81] T. Teichmann and E. P. Wigner, "Electromagnetic field expansions in loss-free cavities excited through holes," *Journal of Applied Physics*, vol. 24, pp. 262-267, March 1953.

[82] J. Van Bladel, "Lorenz or Lorentz?" *IEEE Antennas and Propagation Magazine*, vol. 33, p. 69, April 1991.

[83] T. E. Vandeventer and P. B. Katehi, "An integral equation method for the evaluation of conductor and dielectric losses in high-frequency interconnects," *IEEE Transactions on Microwave Theory and Techniques*, vol. MTT-37, pp. 1964-1972, December 1989.

[84] T. Vu Khac and C. T. Carson, "Coupling by slots in rectangular waveguides with arbitrary wall thickness," *Electronics Letters*, vol. 8, pp. 456-458, September 7, 1972.

[85] T. Vu Khac and C. T. Carson, "Impedance properties of a longitudinal slot antenna in the broad face of a rectangular waveguide," *IEEE Transactions on Antennas and Propagation*, vol. AP-21, pp. 708-710, September 1973.

[86] T. Vu Khac and C. T. Carson, "m=0, n=0 Mode and rectangular waveguide slot discontinuity," *Electronics Letters*, vol. 9, pp. 431-432, September 6, 1973.

[87] T. H. Wang, T. Itoh and H. Ling, "Spectral domain analysis of a coupled slot antenna," *IEEE Transactions on Antennas and Propagation*, vol. AP-36, pp. 1620-1624, November 1988.

[88] D. R. Wilton and S. Govind, "Incorporation of edge conditions in moment method solutions," *IEEE Transactions on Antennas and Propagation*, vol. AP-25, pp. 845-850, November 1977.

[89] S. Yamamoto, T. Azakami and K. Itakura, "Slit-coupled strip transmission lines," *IEEE Transactions on Microwave Theory and Techniques*, vol. MTT-14, pp. 542-553, November 1966.

[90] E. Yamashita and K. Atsuki, "Analysis of microstrip-like transmission lines by nonuniform discretization of integral equations," *IEEE Transactions on Microwave Theory and Techniques*, vol. MTT-24, pp. 195-200, April 1976.

[91] H. Yang and N. G. Alexopoulos, "A dynamic model for microstrip-slotline transition and related structures," *IEEE Transactions on Microwave Theory and Techniques*, vol. MTT-36, pp. 286-293, February 1988.

APPENDIX C

Norman L. VandenBerg and Linda P.B. Katehi

Generalized Full-Wave Treatment of Shielded Multi-Layer Structures Using the Vector Wave Function Field Expansion Method

Generalized Full-Wave Treatment of Shielded Multi-layer Structures Using the Vector Wave Function Field Expansion Method

N. L. VandenBerg
P. B. Katehi
The University of Michigan
Ann Arbor, MI 48109-2122

1991

Abstract

A full-wave, integral equation method is presented which generalizes the treatment of multi-layer substrates and superstrates for shielded circuits so that any combination and number of layers can be handled without reformulation. A vector wave function approach with dyadic analysis is used to expand the fields, producing all components of the dyadic Green's functions in one solution. The approach makes application to the analysis of shielded transmission lines very straightforward including the calculation of the fields in all layers. Application to the determination of fundamental properties of strip transmission lines are emphasized in the examples provided.

I. Introduction

Successful design of microwave circuits depends in part on the availability of accurate analysis and design tools to characterize transmission line structures. The trend towards higher frequencies has increased the need for analytical techniques which account for all electromagnetic phenomena in the structures, including the effects and characteristics of higher-order modes. Many full-wave analyses have been presented in the literature to address these needs, including numerous papers on discontinuities in conventional microstrip for open and closed structures and, more recently, on slot and coplanar waveguide lines.

As systems become more complex, so too do circuit geometries, including the integration of components on multi-layer substrates and superstrates. The approach presented here illustrates a full-wave method, which generalizes the treatment of multi-layer substrates and superstrates for shielded circuits so that virtually any combination of layers can be handled without reformulation. Although the concepts can be easily extended to the three-dimensional case for the treatment of discontinuities, the emphasis here is on the determination of fundamental properties of transmission lines which can be reduced to a problem of two-dimensions.

To accomplish the full-wave treatment, the dyadic Green's functions for a multilayer rectangular waveguide will be found. The functions will be generalized so that they can be applied to a structure with any number of layers. The approach makes application to the analysis of shielded strip transmission lines very straightforward including the calculation of fields in all layers. As will be shown, the

process also makes available the capability to visualize the fields in the structures, providing insight on their electrical behavior.

II. Derivation of the Dyadic Green's Functions

The dyadic Green's functions needed for this case are the solutions to the dyadic Helmholtz equations:

$$\nabla \times \nabla \times \bar{\bar{G}}_{eJ} - k^2 \bar{\bar{G}}_{eJ} = \bar{\bar{I}}\delta(\bar{R} - \bar{R}') \tag{1}$$

$$\nabla \times \nabla \times \bar{\bar{G}}_{mJ} - k^2 \bar{\bar{G}}_{mJ} = \nabla \times [\bar{\bar{I}}\delta(\bar{R} - \bar{R}')] \tag{2}$$

$$\nabla \times \nabla \times \bar{\bar{G}}_{mK} - k^2 \bar{\bar{G}}_{mK} = \bar{\bar{I}}\delta(\bar{R} - \bar{R}') \tag{3}$$

$$\nabla \times \nabla \times \bar{\bar{G}}_{eK} - k^2 \bar{\bar{G}}_{eK} = \nabla \times \bar{\bar{I}}\delta(\bar{R} - \bar{R}') \tag{4}$$

The subscripts on the Green's functions indicate whether the function is of the electric (e) or magnetic (m) field type for electric (J) or magnetic (K) currents. The magnetic current types are needed in the analysis of slot and coplanar waveguide problems, however, will not be covered in detail here since the derivation closely parallels the electric current problem. With the solutions to these equations, the fields are given by

$$\bar{E} = -j\omega\mu \iiint \bar{\bar{G}}_{eJ} \cdot \bar{J}\ dV' - \iiint \bar{\bar{G}}_{eK} \cdot \bar{K}\ dV' \tag{5}$$

$$\bar{H} = \iiint \bar{\bar{G}}_{mJ} \cdot \bar{J}\ dV' - j\omega\epsilon \iiint \bar{\bar{G}}_{mK} \cdot \bar{K}\ dV' \tag{6}$$

The functions $\bar{L}$, $\bar{M}$ and $\bar{N}$ are vector wave functions forming a complete set of solutions to the homogeneous forms of the above equations. They are defined in

the general forms

$$\bar{L} = \nabla\Psi \tag{7}$$

$$\bar{M} = \nabla \times \Psi\hat{x}_i = \frac{1}{\kappa}\nabla \times \bar{N} \tag{8}$$

$$\bar{N} = \frac{1}{\kappa}\nabla \times \nabla \times \Psi\hat{x}_i = \frac{1}{\kappa}\nabla \times \bar{M} \tag{9}$$

where Ψ is a scalar function chosen to satisfy the boundary conditions of the problem, $\hat{x}_i$ is a unit vector called the 'piloting vector' and κ is the separation constant $\kappa^2 = k_x^2 + k_y^2 + k_z^2$. Following the Ohm-Rayliegh method as described by Tai [1], we find the *particular* solutions by expanding the right hand sides of (1-4) in terms of the eigenfunctions $\bar{L}$, $\bar{M}$ and $\bar{N}$ with unknown vector coefficients; derive the value of the coefficients using the orthogonality properties of the VWFs; expand the dyadic in terms of the same functions with unknown scalar coefficients; and find these coefficients by performing the derivative operations and enforcing the equations. From Equations (7-9) it can be seen that only $\bar{L}$ can have non-zero divergence and since the right hand side of (2) has no divergence, the $\bar{L}$ function is not needed for its solution. It is therefore somewhat simpler to find the solution of Equation (2) first. Through Maxwell's equations it can be shown that $\bar{\bar{G}}_{mJ}$ and $\bar{\bar{G}}_{eJ}$ are related by

$$\nabla \times \bar{\bar{G}}_{eJ} = \bar{\bar{G}}_{mJ} \tag{10}$$

$$\nabla \times \bar{\bar{G}}_{mJ} = \bar{\bar{I}}\delta(\bar{R} - \bar{R}') + k^2\bar{\bar{G}}_{eJ} \tag{11}$$

so that $\bar{\bar{G}}_{eJ}$ can be found from (11) once $\bar{\bar{G}}_{mJ}$ is known. This is the essence of the 'method of $\bar{\bar{G}}_m$' in [3].

Dyadic Green's Function for Parallel Plate Waveguide

The solution for the multilayered waveguide problem is built upon the dyadic Green's function solution of a parallel plate waveguide using the method of scattering superposition. The parallel plate waveguide is formed by infinite, perfectly conducting walls at $x = 0$ and $x = a$, filled between with a uniform dielectric material represented by the wavenumber k_i, where i will ultimately represent the $i^{\underline{th}}$ layer of a rectangular waveguide containing the source. The method of solution for this problem has been given by Tai [2] and in our notation $\bar{\bar{\mathrm{G}}}_{\mathrm{mJ}}$ can be written as

$$\begin{aligned}\bar{\bar{\mathrm{G}}}_{\mathrm{mJ}} &= -\int_{-\infty}^{\infty} dk_y \sum_{m=0}^{\infty} \frac{j(2-\delta_m)k_i}{4\pi a k_z (k_x^2+k_y^2)} \\ &\quad \cdot[\bar{\mathrm{M}}_{\mathrm{o}}(m,k_y,\pm k_z)\bar{\mathrm{N}}'_{\mathrm{o}}(m,-k_y,\mp k_z) + \bar{\mathrm{N}}_{\mathrm{e}}(m,k_y,\pm k_z)\bar{\mathrm{M}}'_{\mathrm{e}}(m,-k_y,\mp k_z)] \\ &\qquad\qquad\qquad\qquad\qquad\qquad\qquad\qquad z \gtrless z' \qquad (12)\end{aligned}$$

where $k_z = \sqrt{k_i^2 - k_x^2 - k_y^2}$. As indicated, the top sign applies to $z > z'$ and the bottom sign to $z < z'$. The vector wave functions are defined by

$$\bar{\mathrm{M}}_{\mathrm{o}}(k_x) = \nabla \times \Psi_{\mathrm{o}}(k_x)\hat{z} = \nabla \times [\sin(\frac{m\pi x}{a})e^{-j(k_y y + k_z z)}\hat{z}] \qquad (13)$$

$$\bar{\mathrm{N}}_{\mathrm{e}}(k_x) = \frac{1}{\kappa}\nabla \times \nabla \times \Psi_{\mathrm{e}}(k_x)\hat{z} = \frac{1}{\kappa}\nabla \times \nabla \times [\cos(\frac{m\pi x}{a})e^{-j(k_y y + k_z z)}\hat{z}] \qquad (14)$$

The wavenumbers k_y and k_z are two continuous eigenvalues and $k_x = m\pi/a$ where m is an integer including $m = 0$ for $\bar{\mathrm{N}}_{\mathrm{e}}$. Note that the 'e' and 'o' subscripts indicate the cosine and sine trigonometric dependence, respectively.

$\bar{\bar{\mathrm{G}}}_{\mathrm{eJ}}$ can be derived by performing the operations indicated by Equation (11). This can be done almost by inspection using the relations between $\bar{\mathrm{M}}$ and $\bar{\mathrm{N}}$ from

Equations (8) and (9) except for the discontinuity at which occurs at $z = z'$. As in [3] it can be shown that the relations given by Equations (8 - 9) apply but an additional term is needed to account for the discontinuity at the source as in

$$\begin{aligned}\nabla \times \bar{\bar{G}}_{mJ} &= -\int_{-\infty}^{\infty} dk_z \sum_{m=0}^{\infty} \frac{j(2-\delta_m)k_i^2}{4\pi a k_z (k_x^2+k_y^2)} \\ &\cdot[\bar{M}_e(m,k_y,\pm k_z)\bar{M}_e'(m,-k_y,\mp k_z) + \bar{N}_o(m,k_y,\pm k_z)\bar{N}_o'(m,-k_y,\mp k_z)] \\ &+ \bar{\bar{I}}_t \delta(\bar{R}-\bar{R}') \qquad\qquad z \gtrless z' \end{aligned} \tag{15}$$

where the transverse idemfactor, $\bar{\bar{I}}_t = \hat{x}\hat{x} + \hat{y}\hat{y}$, appears in this case as a result of the combination of the choice of the piloting vector $\hat{z}$ and the partitioning of the z dependence. The singular terms come from the derivative of terms of the form

$$f(z) = \begin{cases} e^{-jk_z(z-z')} & z > z' \\ -e^{jk_z(z-z')} & z < z' \end{cases} \tag{16}$$

which is

$$\frac{\partial f(z)}{\partial z} = -jk_z \begin{cases} e^{-jk_z(z-z')} & z > z' \\ e^{jk_z(z-z')} & z < z' \end{cases} + 2\delta(z-z') \tag{17}$$

This term has sometimes been overlooked with potential function methods as well. Thus, Equation (11) leads to

$$\begin{aligned}\bar{\bar{G}}_{eJ} &= -\frac{1}{k_i^2}\hat{z}\hat{z}\delta(\bar{R}-\bar{R}') - \int_{-\infty}^{\infty} dk_y \sum_{m=0}^{\infty} \frac{j(2-\delta_m)}{4\pi a k_z (k_x^2+k_y^2)} \\ &\cdot[\bar{M}_e(m,k_y,\pm k_z)\bar{M}_e'(m,-k_y,\mp k_z) + \bar{N}_o(m,k_y,\pm k_z)\bar{N}_o'(m,-k_y,\mp k_z)] \\ &\qquad\qquad z \gtrless z' \end{aligned} \tag{18}$$

The solutions for the magnetic current are found with the same procedure. The results are identical to the above with the following replacements: $\bar{\bar{G}}_{eJ} \Longrightarrow \bar{\bar{G}}_{mK}$, $\bar{\bar{G}}_{mJ} \Longrightarrow \bar{\bar{G}}_{eK}$, and $\bar{M} \Longleftrightarrow \bar{N}$.

Dyadic Green's Function for the Rectangular Waveguide

We now construct the dyadic Green's function for the source layer of a multi-layered rectangular waveguide (see Figure 1) by using the parallel plate Green's function solutions above and the method of scattering superposition. Let

$$\bar{\bar{G}}_{mJ} = \bar{\bar{G}}^{(P)}_{mJ} + \bar{\bar{G}}^{(S)}_{mJ} \tag{19}$$

where $\bar{\bar{G}}^{(P)}_{mJ}$ is the parallel plate solution and $\bar{\bar{G}}^{(S)}_{mJ}$ is defined as

$$\bar{\bar{G}}^{(S)}_{mJ} = -\int_{-\infty}^{\infty} dk_y \sum_{m=0}^{\infty} \frac{j(2-\delta_m)k_i}{4\pi a k_z (k_x^2 + k_y^2)}$$
$$\cdot \left[\bar{N}_e(m, k_y, k_z)\,\bar{A}^+ + \bar{N}_e(m, k_y, -k_z)\,\bar{A}^- + \bar{M}_o(m, k_y, k_z)\,\bar{B}^+ + \bar{M}_o(m, k_y, -k_z)\,\bar{B}^-\right] \tag{20}$$

representing fields which are scattered from dielectric layer interfaces located at $z = c$ above the source and $z = d$ below. The unknown vector coefficients, $\bar{A}^+$, $\bar{A}^-$, $\bar{B}^+$ and $\bar{B}^-$, are found by applying upper (η_U) and lower (η_L) impedance boundary conditions for the layer. This approach greatly simplifies the analysis of the total structure by allowing the fields to be found first for the source layer alone, after which, expressions for the fields in the remaining layers can be immediately written in terms of the homogeneous solutions by mode matching.

The boundary conditions require the fields to satisfy

$$\eta = \frac{\hat{x} \cdot \bar{E}}{\hat{y} \cdot \bar{H}} \tag{21}$$

For electric currents, this becomes

$$\frac{\hat{x} \cdot \bar{\bar{G}}_{eJ}}{\hat{y} \cdot \bar{\bar{G}}_{mJ}} = \frac{j\eta}{\omega\mu} \qquad \text{or} \qquad \frac{\hat{x} \cdot \nabla \times \bar{\bar{G}}_{mJ}}{\hat{y} \cdot \bar{\bar{G}}_{mJ}} = j\omega\epsilon\eta \tag{22}$$

Similarly for the equivalent magnetic current Green's functions, the impedance boundary conditions are

$$\frac{\hat{x}\cdot\bar{\bar{G}}_{eK}}{\hat{y}\cdot\bar{\bar{G}}_{mK}} = j\omega\epsilon\eta \qquad \text{or} \qquad \frac{\hat{x}\cdot\bar{\bar{G}}_{eK}}{\hat{y}\cdot\nabla\times\bar{\bar{G}}_{eK}} = \frac{j\eta}{\omega\mu} \tag{23}$$

For simpler notation, η_e will be the wave impedance associated with the LSE modes and η_m will be used for the LSM modes. Furthermore, $\tilde{\eta}_e$ and $\tilde{\eta}_m$ will denote normalization to the intrinsic modal impedance in the layer and are defined as

$$\tilde{\eta}_{ei} = \frac{k_{zi}\eta_{ei}}{\omega\mu} \tag{24}$$

$$\tilde{\eta}_{mi} = \frac{\omega\epsilon\eta_{mi}}{k_{zi}} \tag{25}$$

where i is an index associated with the $i^{\underline{th}}$ layer.

We can then evaluate the impedance conditions using transmission line analysis and wave impedances for the various layers as illustrated in Figure 1. The impedances on a given layer's upper boundary are found by the transmission line equations

$$\tilde{\eta}_{ei} = \frac{k_{zi}}{k_{z(i-1)}}\left[\frac{\tilde{\eta}_{e(i-1)} + j\tan k_{z(i-1)}l_{(i-1)}}{1 + j\tilde{\eta}_{e(i-1)}\tan k_{z(i-1)}l_{(i-1)}}\right] \tag{26}$$

$$\tilde{\eta}_{mi} = \frac{\epsilon_i k_{z(i-1)}}{\epsilon_{(i-1)}k_{zi}}\left[\frac{\tilde{\eta}_{m(i-1)} + j\tan k_{z(i-1)}l_{(i-1)}}{1 + j\tilde{\eta}_{m(i-1)}\tan k_{z(i-1)}l_{(i-1)}}\right] \tag{27}$$

where the index i is iterated from the top layer through successive lower layers to the layer of interest with l_i the thickness of the $i^{\underline{th}}$ layer. (We have assumed $\mu_r = 1$ throughout.) Similarly, for the lower layers, since the wave impedance is negative,

$$\tilde{\eta}_{ei} = \frac{k_{zi}}{k_{z(i+1)}}\left[\frac{\tilde{\eta}_{e(i+1)} - j\tan k_{z(i+1)}l_{(i+1)}}{1 - j\tilde{\eta}_{e(i+1)}\tan k_{z(i+1)}l_{(i+1)}}\right] \tag{28}$$

$$\tilde{\eta}_{mi} = \frac{\epsilon_i k_{z(i+1)}}{\epsilon_{(i+1)}k_{zi}}\left[\frac{\tilde{\eta}_{m(i+1)} - j\tan k_{z(i+1)}l_{(i+1)}}{1 - j\tilde{\eta}_{m(i+1)}\tan k_{z(i+1)}l_{(i+1)}}\right] \tag{29}$$

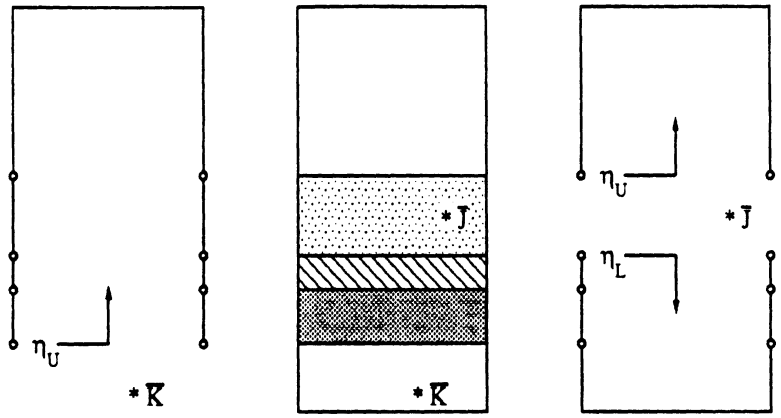

Figure 1: Impedance boundary condition representation of a multi-layered structure.

where here the iteration proceeds from the lowest layer upwards.

Applying the boundary conditions produces two pairs of equations for the unknown coefficients:

$$(\tilde{\eta}_{eU}-1)e^{-jk_zc}\,\bar{\mathrm{A}}^{+}-(\tilde{\eta}_{eU}+1)e^{jk_zc}\,\bar{\mathrm{A}}^{-} = -(\tilde{\eta}_{eU}-1)e^{-jk_zc}\bar{\mathrm{M}}'_{\mathrm{e}}(m,-k_y,k_z) \quad (30)$$

$$(\tilde{\eta}_{eL}-1)e^{-jk_zd}\,\bar{\mathrm{A}}^{+}-(\tilde{\eta}_{eL}+1)e^{jk_zd}\,\bar{\mathrm{A}}^{-} = (\tilde{\eta}_{eL}+1)e^{jk_zd}\bar{\mathrm{M}}'_{\mathrm{e}}(m,-k_y,-k_z) \quad (31)$$

and

$$(\tilde{\eta}_{mU}-1)e^{-jk_zc}\,\bar{\mathrm{B}}^{+}+(\tilde{\eta}_{mU}+1)e^{jk_zc}\,\bar{\mathrm{B}}^{-} = -(\tilde{\eta}_{mU}-1)e^{-jk_zc}\bar{\mathrm{N}}'_{\mathrm{o}}(m,-k_y,k_z) \quad (32)$$

$$(\tilde{\eta}_{mL}-1)e^{-jk_zd}\,\bar{\mathrm{B}}^{+}+(\tilde{\eta}_{mL}+1)e^{jk_zd}\,\bar{\mathrm{B}}^{-} = -(\tilde{\eta}_{mL}+1)e^{jk_zd}\bar{\mathrm{N}}'_{\mathrm{o}}(m,-k_y,-k_z) \quad (33)$$

These four equations decouple into two pairs due to a judicious choice of the piloting vector in the VWFs. Because the piloting vector was chosen as the unit vector normal to the layer interfaces, the $\bar{\mathrm{M}}$ and $\bar{\mathrm{N}}$ VWFs appearing in $\bar{\bar{\mathrm{G}}}_{\mathrm{mJ}}$

correspond to the LSM and LSE modes of the waveguide, respectively. (In contrast, $\bar{\mathrm{M}}$ and $\bar{\mathrm{N}}$ correspond to the LSE and LSM modes, respectively, when they appear in $\bar{\bar{\mathrm{G}}}_{\mathrm{eJ}}$.) As is well known, the LSE and LSM modes are decoupled on the interfaces, that is, the tangential components of an individual mode on the interface can be matched by a like mode in the adjacent layer, therefore the coefficients are decoupled. That there are only four equations is a result of the fact that the field in a given layer depends only on the field in the adjacent layers.

The solutions to Equations (30 - 33) are easily found and when combined with Equations (12,19) and (20), and some algebraic manipulations lead to

$$\begin{aligned}
\bar{\bar{\mathrm{G}}}_{\mathrm{mJ}} \;=\; & \int_{-\infty}^{\infty} dk_y \sum_{m=0}^{\infty} \frac{j(2-\delta_m)k_i}{2\pi a k_z (k_x^2+k_y^2)} \\
& \left\{ \frac{\begin{pmatrix} \bar{\mathcal{M}}_{\mathrm{o}}[\tilde{\eta}_{mU};m,k_z(z-c)]\;\bar{\mathcal{N}}'_{\mathrm{o}}[\tilde{\eta}_{mL};m,k_z(z'-d)] \\ \bar{\mathcal{M}}_{\mathrm{o}}[\tilde{\eta}_{mL};m,k_z(z-d)]\;\bar{\mathcal{N}}'_{\mathrm{o}}[\tilde{\eta}_{mU};m,k_z(z'-c)] \end{pmatrix}}{(\tilde{\eta}_{mU}-\tilde{\eta}_{mL})\cos k_z(c-d) - j(\tilde{\eta}_{mU}\tilde{\eta}_{mL}-1)\sin k_z(c-d)} \right. \\
& \left. + \frac{\begin{pmatrix} \bar{\mathcal{N}}_{\mathrm{e}}[\tilde{\eta}_{eU};m,k_z(z-c)]\;\bar{\mathcal{M}}'_{\mathrm{e}}[\tilde{\eta}_{eL};m,k_z(z'-d)] \\ \bar{\mathcal{N}}_{\mathrm{e}}[\tilde{\eta}_{eL};m,k_z(z-d)]\;\bar{\mathcal{M}}'_{\mathrm{e}}[\tilde{\eta}_{eU};m,k_z(z'-c)] \end{pmatrix}}{(\tilde{\eta}_{eU}-\tilde{\eta}_{eL})\cos k_z(c-d) - j(\tilde{\eta}_{eU}\tilde{\eta}_{eL}-1)\sin k_z(c-d)} \right\} \\
& \qquad\qquad\qquad\qquad\qquad\qquad\qquad\qquad\qquad\qquad \text{for} \quad z \gtrless z' \qquad (34)
\end{aligned}$$

where we have defined the $\bar{\mathcal{M}}_{\mathrm{o}}^{\mathrm{e}}$ and $\bar{\mathcal{N}}_{\mathrm{o}}^{\mathrm{e}}$ functions for the sake of compact notation:

$$\bar{\mathcal{M}}_{\mathrm{o}}[\eta;\alpha] \;=\; \eta\bar{\mathrm{M}}_{\mathrm{oo}}[\alpha] + j\bar{\mathrm{M}}_{\mathrm{oe}}[\alpha] \qquad (35)$$

$$\bar{\mathcal{M}}_{\mathrm{e}}[\eta;\alpha] \;=\; \eta\bar{\mathrm{M}}_{\mathrm{ee}}[\alpha] - j\bar{\mathrm{M}}_{\mathrm{eo}}[\alpha] \qquad (36)$$

$$\bar{\mathcal{N}}_{\mathrm{o}}[\eta;\alpha] \;=\; \eta\bar{\mathrm{N}}_{\mathrm{oo}}[\alpha] + j\bar{\mathrm{N}}_{\mathrm{oe}}[\alpha] \qquad (37)$$

$$\bar{\mathcal{N}}_e[\eta;\alpha] \;=\; \eta\bar{\mathrm{N}}_{ee}[\alpha] - j\bar{\mathrm{N}}_{eo}[\alpha] \tag{38}$$

Since α here is $[m, k_z(z- < c,d >)]$ and m is associated with k_x, we recognize that the 'e' and 'o' subscripts in this case imply trigonometric functions of x and z. Also note that the primed functions use $-k_y$.

We can find $\bar{\bar{\mathrm{G}}}_{eJ}$ as we did in the parallel plate case, by performing the derivatives indicated by Equation (11):

$$\begin{aligned}
\bar{\bar{\mathrm{G}}}_{eJ} \;=\; & -\frac{1}{k_i^2}\hat{z}\hat{z}\delta(\bar{\mathrm{R}}-\bar{\mathrm{R}}') + \int_{-\infty}^{\infty} dk_y \sum_{m=0}^{\infty} \frac{j(2-\delta_m)}{2\pi a k_z(k_x^2+k_y^2)} \\
& \left\{ \frac{\begin{pmatrix} \bar{\mathcal{M}}_e[\tilde{\eta}_{eU};m,k_z(z-c)]\;\bar{\mathcal{M}}'_e[\tilde{\eta}_{eL};m,k_z(z'-d)] \\ \bar{\mathcal{M}}_e[\tilde{\eta}_{eL};m,k_z(z-d)]\;\bar{\mathcal{M}}'_e[\tilde{\eta}_{eU};m,k_z(z'-c)] \end{pmatrix}}{(\tilde{\eta}_{eU}-\tilde{\eta}_{eL})\cos k_z(c-b) - j(\tilde{\eta}_{eU}\tilde{\eta}_{eL}-1)\sin k_z(c-b)} \right. \\
& \left. + \frac{\begin{pmatrix} \bar{\mathcal{N}}_o[\tilde{\eta}_{mU};m,k_z(z-c)]\;\bar{\mathcal{N}}'_o[\tilde{\eta}_{mL};m,k_z(z'-d)] \\ \bar{\mathcal{N}}_o[\tilde{\eta}_{mL};m,k_z(z-d)]\;\bar{\mathcal{N}}'_o[\tilde{\eta}_{mU};m,k_z(z'-c)] \end{pmatrix}}{(\tilde{\eta}_{mU}-\tilde{\eta}_{mL})\cos k_z(c-b) - j(\tilde{\eta}_{mU}\tilde{\eta}_{mL}-1)\sin k_z(c-b)} \right\} \\
& \qquad\qquad\qquad\qquad\qquad\qquad\qquad\qquad\qquad\qquad \text{for} \quad z\gtrless z'
\end{aligned} \tag{39}$$

Both $\bar{\bar{\mathrm{G}}}_{eJ}$ and $\bar{\bar{\mathrm{G}}}_{mJ}$ involve a spectral integral which can be reduced to an additional mode summation index by Cauchy's Theorem, once the impedance functions are specified. For two-dimensional problems, this is not necessary as will be shown.

III. Generalized Application to Multi-layered Shielded Microstrip

Although the derivation of the dyadic Green's functions using the approach above has particular advantages when all of the components are needed, the applications to be discussed in this section will be restricted to one current component to minimize the complexity of the presentation. The objective for this section is to show how the fields in the various levels can be calculated for a known form of current on a single microstrip line in a straightforward way. There is no restriction on the placement of the current or on the number of strips which can be used, however, a simple case here will better serve to outline the method. The procedure for the treatment of more complex multi-layer coupled strips can be found in [4] which also is an example of the use of potential functions with impedance boundary conditions to generalize multiple layers in a similar way. In order to calculate the characteristic impedance, the definition $Z = P/I^2$ is used where P is the time average of power propagating along the guide. Thus, if we set $I = 1$, the characteristic impedance is simply $Z = P$ which can be computed analytically by integration of the average Poynting vector on the cross section of the waveguide.

For our purposes, let us assume a geometry such as shown in Figure 2 with a longitudinal current component on a single narrow strip of the form

$$\bar{J}(x', y', z') = \hat{y} \frac{2\delta(z' - d)}{\pi W \sqrt{1 - 4\left(\frac{x' - x_o}{W}\right)^2}} e^{-jk_g y'} \quad |x' - x_o| < W/2 \qquad (40)$$

i.e. a Maxwellian transverse variation of current which satisfies the edge conditions. The k_g parameter represents the set of characteristic complex phase constants

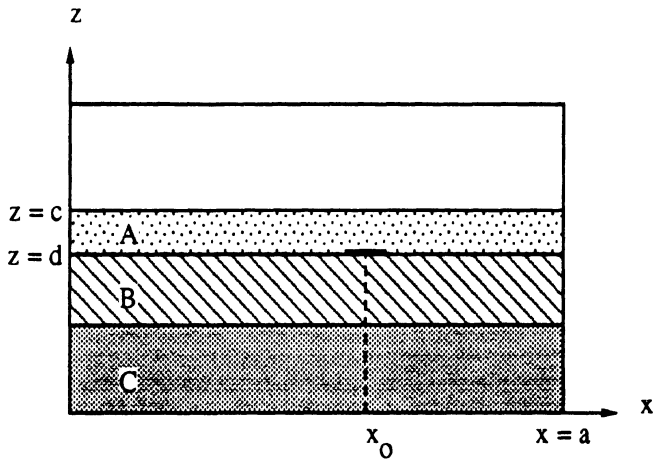

Figure 2: A shielded stripline, uniform in the $\hat{y}$ direction with multi-layered substrate and superstrate.

associated with shielded microstrip modes. They are the eigenvalues of

$$\overline{\mathrm{E}}_t = -j\omega\mu \iiint \hat{n} \times \bar{\bar{\mathrm{G}}}_{\mathrm{eJ}} \cdot \bar{\mathrm{J}}\, dV' = \hat{n} \times \bar{\bar{\mathrm{Z}}}_s \cdot \bar{\mathrm{J}} \tag{41}$$

which enforces an appropriate boundary condition on the surface of the microstrip line [4]. A particular value for k_g must be found first, before the fields of a particular mode can be calculated.

Equation (40) is used in Equation (41) with the $\hat{y}\hat{y}$ component of $\bar{\bar{\mathrm{G}}}_{\mathrm{eJ}}$ as derived above and Galerkin's procedure to enforce the boundary condition. On recognition of the sifting property and integral representation of the delta function:

$$\int_{-\infty}^{+\infty} e^{-j(k_g - k_y)y'} dy' = 2\pi\delta(k_g - k_y) \tag{42}$$

we find that the weighted $\hat{y}$ component of the electric field can be written as

$$\begin{aligned}\tilde{E}_{yy} &= \frac{\omega\mu}{a}\sum_{m=0}^{\infty}\frac{(2-\delta_m)}{k_z(k_x^2+k_g^2)}\sin^2 k_x x_o J_o^2(\frac{k_x W}{2}) \\ &\cdot\left\{k_x^2\left[\frac{\tilde{\eta}_{eL}[\tilde{\eta}_{eU}\cos k_z(c-d)+j\sin k_z(c-d)]}{(\tilde{\eta}_{eU}-\tilde{\eta}_{eL})\cos k_z(c-d)-j(\tilde{\eta}_{eU}\tilde{\eta}_{eL}-1)\sin k_z(c-d)}\right]\right. \\ &\left.+\frac{k_z^2k_g^2}{k_i^2}\left[\frac{\tilde{\eta}_{mL}[\tilde{\eta}_{mU}\cos k_z(c-d)+j\sin k_z(c-d)]}{(\tilde{\eta}_{mU}-\tilde{\eta}_{mL})\cos k_z(c-d)-j(\tilde{\eta}_{mU}\tilde{\eta}_{mL}-1)\sin k_z(c-d)}\right]\right\} \qquad (43)\end{aligned}$$

We now numerically search, using Muller's method for example [5, p.262], to find the values of k_g which satisfy (41) and thus correspond to microstrip modes.

With the propagation constants known, the fields in the $i^{\underline{th}}$ layer can be easily found. These fields in the layers are expressed in terms of the homogeneous solutions to Equations (1) and (2) which can be obtained by inspection of Equations (34 - 39). Their general forms for the $i^{\underline{th}}$ layer are

$$\begin{aligned}\overline{\mathrm{E}}_J &= -\sum_{m=0}^{\infty}\frac{j(2-\delta_m)}{2\pi a k_z(k_x^2+k_y^2)} \\ &\left\{A_i\begin{pmatrix}\left[\tilde{\eta}_{eU}\bar{\mathrm{M}}_{ee}[k_x,k_z(z-c)]-j\bar{\mathrm{M}}_{eo}[k_x,k_z(z-c)]\right] \\ \left[\tilde{\eta}_{eL}\bar{\mathrm{M}}_{ee}[k_x,k_z(z-d)]-j\bar{\mathrm{M}}_{eo}[k_x,k_z(z-d)]\right]\end{pmatrix}\right. \\ &\left.+B_i\begin{pmatrix}\left[\tilde{\eta}_{mU}\bar{\mathrm{N}}_{oo}[k_x,k_z(z-c)]+j\bar{\mathrm{N}}_{oe}[k_x,k_z(z-c)]\right] \\ \left[\tilde{\eta}_{mL}\bar{\mathrm{N}}_{oo}[k_x,k_z(z-d)]+j\bar{\mathrm{N}}_{oe}[k_x,k_z(z-d)]\right]\end{pmatrix}\right\} \qquad (44)\end{aligned}$$

and

$$\begin{aligned}\overline{\mathrm{H}}_J &= -\sum_{m=0}^{\infty}\frac{j(2-\delta_m)k_i}{2\pi a k_z(k_x^2+k_y^2)} \\ &\left\{B_i\begin{pmatrix}\left[\tilde{\eta}_{mU}\bar{\mathrm{M}}_{oo}[k_x,k_z(z-c)]+j\bar{\mathrm{M}}_{oe}[k_x,k_z(z-c)]\right] \\ \left[\tilde{\eta}_{mL}\bar{\mathrm{M}}_{oo}[k_x,k_z(z-d)]+j\bar{\mathrm{M}}_{oe}[k_x,k_z(z-d)]\right]\end{pmatrix}\right.\end{aligned}$$

$$+ A_i \left(\begin{bmatrix} \tilde{\eta}_{eU} \bar{\mathrm{N}}_{\mathrm{ee}}[k_x, k_z(z-c)] - j\bar{\mathrm{N}}_{\mathrm{eo}}[k_x, k_z(z-c)] \\ \tilde{\eta}_{eL} \bar{\mathrm{N}}_{\mathrm{ee}}[k_x, k_z(z-d)] - j\bar{\mathrm{N}}_{\mathrm{eo}}[k_x, k_z(z-d)] \end{bmatrix} \right) \Bigg\} \qquad (45)$$

which are valid for all layers except the source layer. Some of the leading constants are preserved for convenience in later notation. The expansion of these expressions is given in Appendix A. From these, the power density can also be written and integrated analytically to determine the characteristic impedance as shown in Appendix B.

IV. Numerical Results

With these analytical results, the fields, power flow, characteristic impedance and propagation constants can be readily found for shielded strips with any combination of layered substrates and superstrates. Extensive comparisons with measurements available in the literature, other techniques, and a commercial CAD package (*Touchstone* [6]) have been made for the case of microstrip. In all instances, the accuracy of the technique has been shown to be excellent, including the ability to evaluate higher order modes. Some of the details are available in [7] but omitted here, since for the special case of microstrip the formulation could be greatly simplified.

Of greater significance is the application to multilayer structures. Multiple layers may be required by the circumstances, as we have pointed out, but also may be introduced to take advantage of their unique properties. To illustrate, let us examine by numerical experiment, the impedance and propagation behavior of the

structure shown in Figure 2. For convenience, let us assume that the dimensions are fixed except for the strip width, but we are at liberty to set the dielectric constants (cover height = a = 250 mils, $l_A = 50, l_B = l_C = 25$ mils). Furthermore, let us set the relative dielectric constant of layer B to $\epsilon_B = 13$ as if the line were part of a circuit etched on GaAs.

Observe the variation of the line impedance with frequency as a function of ϵ_C in Figure 3. In this figure the line width has been varied as well to achieve an

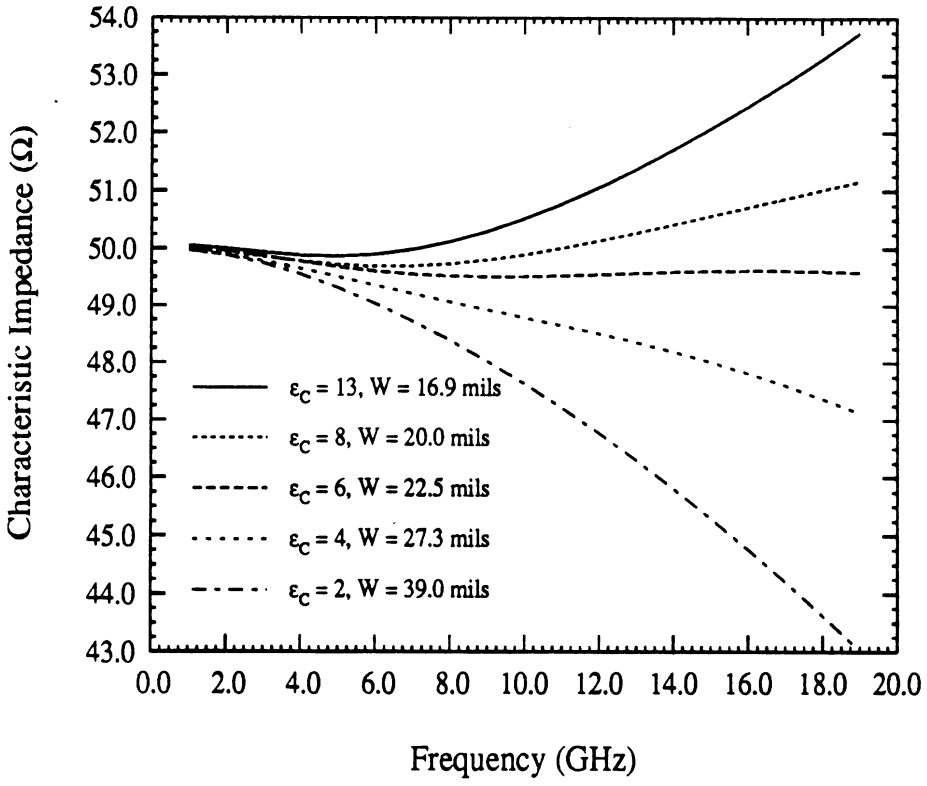

Figure 3: Impedance variation with frequency versus ϵ_C ($\epsilon_A = 2$, $\epsilon_B = 13$)

impedance of 50Ω at f = 1.0 GHz. Thus, by selecting an appropriate value for

the sub-substrate permittivity, the variation of the characteristic impedance with frequency can be minimized. This feature can be used to improve the design of broadband high-performance filters and matching networks in which the frequency response is sensitive to the variation of impedance. A similar effect is observed when the superstrate permittivity is altered.

From a different point of view, consider what happens when the line width is fixed. Figures 4 and 5 shows the variation of the impedance and effective relative dielectric constant as a function of the superstrate permittivity. The sub-substrate

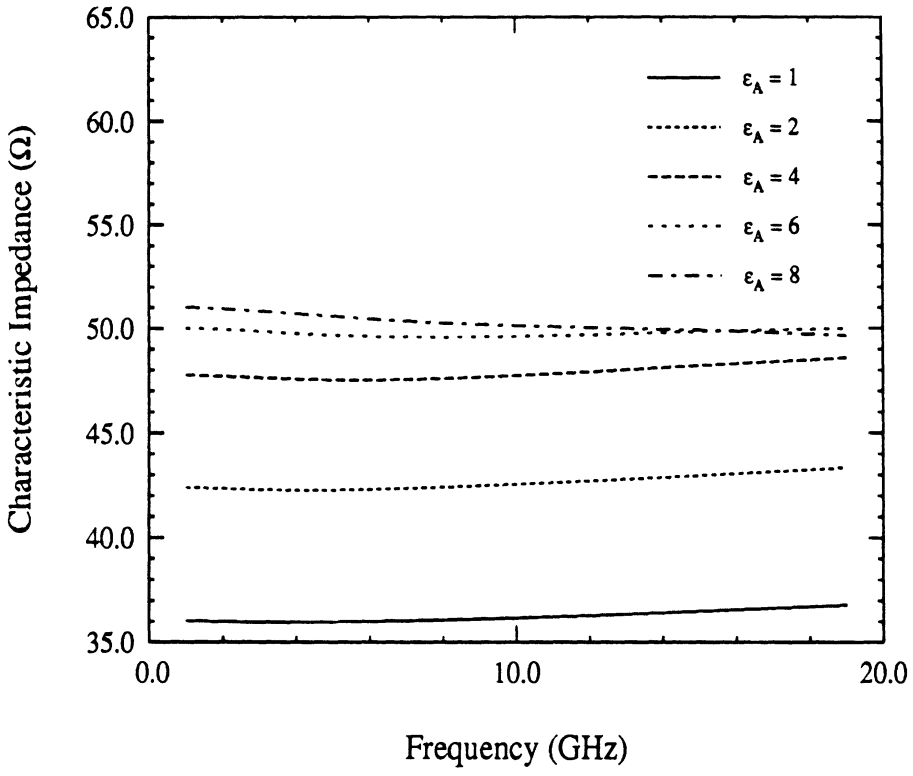

Figure 4: Impedance variation with frequency versus ϵ_A ($\epsilon_B = 13$, $\epsilon_C = 8$, W = 16.8 mils).

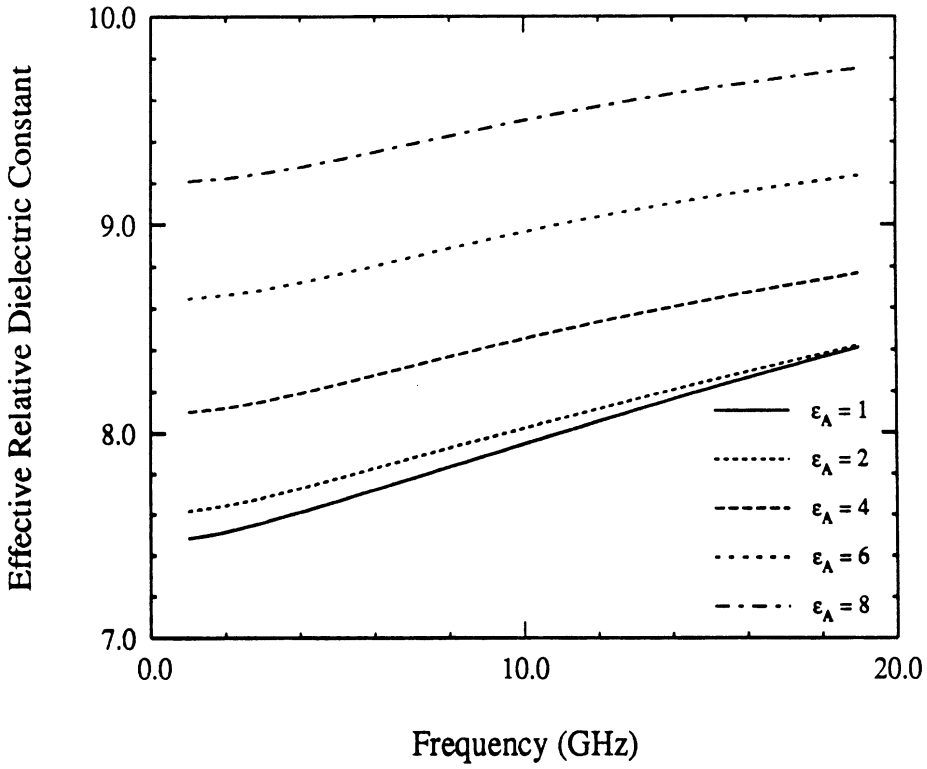

Figure 5: Effective relative dielectric constant variation with frequency versus ϵ_A ($\epsilon_B = 13$, $\epsilon_C = 8$, W = 16.8 mils).

dielectric constant has been set to $\epsilon_C = 8$ to flatten the impedance variation with frequency as before. We note that the propagation constant for the line, indicated by Figure 5, displays the opposite sensitivity to superstrate permittivity, that is, the characteristic impedance becomes more stable as ϵ_A is raised but the propagation constant becomes more sensitive. This suggests a potential mechanism for post fabrication tuning of circuits where the frequency response is sensitive to electrical line lengths. For example, the resonant frequency of a tuning stub could be raised or lowered by changing the value of the superstrate permittivity, relative to a predetermined value. If the nominal relative dielectric constant for the superstrate is high, the impedance of the stub would not be significantly altered. The superstrate could be applied after some preliminary measurements have determined the required value of dielectric constant.

Besides the obvious utility of this type of information for circuit design, the ability to visualize the field or power distribution often provides important insights into why certain structures behave as they do, and also, how the behavior might change when the structure is modified. Examples include the plotting of field magnitudes on the cross section of stripline as shown in Figure 6; microstrip, Figure 7; and suspended microstrip, Figure 8. The upper part of the structure in Figure 8 has the same dimensions as the structure in Figure 7. By comparing the fields in these two cases, especially in the substrates, one can appreciate how one structure behaves quite differently from the other. Consider for example, what would happen if another strip is introduced on the substrate in these two cases.

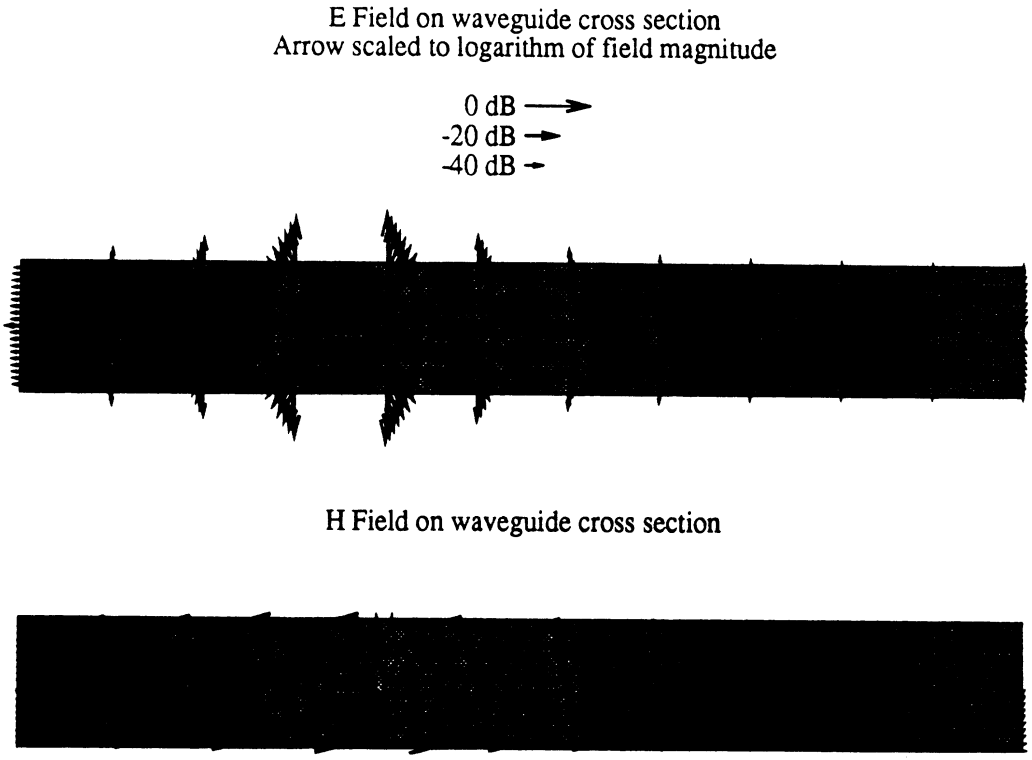

Figure 6: Stripline field distribution for the dominant propagating mode.

Clearly, the suspended microstrip field distribution would be more greatly disturbed than the conventional shielded microstrip, therefore the coupling between strips would likewise be greater. Such an ability to visualize the field demonstrates one of the benefits of this type of analysis: enhancing our intuitive understanding of the behavior of these structures as well as providing quantitative information. Finally, the fields for the multilayer case discussed earlier are shown in Figure 9 with $\epsilon_A = 8, \epsilon_B = 13, \epsilon_C = 6$.

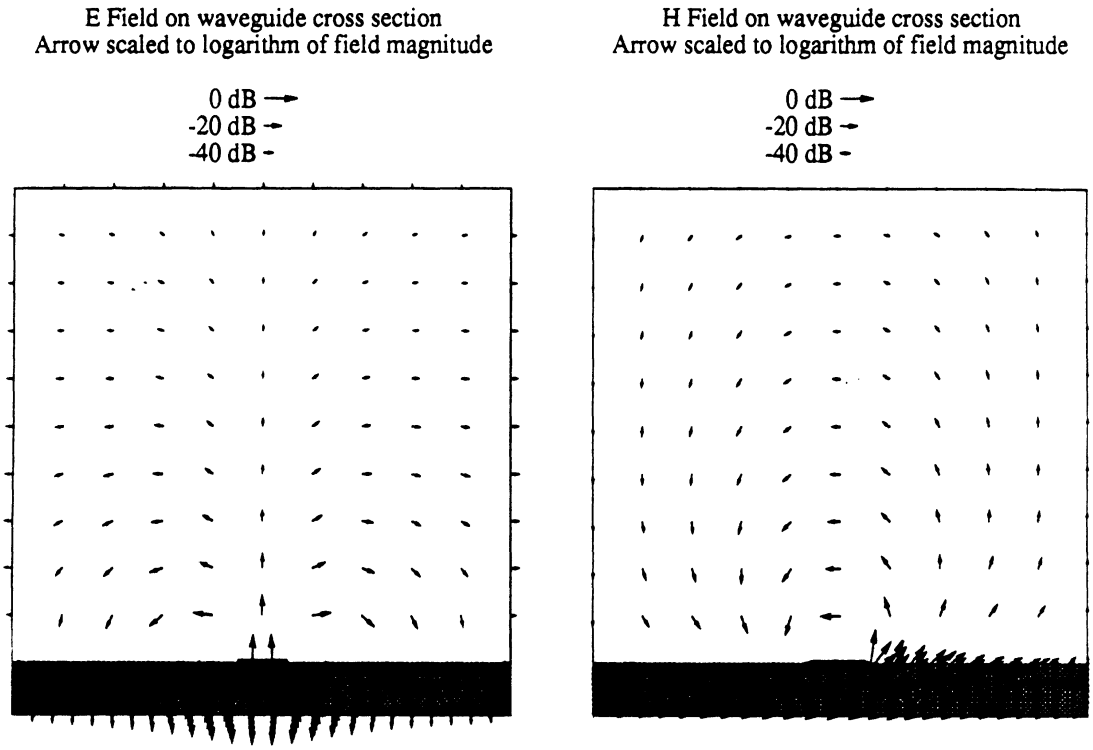

Figure 7: Microstrip field distribution for the dominant propagating mode.

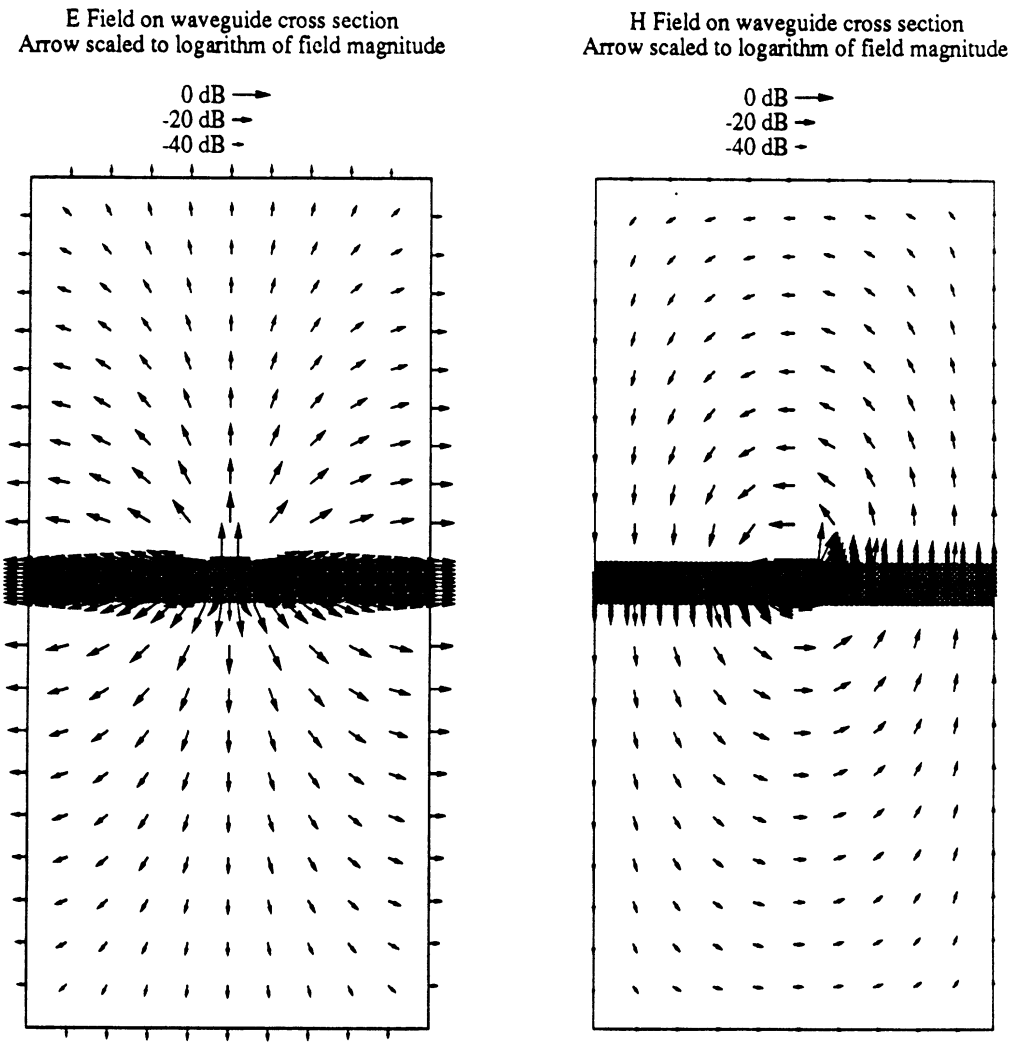

Figure 8: Suspended microstrip field distribution for the dominant propagating mode.

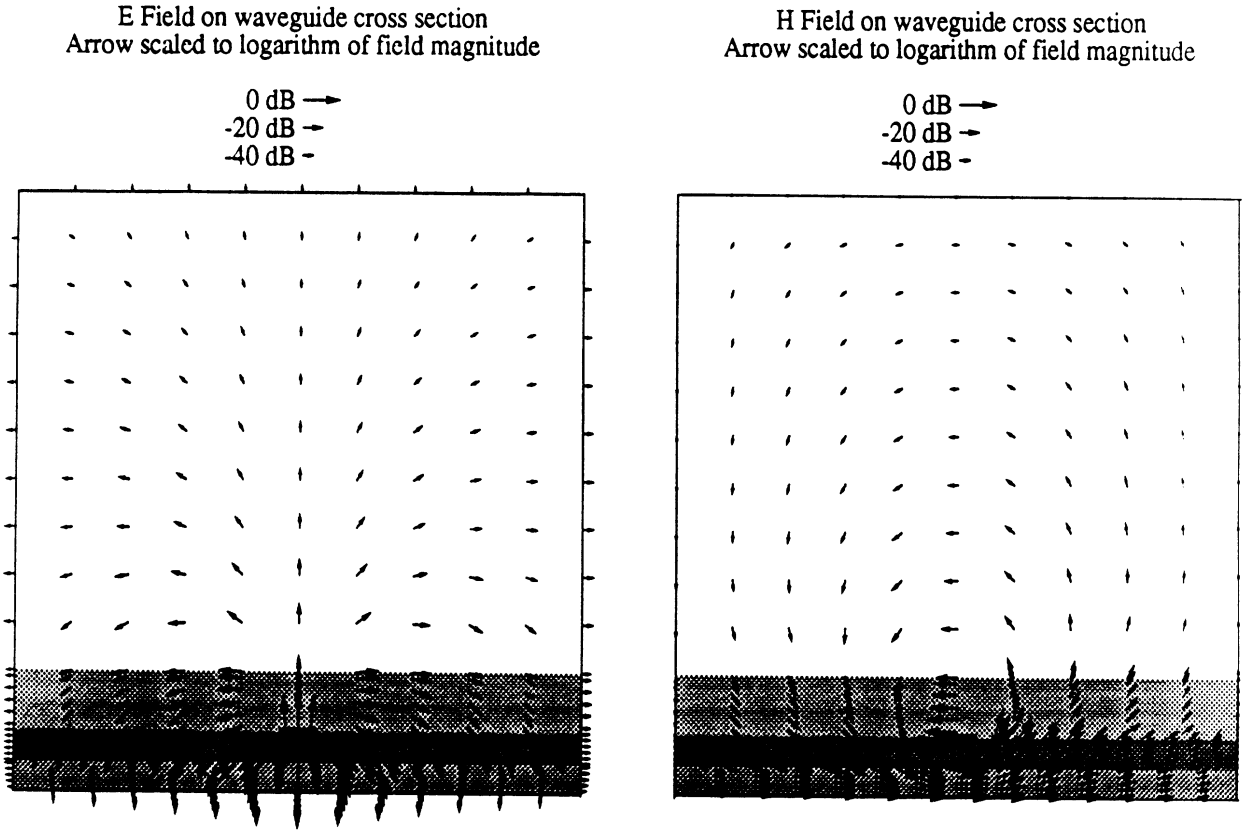

Figure 9: Fields in a multilayer structure for the dominant propagating mode.

Appendices

A. Expansion of Fields

LSE Modes

Expanding the VWFs we find that the LSE mode fields in each layer can be written in the form

$$\overline{\mathrm{E}}_{LSE} = A_i \left[\frac{2\omega\mu_o}{ak_{zi}(k_x^2+k_y^2)}\right] \left[\hat{x}\hat{y}jk_xk_y \cos k_x x \sin k_x x' - \hat{y}\hat{y}k_x^2 \sin k_x x \sin k_x x'\right] \cdot \frac{1}{\cos k_{zi}(c_i-d_i)} \begin{cases} \cos k_{zi}(c_i-z)\left[\tilde{\eta}_{eUi} + j\tan k_{zi}(c_i-z)\right] & (i \le 0) \\ \cos k_{zi}(z-d_i)\left[\tilde{\eta}_{eLi} - j\tan k_{zi}(z-d_i)\right] & (i > 0) \end{cases} \tag{A.1}$$

$$\begin{aligned} \overline{\mathrm{H}}_{LSE} = {} & \mp A_i \left[\frac{2j}{a(k_x^2+k_y^2)}\right] \left[\hat{x}\hat{y}k_x^2 \sin k_x x \sin k_x x' + \hat{y}\hat{y}jk_xk_y \cos k_x x \sin k_x x'\right] \\ & \cdot \frac{1}{\cos k_{zi}(c_i-d_i)} \begin{cases} \cos k_{zi}(c_i-z)\left[\tilde{\eta}_{eUi}\tan k_{zi}(c_i-z) - j\right] & (i \le 0) \\ \cos k_{zi}(z-d_i)\left[\tilde{\eta}_{eLi}\tan k_{zi}(z-d_i) + j\right] & (i > 0) \end{cases} \\ & + A_i \left[\frac{2j}{ak_{zi}}\right] \left[\hat{z}\hat{y}k_x \cos k_x x \sin k_x x'\right] \\ & \cdot \frac{1}{\cos k_{zi}(c_i-d_i)} \begin{cases} \cos k_{zi}(c_i-z)\left[\tilde{\eta}_{eUi} + j\tan k_{zi}(c_i-z)\right] & (i \le 0) \\ \cos k_{zi}(z-d_i)\left[\tilde{\eta}_{eLi} - j\tan k_{zi}(z-d_i)\right] & (i > 0) \end{cases} \end{aligned} \tag{A.2}$$

where $i = 0$ for the layer containing the strip and

$$A_0 = \frac{-\tilde{\eta}_{eL0}}{(\tilde{\eta}_{eU0} - \tilde{\eta}_{eL0})\cos k_z(c_0-d_0) - j(\tilde{\eta}_{eU0}\tilde{\eta}_{eL0} - 1)\sin k_z(c_0-d_0)} \tag{A.3}$$

By matching the tangential components of the field at the interfaces above and below the strip layer, the remaining coupling coefficients are found to be

$$A_1 = A_0 \frac{k_{z1}}{k_{z0}} \left[\frac{\tilde{\eta}_{eU0} + j\tan k_{z0}(c_0-d_0)}{\tilde{\eta}_{eL1} - j\tan k_{z1}(c_1-d_1)}\right] \tag{A.4}$$

$$A_i = \begin{cases} \dfrac{A_{i-1}k_{zi}\tilde{\eta}_{eL(i-1)}}{k_{z(i-1)}\cos k_{z(i-1)}(c_{i-1}-d_{i-1})[\tilde{\eta}_{eLi} - j\tan k_{zi}(c_i - d_i)]} & (i>1) \\ \dfrac{A_{i+1}k_{zi}\tilde{\eta}_{eU(i+1)}}{k_{z(i+1)}\cos k_{z(i+1)}(c_{i+1}-d_{i+1})[\tilde{\eta}_{eUi} + j\tan k_{zi}(c_i - d_i)]} & (i<0) \end{cases} \tag{A.5}$$

LSM Modes

Similarly, the LSM mode fields can be written as

$$\begin{aligned} \overline{\mathrm{E}}_{LSM} = & -B_i\left[\frac{2j\omega\mu k_{zi}}{ak_i^2(k_x^2+k_y^2)}\right]\left[\hat{x}\hat{y}jk_xk_y\cos k_xx\sin k_xx' + \hat{y}\hat{y}k_y^2\sin k_xx\sin k_xx'\right] \\ & \cdot\frac{1}{\cos k_{zi}(c_i-d_i)}\begin{cases}\cos k_{zi}(c_i-z)\,[\tilde{\eta}_{mUi}+j\tan k_{zi}(c_i-z)] & (i\le 0)\\ \cos k_{zi}(z-d_i)\,[\tilde{\eta}_{mLi}-j\tan k_{zi}(z-d_i)] & (i>0)\end{cases} \\ & \pm B_i\left[\frac{2j\omega\mu}{ak_i^2}\right][\hat{z}\hat{y}jk_y\sin k_xx\sin k_xx'] \\ & \cdot\frac{1}{\cos k_{zi}(c_i-d_i)}\begin{cases}\cos k_{zi}(c_i-z)\,[\tilde{\eta}_{mUi}\tan k_{zi}(c_i-z)-j] & (i\le 0)\\ \cos k_{zi}(z-d_i)\,[\tilde{\eta}_{mLi}\tan k_{zi}(z-d_i)+j] & (i>0)\end{cases} \end{aligned} \tag{A.6}$$

$$\begin{aligned} \overline{\mathrm{H}}_{LSM} = & \mp B_i\left[\frac{2j}{a(k_x^2+k_y^2)}\right]\left[\hat{x}\hat{y}k_y^2\sin k_xx\sin k_xx' - \hat{y}\hat{y}jk_xk_y\cos k_xx\sin k_xx'\right] \\ & \cdot\frac{1}{\cos k_{zi}(c_i-d_i)}\begin{cases}\cos k_{zi}(c_i-z)\,[\tilde{\eta}_{mUi}\tan k_{zi}(c_i-z)-j] & (i\le 0)\\ \cos k_{zi}(z-d_i)\,[\tilde{\eta}_{mLi}\tan k_{zi}(z-d_i)+j] & (i>0)\end{cases} \end{aligned} \tag{A.7}$$

where the coefficients are defined by

$$B_0 = \frac{-\tilde{\eta}_{mL0}}{(\tilde{\eta}_{mU0}-\tilde{\eta}_{mL0})\cos k_z(c_0-d_0) - j(\tilde{\eta}_{mU0}\tilde{\eta}_{mL0}-1)\sin k_z(c_0-d_0)} \tag{A.8}$$

$$B_1 = B_0\frac{k_{z0}k_1^2}{k_{z1}k_0^2}\left[\frac{\tilde{\eta}_{mU0}+j\tan k_{z0}(c_0-d_0)}{\tilde{\eta}_{mL1}-j\tan k_{z1}(c_1-d_1)}\right] \tag{A.9}$$

$$B_i = \begin{cases} \dfrac{B_{i-1}k_{z(i-1)}k_i^2\tilde{\eta}_{mL(i-1)}}{k_{zi}k_{(i-1)}^2\cos k_{z(i-1)}(c_{i-1}-d_{i-1})[\tilde{\eta}_{mLi}-j\tan k_{zi}(c_i-d_i)]} & (i>1) \\ \dfrac{B_{i+1}k_{z(i+1)}k_i^2\tilde{\eta}_{mU(i+1)}}{k_{zi}k_{(i+1)}^2\cos k_{z(i+1)}(c_{i+1}-d_{i+1})[\tilde{\eta}_{eUi}+j\tan k_{zi}(c_i-d_i)]} & (i<0) \end{cases} \tag{A.10}$$

To calculate the field at a particular point in the $i^{\underline{th}}$ layer, we then calculate only the coupling coefficients $(A_0 \ldots A_i)$ and $(B_0 \ldots B_i)$ while evaluating Equations (A.1,A.2) and (A.6,A.7).

B. Power Density Integration

Calculation of Power

For computation of power (P), the needed component of Poynting vector is $\hat{y}\cdot\frac{1}{2}\overline{\mathrm{E}}\times\overline{\mathrm{H}^*}$. For the case of LSE modes, power density is given by

$$P = E_xH_z^* = \frac{2\omega\mu}{a^2}\left[\frac{A_ik_xk_y}{k_{zi}(k_x^2+k_y^2)}\right]\left[\frac{A_i^*k_x}{k_{zi}^*}\right]\frac{\cos^2 k_xx\,[\int\sin k_xx']^2}{|\cos k_{zi}(c_i-d_i)|^2} \cdot \begin{cases} |\tilde{\eta}_{eUi}\cos k_{zi}(c_i-z)+j\sin k_{zi}(c_i-z)|^2 & (i\le 0) \\ |\tilde{\eta}_{eLi}\cos k_{zi}(z-d_i)-j\sin k_{zi}(z-d_i)|^2 & (i>0) \end{cases} \tag{B.1}$$

For the LSM modes the required term for calculating power density is

$$P = -E_zH_x^* = \frac{2\omega\mu}{a^2}\left[\frac{B_ik_y}{k_i^2}\right]\left[\frac{B_i^*(k_y^*)^2}{(k_x^2+k_y^2)^*}\right]\frac{\sin^2 k_xx\,[\int\sin k_xx']^2}{|\cos k_{zi}(c_i-d_i)|^2} \cdot \begin{cases} |\tilde{\eta}_{mUi}\sin k_{zi}(c_i-z)-j\cos k_{zi}(c_i-z)|^2 & (i\le 0) \\ |\tilde{\eta}_{mLi}\sin k_{zi}(z-d_i)+j\cos k_{zi}(z-d_i)|^2 & (i>0) \end{cases} \tag{B.2}$$

There are also two sets of cross-terms from the $\overline{\mathrm{E}}_{LSM} \times \overline{\mathrm{H}}_{LSE}$ product needed to calculate power density. They are

$$P = E_x H_z^* = -\frac{2\omega\mu}{a^2}\left[\frac{B_i k_x k_y k_{zi}}{k_i^2(k_x^2+k_y^2)}\right]\left[\frac{A_i^* k_x}{k_{zi}^*}\right]\frac{\cos^2 k_x x\,[\int \sin k_x x']^2}{|\cos k_{zi}(c_i-d_i)|^2}$$
$$\cdot\begin{cases}[\tilde{\eta}_{mUi}\cos k_{zi}(c_i-z)+j\sin k_{zi}(c_i-z)]\,[\tilde{\eta}_{eUi}\cos k_{zi}(c_i-z)+j\sin k_{zi}(c_i-z)]^* & (i\le 0)\\ [\tilde{\eta}_{mLi}\cos k_{zi}(z-d_i)-j\sin k_{zi}(z-d_i)]\,[\tilde{\eta}_{eLi}\cos k_{zi}(z-d_i)-j\sin k_{zi}(z-d_i)]^* & (i>0)\end{cases} \tag{B.3}$$

$$P = -E_z H_x^* = \frac{2\omega\mu}{a^2}\left[\frac{B_i k_y}{k_i^2}\right]\left[\frac{A_i^* k_x^2}{(k_x^2+k_y^2)^*}\right]\frac{\sin^2 k_x x\,[\int \sin k_x x']^2}{|\cos k_{zi}(c_i-d_i)|^2}$$
$$\cdot\begin{cases}[\tilde{\eta}_{mUi}\sin k_{zi}(c_i-z)-j\cos k_{zi}(c_i-z)]\,[\tilde{\eta}_{eUi}\sin k_{zi}(c_i-z)-j\cos k_{zi}(c_i-z)]^* & (i\le 0)\\ [\tilde{\eta}_{mLi}\sin k_{zi}(z-d_i)+j\cos k_{zi}(z-d_i)]\,[\tilde{\eta}_{eLi}\sin k_{zi}(z-d_i)+j\cos k_{zi}(z-d_i)]^* & (i>0)\end{cases} \tag{B.4}$$

The evaluation of total power can be done analytically by integrating the power density on the waveguide cross-section. Integration of the x dependence is trivial and has been indicated in the previous expressions. The z dependence appears in two forms, the first of which is

$$I_{PM} = \int_d^c \begin{Bmatrix}[\eta_1\cos k(c-z)+j\sin k(c-z)][\eta_2\cos k(c-z)+j\sin k(c-z)]^* \\ [\eta_1\cos k(z-d)-j\sin k(z-d)][\eta_2\cos k(z-d)-j\sin k(z-d)]^*\end{Bmatrix} dz$$
$$= \frac{\eta_1\eta_2^*-1}{4\Re e(k)}\sin 2\Re e(k)(c-d) \mp j\frac{\eta_1-\eta_2^*}{2\Re e(k)}\sin^2\Re e(k)(c-d)$$
$$+\frac{\eta_1\eta_2^*+1}{4\Im m(k)}\sinh 2\Im m(k)(c-d) \mp \frac{\eta_1+\eta_2^*}{2\Im m(k)}\sinh^2\Im m(k)(c-d) \tag{B.5}$$

where $\Re e(k)$ and $\Im m(k)$ symbolize the real and imaginary parts of k respectively. The second form is

$$I_{PN} = \int_d^c \begin{Bmatrix}[\eta_1\sin k(c-z)-j\cos k(c-z)][\eta_2\sin k(c-z)-j\cos k(c-z)]^* \\ [\eta_1\sin k(z-d)+j\cos k(z-d)][\eta_2\sin k(z-d)+j\cos k(z-d)]^*\end{Bmatrix} dz$$

$$= -\frac{\eta_1\eta_2^* - 1}{4\Re e(k)} \sin 2\Re e(k)(c-d) \pm j\frac{\eta_1 - \eta_2^*}{2\Re e(k)} \sin^2 \Re e(k)(c-d)$$
$$+\frac{\eta_1\eta_2^* + 1}{4\Im m(k)} \sinh 2\Im m(k)(c-d) \mp \frac{\eta_1 + \eta_2^*}{2\Im m(k)} \sinh^2 \Im m(k)(c-d) \qquad \text{(B.6)}$$

With these expressions, calculation of the characteristic impedance reduces to a simple summation of terms, once the matching coefficients are known for each layer and mode.

References

[1] C. T. Tai, Dyadic Green's Functions in Electromagnetic Theory, International Textbook Company, Scranton, Pennsylvania, 1971.

[2] C. T. Tai, "Dyadic Green's function for a rectangular waveguide filled with two dielectrics.", *Journal of Electromagnetic Waves and Applications*, Vol. 2, No. 3/4, 1988, pp. 245-253.

[3] C. T. Tai, "Dyadic Green's functions for a coaxial line," *IEEE Transactions on Antennas and Propagation*, vol. AP-31, pp. 355-358, March 1983.

[4] T. E. Vandeventer and P. B. Katehi, "An integral equation method for the evaluation of conductor and dielectric losses in high-frequency interconnects", *IEEE Transactions on Microwave Theory and Techniques*, Vol. MTT-37, No. 12, December 1989, pp. 1964-1972.

[5] W. H. Press, B. P. Flannery, S. A. Teukolsky and W. T. Vetterling, Numerical Recipes, Cambridge University Press, Cambridge, 1986.

[6] EESOF Inc., Westlake Village, CA. 91362.

[7] N. L. VandenBerg, "Full-wave Analysis of Microstrip-fed Slot Antennas and Couplers," Ph.D. dissertation, The University of Michigan, 1991.

APPENDIX D

L. Rexberg, N.I. Dib and L.P.B. Katehi

A Microshield Line Loop Antenna for Sub-mm Wavelength Applications

A Microshield Line Loop Antenna for Sub-mm Wavelength Applications

L. Rexberg*
Chalmers University of Technology
Division of Network Theory
412 96 Gothenburg
Sweden

N. Dib, P. Katehi
Radiation Laboratory, University of Michigan
3228 EECS Building
Ann Arbor, MI 48109-2122
U.S.A.

Abstract

A new type of antenna fed by a monolithic planar transmission line is presented. The antenna is formed as a resonant slot loop which is fed by a new recently introduced microshield line. The design offers low-spurious radiation from the feed line and low-loss power transmission in the feed network. The antenna design is applicable at frequencies in the millimeter and sub-mm wavelength region using thin dielectric or membrane technology. The predicted radiation pattern at resonance and input impedance as a function of frequency demonstrates the performance of the new antenna.

Introduction

Recently a new type of monolithic planar transmission line for millimeter and sub-mm wavelength applications has been presented [1]. The line offers low radiation compared to conventional microstrip or coplanar waveguides and can operate without the need for via-holes or air-bridges for equalization of ground voltage. It consists of a pair of narrow slots placed tightly together and excited in the 'odd' mode. The rear side of the structure is shielded by a waveguide with dimensions chosen so that it is below cut-off at the operating frequency (see Fig.1). The presence of the waveguide ensures that only the odd fundamental mode is propagating in the apertures. The front side is unshielded in order to make the lines suitable to feed open radiating structures. Several discontinuities in microshield line have been studied in [1] and have demonstrated lower radiation loss than conventional coplanar waveguide.

In this paper it is proposed that the new microshield line can be used to feed slot antennas working at mm or sub-mm wave frequencies. The need for low loss antenna systems at sub-mm frequencies with front-end mixers calls for solutions where the LO-oscillator can be monolithically integrated with the antenna. Such integrated antennas have sucessfully been designed at millimeter-wave and microwave frequency range [3,

4]. However, using conventional techniques at sub-mm wavelengths makes frequency dependent ohmic losses, dispersion, parasitic radiation and electromagnetic coupling a serious limitation. The new microshield line offers a way to minimize these effects and is proposed for use as an efficient antenna feed.

Description of the antenna

The antenna consists of a slot loop which is excited by a microshield line as depicted in Figure 1. The center conductor of the transmission line and the patch inside the loop can be suspended on silicon or GaAs thin dielectric slabs or membranes. The length of the loop is adjusted so that the two slots numbered (1) and (2) are excited in phase and with equal amplitude when the feed line is excited in the 'odd' mode. This is achieved if the length L is about $\lambda_0/2$. The electric field in the two other parts of the loop, (3) and (4), are then excited out of phase and only radiate in directions off broadside. These parts will radiate more than the feed line since they are spaced more widely and therefore will be the main reason for the cross-polar radiation. The number of basis functions in the various parts of the antenna are given in Figure.1. The length and width of the basis functions are 0.5 mm and 0.25 mm respectively.

Theory

The antenna is analyzed by the space domain integral equation technique [1]. An integral equation is formed by applying the boundary conditions on the apertures and then solved by the method of moments. Piecewise sinusoidal functions are used for both basis and weighting functions in two orthogonal directions of the electric aperture field. This leaves us with two-dimensional integrals for the external part of the antenna and discrete two-dimensional summations for the internal part. The summation points in the internal part exactly correspond to waveguide wavenumbers.

Results

Figure 2 shows the input impedance for the loop antenna in a frequency range from 22.98 to 27.45 GHz with a design frequency of 25.53 GHz. The curve shows a multiple resonance input reflection coefficient which can be matched by a series capacitive stub on the feed line [2]. It is seen that the antenna has a minimum reflection coefficient at the design frequency for radiation. Furthermore, the loops observed on the Smith Chart indicate the potential of the antenna to exhibit wide bandwidth using an appropriate matching network. The matching network can be analyzed separately since the coupling between various parts of the antenna is seen to be very low. Figure 3 shows the E-plane, H-plane and cross-polar radiation patterns at 25.53 GHz. The E-plane pattern is very wide since the in-phase radiating parts (1) and (2) are relatively closely spaced.

Conclusions

It is shown that the microshield loop antenna is a suitable design for use in sub-mm wavelength applications. The multiple resonance characteristics of the input reflection coefficient can be matched by low-loss filters using the same microshield line technique.

Acknowledgements

The authors would like to thank Mr. Bill Harokopus for providing computer subroutines. The work was mainly financed by a research grant from The Royal Swedish Academy of Sciencies and partly by the NSF under contract ECS-8657951 and Texas Instruments.

References

[1] N. Dib, W. Harokopus, P. Katehi, C. Ling, and G. Rebeiz, "Study of a novel planar transmission line", 1991 IEEE MTT-S Digest, pp. 623-626.

[2] N. Dib, P. Katehi, G. Ponchak and R. Simmons, "Theoretical and experimental characterization of coplanar waveguide discontinuities for filter applications.", IEEE Trans. on MTT, pp. 873-881, May. 1991.

[3] N. Wang and S. Schwarz, "Monolithically integrated Gunn oscillator at 35 GHz.", Electron. Lett., pp. 603-604, July 1984.

[4] V. Hwang, T. Uwano and T. Itoh, "Quasi-optical integrated antenna and receiver front end.", IEEE Trans. on MTT, pp. 80-85, January 1988.

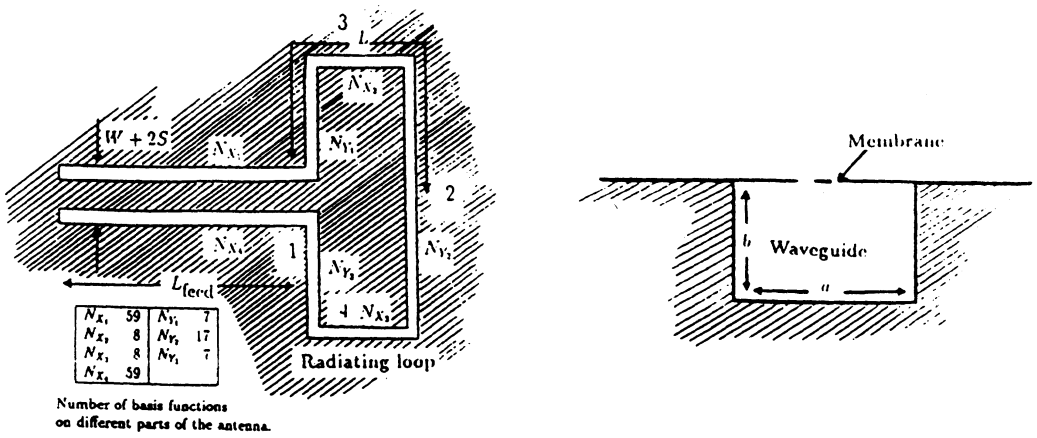

Figure 1: The loop antenna fed by the microshield line. The length L is approximately $\lambda/2$ in order to give in-phase radiation.

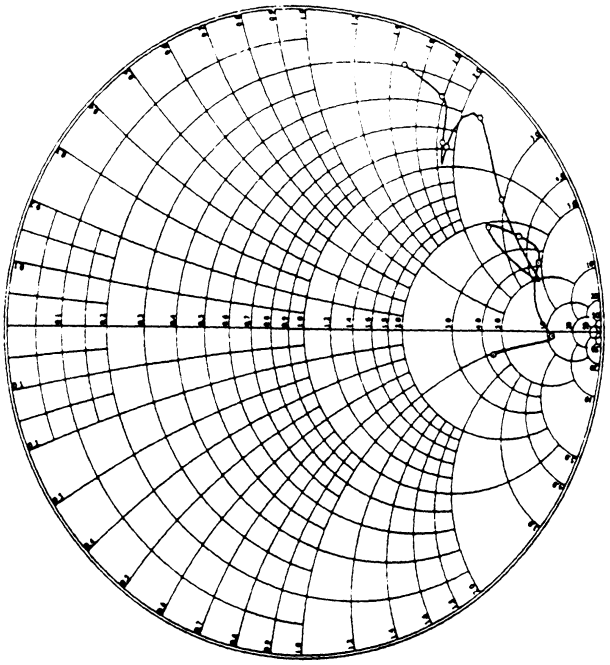

Figure 2: The predicted normalized impedance as a function of frequency for the microshield line-fed loop antenna. The reference plane is at the feed point of the loop.

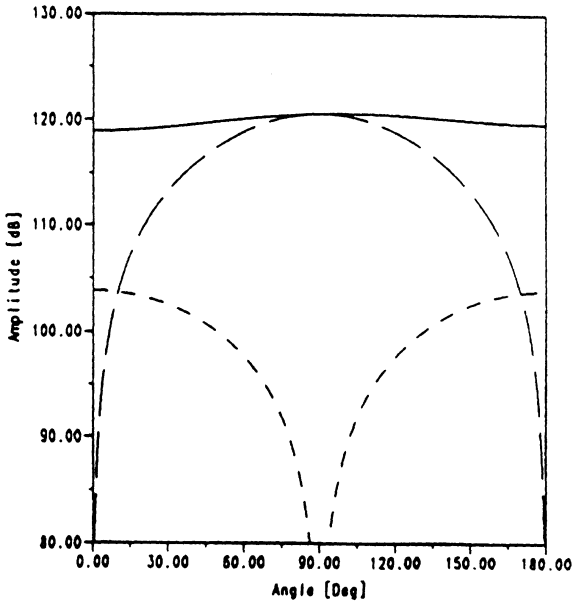

Figure 3: The predicted radiation pattern at the design frequency (25.53 GHz) for the loop antenna. Solid: E-plane cut. Long dash: H-plane cut, Short dash: Cross polarisation.

APPENDIX E

Norman L.VandenBerg

Dimensions for Initial T-Bar Slot Measurements and Progress Report

December 13,1990

Dimensions for Initial T-Bar Slot Measurements and Progress Report

(December 13, 1990)

We have generated some dimensions for the T-Bar fed slot using modified versions of the programs previously developed. As discussed earlier, there are some details which need to be determined before we can be confident of our numerical model, especially since we have examined this structure for a relatively short period of time compared to the two-port strip-fed slot. Nevertheless, we have some early predictions of resonant lengths which we hope to verify by measurements as a first step in the development of the program. Once we have established the capability to predict resonant lengths, we will be able to refine the model for slot impedance.

We have also developed routines to fill the submatrices which represent the coupling from the cross bar to the slot. Originally, we had proposed to study the T-Bar fed slot by treating the cross bar as only a termination for the main feed line, to save time in development. However, we later decided that since this was likely to lead to uncertainty in making comparisons of the numerical model to measurements, it would be better to include these coupling terms. This has been completed and these terms are now included in the matrix.

Below, we describe dimensions for three cases which should help in establishing the validity of the models. The first is a two-port strip fed slot which will serve as a sort of standard by which we can evaluate the basic approach and measurement capability. This case is the basis for the previously existing programs. The second case is an open-end strip-fed slot which will be used to verify some of the intermediate code. The third case is the T-Bar fed slot which is the ultimate focus of this effort. The configurations have been chosen in accordance with your earlier suggestions as to the material and operating frequency to be used. Dimensions common to all three cases are listed in Table 1. Parameters specific to the individual cases are given in Table 2.

Figure 1 shows some of the same information graphically. The cavity is assumed to be completely enclosed by the walls as shown except for an opening for the main feed line, which is illustrated in the detail. It is desirable to minimize the size of the opening to contain the higher order stripline modes while allowing the dominant mode to pass through the wall unperturbed. (These assumptions are used in the analysis but we have found that they also apply as a practical matter). For the given ground plane spacing the strip width was chosen for a 50Ω line at 3.0 GHz. With these dimensions, the dominant mode currents extend to approximately 3X the strip width on the ground planes (using a somewhat arbitrary limit criteria

of 10 %). Therefore the width of the opening was chosen to be about .30 inches. The cavity walls can be constructed by inserting Z-wires through the assembly at a spacing of $.1\lambda$ or less or any another method you may prefer.

Electrical Parameters	
Frequency	3.0 GHz
Dielectric	$\epsilon_r = 2.5$
Mechanical Parameters (inches)	
Ground Plane Spacing (c)	0.125
Strip Width (W)	0.094
Cavity Width (b)	1.750
Cavity Length (a)	1.750
Strip Centerline (y0)	0.875
Slot Width (Ws)	0.094
Slot Center (s)	0.875

Table 1: Common Parameters.

Configuration	Two-port	Open-end	T-Bar
Slot Length (Ls)	1.510	1.410	1.510
Main Line Length (L)	1.750	1.360	—
Cross Line Length (LB)	—	—	1.750
Cross Line Center (X0B)	—	—	1.313

Table 2: Case Parameters.

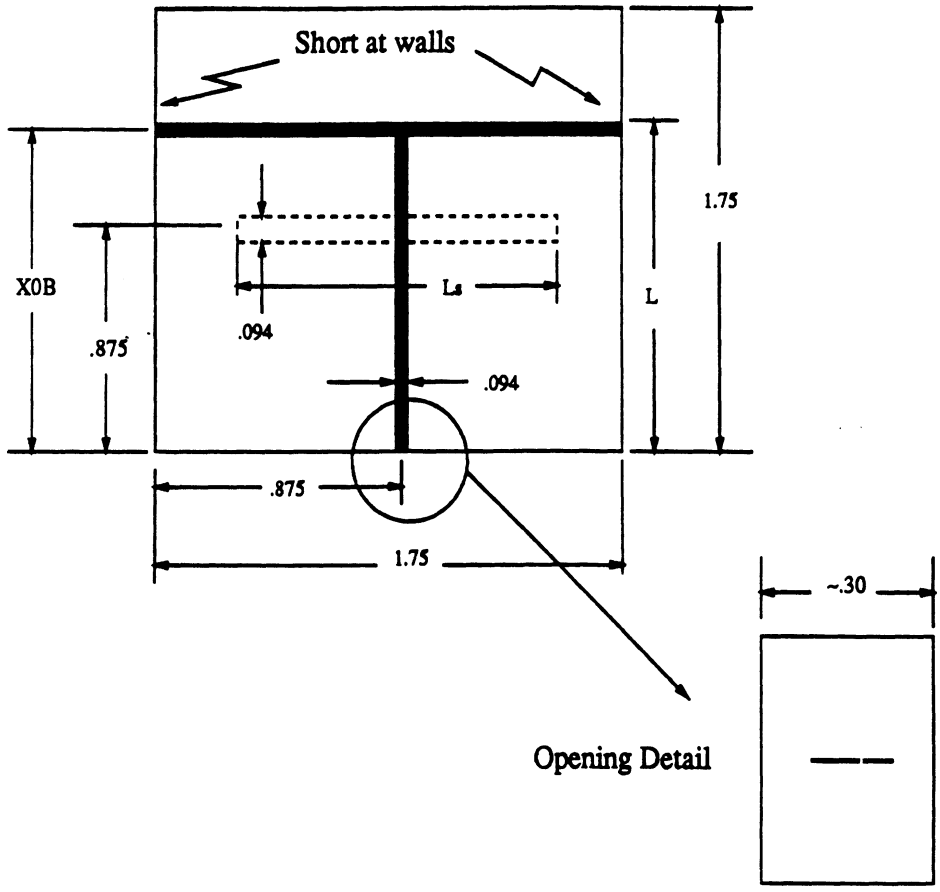

Figure 1: Strip-fed Slot Geometry.

APPENDIX F

Norman L.VandenBerg

An Investigation of a Stripline Slot Coupler

January 16, 1991

An Investigation of a Stripline Slot Coupler

N. L. VandenBerg and P. B. Katehi
Radiation Laboratory, The University of Michigan, Ann Arbor, MI

(January 16, 1991)

Background

Since our last contact late in December, we have generated some data based on our model of aperture-coupled microstrip lines using the dimensions you have specified. For reference, the geometry is duplicated in Figure 1

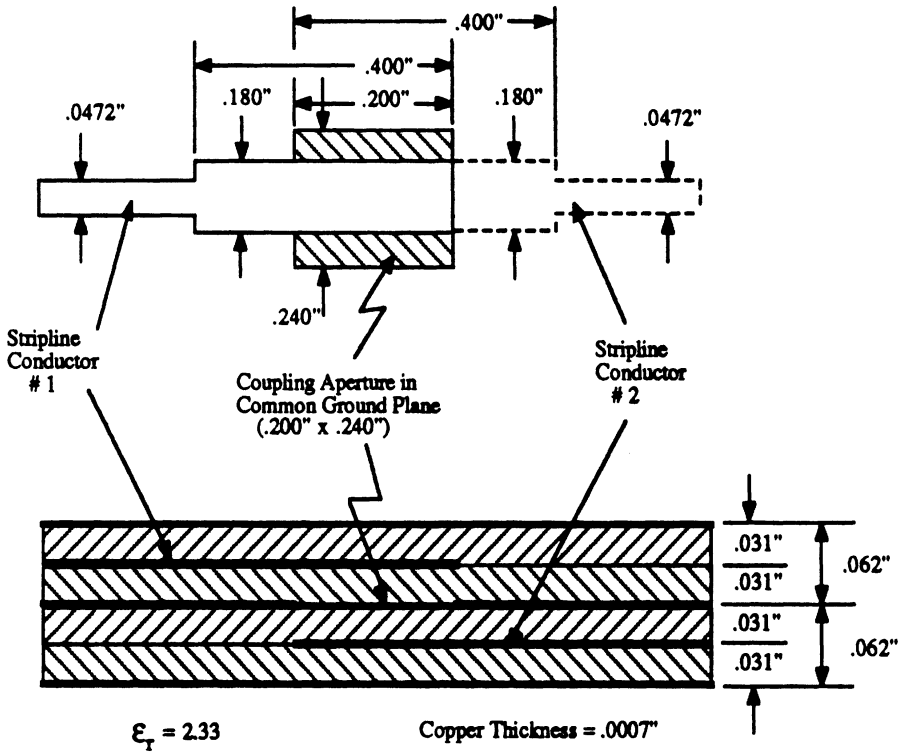

Figure 1: Geometry for stripline-fed slot coupler.

As we have discussed previously, our model is based on an assumption of narrow slots. This is a convenience which requires us to model only one component of the field in the slot, simplifying the numerical implementation. Since the aspect ratio for your geometry is rather low, it is not obvious whether this assumption can be made or not, therefore we must allow the potential for some inaccuracy in the results. On the other hand, the problem has a great deal of symmetry

and arguments can be made for neglecting the transverse electric field component which is omitted in the present model, so we can still be somewhat optimistic. We emphasize that this limitation applies only to the current implementation and not to the general formulation. If necessary, the other component could be added if a compelling need arises, however, this would take some amount of effort which is not currently planned.

A fact that we also discussed is that our model is based on a shielded structure. With the current implementation, the dimensions for the shield are required to be such that the higher order modes of the stripline are cut-off. Again, this limitation is a consequence of convenience and is not a true limitation in the sense that a more flexible program is possible, but not currently available. Of course, this is not a limitation in many cases since we would often expect to analyse these types of couplers in some kind of packaging where we would not want higher-order modes propagating anyway. Indeed, this was the original intent for this program, where now we are attempting to use it for a slightly different purpose. We have also implemented a more general case for *radiating* slots without this kind of restriction but again, a more general implementation of the coupler program is not currently planned.

The potential affect on the data to be included here are as follows:

1. A given slot length – that is, the dimension orthogonal to the axis of the strip – puts a minimum bound on the width of the shielding structure. (We assume the ground plane spacing is smaller than the width to the side walls and thus is not the limiting factor). This produces an upper bound in frequency since this dimension is directly related to the cut-off frequency for the first higher-order mode: for stripline, on the order of one-half the material wavelength.

2. To maximize high frequency capability of the model, the shield is usually chosen to be rather close to the ends of the slot if an actual dimension is not specified. This can have some affect on the response of the coupler due to the fringing effects of the fields at the ends of the slot.

Therefore some caution is advisable in making a comparison of the results of this study to measurements on a structure which is not quite the same. Nevertheless, we would expect good agreement.

Finally, upon seeing your drawing, we immediately noticed the steps in line width which you explained were intended to be part of an quarter-wave impedance transformer scheme. Now, although full-wave modelling of these types of steps is quite straightforward and in fact, we have previously done it in different contexts, this capability is not built into the coupler programs. Consequently, the data we provide will not include the affect of the step discontinuities. However, since the

steps are not very close, electrically, to the slot transition, it may be reasonable to model these transformers using conventional transmission line analysis. At the given frequencies, available CAD programs should provide acceptable performance for these types of steps so it should be relatively simple to produce a set of data comprised of the results we provide for the slot coupling and CAD models for the step transformers. For this purpose, we will provide the numerical data corresponding to the results shown here if desired. The most expedient method for transferring the data is by 'E-mail' or 'remote ftp' but it can also be supplied on diskettes if necessary.

Results

Before discussing the results, let us first define some terms and conventions:

Phase Reference: In all cases we take the phase reference as center of the slot. (Not needed for discussion here but need to interpret the actual data to be supplied later).

Line Stub Length (L) **:** This length will be the length to which the stripline extends beyond the center of the slot which is the phase reference point.

Slot Length (L_s)**:** The length of the slot is measured orthogonal to the longitudinal axes of the striplines.

Slot Width (W_s)**:** The length of the slot in the direction of the stripline axes.

As stated, to analyze the coupler shown we are ignoring the step transitions. We therefore will initially use a strip width of .180 inches. This corresponds to a 19.5Ω line at 10 GHz. Because of the techniques used, in order to generate a frequency response plot, the program is run at each frequency of interest. For each frequency, it is relatively easy to generate a database which has the lengths of the slot and line stubs as parameters. For example, a typical output of a set of runs for 10 GHz is shown in Figure 2. A collection of data for the other frequencies of interest produces similar results. We then use a seperate program to scan this database to assemble a frequency response for a given set of line stub and slot lengths.

The results for the present case is shown in Figure 3. As can be seen, the solid line, labelled L = .100 in., predicts a peak in the frequency response at about 11

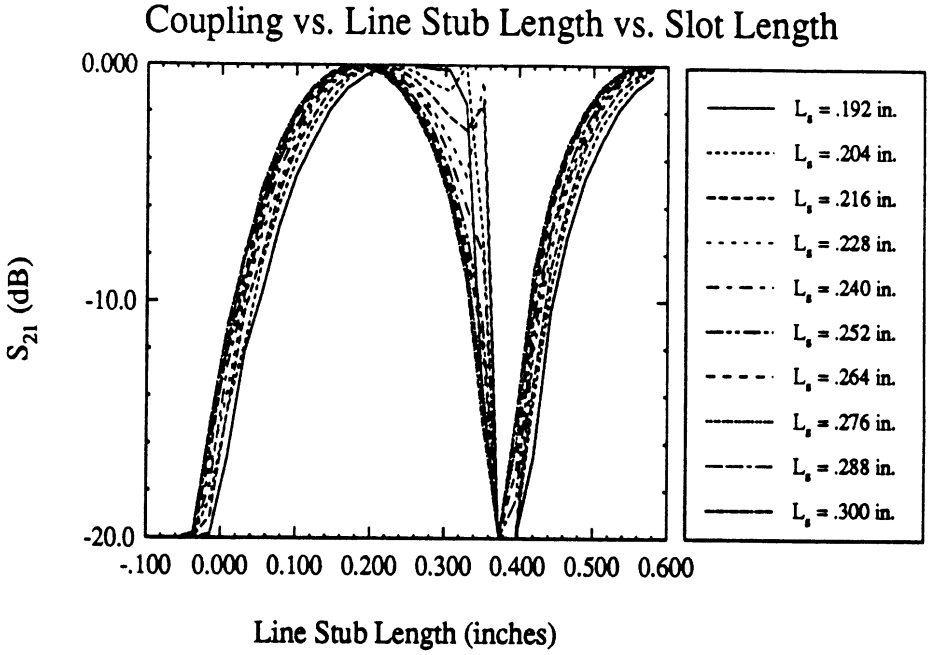

Figure 2: Coupling versus line stub length and slot length for the 19.5Ω lines at 10 GHz.

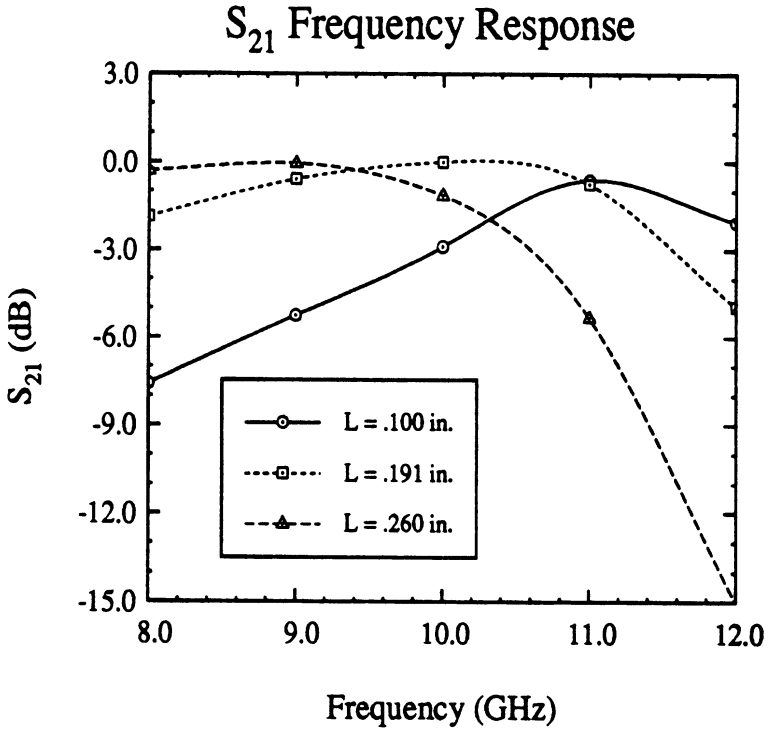

Figure 3: Frequency responses for the 19.5Ω coupler.

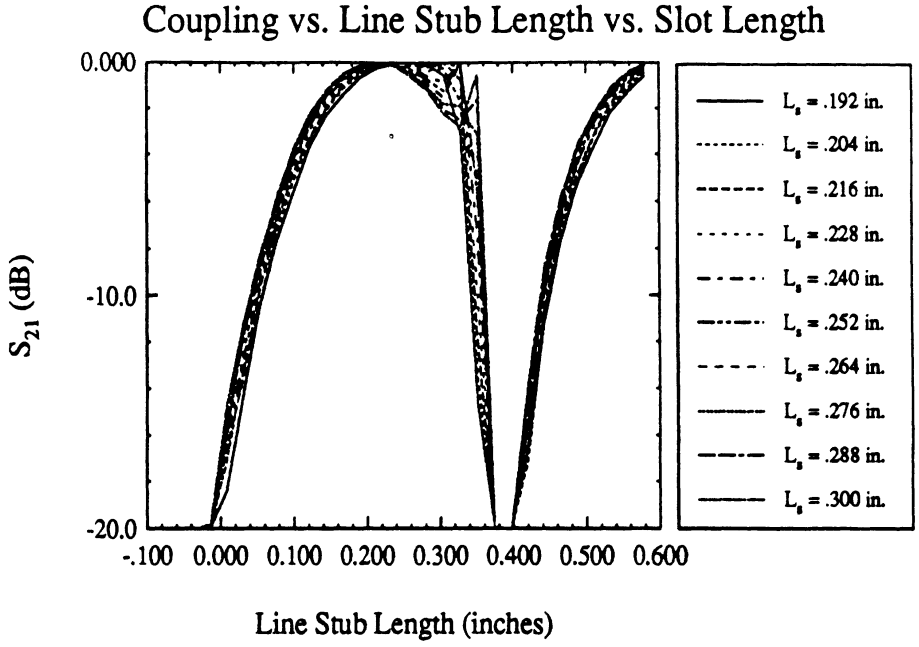

Figure 4: Coupling versus line stub length and slot length for the 49.5Ω lines at 10 GHz.

GHz with about a 3 dB loss at 10 GHz. Note that a line stub length (L) of .100 inch corresponds to the dimensions given in Figure 1 which evidently has already been built and measured. We are interested to know how this compares to the measured results – don't forget though that the step transformers have not been accounted for in this result.

The other two curves in Figure 3 show the influence of the line stub length on the frequency response. Based on this behavior, one would conclude that the stubs in the structure are too short for an optimum response at 10 GHz. We estimate that the proper length would be approximately .200 inches, assuming the step transformers do not significantly alter the behavior.

To avoid the uncertainties introduced by not modelling the transformers, we have also analyzed the identical structure, except the line widths have been changed to .050 inches corresponding to 49.5Ω line impedances at 10 GHz. A typical response versus line stub length and slot length is shown in Figure 4, again at 10 GHz. The rest of the database was assembled in the same manner and used to construct the frequency response plot shown in Figure 5.

You may have noticed from the figures, that the slot length can also play a role in changing the frequency response. This is also true of the slot width and other parameters of the structure. A similar database can be formed based on these parameters and a similar study could be assembled. Hopefully, the results we have

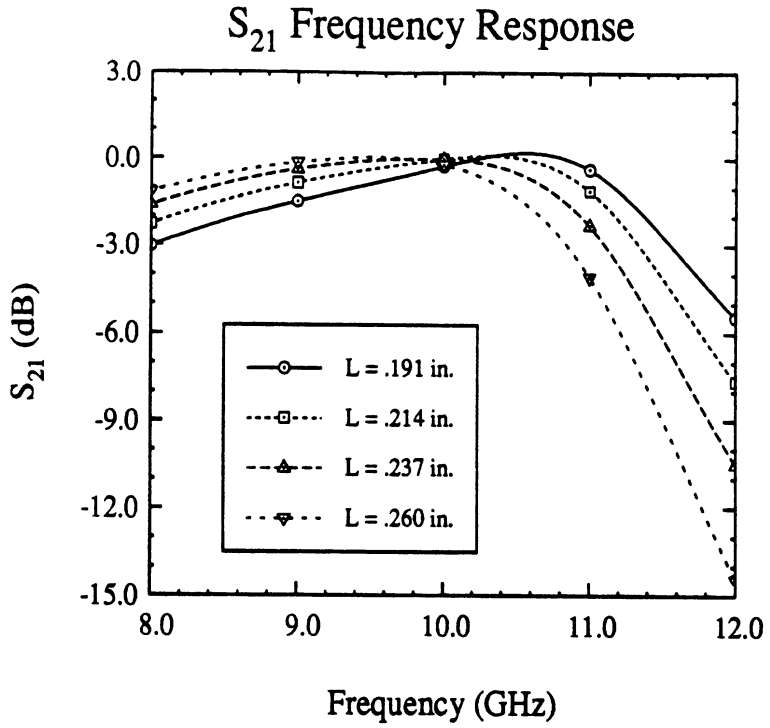

Figure 5: Frequency responses for the 49.5Ω coupler.

shown here will be helpful in your project. We also are interested in seeing how these results compare with the measurements. If there are discrepencies, we may be able and are willing to assist you in determining the causes.

APPENDIX G

Norman L.VandenBerg

On Deriving the Slot Impedance of T-Bar Fed Slot

January 29, 1991

On Deriving the Slot Impedance for T-Bar Fed Slots

(January 29, 1991)

Introduction

The purpose of this report is to clarify our previous discussion on how the impedance properties of the strip-fed slots are derived. Before proceeding however, we should point out that for this discussion we will use the term **impedance** loosely in the sense that what we are concerned with at the moment is the determination of the **value** of the impedance, since we believe that the existing codes will correctly predict the **behavior** of the impedance as a function of frequency or geometric parameters. Of course, we have already seen evidence of this through your measurements in that the resonant length (or frequency) appears to be correct. This of course is significant since resonant length is probably the most important parameter. Specifically, what remains is to develop the ability to predict the impedance values; *i.e.* the resistance goes through a peak and the reactance through zero[1] at the right place but 'how high is the peak' and 'what is the slope of the reactance?'

The approach we have developed for a two-port element, such as the one shown in Figure 1, is based on an application of the Reciprocity Theorem. As I have pointed out, it is now not immediately obvious that the codes developed for deriving the equivalent slot impedance of two-port elements is *directly* applicable to the T-Bar fed slots, although we originally thought they would be. For certain cases however, that is, for the stripline-fed slots we are interested in here, it may still be possible to produce meaningful results without a complete reformulation and massive reprogramming effort for the more general case. Although a general application of the Reciprocity Theorem would undoubtedly work, an effort to use the existing formulation is more likely to produce results in the short term so this seems to be the approach to take for the T-Bar slots.

The necessity to use the Reciprocity Theorem as opposed to other methods, lies in the nature of the structure. As with other full-wave field solution approaches, the model will correctly determine the fields throughout the structure and the associated currents. However, in order to translate these quantities into those

[1] Actually, the reactance at the resonance point does not necessarily equal zero. This is due to parasitic reactances which are not a function of the slot length but can be tuned out by external circuitry. For this reason we usually will define resonance in terms of the peak in the resistance curve.

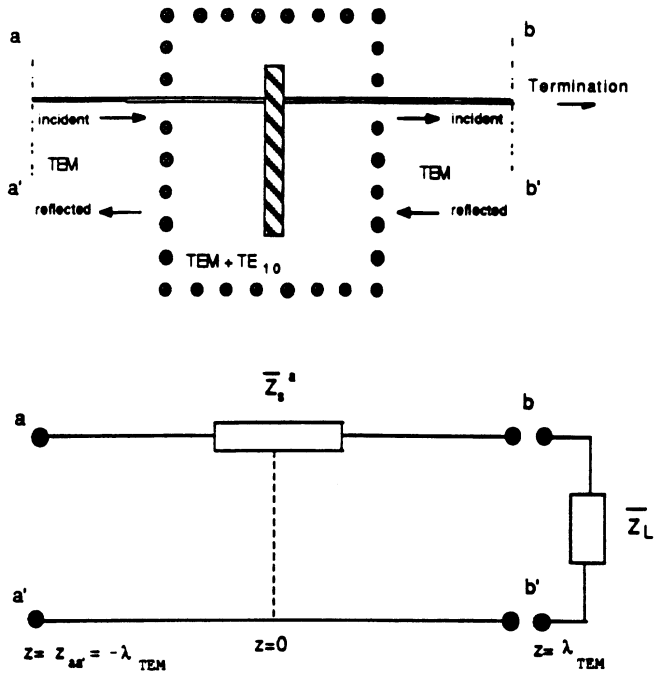

Figure 1: Two-port strip-fed series slot with equivalent circuit.

which can be used in the context of an equivalent circuit such as Z- or S-parameters, the resulting currents or fields must be interpreted.

For our case specifically, in order to derive the scattering parameters from the current on the strip, we need a minimum line length of about one wavelength, measured from the discontinuity (slot), possibly more. If this were the case, the total current found on the strip from the method of moments solution could be separated into 'incident' and 'reflected' currents which immediately indicate the scattering parameters for the discontinuity. The method we usually use for this is a 'Standing Wave Method' which measures the standing wave ratio of the solution and the positions of the current peaks or nulls relative to the discontinuity.

The situation is further complicated for our problems because the line will support more than one propagating mode in the cavity. We believe it would still be possible to derive the parameters for this case except for the fact that we don't have enough line length. In order to increase the line length, one of the cavity walls would have to be moved away from the slot, however, the position of the walls have a strong influence on the resonance behavior of the slot so we would no longer be analyzing the correct problem. In fact, the first higher order mode is allowed to propagate in order to reduce the resonant length of the slot to something less than the width of the cavity. Consequently, we have developed the method

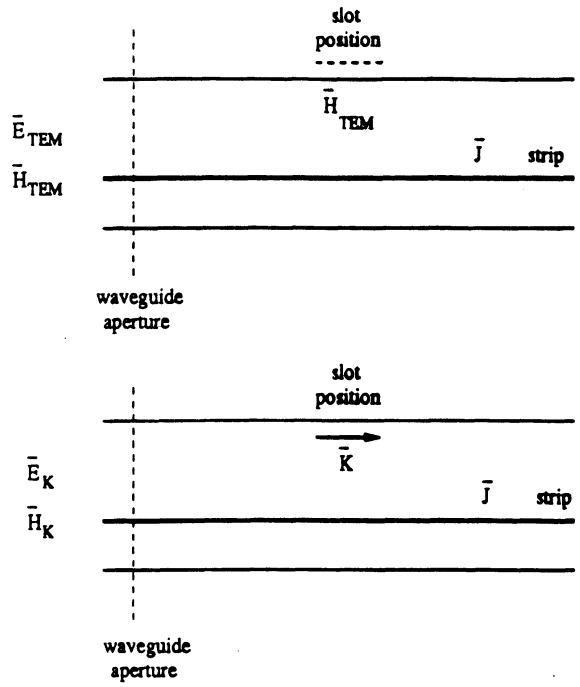

Figure 2: Two cases for the application of the Reciprocity Theorem.

described below which does not require a length of line to determine the scattering parameters.

The Reaction Method

For the two-port problem, the Reaction Method is derived from an application of the Reciprocity Theorem to the cases illustrated in Figure 2, The general form of the Reciprocity Theorem is

$$\int_S (\overline{E}^a \times \overline{H}^b - \overline{E}^b \times \overline{H}^a) \cdot d\bar{S} = \int_V (\overline{E}^b \cdot \bar{J}^a - \overline{H}^b \cdot \overline{K}^a - \overline{E}^a \cdot \bar{J}^b + \overline{H}^a \cdot \overline{K}^b) dV \qquad (1)$$

The upper schematic represent the 'a' case which is an infinite shielded microstrip line with no slot present in the ground plane, although the ultimate position of the slot is indicated. Also there is no cavity present so this line is uniform in the direction of propagation and can be treated as a two-dimensional problem.

The lower schematic illustrates case 'b' which has the same structure as 'a' except the slot is now present, represented by the equivalent magnetic current $\overline{K}$. The presence of the slot is also implies that $\overline{K}$ is derived from the solution to

the cavity problem, although the presence of the walls is inconsequential to the application of the Theorem as will be seen.

To apply the Theorem, we define a volume which conforms to the walls of the cavity except for the walls transverse to the strip. These boundaries are taken to be *outside* the physical dimensions of the cavity which is justified below for the dominate (TEM) mode case. The location of one of these transverse surfaces is indicated in Figure 2 referred to as the 'waveguide aperture'. The fields of interest on this aperture are shown in the upper schematic as $\overline{\mathrm{E}}_{TEM}$ and $\overline{\mathrm{H}}_{TEM}$ which are the dominant mode transverse field components of the shielded microstrip. For the 'b' case, the transverse fields are produced by the magnetic current $\overline{\mathrm{K}}$ (and electric current $\overline{\mathrm{J}}$) in the cavity and are denoted $\overline{\mathrm{E}}_K$ and $\overline{\mathrm{H}}_K$.

In the case of the two port strip-fed slot, several terms can now be eliminated resulting in

$$\iint_{waveguide} \left[\overline{\mathrm{E}}_{TEM} \times \overline{\mathrm{H}}_K - \overline{\mathrm{E}}_K \times \overline{\mathrm{H}}_{TEM}\right] dV \;=\; \iint_{slot} \overline{\mathrm{H}}_{TEM} \cdot \overline{\mathrm{K}} dS \qquad (2)$$

where we have assumed the incident wave is the dominant TEM-like mode on the microstrip line.

Now the pins forming the walls of the cavity are assummed to be sufficiently spaced at the microstrip line so that they do not disturb the dominant mode fields, thus this mode can pass through the wall unperturbed. We also assume that the opening is small enough so that the higher order modes are reflected by essentially, a perfectly conducting wall. (Incidently, we have previously found that the dimensions for this opening in the cavity wall can be a critical factor in building 'well-behaved' slots). The fields for the reflected mode, external to the cavity correspond to the 'TEM' modes and are then given by

$$\overline{\mathrm{E}}_K \;=\; \Gamma(\overline{\mathrm{e}}_{TEM} - \hat{l} \cdot \overline{\mathrm{E}}_{TEM}) e^{j\beta l} \qquad (3)$$

$$\overline{\mathrm{H}}_K \;=\; -\Gamma(\overline{\mathrm{h}}_{TEM} - \hat{l} \cdot \overline{\mathrm{H}}_{TEM}) e^{j\beta l} \qquad (4)$$

where $\overline{\mathrm{e}}$ and $\overline{\mathrm{h}}$ are the field components transverse to the propagation axis direction $\hat{l}$.

Further evaluation and rearrangement of Equation (2) leads to the following expression for the reflection coefficient:

$$\Gamma \;=\; -\frac{1}{2} \frac{\iint_{slot} \overline{\mathrm{H}}_{TEM} \cdot \overline{\mathrm{K}}\; dS}{\iint_{waveguide} (\overline{\mathrm{E}}_{TEM} \times \overline{\mathrm{H}}_{TEM}) \cdot (-\hat{l})\; dS} \qquad (5)$$

This is the central equation needed to produce the equivalent impedance of the slot from which the scattering parameters can be derived. In order to evaluate this

expression, we require field components from the solutions to the two problems illustrated in Figure 2. The first case - referred to as 'the waveguide problem' - is a shielded stripline, from which we need the transverse components of the field on the entire cross-section. From these we calculate the reaction expression in the denominator of Equation (5) which, for the lossless case, is twice the characteristic impedance of the line. Additionally, we will then have the numerator $\overline{H}_{TEM}$ term at the location of the slot which is used as the excitation for the second case - 'the cavity problem'. From the cavity problem we need to find $\overline{K}$, a conductor-backed, equivalent magnetic current representing the tangential electric field in the slot through the Equivalence Principle. With these quantities, Equation (5) is evaluated to produce Γ.

Based on assumptions on the symmetry of the field in the slot, the cavity-backed slot can be treated as a two-port series impedance element as shown in Figure 1. Once Γ is known, we can then determine the equivalent slot impedance (normalized to the microstrip line impedance) given by

$$\tilde{Z}_s = \frac{2\Gamma}{1-\Gamma} \tag{6}$$

from which the equivalent circuit scattering parameters can be derived by standard network theory.

Application to T-Bar Fed Slots

The T-Bar case is a more complicated. The primary difference is that the strip does not continue through cavity but instead branches out to the side walls as shown in Figure 3. An examination of Equation 1 shows that some of the terms

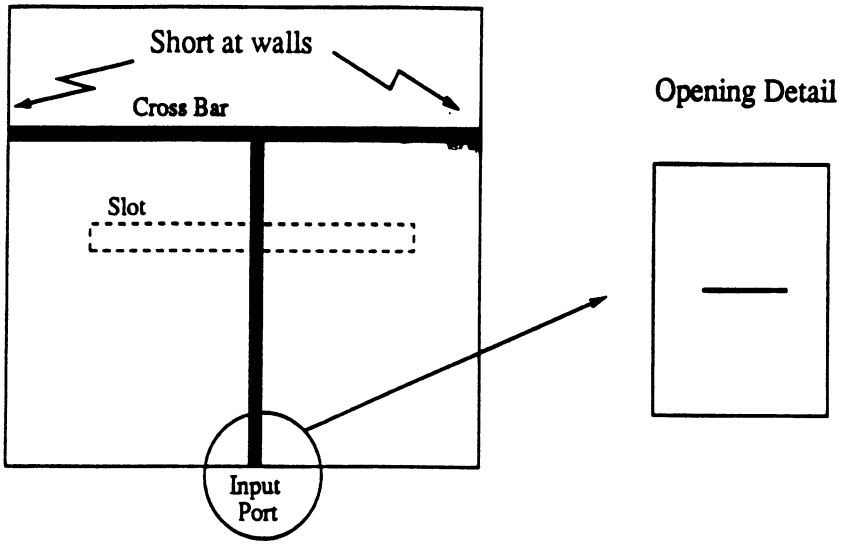

Figure 3: T-Bar fed slot geometry.

which previously were zero, no longer are. Specifically, the first term on the right hand side is not necessarily zero since the $\overline{E}^b$ term is no longer forced to zero on the 'a'-strip location beyond the cross line of the T-Bar. Similarly for the third term, the $\overline{E}^a$ field may be non-zero at the location of the $\bar{J}_b$ current on the cross line. Since the impact of ignoring these terms is uncertain, the required adjustments to the numerical model are also not clear. In addition, there are other terms omitted on the left hand side, however, these are neglected also in the two-port case since we do not explicitly model the feed line openings.

Despite these factors, the field solutions are otherwise rigorous and will give the correct field amplitudes and currents. Therefore, the resonant behavior will be correctly predicted. The question of determining the impedance values is still under investigation. To this end, whatever measurements you can supply will be most useful. To simplify the problem, it may be of interest to measure the input impedance of the open-end case described in our earlier communication.

Equivalent Circuit and Expected Result of Measurements

The equivalent circuit of Figure 1 is also applicable to the T-Bar or open-end cases. The difference is that the load, $\bar{Z}_L$, is actually inside the cavity and the cavity itself then looks like a one-port element. Because the cross-bar is shorted to the walls, $\bar{Z}_L$ presents a purely reactive load to the slot. (This is only true to the extent that we can neglect the coupling between the cross-bar and the slot which is what we had originally planned to do. It is probably a good approximation to first order however, as I mentioned in our conversation, we have expanded the model to include this coupling to remove any uncertainty about this factor).

Thus the one-port impedance of the slot, referenced to the slot location, is simply the sum of the slot impedance and the load impedance referenced to the slot plane. De-embedding the slot impedance from the total measurement then is reduced to accurately determining the reference plane and load impedance. If the reference plane can be accurately set, the load impedance is easy to measure by closing the slot with a conductor and making the measurement. (Copper tape can be used or an identical test piece can be built without the slot).

An alternative is to simply measure the element as you have done and consider the total impedance as the slot impedance, without regard to the separate components inside. This is equally acceptable and at the moment we don't know whether either approach is to be preferred over the other, although this latter approach is conceptually simpler. Perhaps you have a preference or convention. Neither eliminates the difficulties discussed above since the fundamental quantity we derive is Γ.

Plan of Action

The above discussion gives some background which outlines the approach for analysis of the two-port slots. Also included is some discussion of the difficulties encountered in determining the impedance of the T-Bar fed slots.

To resolve these problems, we have not yet looked at the current formulation long enough to know whether the current approach can work or not. We also have in mind, several alternative approaches which can potentially lead to a solution, each requiring a different amount of effort and each, as always, having their own uncertainties as well. In the coming weeks we will continue to look at the present formulation to determine whether or not the correct impedance values can be derived. If not, we will then re-evaluate the situation and explore the other alternatives.

APPENDIX H

Norman L.VandenBerg

Corrected Results for Stripline Slot Coupler

March 7, 1991

Corrected Results for Stripline Slot Coupler

N. L. VandenBerg and P. B. Katehi
Radiation Laboratory, The University of Michigan, Ann Arbor, MI

(March 7, 1991)

This paper reflects changes in the numerical results discussed in our previous communication dated January 11, 1991. As you already know, the changes are a results of a sign error in the program which we identified in the course of making our own measurements on a similar structure. Because of the good agreement we found in that case, we now feel that the present data should give a good indication of how the structure we have been discussing should perform. Of course, this statement must be qualified by the conditions which we have stated previously and which still apply, that is, the present geometry may not meet some of the conditions we have assumed, allowing us to neglect certain factors. Therefore, the potential for some discrepancies in the results for this case still exists and we would suspect these factors play a role in any inaccuracies that may be found.

In general, the new results show that the current geometry does not seem capable of obtaining optimum coupling through the slot, *i.e.* $S_{21} = 0$ dB, at least within the variation of parameters used here. In this case, as before, we have varied two fundamental parameters; the slot length (L_s) and line stub length (l). The effect of varying these parameters is demonstrated in Figure 1 which is similar to Figure 2 of our previous memo except for the peak level of coupling.

You can see that the coupling as a function of line stub length behaves essentially the same as in our previous results. As the slot length (L_s) is varied however, the peak obtainable coupling is increased for each successive lengthening of the slot, up to a peak coupling of about -1.5 dB at a slot length of .300 inches. Careful study of the results also shows that the curves are reaching the point of diminishing returns, that is, it does not seem that a further lengthening of the slot will ultimately lead to 0 dB coupling. In fact, most likely at some point the trend will reverse and coupling will be reduced based on our previous interpretations of the influence of slot length.

As before, an ensemble of similar curves is generated at different frequencies and a frequency response is obtained. For the 19.5Ω lines, the result is shown in Figure 2 for several line stub lengths with the slot length set to .240 inches corresponding to the dimension used in the experiments. Again the curve for l = .100 inches reflects the case which was originally built. The l = .200 inches case is the dimension we suggested in our previous report.

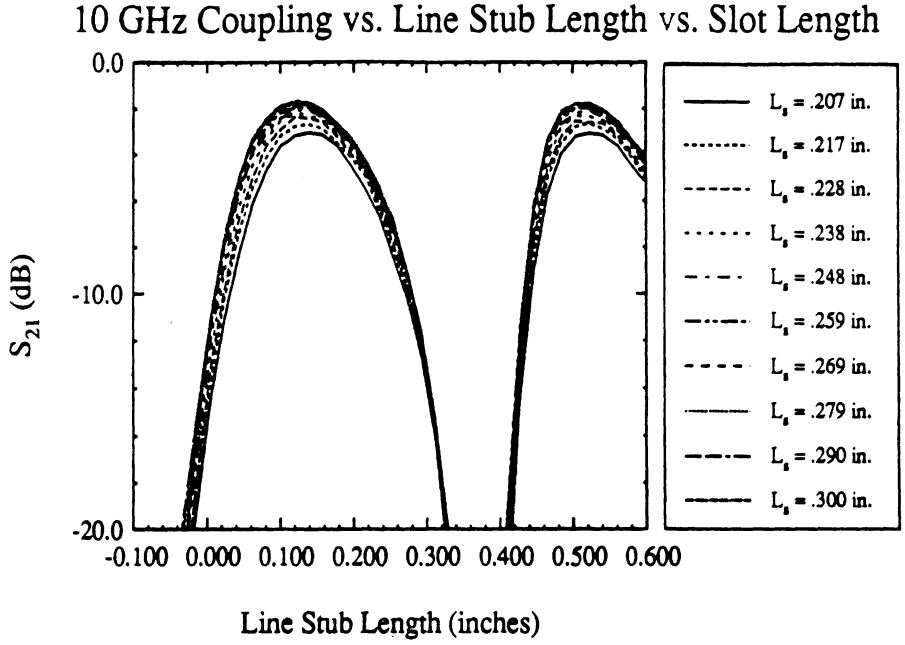

Figure 1: Coupling versus line stub length and slot length for the 19.5Ω lines at 10 GHz.

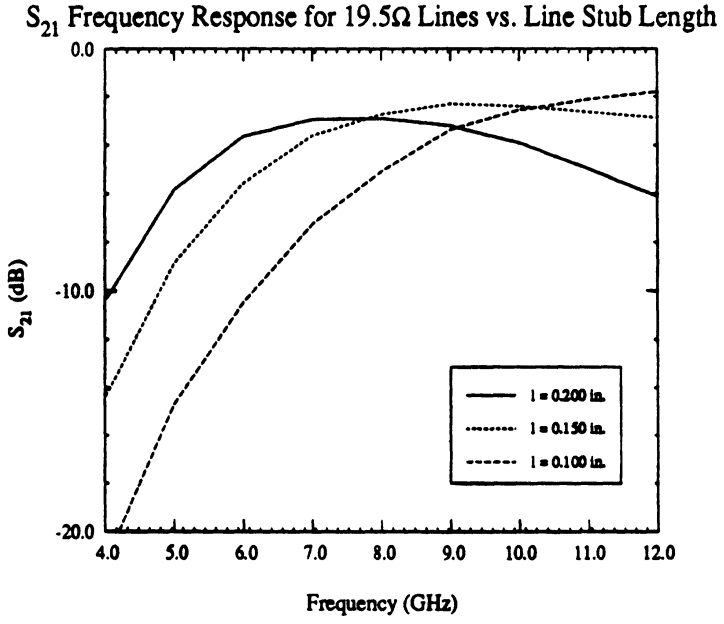

Figure 2: Frequency responses for the 19.5Ω coupler.

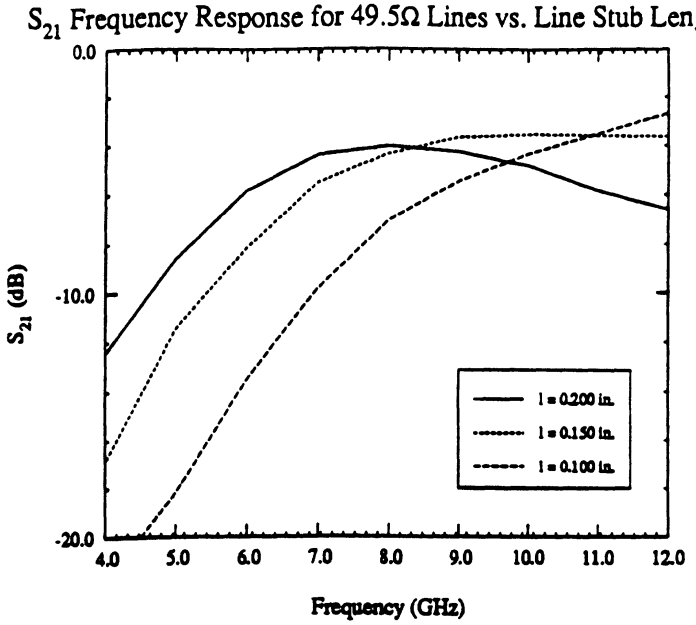

Figure 3: Frequency responses for the 49.5Ω coupler.

A similar procedure was used to generate a frequency response for the 50Ω lines which is shown in Figure 3. You'll notice that the curves have substantially the same shape for this case except the peak coupling is about 1.5 dB lower. Obviously, narrower line widths do not improve the peak coupling but degrade it. Remember that for both cases we have again used uniform lines with no step transformers as explained before.

One final note on the data which is a reminder of the discussion in the previous report. All cases here were generated using a box width of .300 inches, corresponding to a cut-off frequency of approximately 12.9 GHz for the higher order modes. Consequently, since the method of extracting the circuit parameters assumes only one mode is present, the data becomes more and more suspect as this frequency is approached. Therefore, some judgement is required when considering the agreement with experimental data at the high frequency end.

In conclusion, we have seen some changes in the results generated in the previous report due to the discovery of a sign error in the program. This has changed the shape of the expected frequency responses somewhat, the most significant change being the introduction of a 2 to 4 dB loss in the peak coupling. The general behavior however, seems to be substantially the same as what we have seen previously, except for the loss.

Due to the limited gains achieved by lengthening the slot, we suspect that the slot width may now be the limiting factor, although a wider line may improve peak

coupling as well. In fact, by narrowing the slot width, this case becomes closer to the one we have measured for which we obtained ~0 dB coupling over a broad frequency range. Another remaining possibility is that the assumptions we have made concerning the aspect ratio of the slot dimensions may be invalid as discussed in the earlier report. As you may recall, we explained that our current programs are based on an assumption of narrow slot widths for which the transverse component of equivalent magnetic current in the slot may be neglected. Since the ratio of length to width for the proposed slot may not meet this criterion, the assumption may be invalid in this case which may account for any remaining discrepancy between the results shown here and the experimental measurements. We hope that these curves now indicate better agreement with the experimental data.

APPENDIX I

Norman L.VandenBerg

Report on Model Development for T-Bar Fed Slots

October 9, 1991

Report on Model Development for T-Bar Fed Slots

(October 9, 1991)

I. Introduction

In our last report, "Status Report on Model Development for T-Bar Fed Slots" (dated 6/25/91), we discussed a revised application of the Reciprocity Theorem previously applied to the analysis of two-port strip-fed slots. In addition, we presented some observations indicating limitations of the current model. One conclusion was that the omission of an explicit model for the opening(s) in the cavity wall(s) leads to incorrect field values on the slot under certain conditions. This results in incorrect and unreasonable values for the reflection coefficient and slot impedance. Also, the question was raised as to whether or not we should expect to see a substantial increase in bandwidth for the T-bar fed slot as opposed to the two port series fed slot which is inherently narrow band. Since that time, we have made considerable progress in understanding the behavior of both the slots and the models and also have investigated the possibility of increased bandwidth. This report is a summary of the developments.

II. Further Development of the Alternative Reciprocity Theorem Method

The Reciprocity Theorem Method, as developed in the previous report is correct with the exception of the sign before the Γ_L term in Equation (6) of that report (and in Equation (8.5, p.162) of Radiation Laboratory Report RL877 which you also have). The equation should read

$$\Gamma_S = -\frac{1}{2}\frac{\iint_{slot} \overline{H}^a_{TEM} \cdot \overline{K}\ dS}{\iint_{waveguide} (\overline{E}_{TEM} \times \overline{H}_{TEM}) \cdot (-\hat{l})\ dS} + \Gamma_L \qquad (1)$$

Evidence of the correctness of this equation is shown when it is observed that for $\overline{K} = 0$, as in the case without a slot, the reflection coefficient corresponds to the terminating load, as it should. We also note that the $\overline{H}^a_{TEM}$ term can be written as

$$\overline{H}^a_{TEM} = [1 - \Gamma_L]\, \overline{h}_{TEM} \qquad (2)$$

where $\bar{h}_{TEM}$ is the field solution for a travelling wave current on an infinite line - the same as used for the two-port case.

To further explore the limitations of the current model, we first investigated the case of a slot fed by an open-end line. This eliminated an uncertainty on the correctness of the coupling terms between the cross bar and the main strip for the T-bar case. Also, we offset the line from the center of the cavity commensurate with our earlier suspicion that the omission of an explicit model for the apertures was a problem and that this problem would be most severe at the cavity center. Examples of reflection coefficients as a function of slot length for various open-end line lengths are shown in Figure 1. As one can see, the nominal termination impedance moves around the outside of the chart as it should for various length of open end lines. However, for certain line lengths, the reflection coefficients are obviously incorrect since they are outside the Smith chart. This behavior provides a clue, as to the true nature of the model's limitation.

Choosing one set of data which looks reasonable (line length = .50323) and varying the slot offset leads to the set of curves shown in Figure 2. We see that as the slot offset is increased, the reflection coefficient again moves outside the chart. Through an understanding of how these conditions effect the strip current and the coupling between the strip and the line, we conclude that the problem with the model is not the modelling of the apertures *per se*, but is really the improper termination of the line at the aperture. (The present model approximates the line termination at the wall with a short circuit). The parameter which bounds the range over which the Reciprocity Theorem Method will be reasonably accurate is the strength of the coupling between the strip and the slot.

Coupling is controlled by a number of factors, primarily the slot offset and the location of current maxima and minima on the line relative to the slot. For small coupling, that is, for small offsets or if a current null is near the slot, the slot behavior and field values are dominated by the TE_{10} and higher order modes in the cavity. For larger offsets or with a current maximum near the slot, the termination of the line has a much stronger influence on the slot field. Thus if the line is not match terminated at the feed-through aperture, the current on the line will be incorrectly distorted and with strong coupling, the slot field will be significantly effected to incorrect values. This leads to reflection coefficients which are greater than unity since the reaction formulation assumes a matched source.

Since the problem with the model is now recognized to be the termination of the line and not the apertures, we realized that we no longer need to consider the L-Bar geometry as previously suggested, since this would not avoid the true problem anyway. (Note that, most probably, the neglect of the apertures must be compensated for as well, as described in Radiation Laboratory Report RL877). We therefore proceeded with the development of a method to determine Γ_L, the

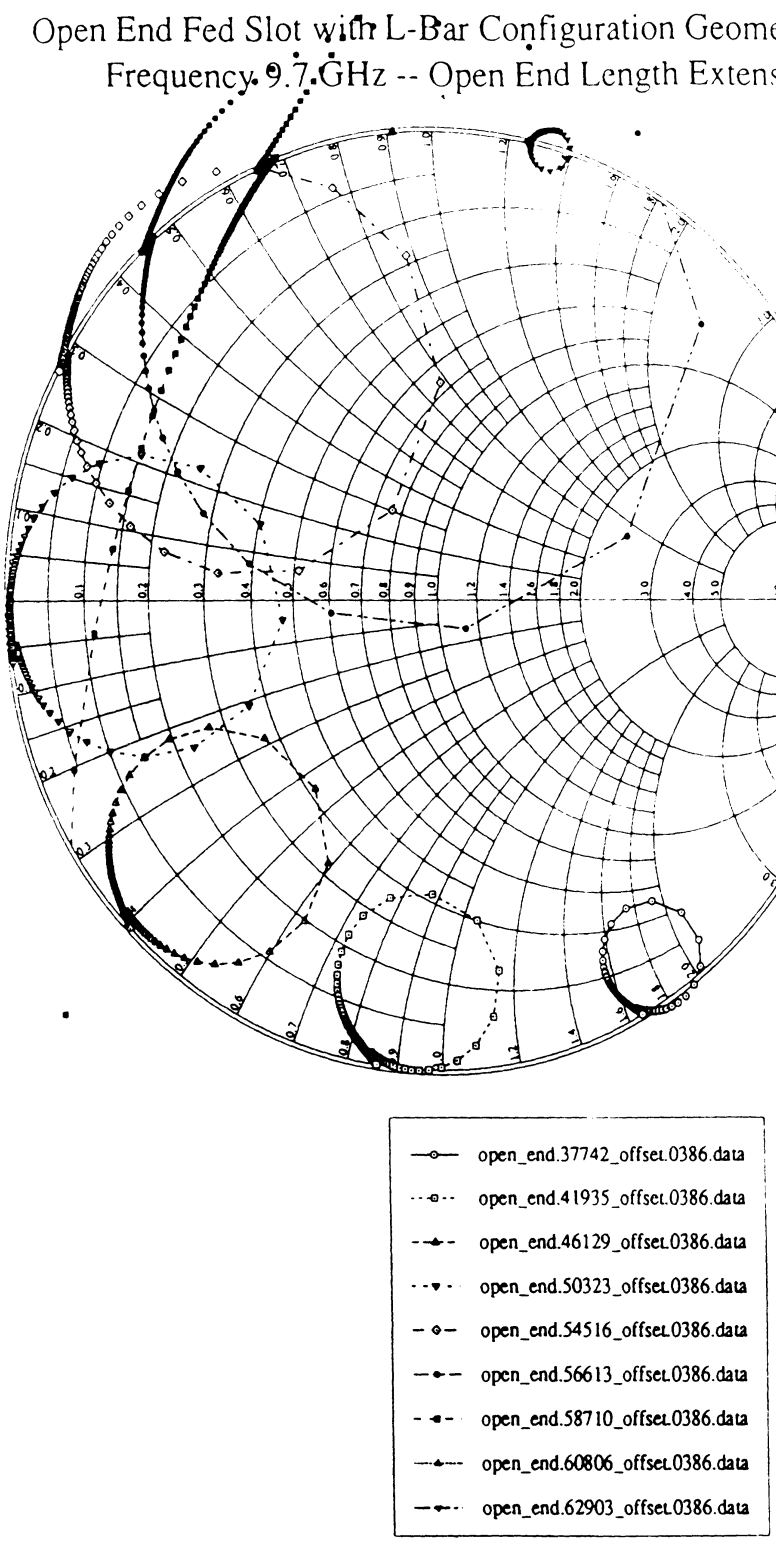

Figure 1: Variation of reflection coefficient with slot length for various lengths of open-end lines.

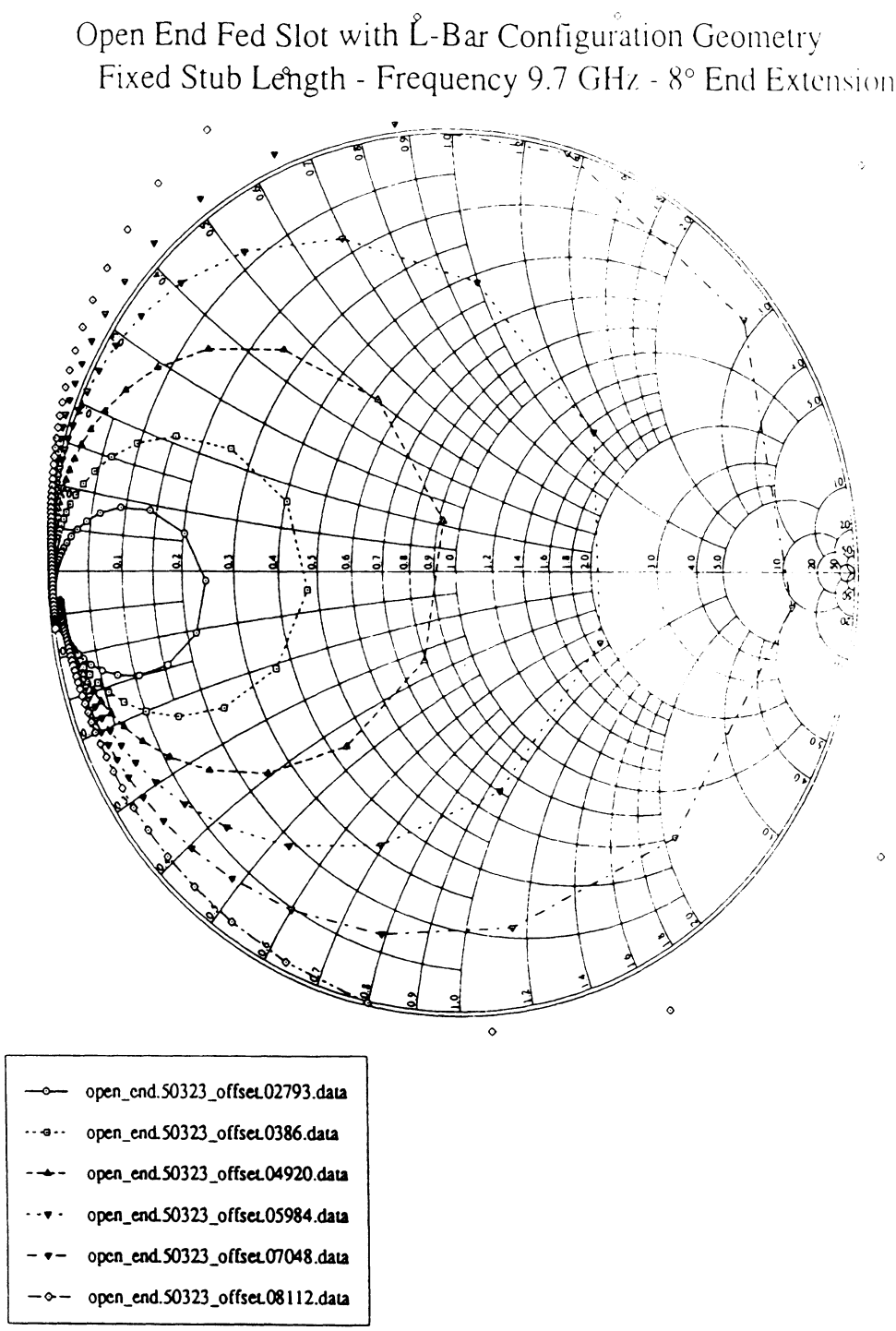

Figure 2: Variation of reflection coefficient with slot length for various slot offsets.

need for which was suggested in the previous report, and which also will provide a solution to the source termination problem.

III. Development of a Method to Determine Γ_L

In previous reports we have explained the difficulties in obtaining scattering parameters from a current distribution on the line if the line is relatively short. These discussions were based on the limitations of the method we have traditionally used which are discussed in Chapter 5 of report RL877 (the 'Standing Wave Method'). Overcoming the limitations of this approach was the original motivation for the development of the Reciprocity Method several years ago. Recently, we have taken a new approach which eliminates these difficulties. The technique uses Prony's method to fit the current on the strip with a set of complex exponentials. From the resulting frequencies, amplitude and phase coefficients, we can derive the reflection coefficient directly, even for short lines.

This method has been implemented to solve for the reflection coefficient of the one port slot problems. By exciting the T-bar with a gap generator at the feed-through aperture and using Prony 's method to evaluate the current, the problem with the short circuit termination at the source is eliminated. Thus, we now have a model which produces reasonable reflection coefficients for the T-bar fed slots. We now can proceed to evaluate the potential of the T-bar fed slots for wider bandwidth, based on the assumption that the model is providing valid results. We note that this method should provide improved accuracy for the two port case as well, especially for large slot offset, however, it has not been implemented in the numerical codes for that case. It also has beneficial features which could improve the efficiency of the codes for the microstrip-to-microstrip slot coupler.

IV. Investigation of Bandwidth for T-Bar Fed Slots

In order to systematically detect errors, we first performed some numerical experiments on the case without the slot. By looking at the behavior of the reflection coefficient as a function of line length in comparison to results for an open-end, and re-examining the formulation in report RL877, we were able to correct two programming errors in the programs which caused the effect of the cross-bar to be less pronounced than it should have been. The current programs now produce strip currents which are reasonable, based on physical expectations and previous experience and are expected to be correct.

To investigate the bandwidth behavior of the T-bar fed slots, we next introduced the slot and examined a case at 9.7 GHz. The geometry is specified in Table 1. We will assume that we intend the slot to be matched at 9.7 GHz so

Electrical Parameters	
Frequency	9.7 GHz
Dielectric	$\epsilon_r = 2.2$
Mechanical Parameters (inches)	
Ground Plane Spacing (c)	0.0625
Strip Width (W)	0.05
Cavity Width (b)	.750
Cavity Length (a)	.650
Slot Width (Ws)	0.05
Main Line Length (L - final)	.5871
Cross Line Center (X0B - final)	.5621

Table 1: T-Bar Case Parameters.

we first must determine the proper dimensions for that condition. Figure 4 shows several runs of the program with different terminations lengths. The termination length is defined as the distance the main line extends beyond the slot, where it is coupled to the cross bar which is shorted at the side walls (see Figure 3). From Figure 4, we see that the termination length has a strong influence on the position of the curves on the chart. We also see the convergence of curve to the value of Γ_L as the slot length approaches zero. (Along each curve, slot length is progressively reduced in the counter-clockwise direction.) Since our original goal is to match the slot at 9.7 GHz we choose the main line length to be fixed at .5621 inches ('tbar.5621.prony.data' case). For this case, the slot is most closely matched at a slot length of .5053 inches, as indicated.

We now generate a frequency response by running the model with this geometry at different frequencies. The results are shown in Figure 5. By finding the data points which correspond to a fixed slot length (.5053 inches indicated), we can plot the frequency response. It would appear that for this case, the projected frequency response has a strong similarity to the 'vs. length' curves. This suggests that the reflection coefficient rapidly traverses the area near $\Gamma = 1$ as a function of frequency, indicating a relatively narrow bandwidth, similar to the behavior of the two-port series fed slots.

In order to find explore the possibility of greater bandwidth further, let us look again at Figure 5. We note three characteristics indicated on the plot:

1. The relative position of the data point for a fixed slot length progresses counter-clockwise on the curves as the frequency is increased. This is an

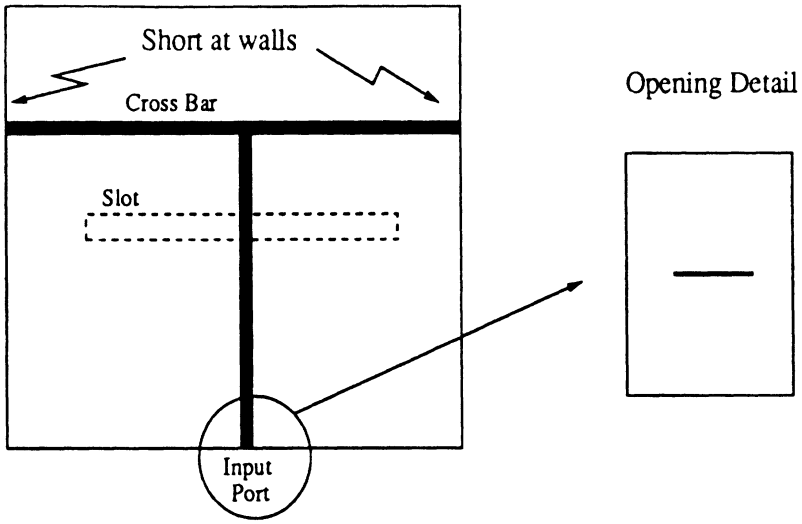

Figure 3: T-Bar fed slot geometry.

indication of the relationship of resonant frequency to slot length. For these types of slots, it is not necessarily inversely related to slot length in wavelengths, as discussed in Chapter 6 of RL877. To improve bandwidth, one must find the geometric or electrical parameters which minimize the sensitivity of resonant frequency to slot length.

2. The endpoints of the circles move around the chart in correspondence with the termination characteristics of the T-bar with frequency. In the case shown, this effect causes the positions of the entire data circles to shift in the *clockwise* direction as frequency is increased. If one can find a geometry such that the movement of these points compensates for the movement of the fixed slot length data point discussed above, the bandwidth of the slot will be enhanced. This possibility is really the only unique characteristic of the T-bar fed slot approach which may make an improvement in bandwidth possible. It is really quite different from the older type of cavity-backed T-bar antenna elements we have previously discussed.

3. The radii of the circles progressively decreases as frequency is increased. This will limit the bandwidth irrespective of the compensations achieved by the effects above. To maximize bandwidth, one must discover the factors which control this behavior and minimize the reduction of radius with frequency.

These features can be explored by repeatedly running the programs to study the parametric behavior of these elements, as is the primary motivation for developing

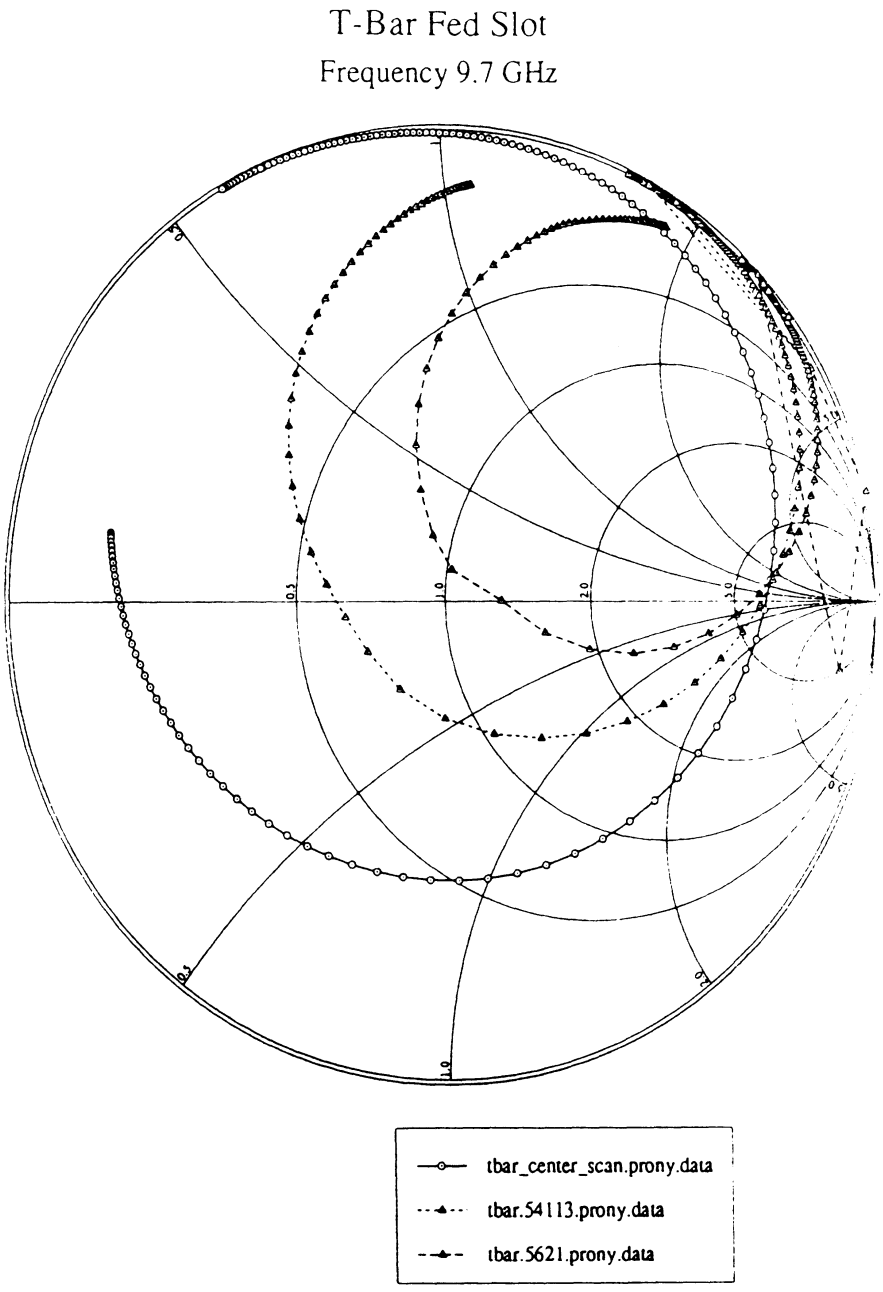

Figure 4: Reflection coefficient for the T-Bar fed slot with several different termination lengths.

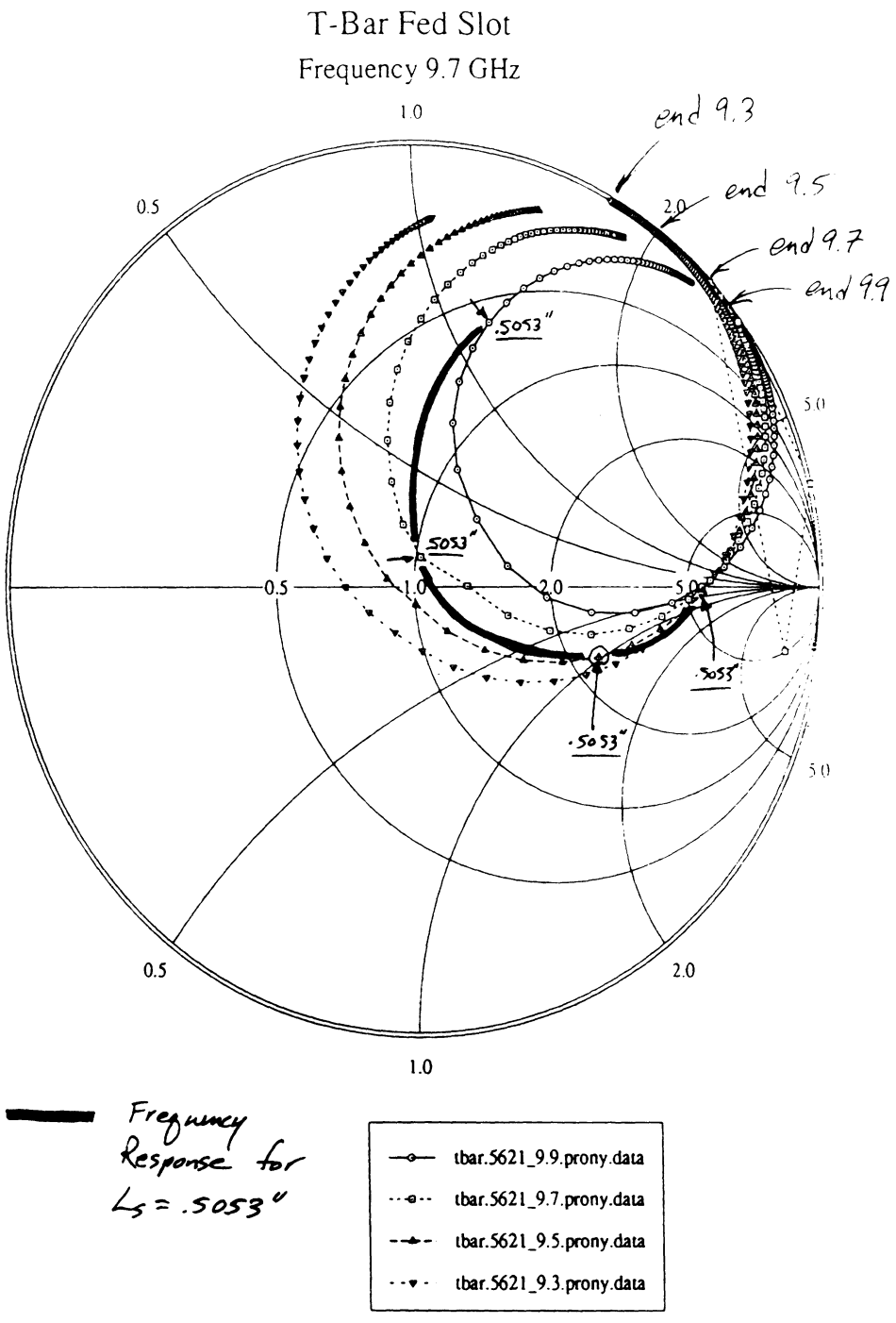

Figure 5: Reflection coefficient for the T-Bar fed slot as a function of frequency. Main feed line length fixed at .5621 inches.

a numerical model. We also note that the results shown in this report have not been validated by experiment nor has any search been made for optimum dimensions or material parameters. The results shown are simply the first set of data produced to develop the programs. However, to this point we are encouraged by the fact that the results are now feasible, since for the most part, the reflection coefficient magnitudes are less than unity.

V. Summary

In summary, we have further investigated the possibility of modelling the T-bar fed slots we have been discussing. The model is now 'complete' in the sense that it now produces results which are feasible. This has been achieved by the development of a new technique for extracting the circuit parameters from the electromagnetic solution of the problem. The technique improves the model by eliminating an approximate condition previously used for the termination of the line at source feed. The approach uses Prony's method to evaluate the current on the line.

We have noted that this method offers some benefits which, if retro-fitted to previously developed programs, could provide an increase in efficiency and accuracy. For example, the coupler analysis programs would increase in efficiency since shorter feed lines could be used. For the two-port series-fed slots, the improvement in terminating the lines at the ports should increase the accuracy of the program, especially for larger slot offsets. One potential drawback of the current implementation, however, is that the routine which implements Prony method may be slightly less autonomous or 'automatic' than the previous approach. On the other hand, most of the curves in this report were generated in an 'automatic' mode, so that the operator doesn't need to tailor the parameters in Prony's method for each data point.

Finally, for the case presented here there is no suggestion that the element will be substantially more broadband than the two-port slots. Because of the way the slot impedance circles traverse the chart, we can see the potential for a slot impedance circle which has relatively constant resistance. This suggests that greater bandwidth might be achieved through the use of external compensating networks which can be purely reactive and thus will not reduce radiation efficiency. However, this is no different from the two-port slot which can be terminated externally to produce a similar result. In conclusion, so far there is no convincing evidence to suggest that this configuration will produce substantially greater bandwidth than the other cases we have examined. Nevertheless, we must recognize that this example by no means represents the optimum set of conditions or a thorough exploration of the problem, but rather is simply the first case used for development of the program.

APPENDIX J

Norman L.VandenBerg

Addendum to Radiation Laboratory Report RL877

October 14, 1991

Addendum to Radiation Laboratory Report RL877

(October 14, 1991)

I. Introduction

The purpose of this addendum is to report and document further progress in the modelling of microstrip-fed slots since the completion of the study summarized in the referenced report. The developments have proceeded from efforts to overcome limitations of the methods previously used, discussed in Chapter 8 of RL877. The focus of the effort was to develop a model for and characterize the T-bar fed slot, also discussed in Chapter 8.

The method proposed for the T-bar case was originally based on a revised application of the Reciprocity Theorem, previously applied to the analysis of two-port strip-fed slots. RL877 notes some limitations of this approach and also demonstrates a technique to correct or compensate for some of their effects. One specific conclusion was that the omission of an explicit model for the opening(s) in the cavity wall(s) leads to incorrect slot characterizations under certain conditions. For the T-bar fed slot, the limitations result in incorrect and unreasonable values for the reflection coefficient and slot impedance.

For the case of two-port slot elements, a method was developed to compensate for the effect of the apertures. However, we also noted that the approach is limited in that it seemed to produce valid results, only for feed lines significantly offset from the center-line of the cavity. We have since discovered, that this interpretation is only partially correct. In this report, further investigation of the model's limitations are described along with

what we believe to be a more accurate interpretation of the phenomena observed. We also present an alternative method which overcomes the deficiencies and which also has significant benefits compared to the previous techniques discussed.

Also, it has been suggested that the T-bar fed slots may display a significantly greater bandwidth compared to two-port series fed slot which is inherently narrow band. Since we have made considerable progress in understanding the behavior of both the structures and the models, we have also further investigated this possibility.

II. Further Development of the Alternative Reciprocity Theorem Method

The Reciprocity Theorem Method, as developed in the previous report is correct with the exception of the sign before the Γ_L term. Equation 8.5, p.162, should read

$$\Gamma_S = -\frac{1}{2}\frac{\iint_{slot} \overline{H}^a_{TEM} \cdot \overline{K}\ dS}{\iint_{waveguide} (\overline{E}_{TEM} \times \overline{H}_{TEM}) \cdot (-\hat{l})\ dS} + \Gamma_L \qquad (1)$$

Evidence of the correctness of this equation is shown when it is observed that for $\overline{K} = 0$, as in a case without a slot, the reflection coefficient corresponds to the terminating load, as it should. We also note that the $\overline{H}^a_{TEM}$ term can be written as

$$\overline{H}^a_{TEM} = [1 - \Gamma_L]\, \overline{h}_{TEM} \qquad (2)$$

where $\overline{h}_{TEM}$ is the field solution for a travelling wave current on an infinite line (Chapter 4) - the same as used for the two-port case.

To further explore the limitations of the current model, we first investigated the case of a slot fed by an open-end line. This eliminated an uncertainty on the correctness of the coupling terms between the cross bar and the main strip for the T-bar case, since

these were not used in any of the previous models verified by experiment. Also, we offset the line from the center of the cavity commensurate with our original suspicion that the omission of an explicit model for the apertures was a problem and that this problem would be most severe at the cavity center. We have called this the 'L-bar configuration'.

Examples of reflection coefficients as a function of slot length for various open-end line lengths are shown in Figure 1. As one can see, the nominal termination impedance moves around the outside of the chart as it should for various lengths of open end lines. However, for certain line lengths, the reflection coefficients are obviously incorrect since they are outside the Smith chart. This behavior provides a clue, as to the true nature of the model's limitation.

Choosing one set of data which looks reasonable (line length = .50323) and varying the slot offset leads to the set of curves shown in Figure 2. We see that as the slot offset is increased, the reflection coefficient again moves outside the chart. Through an understanding of how these conditions effect the strip current and the coupling between the strip and the line, we concluded that the problem with the model is not the modelling of the apertures *per se*, but is really the improper termination of the line at the aperture. (The present model approximates the line termination at the wall with a short circuit, as implied by Figure 3.2, p.49, but not elaborated on.) The parameter which bounds the range over which the Reciprocity Theorem Method will be reasonably accurate is the strength of the coupling between the strip and the slot.

Coupling is controlled by a number of factors, primarily the slot offset and the location of current maxima and minima on the line relative to the slot. For weak coupling, that is, for small offsets or if a current null is near the slot, the slot behavior and field values are

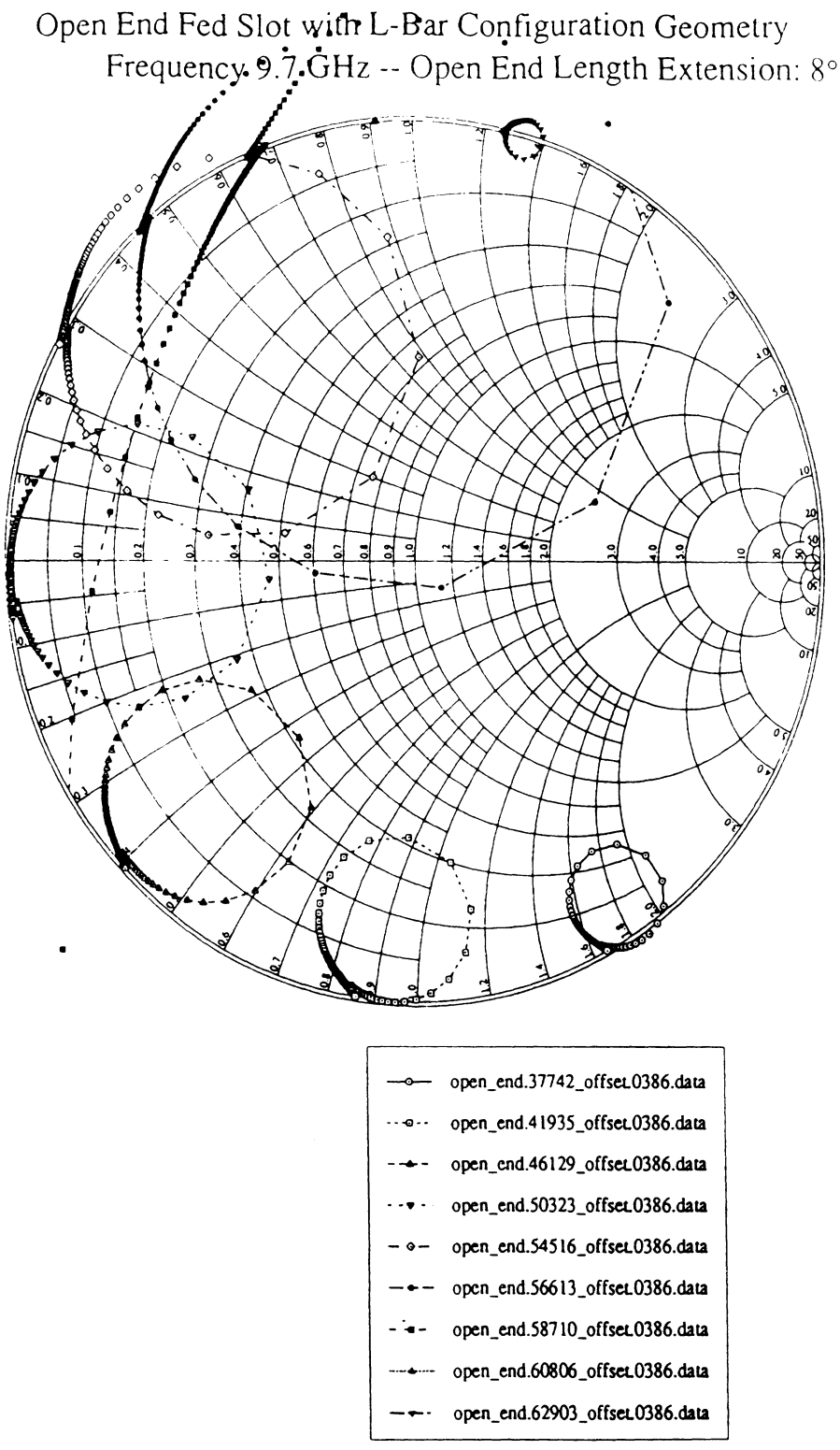

Figure 1: Variation of reflection coefficient with slot length for various lengths of open-end lines.

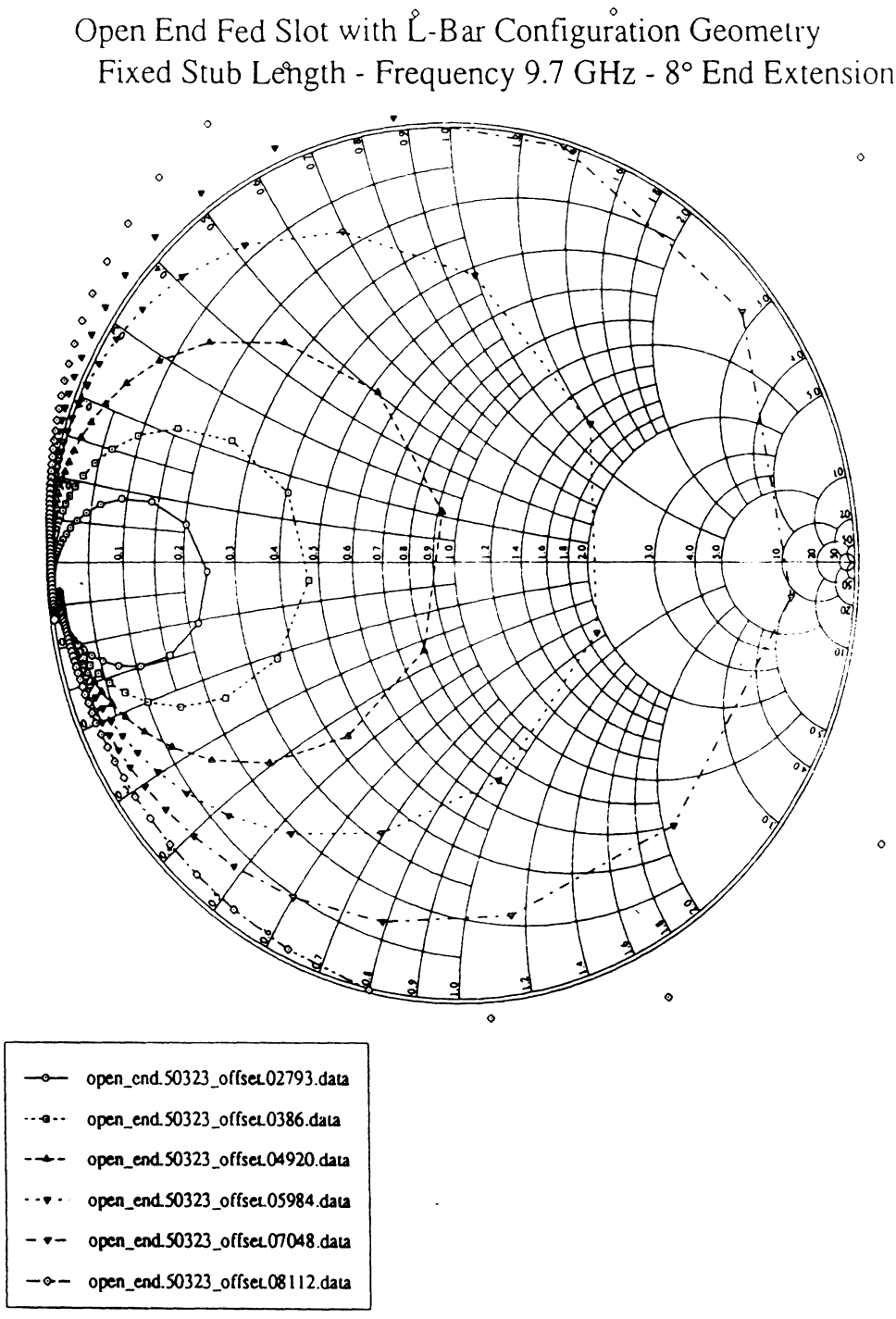

Figure 2: Variation of reflection coefficient with slot length for various slot offsets.

dominated by the TE_{10} and higher order modes in the cavity. For larger offsets or with a current maximum near the slot, the termination of the line has a much stronger influence on the slot field. Thus if the line is not match terminated at the feed-through aperture, the current on the line will be incorrectly distorted and with strong coupling, the slot field will be significantly altered to incorrect values. This leads to reflection coefficients which are greater than unity since the reaction formulation assumes a matched source.

Since the problem with the model is now recognized to be primarily the termination of the line and not the apertures, we realized that we no longer need to consider the L-Bar geometry as previously suggested, since this would not avoid the true problem anyway. (Note that, most probably, the neglect of the apertures still must be compensated for as well, as described in RL877, Ch. 6.) We therefore proceeded with the development of a method to determine Γ_L, which ultimately provided a solution to the source termination problem.

III. Development of a Method to Determine Γ_L

In RL877, we explained the difficulties in obtaining scattering parameters from a current distribution on the line if the line is relatively short. These discussions were based on the limitations of the method we have traditionally used which is discussed in Chapter 5 of RL877: the 'Standing Wave Method'. Overcoming the limitations of this approach was the original motivation for the development of the Reciprocity Method several years ago. Recently, we have taken a new approach which eliminates these difficulties. The technique uses Prony's method to fit the current on the strip with a set of complex exponentials. From the resulting spatial frequencies, amplitude and phase

coefficients, we can derive the reflection coefficient directly, even for short lines.

This method has been implemented to solve for the reflection coefficient of the one-port slot problems. By exciting the main feed line with a gap generator at the feed-through aperture and using Prony 's method to evaluate the current, the problem with the short circuit termination at the source is eliminated. By comparing to previously known results for open-end lines, we have found the technique to be adequate for lines as short as one-quarter wavelength, possibly shorter. Since such short lines can be accommodated, we can use the method directly even for the strip-fed slot cases, eliminating the Reciprocity Theorem Method altogether.

We now then have a model which produces reasonable reflection coefficients for the T-bar fed slots. Therefore, we now can proceed to evaluate the potential of the T-bar fed slots for wider bandwidth, based on the assumption that the model is providing valid results. We note that this method should provide improved accuracy for the two port case as well, especially for large slot offsets, however, it has not been implemented in the numerical codes or tested for that case. It also has beneficial features which could improve the efficiency of the codes for the microstrip-to-microstrip slot coupler (Chapter 5), since the main feed lines can now be much shorter.

IV. Investigation of Bandwidth for T-Bar Fed Slots

To investigate the bandwidth behavior of the T-bar fed slots, examine a specific case at 9.7 GHz. The geometry is specified in Table 1. We assume that we intend the slot to be matched at 9.7 GHz so we first must determine the proper dimensions for that condition. Figure 3 shows the effect of the terminations length on the slot reflection

Electrical Parameters	
Frequency	9.7 GHz
Dielectric	$\epsilon_r = 2.2$
Mechanical Parameters (inches)	
Ground Plane Spacing (c)	0.0625
Strip Width (W)	0.05
Cavity Width (b)	.750
Cavity Length (a)	.650
Slot Width (Ws)	0.05
Main Line Length (L - final)	.5871
Cross Line Center (X0B - final)	.5621

Table 1: T-Bar Case Parameters.

coefficient. The termination length is defined as the distance the main line extends beyond the slot, where it is coupled to the cross bar which is shorted at the side walls (see Figure 8.1, p.61). From Figure 3, we see that the termination length has a strong influence on the position of the curves on the chart. We also see the convergence of the curves to the value of Γ_L as the slot length approaches zero. (Along each curve, slot length is progressively reduced in the counter-clockwise direction.) Since our original goal is to match the slot at 9.7 GHz we choose the main line length to be fixed at .5621 inches ('tbar.5621.prony.data' case). For this case, the slot is most closely matched at a slot length of .5053 inches, as indicated.

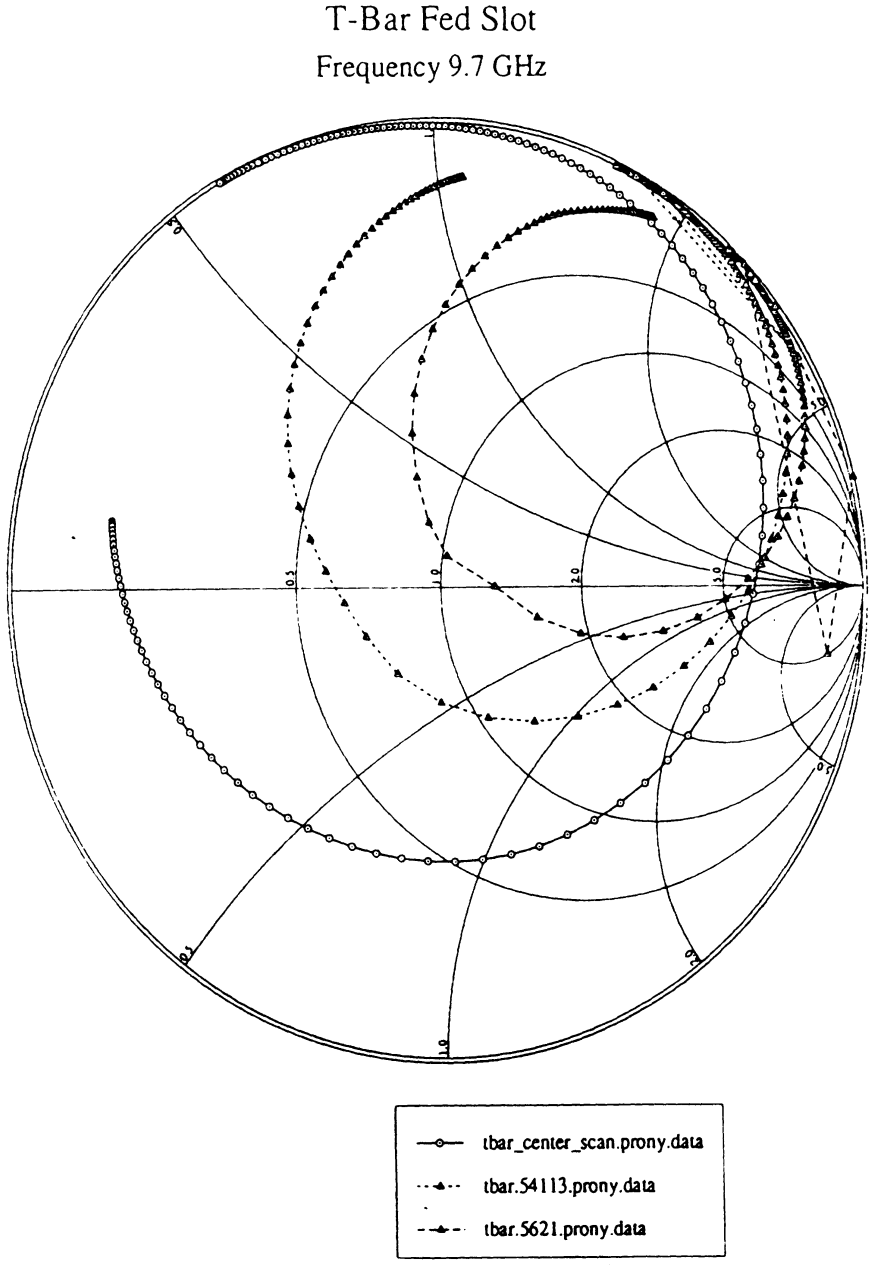

Figure 4: Reflection coefficient for the T-Bar fed slot with several different termination lengths.

We now generate a frequency response by running the model with this geometry at different frequencies. The results are shown in Figure 4. By finding the data points which correspond to a fixed slot length (.5053 inches indicated), we can plot the frequency response. It would appear that for this case, the projected frequency response has a strong similarity to the 'vs. length' curves. This suggests that the reflection coefficient rapidly traverses the area near $\Gamma = 0$ as a function of frequency, indicating a relatively narrow bandwidth, similar to the behavior of the two-port series fed slots.

In order to explore the possibility of greater bandwidth further, let us look again at Figure 4.. We note three characteristics indicated on the plot:

1. The relative position of the data point for a fixed slot length progresses counter-clockwise on the curves as the frequency is increased. This is an indication of the relationship of resonant frequency to slot length. For these types of slots, it is not necessarily inversely related to slot length in wavelengths, as discussed in Chapter 6 of RL877. To improve bandwidth, one must find the geometric or electrical parameters which minimize the sensitivity of resonant frequency to slot length.

2. The endpoints of the circles move around the chart in correspondence with the termination characteristics of the T-bar with frequency. In the case shown, this effect causes the positions of the entire data circles to shift in the *clockwise* direction as frequency is increased. If one can find a geometry such that the movement of these circles compensates for the movement of the fixed slot length data point discussed above, the bandwidth of the slot will be enhanced. This possibility is really the only unique characteristic of the T-bar fed slot approach which may make

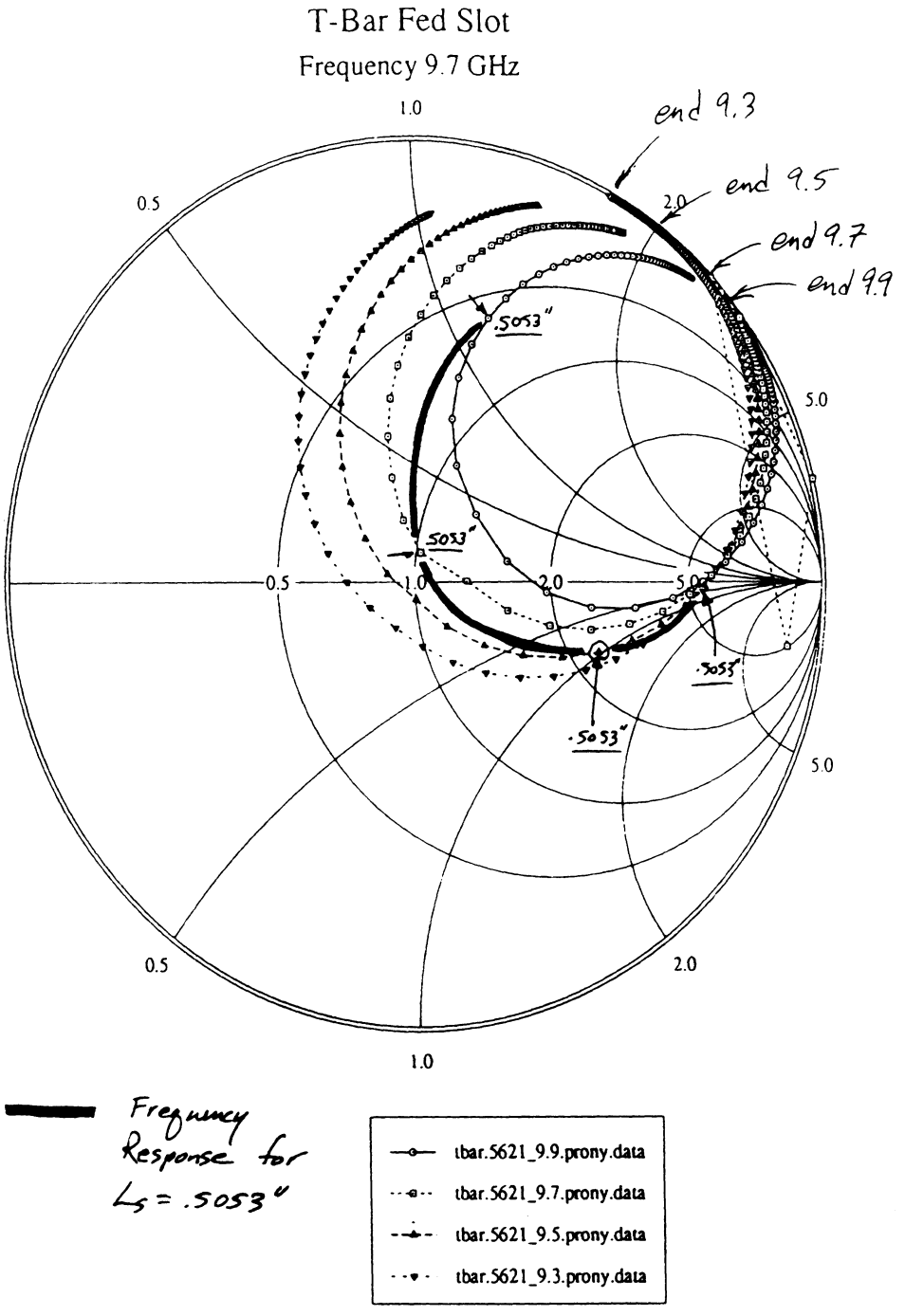

Figure 5: Reflection coefficient for the T-Bar fed slot as a function of frequency. Main feed line length fixed at .5621 inches.